

Slumps, slides and debris flows of the St. Pierre Slope:
a reanalysis of slope instability due to the 1929 Grand Banks Earthquake

by

Irena Schulten

Submitted in partial fulfilment of the requirements
for the degree of Doctor of Philosophy

at

Dalhousie University
Halifax, Nova Scotia
April 2019

© Copyright by Irena Schulten, 2019

DEDICATION

I dedicate this thesis to my family in particular my parents Leo and Margret Schulten, who always support me in my decisions and kept me going in difficult situations. They keep cheering me on with “Da musst du nun mal durch. Nützt ja nichts.” This thesis is further dedicated to everyone who helped me, even so I had to convince some of them with the promise that I spend a dinner and drink or two once this is over. Thanks a lot.

TABLE OF CONTENTS

| | |
|---|-------------|
| LIST OF TABLES | vi |
| LIST OF FIGURES | viii |
| ABSTRACT..... | xvi |
| LIST OF ABBREVIATIONS USED..... | xvii |
| ACKNOWLEDGEMENTS | xix |
| CHAPTER 1: INTRODUCTION..... | 1 |
| 1.1 RESEARCH OBJECTIVE | 1 |
| 1.2 THE 1929 GRAND BANKS EVENT | 8 |
| 1.3 CHAPTER SYNOPSIS..... | 11 |
| 1.3.1 Chapter 2..... | 11 |
| 1.3.2 Chapter 3..... | 13 |
| 1.3.3 Chapter 4..... | 15 |
| 1.3.4 Chapter 5..... | 17 |
| 1.4 REFERENCES CITED IN CHAPTER 1 | 17 |
| CHAPTER 2: SURFICIAL SEDIMENT FAILURES DUE TO THE 1929 GRAND BANKS EARTHQUAKE, ST. PIERRE SLOPE | 21 |
| 2.1 ABSTRACT..... | 21 |
| 2.2 INTRODUCTION AND OBJECTIVE..... | 22 |
| 2.3 PREVIOUS STUDIES | 24 |
| 2.4 METHODS..... | 25 |
| 2.5 RESULTS | 30 |
| 2.5.1 Morphological analysis..... | 30 |
| 2.5.2 Acoustic analysis..... | 30 |
| 2.6 DISCUSSION | 35 |
| 2.6.1 Seismic stratigraphy..... | 35 |
| 2.6.2 Mass transport deposits | 36 |
| 2.6.3 Fault and head scarps..... | 38 |
| 2.6.4 Sediment budget | 39 |
| 2.6.5 Implication on potential tsunami source..... | 40 |
| 2.7 CONCLUSION..... | 41 |
| 2.8 ACKNOWLEDGMENTS..... | 43 |
| 2.9 REFERENCES CITED IN CHAPTER 2 | 43 |
| CHAPTER 3: A MASSIVE SLUMP ON THE ST. PIERRE SLOPE, A NEW PERSPECTIVE ON THE 1929 GRAND BANKS SUBMARINE LANDSLIDE..... | 50 |
| 3.1 ABSTRACT..... | 50 |
| 3.2 INTRODUCTION..... | 51 |

| | |
|--|------------|
| 3.3 METHODS..... | 54 |
| 3.3.1 High resolution single- and multi-channel 2D seismic reflection data | 55 |
| 3.3.2 Other data | 58 |
| 3.4 RESULTS | 58 |
| 3.4.1 Seismic facies distribution..... | 58 |
| 3.4.2 Seismic stratigraphy..... | 60 |
| 3.4.3 Seismic units..... | 62 |
| 3.4.4 Reflection offsets | 63 |
| 3.5 DISCUSSION | 76 |
| 3.5.1 Stratigraphic evolution | 76 |
| 3.5.2 Evidence of slumping | 78 |
| 3.5.3 Fault movement..... | 82 |
| 3.5.4 Implications of the role of observed specific structures in the 1929 event .. | 86 |
| 3.5.5 Comparison to other continental slopes failures | 88 |
| 3.6 CONCLUSIONS | 89 |
| 3.7 ACKNOWLEDGMENTS AND DATA..... | 91 |
| 3.8 REFERENCES CITED IN CHAPTER 3 | 91 |
| CHAPTER 4: STRESS HISTORY AND SLOPE STABILITY IN THE 1929 GRAND BANKS FAILURE AREA..... | 100 |
| 4.1 ABSTRACT..... | 100 |
| 4.2 INTRODUCTION..... | 101 |
| 4.3 METHODS..... | 104 |
| 4.3.1 Sediment coring..... | 104 |
| 4.3.2 Core Physical properties..... | 105 |
| 4.3.3 Advanced Geomechanical Testing | 107 |
| 4.3.4 Factor of Safety – Infinite Slope Analysis | 112 |
| 4.3.5 Uncertainty assessment..... | 114 |
| 4.4 RESULTS | 115 |
| 4.4.1 Physical Properties | 115 |
| 4.4.2 Geomechanical properties | 121 |
| 4.4.3 Infinite Slope Stability Analysis | 124 |
| 4.5 DISCUSSION | 132 |
| 4.5.1 Consolidation status..... | 132 |
| 4.5.2 Present day slope stability | 134 |
| 4.5.3 Implications for the 1929 event..... | 137 |
| 4.6 CONCLUSION..... | 139 |
| 4.7 ACKNOWLEDGEMENTS..... | 140 |
| 4.8 REFERENCES CITED IN CHAPTER 4 | 141 |
| CHAPTER 5: CONCLUSIONS..... | 147 |
| 5.1 DIMENSION, DISTRIBUTION AND KINEMATICS OF 1929 SURFICIAL SEDIMENT FAILURES..... | 147 |
| 5.2 REFLECTION OFFSETS WITHIN THE QUATERNARY SECTION OF THE SLOPE - THE ST. PIERRE SLUMP..... | 148 |
| 5.3 PRESENT-DAY SLOPE STABILITY AND IMPLICATIONS ON THE 1929 EVENT..... | 151 |
| 5.4 POTENTIAL SOURCE MECHANISMS OF THE 1929 TSUNAMI..... | 152 |

| | |
|---|------------|
| 5.5 IMPLICATIONS ON OTHER, MORPHOLOGIC SIMILAR AREAS | 152 |
| REFERENCES..... | 154 |
| APPENDIX 1: CHAPTER 1 | 170 |
| APPENDIX 2: CHAPTER 4 | 172 |
| A2.1 DETERMINATION OF SEDIMENT PROPERTIES | 172 |
| <i>A2.1.1 Core Physical properties</i> | <i>172</i> |
| <i>A2.1.2 Consolidation testing.....</i> | <i>174</i> |
| <i>A2.1.3 Triaxial testing.....</i> | <i>178</i> |
| A2.2 FACTOR OF SAFETY – PEAK GROUND ACCELERATION CONVERSIONS..... | 178 |
| <i>A2.2.1 Equation used according to Atkinson and Boore (2006).....</i> | <i>178</i> |
| <i>A2.2.2 Equations used according to Campbell and Bozorgnia (2008).....</i> | <i>179</i> |
| <i>A2.2.3 Sediment density calculation using porosity information derived from Kominz et al. (2011)</i> | <i>181</i> |
| A2.3 RESULTS..... | 182 |
| <i>A2.3.1 Lithological core description.....</i> | <i>182</i> |
| <i>A2.3.2 Results Atterberg testing.....</i> | <i>184</i> |
| <i>A2.3.3 Results consolidation testing</i> | <i>188</i> |
| <i>A2.3.4 Results Triaxial testing</i> | <i>192</i> |
| <i>A2.3.5 Infinite Slope stability Analysis – Magnitude-PGA conversions.....</i> | <i>193</i> |

LIST OF TABLES

| | | |
|------------|---|-----|
| Table 1.1: | Parameters used in the tsunami simulation of Fine et al. (2005) versus reported observations from earlier studies e.g. Piper et al. (1988; 1999). | 11 |
| Table 1.2: | Authors contribution to chapter 2 “Surficial Sediment Failures due to the 1929 Grand Banks Earthquake, St. Pierre Slope”. | 12 |
| Table 1.3: | Author contribution to chapter 3 “A massive slump on the St. Pierre Slope, a new perspective on the 1929 Grand Banks submarine landslide”..... | 14 |
| Table 1.4: | Author contribution to chapter 4 “Stress history and slope stability in the 1929 Grand Banks failure area”. | 16 |
| Table 2.1: | Acoustic facies along St. Pierre Slope | 27 |
| Table 2.2: | Seismic relationships along St. Pierre Slope. | 27 |
| Table 3.1: | Seismic reflections recognized in this study in comparison to earlier studies and their estimated age. Horizons R2, R4 and R5 are not shown, as they do not correlate with dated reflectors of earlier studies. | 57 |
| Table 3.2: | Seismic facies A to E and acoustic facies F to G on the St. Pierre Slope. Facies B to G that are interbedded with, or overly, facies A are highlighted in pink. | 59 |
| Table 3.3: | Seismic units that are distinguished on the St. Pierre Slope and identified unit boundaries..... | 62 |
| Table 3.4: | Examples of structural features at the St. Pierre Slope. Important features are highlighted in pink. | 64 |
| Table 3.5: | Comparison of seismic stratigraphies mapped across St. Pierre Slope. Sedimentation rates are calculated using sediment thickness distribution of apparent un-failed areas..... | 77 |
| Table 4.1: | Results from Atterberg testing on samples from core 2015MSM_0002GC and MSM47-24-01 with percentage of natural water content (w), liquid limit (LL), plastic limit (PL), plasticity index (PI), liquidity index (LI) and sediment classification. See appendix A2.3.2 (Figs. A2.7-A2.14). | 116 |
| Table 4.2: | Summary of the most important sediment properties derived from geomechanical testing. For more information see appendices A2.3.3 and A2.3.4. | 121 |

| | |
|---|-----|
| Table 4.3: Summary of parameters used in the four different scenarios and resultant critical FOS..... | 124 |
| Table 4.4: Summary of results from pseudo-static infinite slope stability analysis showing the critical PGA (g) corresponding to a FOS of 1 and conversion to magnitude and distance using AB2006 and CB2008. | 129 |
| Table A1.1: Multibeam swath bathymetry data used in this research thesis. | 170 |
| Table A1.2: Ultra-high resolution seismic data used in this research thesis. | 170 |
| Table A1.3: 2D seismic reflection data used in this thesis. All data are high-resolution seismic (<2 km signal penetration), except for TGS and STP data sets that are industry-scale seismic data (>5 km signal penetration). | 171 |
| Table A2.1: PGA (g) using equations from Atkinson and Boore (2006)..... | 193 |
| Table A2.2: PGA (g) using equations from Campbell and Borzognia (2008)..... | 193 |

LIST OF FIGURES

| | | |
|-----------|---|----|
| Fig. 1.1: | Regional bathymetric map of Atlantic Canada with the location of the Laurentian Fan indicated within the red dotted rectangle off the southwestern Grand Banks of Newfoundland. Coloured dots indicate earthquake epicenters from 1985 to present (Earthquakes Canada, 2018). The red star indicates the location of the M_w 7.2 November 18 th , 1929 earthquake, as relocated by Bent (1995). The violet line indicates approximate location of the Cobequid-Chedabucto transform fault and the Newfoundland Fracture Zone. The globe was created using ArcGlobe, while seafloor renders were derived using the GEBCO 2014 global bathymetric grid and imaged in ArcMap. NS = Nova Scotia, NF = Newfoundland and GB = Grand Banks of Newfoundland.2 | 2 |
| Fig. 1.2: | A seafloor render of the Laurentian Fan region, including the St. Pierre Slope study area. The red dashed polygon represents the area where 100% of the seafloor sustained sediment failure and the black dashed line outlines the total region where local failures are observed (Piper et al., 1999; Mosher & Piper, 2007). The epicenter location of the M_w 7.2 1929 Grand Banks earthquake is shown with a red star. The coloured areas of the seafloor render were generated from multibeam data while the light grey areas were derived from the GEBCO 2014 global bathymetric grid.3 | 3 |
| Fig. 1.3: | Seafloor bathymetric map of the area of the continental slope seaward of the southwestern Grand Banks, including a portion of the Laurentian Fan. The area outlined by the dashed pink line is the research area for this thesis – the St. Pierre Slope.6 | 6 |
| Fig. 1.4: | Maps showing the different sets of data (BIO legacy data, analog and digital, and new data from MSM45 and MSM47) available for this thesis.7 | 7 |
| Fig. 2.1: | (A) Regional overview map of Atlantic Canada. The study area (C, red box) is located at the eastern part of the Laurentian Fan system (B, red dotted box) of the southwestern Grand Banks of Newfoundland. (B) Laurentian Fan with presumed main failure area (red shaded area), and area of local sediment failure (black dotted area) as indicated by the cable breaks (red dots on yellow lines = instantaneous; white dots = sequential) by Piper et al. (1999) and Mosher and Piper (2007). (C & D) Multibeam swath bathymetry of the St. Pierre Slope (pink dotted area), including epicenter location of the M_w 7.2 1929 Grand Banks earthquake (red star). (C) Location of high-resolution seismic profiles and locations of profiles presented in Fig. 2.2 (A = yellow line, B, C, D & E = red lines) and Fig. 2.4 (blue line) are highlighted. (D) Morphological characteristics are highlighted.24 | 24 |

| | | |
|-----------|---|----|
| Fig. 2.2: | Examples of different morphologies and distribution of surficial failure deposits along St. Pierre Slope. (A) N-S-trending profile across the upper slope. (B) and (C) are zoomed sections, displaying a fault scarp and head scarp, typically observed at this slope. (D) The middle slope shows ~35 m-thick failure deposits. (E) The lower slope is characterized by thin (~4 m) slide deposits on the levees and thick (10-25 m thick) side deposits within the channels. The locations of profiles are indicated in Fig. 2.1..... | 32 |
| Fig. 2.3: | (A) The estimated volume of sediment that failed in 1929 illustrating that most sediment is missing below the deep-water head scarps. Note: Estimates are restricted to the upper study area down to 2100 mwd, as the reference horizon (Q91) needed to assess the volume of sediment missing could not be correlated further downslope. (B) Surficial failure deposits along St. Pierre Slope. Failure deposits are in the order of 2-5 m from 730 to 1700 mwd and 2800 to 4000 mwd, but ~35 m-thick from 1700 to 2800 mwd. Fault scarps (dashed, thick black lines) and head scarps (thin black lines) are highlighted..... | 34 |
| Fig. 2.4: | Multichannel 2D seismic reflection profile across the upper St. Pierre Slope, acquired in 2015. Faults associated with upper fault scarps extend down to 350 m depth. Note: Slightly wavy horizon in ~400 m sub-bottom depth. Other 2D seismic reflection profiles indicate that faults are restricted to this wavy reflection horizon. For location of profile, see Fig. 2.1..... | 35 |
| Fig. 3.1: | Regional bathymetric map of Atlantic Canada with the location of the study area indicated within the red dotted rectangle off the southwestern Grand Banks of Newfoundland. Coloured dots indicate earthquake epicentres available from 1985 to present (Earthquakes Canada). The red star indicates the location of the M_w 7.2 November 18th, 1929 earthquake, as relocated by Bent (1995). The globe was created using ArcGlobe, while seafloor renders were derived using the GEBCO 2014 global bathymetric grid and imaged in ArcMap. NS = Nova Scotia, NF = Newfoundland and GB = Grand Banks of Newfoundland..... | 52 |
| Fig. 3.2: | A seafloor render of the upper slope region of the Laurentian Fan, including the St. Pierre Slope study area. The epicenter location of the M_w 7.2 1929 Grand Banks earthquake is shown with a red star. The red dashed polygon represents the area where 100% of the seafloor sustained sediment failure and the black dashed line outlines the total region where local failures are observed (Piper et al., 1999; Mosher & Piper, 2007). The dark grey areas of the seafloor render were generated from multibeam data while the light grey areas were derived from the GEBCO 2014 global bathymetric grid..... | 53 |

| | | |
|-----------|---|----|
| Fig. 3.3: | Left: Tracklines showing the location of 2D seismic reflection data acquired in the Laurentian Fan area over the past three decades. The red star marks the epicenter of the 1929 earthquake. The red rectangle outlines the area shown to the right..... | 54 |
| Fig. 3.4: | Left: Multibeam sonar bathymetric render of the St. Pierre Slope study area. The location of the 1929 Grand Banks earthquake is shown with a red star, while the red lines represent tracks of seismic data shown in Figs. 3.5 to 3.13. Right: A slope angle map of the same area that accentuates some of the steeper morphologic features such as escarpments and channel walls; a few of which are labelled..... | 55 |
| Fig. 3.5: | A strike-profile across the upper St. Pierre Slope between 800 and 1000 mwd, see Fig. 3.4 for location. The upper panel is without interpretation, the lower panel is with interpretations and shows horizons mapped across the slope area (R1 to R9) and interpreted seismic units 1 to 5. The black dashed lines connect reflection offsets. Offset “I” is discussed in section “3.4.4”. Red arrows in the upper panel highlight intersections with other seismic profiles..... | 61 |
| Fig. 3.6: | Dip-oriented seismic reflection profile along the eastern part of the upper St. Pierre Slope (see Fig. 3.4 for location). A reflection offset is evident underneath the escarpment in ~750 mwd. The upper panel is the seismic profile without interpretation and the middle and lower panels show the interpreted section. The section of the profile that corresponds with that shown in Fig. 3.7 is indicated by the red bar. The black dashed lines follow the line of reflection offsets. This offset is labelled “I”. The inset profiles in the upper right corner of the middle panel show an enlargement of the upper strata down to ~150 m sub-bottom depth (their locations are indicated with red boxes), The bottom image shows an enlarged section of the profile (green dotted box) to highlight the nature of the offset. Facies C and D are labelled and highlighted in both insets. The red arrow in the upper panel highlight intersections with other seismic profiles. | 67 |
| Fig. 3.7: | Example of ultra-high resolution seismic data. Offset “I” is highlighted. Stratified reflections (Q91 to Q99) continue to both sides of offset “I”. Reflection interpretations are from Schulten et al. (2019). The profile location is shown in Fig. 3.6. | 67 |
| Fig. 3.8: | A dip-oriented seismic reflection profile along the central part of the upper St. Pierre Slope (see Fig. 3.4 for location). The upper panel shows the profile without interpretation, the lower panel is with interpretation. The location of offsets “I”, “II” and “III” are indicated with black dashed lines. Red arrows in the upper panel highlight intersections with other seismic profiles. | 68 |

| | | |
|------------|--|----|
| Fig. 3.9: | Strike-oriented seismic reflection profile across the upper St. Pierre Slope (see Fig. 3.4 for location). The upper panel shows the seismic profile without interpretation, the lower panel is with interpreted horizons and labelled structural features. Note the indistinct, westward dipping plane of reflection offsets (black dashed line) and deep incision of St. Pierre Valley. Red arrows in the upper panel highlight intersections with other seismic profiles. | 70 |
| Fig. 3.10: | Dip-oriented seismic reflection profile from the western upper St. Pierre Slope (see Fig. 3.4 for location). The upper panel is the profile without interpretation, the lower panel is interpreted with mapped horizons. Displacement “III”, indicated with a black dashed line, is evident beneath a low gradient seafloor escarpment. There is no displacement evident beneath a larger seafloor escarpment further downslope. A rhombic shaped body formed by offset “III” is imaged by the data and indicated in the lower panel. Reflection offsets above this rhombic shaped body are indistinct. The red arrow in the upper panel highlight intersections with other seismic profiles. | 71 |
| Fig. 3.11: | A dip-oriented seismic reflection profile from the middle to lower slope. Its location is shown in Fig. 3.4. The upper panel is without interpretation, the lower panel is with interpretation of mapped horizons. Black dashed lines labelled “IV” and “V” indicate the location of reflection offsets. Indistinct reflection offsets (“V”) are evident underneath a 20-50 m-high escarpment. A more distinct offset (“IV”) is visible towards the lower slope channel, which shows erosion down to horizon R5. | 73 |
| Fig. 3.12: | Dip-oriented seismic reflection profile across the middle and lower St. Pierre Slope (location is shown in Fig. 3.4) with interpretation. The area encased by the oval shows undulating seismic reflections with amplitude reductions. The black dashed line connects reflection offsets (“IV”). | 74 |
| Fig. 3.13: | Industry seismic profile across the eastern part of the upper, middle and lower St. Pierre Slope (see Fig. 3.4) indicating the concave nature of horizon R6. The black dashed line indicates the plane of offset “IV”. Data compliments of TGS-Nopec reproduced with permission. | 74 |
| Fig. 3.14: | Overview map of the St. Pierre Slope indicating the location of mapped reflection offsets and their sub-bottom depths. Dashed lines indicate reflection offsets with similar structure and depth. Question marks denote areas where seismic data did not provide sufficient information due to low seismic resolution. The red star indicates the epicenter of the 1929 earthquake. Labels “I” to “V” show the seafloor outcrop location of mapped reflection offsets. Offsets “IV” are often covered by thick, chaotic deposits. | 75 |

| | | |
|------------|---|-----|
| Fig. 3.15: | Depth versus displacement of fault planes of the main slump system. The amount of displacement generally increases with depth..... | 83 |
| Fig. 3.16: | Three scenarios that account for displacement observed along a fault system. Examples show fault developments from horizon R6 to the seafloor..... | 84 |
| Fig. 3.17: | Top: Block diagram of the St. Pierre Slope that shows development of the fault systems and related slump. The blue surface indicates displacements observed along horizon R6. Red arrows indicate the direction of sediment displacement. Bottom: Schematic N-S dipping profile illustrating the identified décollements (R6, R1, R0) and main slump direction (red arrows) along these décollements..... | 87 |
| Fig. 4.1: | Right: Regional overview map of Atlantic Canada. The location of the study area is shown within the red box and the red star indicates the location of the M_w 7.2 1929 earthquake. Other earthquakes are highlighted as coloured dots as recorded since 1985 by Earthquake Canada (2018). The violet line indicates approximate location of the Cobequid-Chedabucto transform fault and the Newfoundland Fracture Zone. GEBCO 2014 global bathymetric grid was used and imaged in ArcMap. NS = Nova Scotia, NF = Newfoundland and GB = Grand Banks of Newfoundland. Left: Location map showing core sites used in this study and 1929 earthquake epicentre (red star). Black lines (A to D) indicate the location of ultra-high resolution profiles shown in Fig. 4.2..... | 103 |
| Fig. 4.2: | (A & B) Hunttec DTS sparker profile, acquired during CCGS Hudson cruise 2007-020 and (C & D) parasound subbottom profiler data acquired during RV Maria S. Merian cruise MSM47. Locations of the seismic profiles are shown in Fig. 4.1. The seismic profiles show undisturbed, stratified sediments at the core locations (red & black arrow). A small, approximately 8 m-high escarpment is present to the south of the core location. The orange line shows the location of a failure plane, Q99 (McCall, 2006; Schulten et al., 2019). | 104 |
| Fig. 4.3: | Lithology and physical property measurements for core 2015MSM_0002GC..... | 118 |
| Fig. 4.4: | Lithology and geotechnical properties measured from physical and geomechanical testing on sediment core MSM47-24-01 and its FOS. Minimum FOS observed within the core are highlighted as transparent green boxes..... | 119 |

| | | |
|------------|--|-----|
| Fig. 4.5: | Lithology and geotechnical properties of sediment core 99036-003pc retrieved from the NRCan database. The lithological description is published in McCall (2006). The FOS values were calculated as part of this study. The minimum FOS at ~640 cm is highlighted..... | 120 |
| Fig. 4.6: | A plot of geotechnical properties measured from physical and geomechanical testing on the sediment core and its FOS. Minimum FOS observed within the core is highlighted as transparent blue box. | 123 |
| Fig. 4.7: | A comparison of shear strength trends from each single core and a compiled trend (red line) from five undisturbed cores. Significant outliers were removed before calculation of the trends. | 125 |
| Fig. 4.8: | Peak-ground acceleration (PGA) at the St. Pierre Slope for different earthquake magnitudes (M_w) and distances using an equation from Atkinson and Boore (2006) (AB2006). The red square shows the 1929 earthquake (M_w 7.2, 26 km). | 126 |
| Fig. 4.9: | Peak-ground acceleration (PGA) at the St. Pierre Slope for different earthquake magnitudes (M_w) and distances using an equation from Campbell and Bozorgnia (2008) (CB2008). The red square shows the 1929 earthquake (M_w 7.2, 26 km). | 126 |
| Fig. 4.10: | Results of infinite slope stability analysis over a range of slope angles for sediment cores 2015MSM_0002GC, MSM47-24-01 and 99036-003pc. The marker on each line indicates present day slope angle in the study area of 2.5-4.9°, that corresponds to a FOS>1..... | 127 |
| Fig. 4.11: | Results of a slope stability analysis over a range of sediment failure thicknesses (2-550 m). Solid lines represent results using extrapolated trends in shear strength and effective overburden (SSA-case 1). Dashed lines represent results using the Kominz et al. (2011) equation to estimate sediment bulk density (SSA-case 2). | 128 |
| Fig. 4.12: | Slope stability analysis over a range of PGA's. The critical PGA in the study area under present day and pseudo-static conditions is 0.09-0.125 g..... | 129 |
| Fig. 4.13: | Results of a stability analysis for different PGA's over a range of sediment failure thicknesses (2-550 m). From top to bottom: Results of slope stability analysis using PGA-case 1 (S_u trend, $P'_{vo.trend}$), PGA-case 2 (S_u trend, $P'_{vo.porosity}$) and PGA-case 3 (S_u NSP, $P'_{vo.porosity}$) (Table 4.3). | 131 |
| Fig. 5.1: | 3D image of the St. Pierre Slope with 2D reflection seismic (envelope) showing structures in the sub-bottom down ~550 m. Identified décollements (R0, R1 & R6) are highlighted and trajectories indicate the suggested movement of the St. Pierre Slump. The red dashed lines show the position of reflection offsets interpreted as faults..... | 150 |

| | | |
|-------------|---|-----|
| Fig. A2.1: | E - log p' curve derived from the consolidation testing on a sample (553 cm) from sediment core 2015MSM_0002GC. Cassagrande's method to derive P _c over the point of maximum curvature is illustrated. | 174 |
| Fig. A2.2: | Square-root-of-time method according to Taylor (1942). | 176 |
| Fig. A2.3: | Plot of derived void ratio (e) versus the hydraulic conductivity (k) derived for different load increments. The derived linear relationship of this e - log k curve can be used to calculate the hydraulic conductivity at the effective pre-consolidation state. | 177 |
| Fig. A2.4: | Stress path's derived for the triaxial sample of sediment core 2015MSM_0002GC, 563-575cm. Red line shows the derived failure envelope, as described by the Mohr-Coulomb criterion. | 178 |
| Fig. A2.5: | Results of the lithological core description of marine sediment core 2015MSM_0002GC. | 182 |
| Fig. A2.6: | Results of the lithological core description of marine sediment core MSM47-24-01. | 183 |
| Fig. A2.7: | Result of the Atterberg limits testing according to the Cassagrande diagram. Sample at 106 cm core depth of sediment core 2015MSM_0002GC is a lean clay with low to intermediate plasticity. | 184 |
| Fig. A2.8: | Result of the Atterberg limits testing according to the Cassagrande diagram. Sample at 114 cm core depth of sediment core 2015MSM-0002GC is a lean clay with low to intermediate plasticity. | 184 |
| Fig. A2.9: | Result of the Atterberg limits testing according to the Cassagrande diagram. Sample at 552 cm core depth of sediment core 2015MSM_0002GC is a lean clay with low to intermediate plasticity. | 185 |
| Fig. A2.10: | Result of the Atterberg limits testing according to the Cassagrande diagram. Sample at 190 cm core depth of sediment core MSM47-24-01 is a lean clay with low to intermediate plasticity. | 185 |
| Fig. A2.11: | Result of the Atterberg limits testing according to the Cassagrande diagram. Sample at 195 cm core depth of sediment core MSM47-24-01 is a lean clay with low to intermediate plasticity. | 186 |
| Fig. A2.12: | Result of the Atterberg limits testing according to the Cassagrande diagram. Sample at 350-355 cm core depth of sediment core MSM47-24-01 is a lean clay with low to intermediate plasticity. | 186 |

| | | |
|-------------|---|-----|
| Fig. A2.13: | Result of the Atterberg limits testing according to the Cassagrande diagram. Sample at 355-360 cm core depth of sediment core MSM47-24-01 is a lean clay with low to intermediate plasticity. | 187 |
| Fig. A2.14: | Result of the Atterberg limits testing according to the Cassagrande diagram. Sample at 712-717 cm core depth of sediment core MSM47-24-01 is a lean clay with low to intermediate plasticity. | 187 |
| Fig. A2.15: | Summary derived from the consolidation testing on a sample extracted from 553-555.5 cm core depth of sediment core 2015MSM_0002GC. The corresponding $e - \log p'$ curve is shown in Fig. A2.1. | 188 |
| Fig. A2.16: | Summary (top) and $e - \log p'$ curve (bottom) derived from the consolidation testing on a sample extracted from 351-353 cm core depth of sediment core MSM47-24-01. Cassagrande's method to derive P'_c over the point of maximum curvature is illustrated. | 189 |
| Fig. A2.17: | Summary (top) and $e - \log p'$ curve (bottom) derived from the consolidation testing on a sample extracted from 357-358.5 cm core depth of sediment core MSM47-24-01. Cassagrande's method to derive P'_c over the point of maximum curvature is illustrated. | 190 |
| Fig. A2.18: | Summary (top) and $e - \log p'$ curve (bottom) derived from the consolidation testing on a sample extracted from 713-714.5 cm core depth of sediment core MSM47-24-01. Cassagrande's method to derive P'_c over the point of maximum curvature is illustrated. | 191 |
| Fig. A2.19: | Summary (top) and the Mohr Coloumb failure envelope (bottom) derived from the triaxial testing on a sample extracted from 116.5-128 cm core depth of sediment core 2015MSM_0002GC. | 192 |
| Fig. A2.20: | Summary derived from the triaxial testing on a sample extracted from 563-575 cm core depth of sediment core 2015MSM_0002GC. The derived Mohr Coloumb failure envelope is shown in Fig. A2.4. | 193 |

ABSTRACT

The 1929 Grand Banks submarine landslide on the southwestern Grand Banks of Newfoundland was triggered by a M_w 7.2 strike-slip earthquake. It is the first studied example with an unequivocal connection between earthquake, landslide and tsunami and led to the first recognition of naturally occurring submarine turbidity currents. It ultimately caused 28 casualties and significant economic damage. The landslide has been identified as a widespread, retrogressive, shallow sediment failure (upper 20 m) in 730 m water depth (mwd). It is difficult to reconcile that this style of failure in deep water generated a large tsunami. The objective of this thesis is to investigate other potential causal mechanisms and contributing factors involved in the 1929 event. The study focusses on St. Pierre Slope, the main failure area. A comprehensive analysis of multiscale 2D seismic reflection data, multibeam echosounder data and geomechanical testing indicated that sediment failure at St. Pierre Slope is more complex than previously suggested. Results show that surficial sediment failures occurred predominately from ~ 25 m-high escarpments in >1700 mwd. The translational, possible retrogressive failures involved ~ 100 km³ of sediment material that either rapidly deposited on the slope (~ 60 km³) or became entrained into channelized turbidity currents (~ 40 km³). Numerous oblique, low angle ($\sim 17^\circ$) faults are evident underneath escarpments to ~ 550 m below seafloor (mbsf) with up to 100 m-high vertical displacement. The faults are interpreted as part of a massive (560 km³) complex slump with evidence of multiple décollements (250, 400-550 mbsf) and slumping in at least two directions. It is interpreted that the 1929 earthquake triggered slumping of the 550 m-thick strata of sediment. Displacement of the slump possible resulted in seafloor volume displacement of 70 to 130 km³. Instantaneous displacement of the slump, therefore, is likely more efficient for tsunami generation than translational, shallow failures. Slope stability analysis indicates that the 1929 earthquake, presence of weak layers and possible displacement of the slump caused the surficial failures. These findings indicate two failure mechanisms for the 1929 submarine landslide that both likely contributed to tsunami generation: massive slumping (~ 550 m thick) and widespread, surficial (<25 m) sediment failures.

LIST OF ABBREVIATIONS USED

| | |
|--------|---|
| A_c | correction for anisotropic consolidation |
| A_f | Skempton's pore pressure parameter at failure |
| A_r | correction for cyclic loading |
| AOC | apparent overconsolidation |
| ASTM | originally stands for American Society for testing and materials, an international standards organization |
| AB2006 | equation from Atkinson and Boore (2006) |
| BIO | Bedford Institute of Oceanography |
| BP | before present |
| c' | effective cohesion |
| C_c | compression index |
| C_r | recompression index |
| C_v | coefficient of consolidation |
| CB2008 | equation from Campbell and Bozorgnia (2008) |
| CCGS | Canadian Coast Guard Ship |
| CIU | multistage isotropically-consolidated-undrained triaxial test |
| CL | lean clay |
| DTS | deep tow survey |
| e | void ratio |
| FOS | factor of safety |
| GB | Grand Banks |
| GC | gravity core |
| GDS | Global Digital Systems |
| GEBCO | General Bathymetric Chart of the Oceans |
| GIESA | name of direct shear manufacturer |
| GSCA | Geological Survey of Canada, Atlantic |
| IRD | ice rafted debris |
| k | hydraulic conductivity |
| K_0 | coefficient of lateral earth pressure at rest |
| LGM | last glacial maximum |
| LI | liquidity index |
| LL | liquid limit |
| m | a soil constant = 0.8 |
| Marum | Center for Marine Environmental Science, University of Bremen |
| mbsf | meter below seafloor |
| msbsf | milliseconds below seafloor |
| M_w | moment magnitude |
| MSCL | multi-sensor core logger |
| MSM | Maria S. Merian |
| MTD | mass transport deposit |
| NC | normal consolidated |
| NF | Newfoundland |
| NRCan | Natural Resources of Canada |

| | |
|----------------------------|--|
| NS | Nova Scotia |
| NSP | Normalized Soil Properties |
| NSP _{ds} | NSP calculated using results from the direct shear test |
| NSP _{triax} | NSP calculated using results from triaxial testing |
| OC | overconsolidated |
| OCR | overconsolidation ratio |
| p-wave | pressure wave |
| pc | piston core |
| P'_c | pre-consolidation stress |
| P'_r | residual stress |
| P'_{vo} | total effective overburden stress |
| $P'_{vo \text{ porosity}}$ | effective overburden stress estimate using porosity information calculated with the equation of Kominz et al. (2011) |
| $P'_{vo \text{ trend}}$ | extrapolated effective overburden stress using core data |
| PGA | Peak ground acceleration |
| PGA-case | cases made for pseudo-static slope stability analysis |
| PI | plasticity index |
| PL | plastic limit |
| Q91-Q99 | seismic reflections, dated by McCall (2006) on the basis of sediment cores |
| ROWE | manufacturer name of GDS consolidation cell |
| RV | research vessel |
| s' | effective average mean stress |
| S | ratio of measured S_u to triaxial consolidation stress |
| SSA-case | cases made for static slope stability analysis |
| S_u | undrained shear strength |
| $S_{u \text{ NSP}}$ | normalized shear strength trend using NSP methodology |
| $S_{u \text{ trend}}$ | linearly extrapolated shear strength trend using core data |
| S_u/P'_v | normalized shear strength ratio derived from the CIU triaxial test |
| t' | maximum shear stress |
| τ_f | shear strength |
| τ_m | shear stress |
| v_{30} | shear wave velocity in 30 m sub-bottom depth |
| UC | underconsolidated |
| w | water content |
| ϕ' | specific effective friction angle |
| σ_1 | deviator stress |
| β | slope angle |
| η | porosity |

ACKNOWLEDGEMENTS

I would like to thank my supervisor committee, Drs. David C. Mosher, Markus Kienast, Sebastian Krastel, David J. W. Piper, and Stephanie Kienast for guidance, constructive criticism and feedback, and their commitment towards this thesis project.

Special thanks goes to my primary supervisor Dr. David Mosher for offering me this thesis project and advising me over the past five years with constructive feedback, discussions and especially for his patient editing of this thesis. Special thanks goes further to Dr. David Piper for providing financial support during the last year, guidance and advice regarding the thesis. Thanks to Drs. Sebastian Krastel and Ralph Schneider I was able to participate in two joint research expeditions between the Geological Survey of Canada Atlantic (GSCA), Dalhousie University, the University of Kiel and the University of Bremen, Germany. Both DFG-funded Expeditions, MSM45 (Ralph Schneider) and MSM47 (Sebastian Krastel), took place in 2015 onboard the German research vessel *Maria S. Merian* and contributed important research information towards this thesis project. In this context I also like to acknowledge the scientific staff and crew of the *Maria S. Merian* expeditions. The software ps32sgy developed by Hanno Keil (University of Bremen) was used to convert Parasound data into SEG-Y formats. Dr. Achim Kopf at Marum of the University of Bremen, Germany and his working group allowed me to use their facility during a two-month research stay and assisted me in using their equipment.

I like to thank Dr. Finn Løvholt for agreeing upon request from Dr. David Mosher to simulate the 1929 tsunami based on the new findings in this project and for including me in his manuscript “Modelling of the 1929 Grand Banks slump and landslide tsunami” that was published in the Special Volume 477 of the Geological Society of London.

Over the past five years the GSCA at the Bedford Institute of Oceanography (BIO) kindly supplied office space, computing facilities and laboratory equipment. Key data sets used in this thesis were acquired by the GSCA. Kevin MacKillop allowed me to use his laboratory for the geotechnical tests and who was a great help for the geotechnical analysis

on the sediment cores. Jenna Higgins and Kate Jarret assisted with physical analysis in the core laboratory of the BIO. The software REGJP2000 developed by Bob Courtney was used to digitize the analog seismic data into SEG-Y formats in order to use them in IHS Kingdom Suite™. Thank you to TGS-Nopec for allowing use of their seismic profile.

Financial support for this project was provided through the NSERC CREATE Transatlantic Ocean System Science and Technology (TOSST) grant to Dalhousie University and the NSERC Discovery Grants to Drs. David Mosher and David Piper. TOSST, S4SLIDE, IGCP, UNESCO, DSU and DAGS provided travel grants for conference visits.

I like to acknowledge fellow grad students and scientists at the Geological Survey of Canada Atlantic at BIO that supported me in various ways. Among them are Dr. John Evangelatos, Meng Tang, Jane Hawken, Laura-Ann Broom, Kimberley A. Jenner and Dr. Kevin Sorochan, as well as Drs. Alexandre Normandeau and Calvin Campbell.

I also like to thank my friends in Halifax and Germany, in particular Jessika, Britta & Matthias, Melanie, Mithat, Mareike & Thorsten, Yvonne, Imke, and Jennifer. I further thank my roommates for their support, especially. Dudley, Florian, and Raphael.

Finally, I like to especially thank my parents, Leo and Margret Schulten and my sister, Andrea Meyer and family for their support and patience.

CHAPTER 1: INTRODUCTION

1.1 RESEARCH OBJECTIVE

Gravitational mass-failure of sediment on submarine slopes is a geologically common process found in a variety of marine environments (Mosher et al., 2010). The volume of sediment remobilised by submarine slope failures can be far larger than any subaerial landslide and even exceed the total annual river input to the ocean (Talling et al., 2007; Mosher, 2008; Clare et al., 2014). Submarine sediment mass failures occur on a variety of scales, styles and involve different flow types ranging from avalanches to slumps, slides, and debris flows that move different distances downslope and at different velocities (Heezen & Ewing, 1952; Talling et al., 2007; Mosher et al., 2010). These processes are not only important for understanding global sediment flux to the deep sea, but they also shape the continental margin (Rebesco et al., 2017), play a role in development of sedimentary basins and control sediment facies distributions (Mosher et al., 2010; Clare et al., 2014). In addition, slope failures represent a hazard to seafloor structures such as underwater pipelines, cables and hydrocarbon development platforms. They also have the potential to generate tsunamis (Twichell et al., 2009; Mosher et al., 2010; Clare et al., 2014; Harbitz et al., 2014).

The 1929 submarine landslide that occurred on the southwestern Grand Banks of Newfoundland (Fig. 1.1) is a perfect example for an historic mass failure event that had severe consequences. The landslide rapidly evolved into a massive turbidity current that moved an estimated 100 km³ of sediment to the deep sea and severed telecommunication cables (Fig. 1.2) (Heezen & Ewing, 1952; Piper & Aksu, 1987; Hughes Clarke, 1988; McCall, 2006). The 1929 landslide also generated a large tsunami that caused 28 casualties and destroyed coastal infrastructure on southern Newfoundland and parts of Nova Scotia (Ruffman, 2001; Fine et al., 2005).

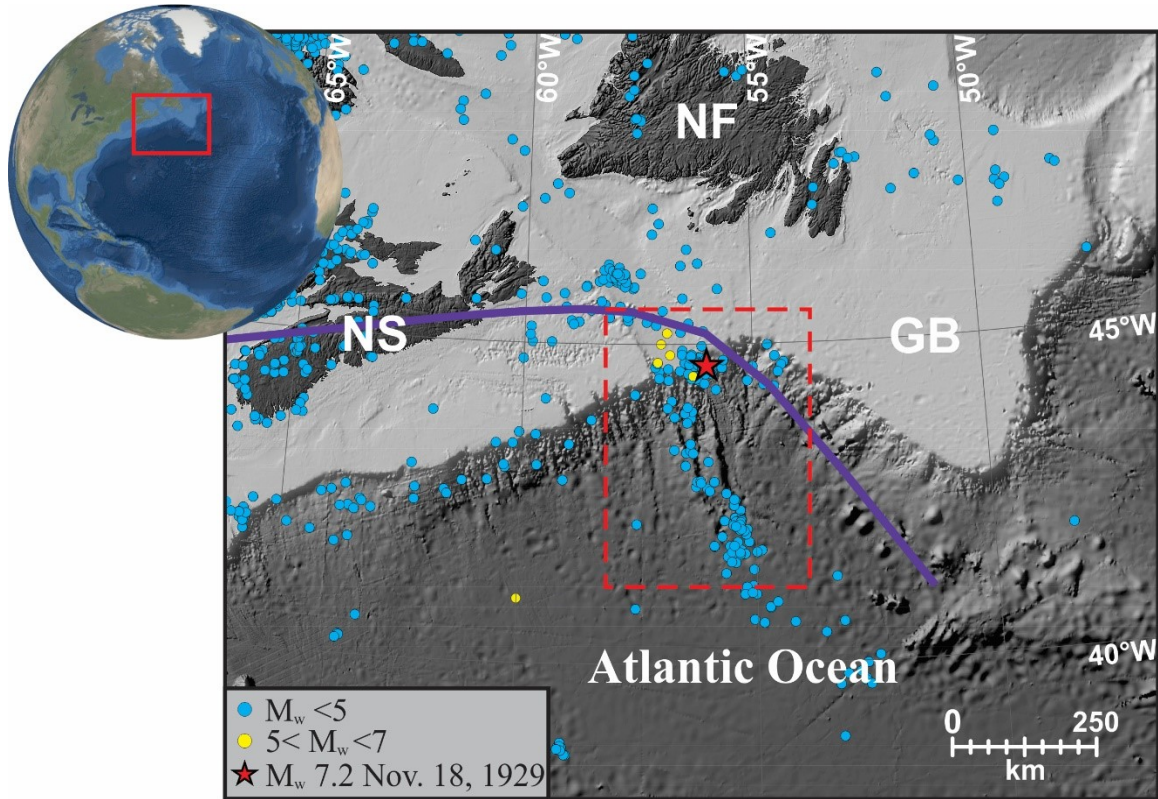


Fig. 1.1: Regional bathymetric map of Atlantic Canada with the location of the Laurentian Fan indicated within the red dotted rectangle off the southwestern Grand Banks of Newfoundland. Coloured dots indicate earthquake epicenters from 1985 to present (Earthquakes Canada, 2018). The red star indicates the location of the M_w 7.2 November 18th, 1929 earthquake, as relocated by Bent (1995). The violet line indicates approximate location of the Cobequid-Chedabucto transform fault and the Newfoundland Fracture Zone. The globe was created using ArcGlobe, while seafloor renders were derived using the GEBCO 2014 global bathymetric grid and imaged in ArcMap. NS = Nova Scotia, NF = Newfoundland and GB = Grand Banks of Newfoundland.

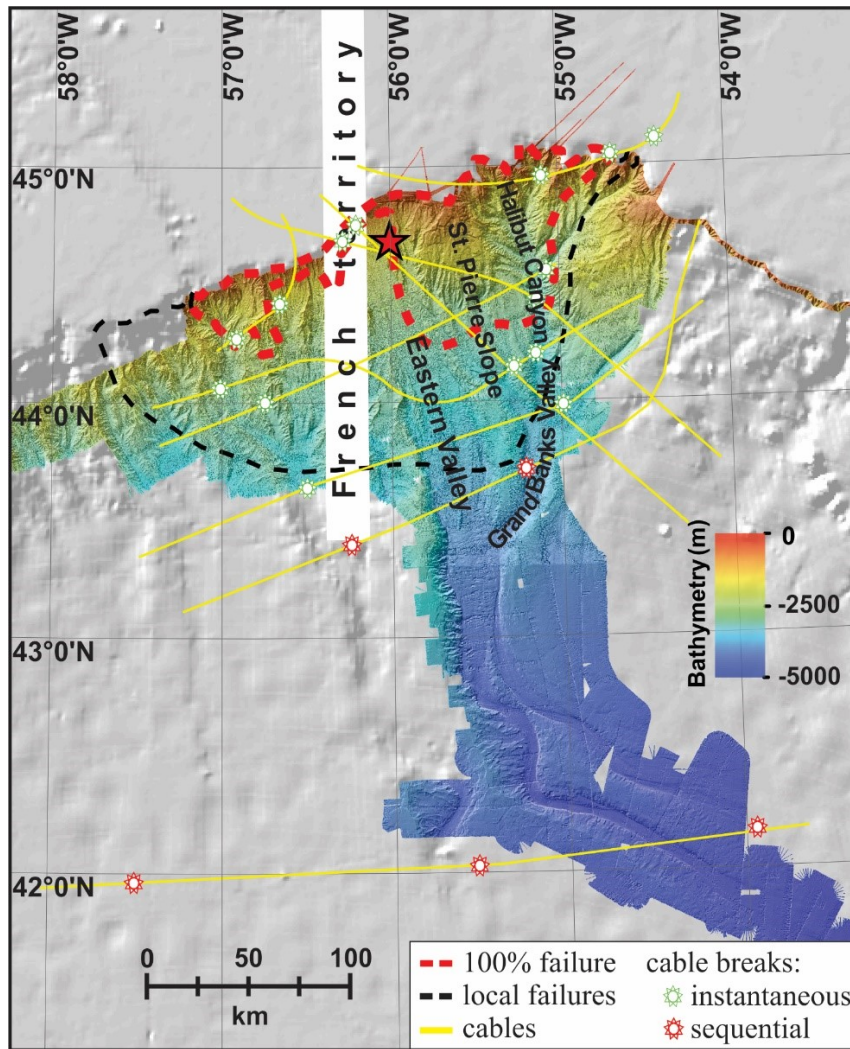


Fig. 1.2: A seafloor render of the Laurentian Fan region, including the St. Pierre Slope study area. The red dashed polygon represents the area where 100% of the seafloor sustained sediment failure and the black dashed line outlines the total region where local failures are observed (Piper et al., 1999; Mosher & Piper, 2007). The epicenter location of the M_w 7.2 1929 Grand Banks earthquake is shown with a red star. The coloured areas of the seafloor render were generated from multibeam data while the light grey areas were derived from the GEBCO 2014 global bathymetric grid.

The submarine landslide is believed to have resulted from retrogressive failure of the uppermost sediment column (<20 m) over portions of the St. Pierre Slope and the upper Laurentian Fan/Valley system (Figs. 1.2 & 1.3) (Piper et al., 1988; 1999). It is difficult to consider that these seafloor failures in relative deep water and in retrogressive fashion were capable of generating a tsunami. It is presumed that in deep water, a relatively large and

instantaneous volume displacement is required to generate such a large tsunami (Harbitz et al., 2014).

This observation leads to the following questions:

1. Is the 1929 submarine landslide unique, or do all failures that generate small escarpments have the potential to be tsunamigenic?
2. What styles of failure and kinematic evolution was involved in the 1929 slope failure?
3. Are there any indications for stratigraphic features in the deeper sub-bottom that potentially contributed to the 1929 slope failure?

The hypotheses of this thesis are:

- I. A massive failure occurred on the St. Pierre Slope in 1929.
- II. This underpinning failure precipitated the seafloor sediment failures and was responsible for the water column volume displacement to generate the tsunami.

The scope of this thesis is to investigate structures as evidence for different styles of slope failure on the St. Pierre Slope and to identify factors (pre-conditioning factors, stability conditions, trigger mechanisms) involved in these slope failures. Furthermore, the study investigates the kinematics of slope failure on the St. Pierre Slope and how these may be linked to tsunami generation. This objective is met through detailed seismic-stratigraphic analysis of the region using a comprehensive data set of newly acquired and legacy multiscale 2D seismic reflection data and multibeam swath bathymetry data (Figs. 1.3 & 1.4; appendix Table A1.1-A1.3). Geotechnical testing on two sediment cores is used to assess the static and pseudo-static slope stability and evaluate contributing factors. This thesis uses a large amount of legacy data that was assessed through the NRCan data base and new data that were acquired more recently (appendix Table A1.1-A1.3) (e.g. Mosher & West, 2007; Schneider, 2015; Krastel et al., 2016). Analog seismic data were scanned, rectified, digitized to standard SEG-Y format and georeferenced. These digitized and georeferenced analog data and newer data, especially multibeam swath bathymetry, allow a more concise analysis compared to previous studies; most of which were conducted in

the late 1980s and early 1990s (e.g. Hughes Clarke, 1986; Piper et al., 1988; 1999; McCall, 2006; Mosher & Piper, 2007). In addition, new software and analyzing techniques that use digital, georeferenced data allow a integrative and interactive analysis of the data. Especially, the software IHS Kingdom Suite™ and ArcGIS allow detailed mapping and a high correlation between different data sets.

The results of this thesis, therefore, will provide a better understanding of failure dynamics on the St. Pierre Slope and the 1929 slope failure specifically. Understanding causal failure mechanisms and the kinematics involved in the failure process will lead to a better understanding of submarine mass movements in general, which in turn contributes important information to assess hazards associated with continental margin landslides and their tsunami generation potential. The importance of understanding factors involved in submarine slope failures is evident through historic events such as the 2018 tsunami in Indonesia caused by a flank collapse of the Anak Krakatau volcano, the 1998 Papua New Guinea landslide and tsunami (Tappin et al., 2001; Harbitz et al., 2014), and the 1964 Great Alaska earthquake and tsunami (Lee et al., 2006) that all resulted in in a high number of casualties.

The 1929 submarine landslide source area is morphologically similar to many other regions on passive continental margins, as there is no major failure scarp. A typical morphological investigation of the St. Pierre Slope, therefore, would probably not have considered this slope as source region for a tsunamigenic landslide. If the hypothesis of this thesis is correct, then it implies that a reassessment of the tsunami generation potential for other slopes might be required.

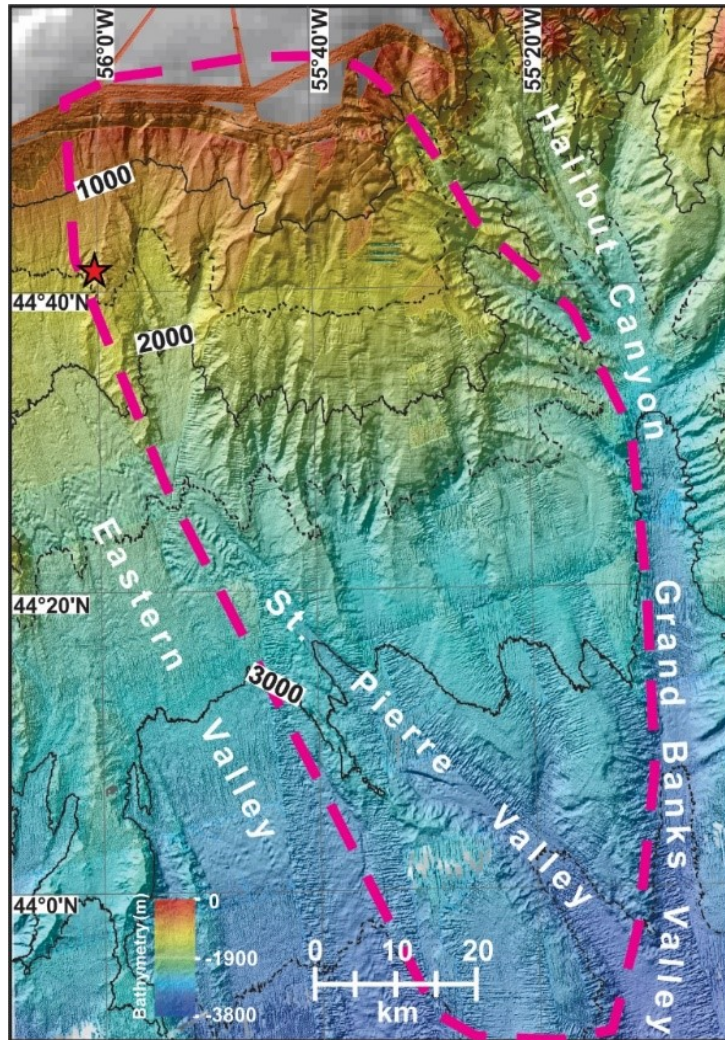
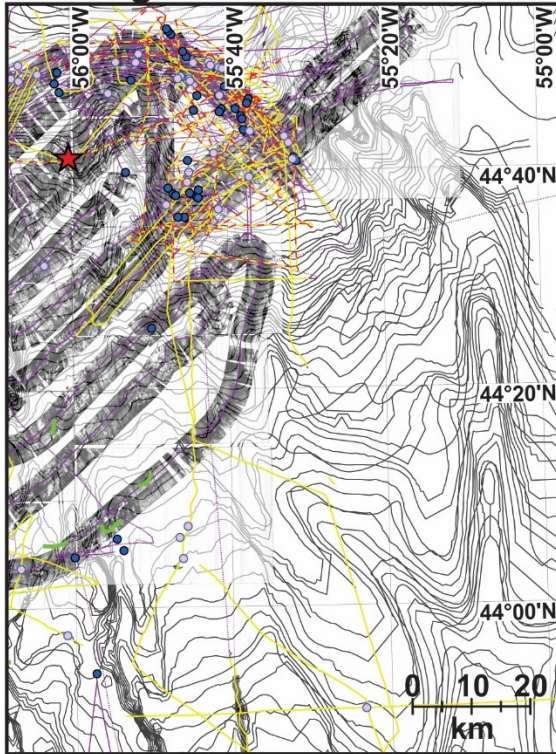
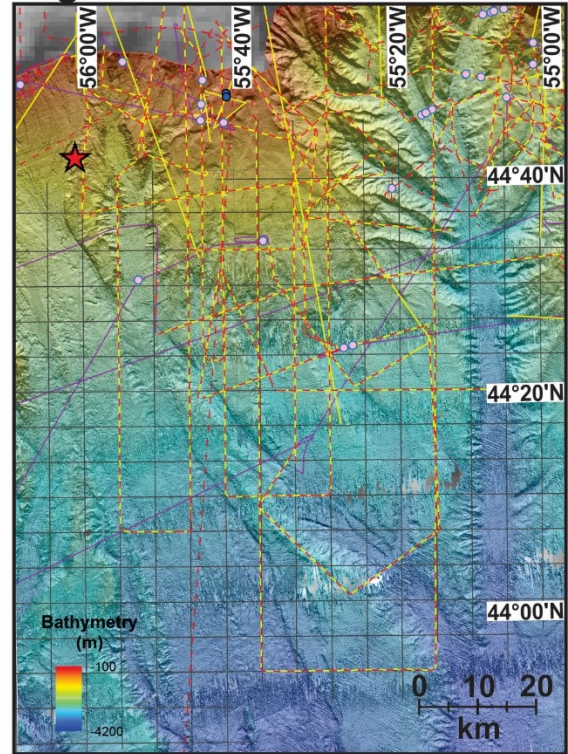


Fig. 1.3: Seafloor bathymetric map of the area of the continental slope seaward of the southwestern Grand Banks, including a portion of the Laurentian Fan. The area outlined by the dashed pink line is the research area for this thesis – the St. Pierre Slope.

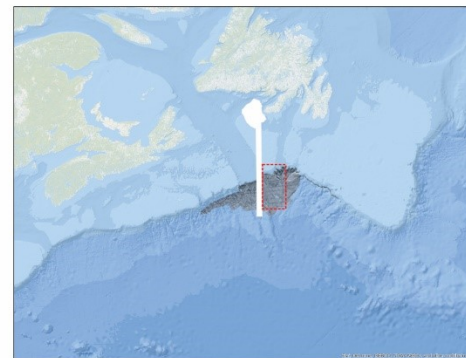
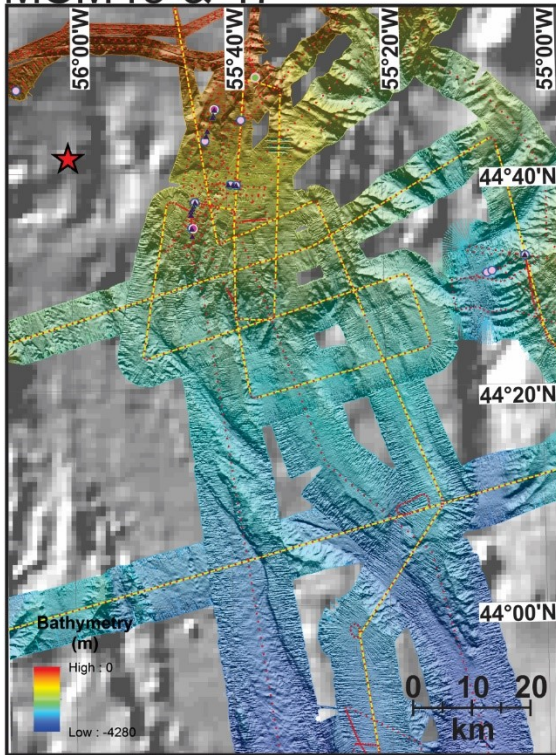
Analog data



Digital data



MSM45 & 47



- ★ 1929 earthquake
- Alvin dives
- SAR/SeaMARC1
- ▲ CPT measurements
- gravity cores
- piston cores
- geotechnical cores
- MSM45
- MSM47
- 2D reflection seismic
- TGS
- - - Huntec
- · · Parasound
- 3.5 kHz

Fig. 1.4: Maps showing the different sets of data (BIO legacy data, analog and digital, and new data from MSM45 and MSM47) available for this thesis.

1.2 THE 1929 GRAND BANKS EVENT

On the 18th of November 1929, a magnitude Mw 7.2 earthquake struck the southwestern Grand Banks of Newfoundland (Fig. 1.1) (Bent, 1995). Two hours after the earthquake, a destructive tsunami hit the coast of Newfoundland as well as parts of Nova Scotia (Hodgson & Doxsee, 1930; Heezen & Ewing, 1952). This event is considered one of the most catastrophic events of Eastern Canada, as it caused 28 casualties and significant economic damage due to destruction of infrastructure including twelve transatlantic telecommunication cables (Fig. 1.2) (Hodgson & Doxsee, 1930; Doxsee, 1948; Ruffman, 2001).

The cable breaks (Fig. 1.2) are of specific interest, as they led to the first evidence of naturally occurring submarine turbidity currents (Heezen & Ewing, 1952; Heezen et al. 1954). Resistance measurements and telegraph machines recorded the location and time of the cable breaks and showed that six of the cables that lay in the vicinity of the epicenter broke instantaneously at the time of the earthquake (Fig. 1.2), while another six cables to the south broke in a sequential order up to 13 hours after the earthquake (Doxsee, 1948; Heezen & Ewing, 1952; Piper et al. 1988). A total number of 28 breaks were recorded with up to three breaks on one single cable (Doxsee, 1948). Some of these cables had more than one break, but sometimes multiple breaks at the same cable have the same breakage time. Some of these breakage times, therefore, need to be treated with care as they might be incorrect (Hughes Clarke, 1988).

Early hypotheses, such as rupture along a large fault that spans from the Laurentian Channel towards the Sohm Abyssal Plain, did not sufficiently explain the sequential cable breaks (Hodgson & Doxsee, 1930; Doxsee, 1948; Heezen & Ewing, 1952). Heezen and Ewing (1952) were the first to argue that this sequence of cable breaks can only be explained by a submarine landslide transforming from a slump at the upper continental slope into a turbidity current. Cores from the Sohm Abyssal Plain containing recently deposited, ~1 m-thick graded silt and sand verified the turbidity current theory (Heezen et al., 1954). Based on the observed cable breaks, the flow velocity of the turbidity current is estimated to be ~19 m s⁻¹ close to the source area, down to ~6 m s⁻¹ where the last cable

broke (Heezen & Ewing, 1952; Piper et al., 1988). The existence of gravel waves along the middle to lower Eastern Valley that were remoulded by the 1929 event reflect the high velocity and therefore transport capacity of the turbidity current (Piper et al., 1988; Hughes Clarke, 1988). The gravel itself was delivered during an earlier sub-glacial outburst flood, the 19.5 cal ka event (Piper et al., 2007).

Heezen and Drake (1964) hypothesized that the turbidity current evolved from a massive slump on the upper continental slope, however, until now no evidence of a single major slump near the source area had been detected (Fig. 1.2) (Hughes Clarke, 1988; Piper et al., 1988; Mosher & Piper, 2007). Instead, Piper et al. (1988; 1999) and Mosher and Piper (2007) demonstrated that the only evidence of sediment failure consisted of 20-25 m-high escarpments in water depths greater than 650 m of the St. Pierre Slope (Fig. 1.3). This region corresponds to the main area of instantaneous cable breaks (Fig. 1.2). The submarine landslide, therefore, is interpreted to have been a widespread, surficial failure (Fig. 1.2) (Piper et al., 1988; 1999). Initially, shallow (~20 m) retrogressive rotational slumps on the upper and middle slope transformed into debris flows. Failed sediments transformed into a 100 to 300 m-thick turbidity current downslope as a result of hydraulic jumps across the steep bathymetry into the adjacent valleys and channels (Piper & Aksu, 1987; Hughes Clarke, 1988; Piper et al. 1999). Estimates of the volume of sediment that failed in the 1929 event range up to 200 km³, based on turbidity current deposits on the Sohm Abyssal Plain (Piper & Aksu, 1987; Piper et al., 1988, Fine et al., 2005). The turbidites, however, consists mostly of sand, while the source area of the landslide is characterised by muddy sediments (Piper & Aksu, 1987; Piper et al., 1999). This fact implies that the turbidity current was deeply erosive and entrained sand from the valley floors of Eastern and Western Valley (Piper & Aksu, 1987; Hughes Clarke, 1988), the two main conduits of the Laurentian Fan, while the mud was suspended into plumes and transported away with the currents (Piper & Aksu, 1987).

McCall (2006) interpreted hardcopies of ultra-high resolution seismic data to estimate that about 93.5 km³ of sediment initially failed on the St. Pierre Slope and surrounding areas, of which roughly 46.4 km³ was transported downslope and became entrained into the

turbidity current. These volumes, however, need to be considered with caution, as seismic coverage was relatively sparse and no multibeam swath bathymetry data were available. Factors described by Giles et al. (2010) to have pre-conditioned the slope failure include salt tectonism, high sedimentation rates during the last deglaciation, abundant dissolved and free gas, and local high slope gradients e.g. steep-canyon walls. The final trigger of the 1929 failure was the earthquake, with an epicenter beneath the Laurentian Fan northwest of the St. Pierre Slope (Fig. 1.3) (Piper et al., 1999).

Early studies of the 1929 event focused on the submarine landslide; the tsunami became scientifically more relevant during the last 20 years due to recent catastrophic events such as the 1998 Papua New Guinea tsunami (Tappin et al., 2001; Harbitz et al., 2014). In this context, the 1929 tsunami is one of the first recognized landslide-triggered tsunamis and in addition one of the few slide-generated tele-tsunamis that crossed the Atlantic Ocean (Fine et al., 2005). Bent (1995) excluded the earthquake as a source of the 1929 tsunami, as the hypocenter was about 20 km deep at the base of the lower crust and occurred along a strike-slip surface with only a small thrust component. A calculated “worst case” scenario showed a vertical seafloor displacement of less than 20 cm (Bent, 1995). This kind of displacement cannot generate a 3 m-high tsunami (Bent, 1995) with run-up heights of up to 13 m along the coasts of the Burin Peninsula, Newfoundland (Ruffman, 2001). A specific fault for the earthquake could not be assigned as regional seismotectonics of the area are complex, but it is assumed to be related to movements along the Cobequid-Chedabucto transform fault and the Newfoundland Fracture Zone (Fig. 1.1) (Bent, 1995).

The first attempt to numerically simulate the 1929 tsunami was made by Fine et al. (2005) as computational power allowed highly complex 3D models of landslide-generated tsunamis. The model, however, was highly simplified as precise data of some of the important landslide properties were not available (Table 1.1). Assumptions included uniform, 5 m-thick, instantaneous sediment failure over an area of 20 000 km². The initial simulation was described as being successful, but some of the computed arrival times did not fit with observed times (Fine et al., 2005). Fine et al. (2005) indicated that improvements on the model are necessary once the required information becomes

available. Fundamental information includes precise initial position and thickness of slide mass as well as exact timing of sediment failure (Fine et al., 2005).

Table 1.1: Parameters used in the tsunami simulation of Fine et al. (2005) versus reported observations from earlier studies e.g. Piper et al. (1988; 1999).

| Model Fine et al., 2005 | Observation e.g. Piper et al., 1988; 1999 |
|---|---|
| uniform thickness = 5 m | various thickness = 5-30 m |
| simultaneous failure | retrogressive failure |
| initial failure area = 20 000 km ² | main failure area = 7 000 km ² |
| | local failure area = 15 000 km ² |

The principal outstanding uncertainties concerning the 1929 event on the St. Pierre Slope are characteristics of the sediment preconditioning factors, initial sediment failure and kinematic evolution. In terms of tsunami generation potential, these uncertainties include precise source area location, water depth and acceleration of the failure, as well as volume of seafloor displacement, evolution of the failure (e.g. instantaneous or retrogressive) and bathymetric (seafloor depth and morphology) influences on wave propagation (Harbitz et al. 2014). This study will provide detailed information that address and reduce all of these uncertainties.

1.3 CHAPTER SYNOPSIS

1.3.1 Chapter 2

1.3.1.1 TITLE AND AUTHOR CONTRIBUTION

Chapter 2 is a pre-typeset version of “Schulten, I., Mosher, D. C., Krastel, S., Piper, D. J. W., and Kienast, M., 2019. Surficial Sediment Failures due to the 1929 Grand Banks Earthquake, St. Pierre Slope (<https://doi.org/10.1144/SP477.25>, updated version).” The Geological Society of London (GSL) published this manuscript on May 3rd, 2018 in the GSL Special Publication SP477 “Lintern, D. G., Mosher, D. C., Moscardelli, L. G., et al.

(eds.) Subaqueous Mass Movements. Geological Society, London, Special Publications 477”.

Results of this study were used in “Løvholt, F., Schulten, I., Mosher, D., Harbitz, C., and Krastel, S., 2019. Modelling of the 1929 Grand Banks slump and landslide tsunami. From: Lintern, D. G., Mosher, D. C., et al. (eds). Subaqueous Mass Movements. Geological Society, London, Special Publications, 477. <https://doi.org/10.1144/SP477.28>”.

Details on each author’s contribution are provided in Table 1.2. Each author is evaluated based on the CRediT taxonomy (<https://casrai.org/credit/>) and each contribution is rated as either lead, equal or supportive.

Table 1.2: Authors contribution to chapter 2 “Surficial Sediment Failures due to the 1929 Grand Banks Earthquake, St. Pierre Slope”.

| 1st manuscript contribution, CRediT taxonomy | authors | | | | |
|---|--------------|---------------|-------------|-----------------|-------------|
| | Schulten, I. | Mosher, D. C. | Krastel, S. | Piper, D. J. W. | Kienast, M. |
| Conceptualization | xx | xx | x | xx | x |
| Data Curation | xx | xx | xx | x | |
| Formal analysis | xxx | | | x | |
| Funding acquisition | x | xx | x | | x |
| Investigation | xxx | | | | |
| Methodology | xxx | xx | x | xx | |
| Project administration | xxx | | | | |
| Resources | | xx | x | xx | |
| Supervision | | xxx | x | x | x |
| Validation | xxx | | | | |
| Visualisation | xxx | x | | | |
| Writing, original draft | xxx | x | | | |
| Writing, review & edits | xx | xxx | x | x | x |

xxx Lead

xx Equal

x Supporting

1.3.1.2 SUMMARY

Chapter 2 presents an assessment of the seafloor and near seafloor sediments of the St. Pierre Slope to re-evaluate volume and kinematics involved in the surficial sediment failures that occurred in the event. A new compilation of ultra-high resolution seismic data

and new multibeam swath bathymetry data (appendix Table A1.1 & A1.2) were used to map: 1) the dimension of the failure area, 2) the thickness and volume of failed sediment, 3) fault patterns and displacements, and 4) styles of sediment failure. The results show the seafloor of the St. Pierre Slope hosts 20 to 100 m-high escarpments and a total failure area of $\sim 5200 \text{ km}^2$. Surficial failure deposits are mostly debrites. The majority of sediment failures occurred along the head scarps in deep water ($> 1700 \text{ m}$). The failures were widely distributed, translational, and apparently retrogressive. They liquefied to become debris flows and rapidly coalesced and evolved into a massive channelized turbidity current. Sediment failures associated with the fault scarps in 730 to 1300 m water depth are identified as localised along failure planes in 10 to 15 m sub-bottom depth. It is estimated that $\sim 100 \text{ km}^3$ of sediment failed on St. Pierre Slope. Approximately 60 km^3 of the sediment that failed was deposited directly on the slope and $\sim 40 \text{ km}^3$ became entrained into the channelized turbidity current. The presence of fault scarps suggests instantaneous displacement as a consequence of faulting. Two failure mechanisms seem to be involved in the 1929 submarine landslide: faulting and translation. The deep-water location and retrogressive nature of the surficial failures that occurred along the head scarps make them an unlikely main contributor for tsunami generation. Vertical displacement along the fault scarps in shallower water seems to be a more likely candidate for generation of the tsunami.

1.3.2 Chapter 3

1.3.2.1 TITLE AND AUTHOR CONTRIBUTION

Chapter 3 is the submitted version of “Schulten, I., Mosher, D. C., Piper, D. J. W. and Krastel, S., A massive slump on the St. Pierre Slope, a new perspective on the 1929 Grand Banks submarine landslide” to the AGU Journal of Geophysical Research: Solid Earth and currently in revision. Details on each author’s contribution are shown in Table 1.3.

Table 1.3: Author contribution to chapter 3 “A massive slump on the St. Pierre Slope, a new perspective on the 1929 Grand Banks submarine landslide”.

| 2nd manuscript contribution, CRediT taxonomy | authors | | | |
|---|--------------|---------------|-----------------|-------------|
| | Schulten, I. | Mosher, D. C. | Piper, D. J. W. | Krastel, S. |
| Conceptualization | xxx | xx | xx | x |
| Data Curation | xx | xx | | xx |
| Formal analysis | xxx | | x | |
| Funding acquisition | x | xx | xx | x |
| Investigation | xxx | | | |
| Methodology | xxx | xx | x | x |
| Project administration | xxx | x | x | |
| Resources | | xx | xx | x |
| Supervision | | xx | xx | x |
| Validation | xxx | x | x | |
| Visualisation | xxx | x | x | |
| Writing, original draft | xxx | | | |
| Writing, review & edits | xx | xxx | x | x |

XXX Lead

xx Equal

x Supporting

1.3.2.2 SUMMARY

In Chapter 3, investigation of deep-seated stratigraphic and structural features is presented and their potential contribution to the 1929 event is discussed. This investigation includes analysis of high-resolution and industrial scale multi- and single-channel 2D seismic reflection data (appendix Table A1.3). Regional stratigraphic information from earlier studies such as Piper and Normark (1982; 1989) and Piper et al. (2005) were compiled and corresponding horizons mapped throughout sub-bottom seismic data of the St. Pierre Slope. The results show that there are numerous, low-angle ($\sim 17^\circ$) faults with up to 100 m-high vertical displacement and ~ 330 m of horizontal displacement. They are present throughout the Quaternary section of the St. Pierre Slope down to 500-600 m below the seafloor (mbsf) and occur underneath seafloor escarpments that are present between 750 to 2000 m water depth (mwd). The faults are interpreted as part of a massive (~ 560 km³), complex slump. The slump shows multiple décollements in 250 and 400-550 mbsf that seem to be associated with buried mass transport deposits and there is indication of

slumping in at least two directions. Erosion through high meltwater discharge during deglaciation seems to have facilitated evacuation of the sediment package down to 250 mbsf into the adjacent, deeply incised St. Pierre and Eastern Valley to the west-southwest and southward towards the lower slope channel systems. Slumping of the deeper component from ~250 to ~550 mbsf is inferred to have propagated towards the SSW. Seafloor escarpments are almost the same height as reflection offsets of sub-bottom horizons measured along the fault planes suggesting recent reactivation. The 1929 earthquake likely triggered reactivation along these faults, which resulted in slumping of the ~500 m-thick strata of sediment. Two failure mechanisms are therefore associated with the 1929 event: massive slumping (~500 m-thick) and consequent widespread, surficial (upper ~20 m) sediment failures. Both failure mechanisms possibly contributed to tsunami generation, as shown by Løvholt et al. (2019).

1.3.3 Chapter 4

1.3.3.1 TITLE AND AUTHOR CONTRIBUTION

Chapter 4 is a manuscript in preparation: “Schulten, I., MacKillop, K., and Mosher, D. C., Stress history and slope stability in the 1929 Grand Banks failure area”. Details on each author’s contribution are shown in Table 1.4.

1.3.3.2 SUMMARY

Chapter 4 contains an evaluation of the strength characteristics and stress history of shallow sediment of the upper St. Pierre Slope through detailed physical property measurements and advanced geomechanical testing on marine sediment cores. This information is used to assess the static and pseudo-static infinite slope stability for core sites and over a range of sediment thicknesses (2-550 m) as observed in the 1929 submarine landslide. Based on the findings potential pre-conditioning factors involved in the 1929 sediment failure are evaluated. The results indicate normal consolidation with slight under-consolidation of sediments in water depth shallower than 800 m. Underconsolidation is identified at a depth of 3 to 9 m and is attributed to 1) high sedimentation rates, 2) a mass transport deposit (MTD) and/or sandy turbidites, or 3) the presence of shallow free gas. A weak layer is identified at boundary layers between clay-rich mud and sandy turbidites in the upper 4 to

6 m of the sediment cores. The MTD, sandy turbidites and the presence of gas coincide with the presence of a potential failure plane as indicated by a nearby escarpment that is approximately 8 to 10 m in height. The sediment cores show gas expansion cracks below MTD's and sandy turbidites, which could be suggestive of additional excess pore pressure at this depth. Slope stability analyses indicate present-day stable conditions. Slope angles in excess of 6.8° or a $M_w > 4.7$ in < 5 km distance from the core locations are needed to introduce unstable conditions in the studied area. In 1929, both ground shaking and the presence of weak layers were needed to cause surficial sediment (10-25 m-thick) failures and instability of a 250 m-thick block. It is further shown that the 1929 earthquake was sufficient to cause instability of a 550 m-thick block. It is believed that displacement of a 550 m-thick sediment block as a consequence of the 1929 earthquake likely contributed to the surficial sediment failures. Movement of the sediment mass may be related to excess pore pressure along one or more sedimentary layers associated with MTD's.

Table 1.4: Author contribution to chapter 4 “Stress history and slope stability in the 1929 Grand Banks failure area”.

| 3rd manuscript contribution, CRediT taxonomy | authors | | |
|--|--------------|--------------|---------------|
| | Schulten, I. | McKillop, K. | Mosher, D. C. |
| Conceptualization | xx | x | xxx |
| Data Curation | xx | xxx | |
| Formal analysis | xxx | xx | |
| Funding acquisition | x | | xx |
| Investigation | xx | xx | x |
| Methodology | xx | xxx | x |
| Project administration | xxx | xx | xx |
| Resources | | xxx | x |
| Supervision | | xx | xx |
| Validation | xxx | xx | xx |
| Visualisation | xxx | x | x |
| Writing, original draft | xxx | x | |
| Writing, review & edits | xx | xx | xx |

xxx Lead xx Equal x Supporting

1.3.4 Chapter 5

Chapter 5 provides the conclusions of the various aspects of this study and their significance on a regional and global scale.

1.4 REFERENCES CITED IN CHAPTER 1

- Bent, A. L., 1995. A complex double-couple source mechanism for the Ms 7.2 1929 Grand Banks earthquake. *Bulletin of the Seismological Society of America*, Vol. 85, p. 1003-1020.
- Clare, M. A., Talling, P. J., Challenor, P., Malgesini, G., and Hunt, J., 2014. Distal turbidites reveal a common distribution for large (>0.1 km³) submarine landslide recurrence. *Geology*, Vol. 42, p. 263-266. Doi: 10.1130/G35160.1.
- Doxsee, W. W., 1948. The Grand Banks Earthquake of November 18, 1929. *Publications of the Dominion Observatory, Ottawa*, Vol. 7, No. 7, p. 323-335.
- Fine, I. V., Rabinovich, A. B., Bornhold, B. D., Thomson, R. E., and Kulikov, E. A., 2005. The Grand Banks landslide-generated tsunami of November 18, 1929: preliminary analysis and numerical modeling. *Marine Geology*, Vol. 215, p. 45-57.
- Giles, M. K., Mosher, D. C., Piper, D. J. W., and Wach, G. D., 2010. Mass Transport Deposits on the Southwestern Newfoundland Slope. In: Mosher, D. C., Shipp, R. C. et al. (eds.), *Submarine Mass Movements and Their Consequences, Advances in Natural and Technological Hazards Research*, Vol. 28, p. 657-665. Springer, Dordrecht.
- Harbitz, C. B., Løvholt, F., and Bungum, H., 2014. Submarine landslide tsunamis: how extreme and how likely? *Natural Hazards*, Vol. 72, p. 1341-1374. doi: 10.1007/s11069-013-0681-3.
- Heezen, B. C., and Drake, G. L., 1964. Grand Banks slump. *American Association of Petroleum Geologist Bulletin*, Vol. 48, p. 221-233.
- Heezen, B. C., and Ewing, M., 1952. Turbidity currents and submarine slumps, and the 1929 Grand Banks earthquake. *American Journal of Science*, Vol. 250, p. 849-878.
- Heezen, B. C., Ericson, D. B., and Ewing, M., 1954. Further evidence for a turbidity current following the 1929 Grand Banks earthquake. *Deep-Sea Research*, Vol. 1, p. 193-202.

- Hodgson, E. A., and Doxsee, W. W., 1930. The Grand Banks earthquake, November 18, 1929. Eastern section of the seismological society of America, proceedings of the 1939 meeting, Washington, D. C., p. 72-81.
- Hughes Clarke, J. E., 1988. The geological record of the 1929 “Grand Banks” earthquake and its relevance to deep-sea clastic sedimentation. PhD thesis, Dalhousie University, Halifax, Nova Scotia.
- Lee, H., Ryan, H., Kayen, R. E., Haeussler, P. J., Dartnell, P., and Hampton, M. A., 2006. Varieties of submarine failure morphologies of seismically-induced landslides in Alaskan fjords. *Norwegian Journal of Geology*, Vol. 86, p. 221-230.
- McCall, C. W., 2006. A Geological and Geophysical study of the 1929 Grand Banks slide. Master Thesis, Saint Mary’s University, Halifax, Nova Scotia.
- Mosher, D. C., 2008. Submarine Mass Movements in Canada: Geohazards with far-reaching implications. In: Locat, J., Perret, D., Turmel, D., Demers, D., and Leroueil, S., (eds.): 4e Conférence canadienne sur les géorisques: des causes à la gestion, 4th Canadian Conference on Geohazards: From Causes to Management. Presse de l'Université Laval, Québec, p. 55-62.
- Mosher, D. C., and Piper, D. J. W., 2007. Analysis of Multibeam seafloor imagery of the Laurentian Fan and the 1929 Grand Banks landslide area. In: Lykousis, V., Sakellariou, D., and Locat, J. (eds.), *Submarine Mass Movements and Their Consequences, Advances in Natural and Technological Hazards Research*, Vol. 27, p. 77-88. Springer, Dordrecht.
- Mosher, D. C., Moscardelli, L., Shipp, C., Chaytor, J., Baxter, C., Lee, H., and Urgeles, R., 2010. Submarine Mass Movements and Their Consequences. In: Mosher, D. C., Shipp, R. C. et al. (eds.), *Submarine Mass Movements and Their Consequences, Advances in Natural and Technological Hazards Research*, Vol. 28, p. 1-10, Springer, Dordrecht. DOI 10.1007/978-90-481-3071-9.
- Piper, D. J. W., and Aksu, A. E., 1987. The source and origin of the 1929 Grand Banks turbidity current inferred from sediment budgets. *Geo-Marine Letters*, Vol. 7, p. 177-182.

- Piper, D. J. W., and Normark, W. R., 1982. Acoustic interpretation of Quaternary sedimentation and erosion on the channelled upper Laurentian Fan, Atlantic margin of Canada. *Canadian Journal of Earth Sciences*, Vol. 19, p. 1974-1984.
- Piper, D. J. W., and Normark, W. R., 1989. Late Cenozoic sea-level changes and the onset of glaciation: impact on continental slope progradation off eastern Canada. *Marine and Petroleum Geology*, Vol. 6, p. 336-347.
- Piper, D. J. W., Shor, A. N., and Hughes Clarke, J. E., 1988. The 1929 "Grand Banks" earthquake, slump, and turbidity current. In: *Sedimentological Consequences of Convulsive Geologic Events* (Ed. By H. E. Clifton), Geological Society of America Special Paper, Vol. 229, p. 77- 92.
- Piper, D. J. W., Cochonat, P., and Morrison, M. L., 1999. The sequence of events around the epicentre of the 1929 Grand Banks earthquake: initiation of debris flows and turbidity current inferred from sidescan sonar. *Sedimentology*, Vol. 46, p. 79-97.
- Piper, D. J. W., Macdonald, A. W. A., Ingram, S., Williams, G. L., and McCall, C., 2005. Late Cenozoic architecture of the St. Pierre Slope. *Canadian Journal of Earth Sciences*, Vol. 42, p. 1987-2000, doi:10.1139/E05-059.
- Piper, J. W., Shaw, J., and Skene, K. I., 2007. Stratigraphic and sedimentological evidence for late Wisconsinan sub-glacial outburst floods to Laurentian Fan. *Paleogeography, Paleoclimatology, Paleoecology*, Vol. 246, p. 101-119.
- Rebesco, M., Mosher, D., and Piper, D. J. W., 2017. Advancements in Understanding Deep-Sea Clastic Sedimentation Processes: a preface. *Marine Geology*, Vol. 393, p. 1-3.
- Ruffman, A., 2001. Potential for large-scale submarine slope failure and tsunami generation along the U. S. mid-Atlantic coast: Comment. *Geology*, Vol. 29, No. 10, p. 967.
- Talling, P. J., Wynn, R. B., Masson, D. G., Frenz, M., Cronin, B. T., Schiebel, R., Akhmetzhanov, A. M., Dallmeier-Tiessen, S., Benetti, S., Weaver, P. P. E., Georgiopoulou, A., Zühlsdorff, C., and Amy, L. A., 2007. Onset of submarine debris flow deposition far from original giant landslide. *Nature letters*, Vol. 450, p. 541-544, doi:10.1038/nature06313

- Tappin, D. R., Watts, P., McMurty, G. M., Lafoy, Y., and Matsumoto, T., 2001. The Sissano, Papua New Guinea tsunami of July 1998 – offshore evidence on the source mechanism. *Marine Geology*, Vol. 175, p. 1-23.
- Twichell, D. C., Chaytor, J. D., ten Brink, U. S., and Buczkowski, B., 2009. Morphology of late Quaternary submarine landslides along the U. S. Atlantic continental margin. *Marine Geology*, Vol. 264, p. 4-15.

CHAPTER 2: SURFICIAL SEDIMENT FAILURES DUE TO THE 1929 GRAND BANKS EARTHQUAKE, ST. PIERRE SLOPE

Chapter 2 is a pre-typeset version of “Schulten, I., Mosher, D. C., Krastel, S., Piper, D. J. W., and Kienast, M., 2019. Surficial Sediment Failures due to the 1929 Grand Banks Earthquake, St. Pierre Slope (<https://doi.org/10.1144/SP477.25>, updated version).” The Geological Society of London (GSL) published this manuscript on May 3rd, 2018 in the GSL Special Publication SP477 Subaqueous Mass Movements and their Consequence. Details on each author’s contribution are shown in Table 1.2.

2.1 ABSTRACT

On November 18th, 1929, a Mw 7.2 earthquake centred beneath the upper Laurentian Fan of the SW Newfoundland continental slope triggered a damaging turbidity current and tsunami. The turbidity current broke telecommunication cables and the tsunami killed 28 people and caused major infrastructure damage along the south coast of Newfoundland. Both events are believed to have been derived from sediment mass failure as a result of the earthquake. This study aims to identify the volume and kinematics of the 1929 slope failure in order to understand the geohazard potential of this style of sediment failure. Ultra-high resolution seismic reflection and multibeam swath bathymetry data are used to determine: 1) the dimension of the failure area, 2) the thickness and volume of failed sediment, 3) fault patterns and displacements, and 4) styles of sediment failure. The total failure area at St. Pierre Slope is estimated to be 5200 km², recognized by escarpments, debris fields and eroded zones on the seafloor. Escarpments are typically 20 to 100 m high, suggesting failed sediment consisted of this uppermost portion of the sediment column. Landslide deposits consist mostly of debris flows with evidence of translational, possible retrogressive sliding in deeper water (>1700 m) and evidence of instantaneous sediment failure along fault scarps in shallower water (730-1300 m). Thus, two failure mechanisms seem to be involved in the 1929 submarine landslide; faulting and translation. The main surficial sediment failure concentrated along the deep-water escarpments consisted of widely distributed, translational failure that liquefied to become a debris flow and rapidly evolved into a massive channelized turbidity current. Although most of the surficial failures occurred at

these deeper head scarps, their deep-water location and possible retrogressive nature make them an unlikely main contributor for the tsunami generation. The localised fault scarps in shallower water are a more likely candidate for the generation of the tsunami, but further research is needed in order to address the characteristics of these fault scarps.

2.2 INTRODUCTION AND OBJECTIVE

The St. Pierre Slope of the eastern Laurentian Fan, located seaward of the southwestern Grand Banks of Newfoundland, has been identified as the main failure area of the 1929 Grand Banks submarine landslide (Figs. 2.1A to D) (Piper et al., 1988; 1999; Mosher & Piper, 2007). This landslide is one of the few globally that is known to have generated a tsunami (Fine et al., 2005; Harbitz et al., 2014) and led to the first recognition of naturally occurring submarine turbidity currents (Heezen & Ewing, 1952; Hughes Clarke, 1988; Piper et al., 1988). The submarine landslide is believed to have been triggered by a magnitude M_w 7.2 earthquake beneath the mid-slope region of the Laurentian Fan on November 18th, 1929 (Fig. 2.1B) (Bent, 1995). Bent (1995) excluded the earthquake as a direct source of the 1929 tsunami, as the hypocenter was about 20 km deep at the base of the lower crust, and occurred with a strike-slip motion and only a small (<20 cm) thrust component. The tsunami struck the south coast of Newfoundland, Saint-Pierre et Miquelon and parts of Nova Scotia about 2 hrs after the earthquake (Hodgson & Doxsee, 1930; Heezen & Ewing, 1952). This event is considered one of the more catastrophic natural events of Eastern Canada, as it caused 28 casualties and significant economic damage due to destruction of infrastructure that included severing twelve transatlantic telecommunication cables (Fig. 2.1B) (Hodgson & Doxsee, 1930; Doxsee, 1948; Ruffman, 2001).

Earlier investigations of the area identified laterally extensive, shallow mass failures (20-25 m high escarpments), but no major head scarp (Piper et al., 1999; Mosher & Piper, 2007). The outstanding question, therefore, relates to the mechanism with which this distributed shallow failure that rapidly evolved into a turbidity current, generated a tsunami. Is the 1929 landslide unique, or do all failures that generate small escarpments have the potential to be tsunamigenic? This study aims to identify the characteristics of the

initial sediment failure to determine its dimensions (thickness, area and volume), water depth of occurrence and kinematic evolution (e.g. instantaneous or retrogressive), in order to assess the geohazard potential that this style of failure represents. Building on earlier interpretations, and based on new data, this study allows a more comprehensive data analysis and significantly improves the current knowledge about the 1929 submarine landslide.

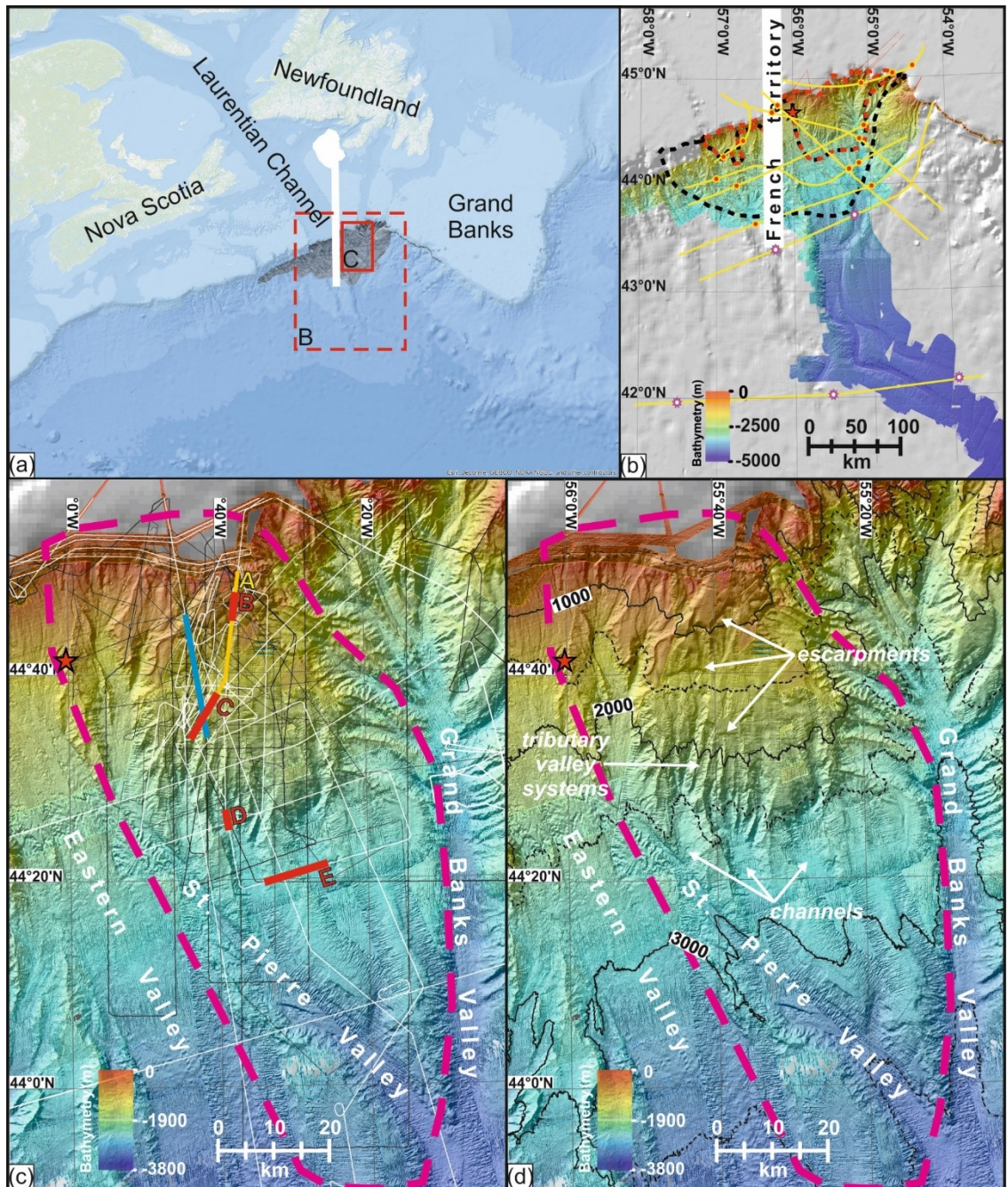


Fig. 2.1: (A) Regional overview map of Atlantic Canada. The study area (C, red box) is located at the eastern part of the Laurentian Fan system (B, red dotted box) of the southwestern Grand Banks of Newfoundland. (B) Laurentian Fan with presumed main failure area (red shaded area), and area of local sediment failure (black dotted area) as indicated by the cable breaks (red dots on yellow lines = instantaneous; white dots = sequential) by Piper et al. (1999) and Mosher and Piper (2007). (C & D) Multibeam swath bathymetry of the St. Pierre Slope (pink dotted area), including epicenter location of the M_w 7.2 1929 Grand Banks earthquake (red star). (C) Location of high-resolution seismic profiles and locations of profiles presented in Fig. 2.2 (A = yellow line, B, C, D & E = red lines) and Fig. 2.4 (blue line) are highlighted. (D) Morphological characteristics are highlighted.

2.3 PREVIOUS STUDIES

The 1929 Grand Banks landslide has been described as a widespread, retrogressive, surficial (top 5-100 m) sediment failure (Piper et al., 1999; Mosher & Piper, 2007). There are numerous shallow escarpments (on average 20-25 m high) and debris fields below these escarpments, but there is no evidence of a single major headwall scarp (>100 m long, >60 m high) and no evidence of a single major slump deposit near the source area (Hughes Clarke, 1988; Piper et al., 1988; Mosher & Piper, 2007). Instantaneous cable breaks in the source area indicate a main failure area of approximately 7000 km² (Fig. 2.1B) (Mosher & Piper, 2007). It is assumed that initial retrogressive, rotational slumps at the upper and middle slope transformed into debris flows and, as a result of hydraulic jumps, further transformed into a 100 to 300 m-thick turbidity current (Piper & Aksu, 1987; Hughes Clarke, 1988; Piper et al., 1999). Flow transformation is indicated by the cable breaks and an approximately one-metre-thick turbidite bed on the Sohm Abyssal Plain that comprises up to 200 km³ of mainly silt and sand deposits (Heezen & Ewing, 1952; Heezen et al., 1954; Piper & Aksu, 1987; Piper et al., 1988). The source area of the landslide is, however, characterised by muddy sediments, which implies that the turbidity current must have been deeply erosive and entrained sand from the valley floors of Eastern Valley and Western Valley (Piper & Aksu, 1987; Hughes Clarke, 1988; Piper et al., 1999), the two main conduits of the Laurentian Fan, while the mud was suspended into plumes and transported away with the currents (Piper & Aksu, 1987). Measured times of the cable breaks indicate that the turbidity current had an initial velocity of about 67 km hr⁻¹, but slowed down to 22 km hr⁻¹ by the time it reached the last cable (Heezen & Ewing, 1952; Piper et al., 1988).

McCall (2006) using paper copies of a subset of available ultra-high resolution seismic data, but with sparse seismic coverage and no multibeam swath bathymetry data, estimated that 93.5 km³ of sediment initially failed, of which roughly 46.4 km³ was transported downslope assuming a failure area of 9000 km². Potential preconditioning factors that led to the 1929 slope failure include salt tectonism, high sedimentation rates during the last deglaciation, abundant dissolved and free gas within seafloor sediments, as observed in shallow core samples, and local increased slope gradients especially along canyon walls (Mosher & Piper, 2007; Giles et al., 2010). Fine et al. (2005) made a first attempt to simulate the 1929 tsunami using a relatively simple model of landslide-generated tsunamis. The simulation was limited in precision as some of the important landslide properties, such as precise initial position and thickness of slide mass, were not available. Their model assumed instantaneous failure and did not account for retrogressive failure, as interpreted by Piper et al. (1999).

2.4 METHODS

This study uses a large quantity of legacy data acquired over the last three decades by the Geological Survey of Canada and data acquired recently as part of a co-operative project between the Geological Survey of Canada, the University of Kiel, Germany, and the University of Bremen, Germany (Figs. 2.1C & D).

Multibeam swath bathymetry data that cover ~50000 km² of the upper Laurentian Fan were acquired in 2006 using a Kongsberg Simrad EM120 system (Mosher & Piper, 2007) and in 2015 using a Kongsberg Simrad EM122 system (Figs. 2.1B to D) (Krastel et al., 2016). Horizontal resolution of these systems is 35 to 40 m and the vertical resolution is 2 to 6 m in 1000 m water depth (mwd), according to manufacturer specifications (Kongsberg, 2017). Data from the different surveys were merged and EM120 data gridded at 30 m and EM122 gridded at 40 m to produce surficial morphological renders and derivative products (e.g. slope angle).

Ultra-high resolution sub-bottom seismic reflection data acquired over the last three decades (1985-2015) using the Hunttec DTS boomer and sparker and Atlas Parasound P70

(MSM45 & MSM47, 2015) systems (Fig. 2.1C), image the upper ~100 m of the sub-bottom for shallow stratigraphic and sedimentological assessments. The Hunttec DTS boomer and sparker source is nearly omnidirectional, so the minimum horizontal resolution is governed by the Fresnel zone, which is ~15 m in 500 mwd and ~45 m in 4000 mwd, considering a centre frequency of 1500 Hz (500-2500 Hz bandwidth). In sediments, the maximum penetration is ~120 m with a maximum vertical resolution of 0.1 to 0.2 m (Hutchins et al., 1976; Mosher & Simpkin, 1999). Atlas Parasound P70 uses the parametric effect to generate secondary signals of 4 and 40 kHz. The system images to a vertical depth of ~100 m with a vertical resolution of ~0.15 m (Kraestel et al., 2016; Teledyne Reson, 2017). The narrow beam angle of 4.5° allows ensonification of a smaller target area and data are subject to fewer side echoes when compared to the Hunttec DTS system. Horizontal resolution is 7% of the water depth, which at the Laurentian Fan area is 35 m in 500 mwd and 280 m in 4000 mwd (Spieß, 1993). Figure 2.1C shows that seismic data coverage is dense along the upper slope area and relatively sparse in the lower slope. Over the past 20 years, since digital data acquisition became possible, ~3700 km of ultra-high resolution seismic data were acquired along the St. Pierre Slope in addition to the ~3000 km of existing analog data. Paper records of these analog data were scanned, rectified, converted to digital seismic data in industry-standard SEG-Y format, and georeferenced.

IHS Kingdom Suite™ was used to interpret the shallow stratigraphy of the ultra-high resolution seismic reflection data (WGS84 UTM Zone 21N projection). Four acoustic facies, as well as stratigraphic and structural relationships of reflections were mapped according to depth and lateral distribution (Tables 2.1 & 2.2). In addition, five reflections, previously identified by McCall (2006) and labelled as Q91 (yellow), Q93 (blue), Q95 (red), Q97 (green) and Q99 (orange), were correlated regionally throughout the upper study area (Figs. 2.2B to D). McCall (2006) provided radiocarbon ages for reflection Q91 to Q99 that range from ~33 ka (Q91) to ~17 ka (Q99). Each reflection was correlated back to its point of origin using the seismic grid to ensure consistent stratigraphic correlation. Seismic units were converted from travel-time to depth domain using a velocity of 1500 m s⁻¹; which is considered appropriate for the shallow sediment section.

Table 2.1: Acoustic facies along St. Pierre Slope


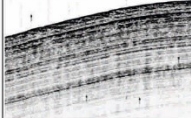
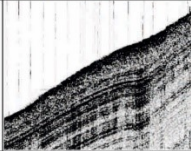
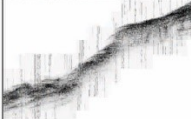
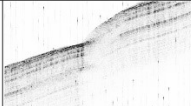
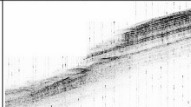
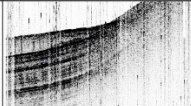
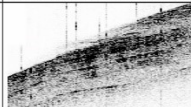
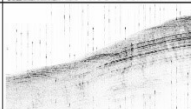
| Facies | Examples | Description |
|--------|---|--|
| A |  | Indistinct hummocky, prolonged bottom echoes with no to rarely intermittent subbottom reflections (acoustic penetration >10 m). |
| B |  | Distinct, continuous, sharp bottom echoes with continuous, at times intermittent, parallel subbottom reflections (acoustic penetration >100 m). |
| C |  | Indistinct, prolonged to semi-prolonged bottom echoes with transparent or incoherent internal character commonly in multiple external forms such as irregular/hummocky wedge, fill or lens-shaped (acoustic penetration <5 to >100 m). |
| D |  | Indistinct, small, regular overlapping hyperbolic bottom echoes with varying vertex elevations, subbottom echoes mostly absent (acoustic penetration <20 m). |

Table 2.2: Seismic relationships along St. Pierre Slope.

| Type | Examples | Description |
|------|---|--|
| I |  | Termination of coherent, well-stratified subbottom reflections and continuation of these reflections after a 20-100 ms-high reflection offset. . |
| II |  | Truncation of stratified seismic reflections against an escarpment with characteristic staircase morphology. |
| III |  | Onlap of acoustic incoherent body on top of well-stratified subbottom reflections against a incoherent truncation surface |
| IV |  | Downlap of acoustic incoherent body on well-stratified subbottom reflections. |
| V |  | Truncation of stratified seismic reflections that are fully covered by acoustic incoherent bodies. |

4100 km of single- and multi-channel 2D reflection seismic data (1984-2015) often were acquired simultaneously with ultra-high resolution sub-bottom seismic reflection data throughout the St. Pierre Slope region. For system details of the most relevant surveys, see expedition reports by Mosher and West (2007) and Krastel et al. (2016), for example. These

lower resolution 2D reflection seismic data image to depths >500 m below the seafloor. They provide, therefore, structural and stratigraphic framework information. They also image below the shallow sediment failure deposits, allowing deposit thickness calculations.

Sediment cores provide ground-truth to ultra-high resolution seismic data interpretation. Numerous sediment cores are available from the St. Pierre Slope in addition to ten sediment cores that were collected during the 2015 expedition of the vessel *Maria S. Merian* (Krastel et al., 2016).

An estimate of the volume of sediment missing was derived by reconstructing the pre-failure surface of St. Pierre Slope. Ten (two cross, eight dip) seismic profiles were chosen to derive the thicknesses of the sequence in travel-time from the seismic reflection Q91 to the seismic reflections of Q97, Q99 and the undisturbed seafloor. In all three cases, the sediment column thickened downslope. An exponential increase in sediment thickness downslope was estimated to reconstruct the pre-failure sediment thickness along St. Pierre Slope as time between the reference seismic reflection Q91 and undisturbed seafloor reflection. Other methods, one assuming a constant distribution and the other one assuming a linear increase in sediment thickness downslope were tested, but the exponential method showed the best fit to the seismic data. The amount of missing sediment was then estimated as time from the calculated pre-failure surface to the base of mapped surficial sediment deposits and gridded to retrieve a volume of the sediment that initially failed during the 1929 event. This assessment is based on the assumption that the surficial sediment sequence at the St. Pierre Slope was intact prior to the 1929 event and that any pre-1929 sediment failures during the last ~30 ka BP can be volumetrically discounted. Calculations were restricted to the mapped reference seismic reflection Q91, which was mapped down to ~2100 mwd. The volume of missing sediment for water depths between 2100 down to 2800 m was estimated by extrapolating the thicknesses of sediment failure known for 1700 to 2100 mwd. The volume estimate of missing sediment for the 2800 to 4000 mwd interval is a conservative estimate as its calculation was largely based on the assumption that failure thickness is equivalent to observations from 500 to 1700 mwd.

Uncertainty Assessment

Resolution of multibeam bathymetry data is limited by water velocity determination, acoustic ray-path refractions and corrections therein, as well as positioning (Mosher et al., 2006; Mosher, 2011). The multibeam bathymetry data were gridded to cell sizes of 30 m (EM120) and 40 m (EM122). Given Nyquist sampling limitations, it is not possible to resolve horizontal targets less than 80x80 m, therefore. Vertical resolution, on the other hand, is on the order of decimetres; system specifications suggest 0.2 to 0.6 % of the water depth (Kongsberg, 2017). A decrease in horizontal sampling results in a smoother rendered bathymetric surface model (Mosher et al., 2006; Mosher, 2011). This smoothing effect leads to lower apparent slope angles, so that derived gradients need to be considered as minimum values (Mosher, 2011).

Sources of uncertainty in seismic data, such as ship position and seismic shotpoint position, are on the order of a few metres. Scanned seismic data, in particular data acquired prior to global positioning systems (GPS), however, may have errors in navigation, vertical offsets and gaps in the records that account to more than this interval. Seismic interpretation, therefore, focused on newer digital data and analog data were used only where necessary. Sparse line spacing requiring interpolation led to the greatest uncertainty. The uncertainty, however, is difficult to assess as line spacing is highly variable, ranging from tens of metres to kilometres.

Measurements of the volume of seismic units has uncertainties in the range of $\pm 1 \text{ km}^3$ for 500 to 1700 mwd, $\pm 7 \text{ km}^3$ for 1700 to 2800 mwd and $\pm 7 \text{ km}^3$ for 2800 to 4000 mwd assuming an acoustic velocity of $\sim 1500 \text{ m s}^{-1}$. Most errors occur below 2000 mwd, as seismic coverage is sparse, requiring lengthy interpolation between seismic lines. Missing sediment volume estimation has the highest uncertainty because of the combination of various errors in its calculation. Errors include the derivation of the pre-failure surface, insufficient information about pre-failure sediment thickness, projection of a small amount of known failure volume to water depths of 2100 to 2800 mwd and assumption of minimum failure in the lower slope area. The total uncertainty is estimated to be $\pm 2 \text{ km}^3$ for 500 to

1700 mwd, $\pm 30 \text{ km}^3$ for 1700 to 2800 mwd and $\pm 10 \text{ km}^3$ for 2800 to 4000 mwd, giving a total uncertainty of $\pm 42 \text{ km}^3$ for the volume of missing sediment along the St. Pierre Slope.

2.5 RESULTS

The St. Pierre Slope is a $\sim 50 \text{ km}$ -wide relatively flat ($1\text{-}3^\circ$) inter-canyon platform bounded to the east by Grand Banks Valley and to the west by Eastern Valley (Figs. 2.1C & D). It extends 130 km from the shelf break of St. Pierre Bank in 500 mwd down to $\sim 4000 \text{ mwd}$ at the confluence of the two valleys (Figs. 2.1C & D). The total area of St. Pierre Slope is $\sim 5200 \text{ km}^2$.

2.5.1 Morphological analysis

Multibeam swath bathymetry data display numerous sinuous escarpments along the relatively smooth, gentle ($\sim 2^\circ$) upper slope from 500 to 2300 mwd (Fig. 2.1D). Between 500 and 1500 mwd, escarpments are relatively steep ($\sim 7.5^\circ$) and 40 to 100 m high (Fig. 2.1D). They extend laterally for 8 to 24 km and occur predominately along the western part of the slope area (Fig. 2.1D). The most prominent feature is the uppermost, $< 100 \text{ m}$ -high, escarpment that lies in ~ 750 to 900 mwd (Fig. 2.1D). The southern part of the upper slope from 1500 to 2300 mwd shows a terraced morphology of numerous $\sim 40 \text{ km}$ -long steep ($10\text{-}22^\circ$) escarpments (Fig. 2.1D). These escarpments appear to be less high (20-25 m) than the escarpments observed further upslope. The slope becomes relatively steep ($\sim 3^\circ$) and dissected by numerous tributary valley systems between 2000 and 2500 mwd (Fig. 2.1D). The tributary valley systems are 2 to 4 km wide, $\sim 16 \text{ km}$ long and up to 200 m deep. The lower slope lies below 2500 mwd, has a lower gradient ($\sim 1^\circ$) and hosts three major N-S-trending channel-and-levee systems that lead into St. Pierre Valley and Grand Banks Valley (Fig. 2.1D).

2.5.2 Acoustic analysis

2.5.2.1 ACOUSTIC FACIES CLASSIFICATION AND DISTRIBUTION

Four major acoustic seismic facies were identified based on echo-characteristics of the ultra-high resolution sub-bottom seismic reflection data (c.f., Damuth, 1975; 1980; Damuth & Olson, 2015) and are shown in Table 2.1. Indistinct and prolonged bottom echoes with

no to rarely intermittent sub-bottom reflections (facies A) are recorded in proximity to the shelf break. These reflection returns rapidly pinch out into distinct parallel high amplitude bottom and sub-bottom reflections (facies B) that are recorded from 500 to 700 mwd (Figs. 2.2A & 2B). From 700 to 1700 mwd, 7 ms-thick indistinct, prolonged to semi-prolonged bottom echoes with incoherent internal reflections (facies C) are noted. These overly, interbed with, or are even buried within intermittent to distinct parallel sub-bottom reflections of facies B (Fig. 2.2C). Indistinct, small, regular overlapping hyperbolic bottom echoes with no sub-bottom reflections (facies D) are recorded from 1700 to 2800 mwd (Fig. 2.2D). Facies D appears associated with ~45 ms-thick deposits of facies C that are noted from 1700 to 2800 mwd. These facies prevent acoustic imaging of the deeper section (Fig. 2.2D). Seismic reflection data were, therefore, used to map the bottom of facies C and D deposits. From 2800 to 4000 mwd, ~5 ms-thick facies C deposits with underlying stratified reflections of facies B occur on top of levee systems and 25 to 35 ms-thick stacked units of facies C are evident within ~5 km wide and 150 to 200 m deep channels (Fig. 2.2E). Five high amplitude reflections of facies B that form part of the seismic stratigraphy developed by McCall, (2006) are mapped along the upper slope from 500 mwd down to 2100 mwd (Figs. 2.2B & C). Facies C and D deposits, however, restrict a correlation of the seismic stratigraphy further downslope.

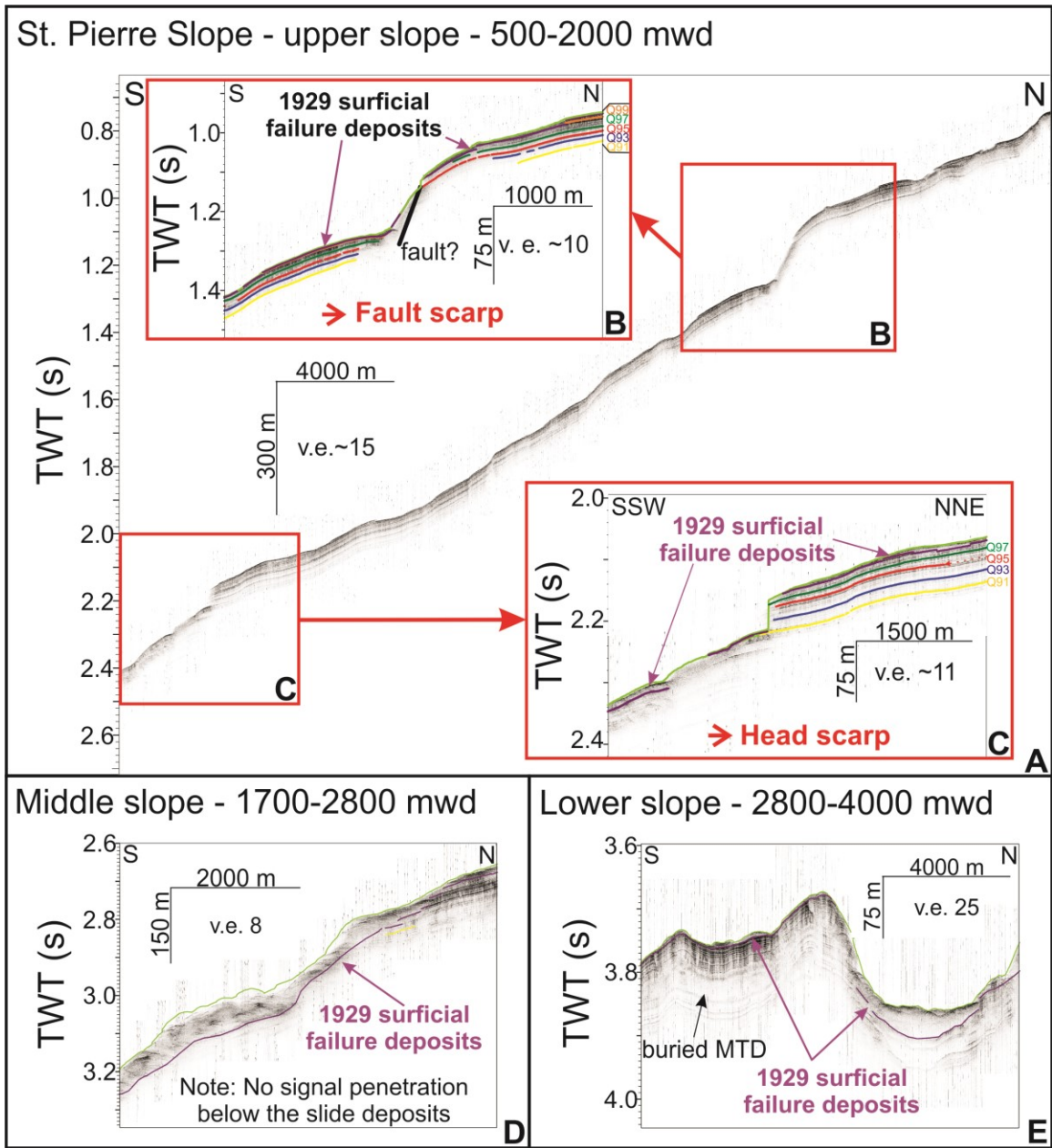


Fig. 2.2: Examples of different morphologies and distribution of surficial failure deposits along St. Pierre Slope. (A) N-S-trending profile across the upper slope. (B) and (C) are zoomed sections, displaying a fault scarp and head scarp, typically observed at this slope. (D) The middle slope shows ~35 m-thick failure deposits. (E) The lower slope is characterized by thin (~4 m) slide deposits on the levees and thick (10-25 m thick) side deposits within the channels. The locations of profiles are indicated in Fig. 2.1.

2.5.2.2 SEISMIC RELATIONSHIPS CLASSIFICATION AND DISTRIBUTION

Five seismic reflection relationships between the four acoustic facies are recognized (Table 2.2). Facies B reflections truncate against an escarpment in ~750 to 900 mwd that is associated with a 65 to 130 ms-high reflection offset (type I), as demonstrated by layered reflections (Q91 to Q99) of facies B that are mapped to both sides of this escarpment (Fig. 2.2B). The internal layer thickness of facies B reflections (Q91 to Q99) is consistent across this reflection offset within the upper 130 ms of the sediment column. The offset is laterally asymmetric with a lower (65 ms) offset in the western and a higher (130 ms) offset in the eastern part of the study area. Above this type I escarpment, facies B reflections, down to the seismic reflection Q99, truncate against a 10-15 ms high escarpment, but without any evidence of a reflection offset (type II) (Fig. 2.2B). Facies C deposits are recorded seaward of type II escarpments where they top lap facies B units and further downslope onlap (type III) the lower end of the type I escarpments (Fig. 2.2B). The seismic stratigraphy (reflections Q91 to Q99) reveals that Q99 is either missing or forms the base of these facies C deposits (Fig. 2.2B). Type I escarpments are further evident in 1100 mwd and in 1300 mwd (Figs. 2.3A & B), but with smaller reflection offsets of 25 to 55 ms. Deep reflection seismic data indicate that reflection offsets associated with type I escarpments appear down to a depth of ~520 ms below the seafloor, where they terminate in a horizon of wavy reflections (Fig. 2.4). Smaller (4-14 ms) reflection offsets with low penetration depth (~50 ms) are observed along the slope down to 2200 mwd.

Facies C deposits are shown to downlap (type IV) in about 1700 to 2000 mwd or pinch out above type II escarpments that are widely observed around the same water depth (Fig. 2.2C). Type II escarpments with truncations of facies B characteristically occur as 28 ms-high steps along map-able seismic horizons (Figs. 2.2C & D). The maximum combined height of these steps is ~70 ms (Fig. 2.2C). Facies C and D deposits occur seaward of these type II escarpments and cover numerous buried reflection truncations against 12 to 25 ms-high escarpments (type V) that are evident from 2000 to 2300 mwd (Fig. 2.2D).

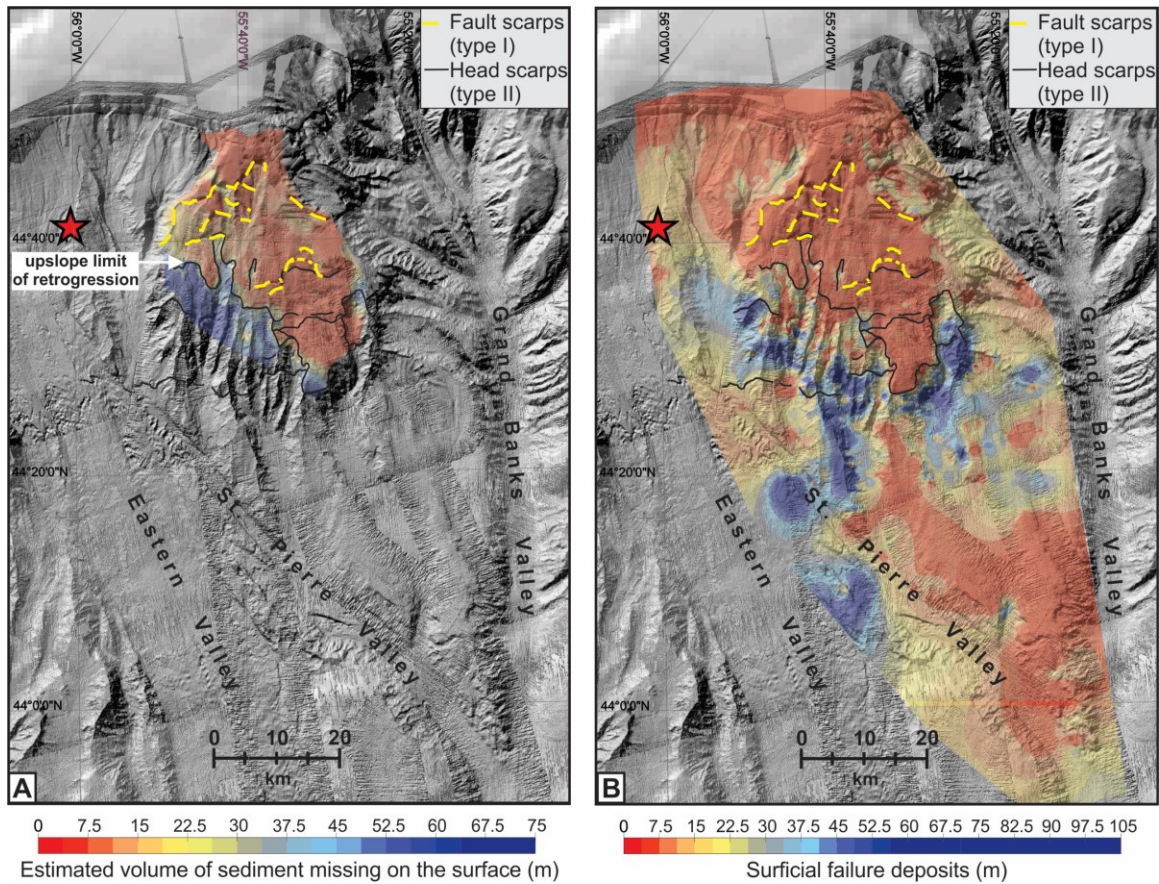


Fig. 2.3: (A) The estimated volume of sediment that failed in 1929 illustrating that most sediment is missing below the deep-water head scarps. Note: Estimates are restricted to the upper study area down to 2100 mwd, as the reference horizon (Q91) needed to assess the volume of sediment missing could not be correlated further downslope. (B) Surficial failure deposits along St. Pierre Slope. Failure deposits are in the order of 2-5 m from 730 to 1700 mwd and 2800 to 4000 mwd, but ~35 m-thick from 1700 to 2800 mwd. Fault scarps (dashed, thick black lines) and head scarps (thin black lines) are highlighted.

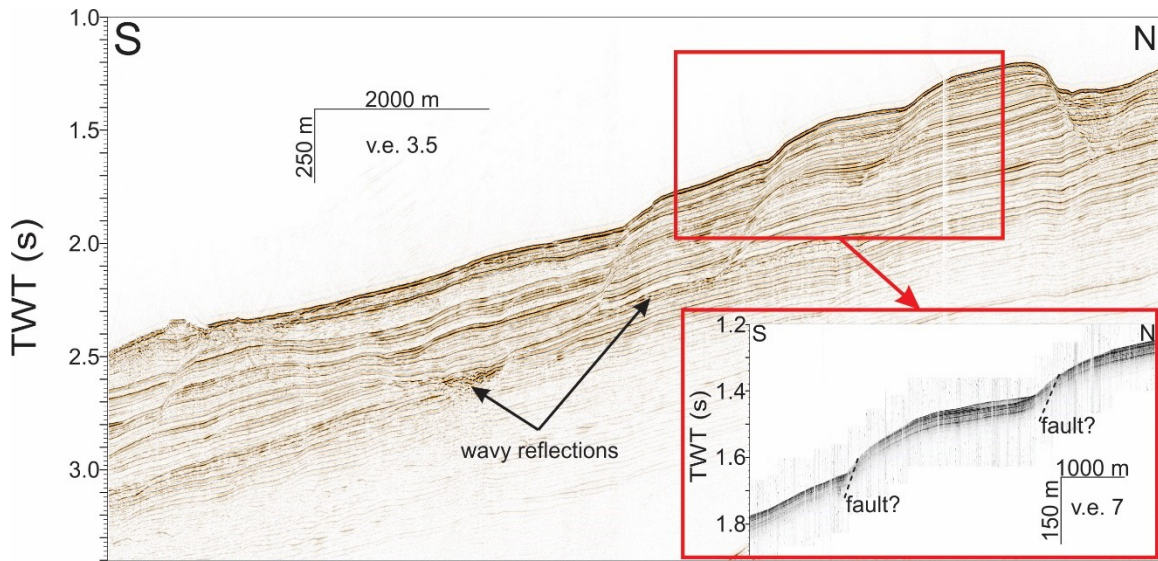


Fig. 2.4: Multichannel 2D seismic reflection profile across the upper St. Pierre Slope, acquired in 2015. Faults associated with upper fault scarps extend down to 350 m depth. Note: Slightly wavy horizon in ~400 m sub-bottom depth. Other 2D seismic reflection profiles indicate that faults are restricted to this wavy reflection horizon. For location of profile, see Fig. 2.1.

2.6 DISCUSSION

2.6.1 Seismic stratigraphy

Facies A dominates in the shelf break and uppermost slope region of St. Pierre Slope (Table 2.1). Given this location and its echocharacteristics, it is interpreted as representing glacial till or proximal glacial diamict. Bonifay and Piper (1988) described the same facies as coarse sediments deposited during Pleistocene ice surges forming glacial and reworked glacial till. Downslope, facies A progressively evolves into a well-stratified reflection sequence of facies B (Table 2.1, Fig. 2.2A).

Facies B consists of a sequence of coherent, high frequency parallel reflections (Table 2.1). This characteristic is interpreted to represent a complete uninterrupted stratigraphic sequence. Five seismic reflections horizons within this facies, named Q91, Q93, Q95, Q97 and Q99, correlate through the upper study area down to 2100 mwd (Figs. 2.2B & C). These five reflection horizons are used to estimate the pre-failure sediment thickness in order to assess the volume of sediment that failed as a result of the 1929 earthquake (Fig. 2.3A). Q91 is selected as a reference horizon, as it is present more broadly throughout

St. Pierre Slope than the other four reflection horizons (Figs. 2.2B & C). Reconstruction of the pre-failure sediment thickness required information from sediment sections that remained stable during the 1929 slope failure. The slope above the upper escarpment (500-700 mwd) is interpreted as one of these stable areas, as all five reflections are present and laterally correlateable demonstrating a complete stratigraphic section (Fig. 2.2B). Box and gravity cores (e.g., MSM47-10-01 & MSM47-10-02) indicate that this section consists of stratified sediment with interbedded thin silt and fine-sand layers and laminae (Krastel et al., 2016). Downslope of the uppermost escarpment, the pre-failure stratigraphic thickness is derived from areas that show this complete section of five horizons. Overall, seismic stratigraphic correlation indicates downslope thickening of the sediment section in un-failed regions from ~49 m in 730 mwd, to ~56 m in 1500 mwd and 69 m in 2000 mwd.

This failure volume assessment assumes an intact sediment sequence prior to the 1929 event. Pre-1929 surficial sediment removal cannot be completely ruled out, but the absence of major mass-transport deposits and buried escarpments within the upper sediment column (upper ~100 m) of the St. Pierre Slope, as well as the absence of thick sandy turbidites in sediments (upper 10 m) of the Eastern Canadian continental margin, indicate that major sediment failures were rare and volumetrically small (Piper et al., 1988; Piper et al., 2005). In addition, the recurrence interval of an event similar to 1929 is estimated to be ~150 ka (Piper & Normark, 1982; Piper et al., 2003). The surficial sediment failure along St. Pierre Slope, however, only affected sediment down to the Q91 reflection, which is dated back to ~29 ka BP (McCall, 2006).

2.6.2 Mass transport deposits

Deposits of facies C occur from 700 down to 4000 mwd (Table 2.1; Fig. 2.3B). They are observed laterally extensive below type I escarpments (5 m thick), become massive below type II escarpments (on average ~35 m) and then thin out towards the lower slope where they appear confined as stacked units within the channel systems and as thin layers (3.5 m thick) on top of the levee systems (Figs. 2.2B to E, 2.3B). Based on their positions and echo-character, they are interpreted as gravity-driven flow deposits (e.g., Piper et al., 1999; McCall, 2006, Giles et al., 2010). Gravity cores from the MSM47 expedition confirm

facies C as comprising poorly sorted and structureless sediment, thus interpreted as debrite (Krastel et al., 2016). The proximal onlap (type III) and distal downlap (type IV) of facies C deposits on fault and head scarps further marks the lateral beginning and ending of these gravity-controlled flow deposits (Table 2.2) (e.g., Mitchum et al., 1977; Sangree & Widmier, 1979).

Facies D deposits are mapped from 1700 to 2800 mwd, and are especially common proximal to type II escarpments (Table 2.1 & 2.2). Hyperbolic reflections of facies D are a result of diffraction of the acoustic signal. Given their location and this echocharacteristic, facies D deposits are interpreted as slump blocks and semi-coherent slides (c.f., Damuth & Olson, 2015). Piper et al. (1999) observed retrogressive slump blocks analysing side-scan sonar data where facies D reflections were mapped.

Distribution of facies C (debris flows) and D (slumps and slides) identify two characteristics of the 1929 submarine landslide:

- a) Localised failures resulting in thin mass transport deposits along the upper slope were initiated at the type I escarpments (Table 2.2, Fig. 2.2B). Rapid flow transformation into a flow slide is indicated by the presence of debrites (Krastel et al., 2016).
- b) Retrogressive slump deposits (facies D) in proximity to the type II escarpments from 1700 to 2800 mwd and massive (~35 m thick) slide deposits (facies C) indicate that surficial failures most likely rapidly transformed into debris flows leading down gullies and tributary systems to the channels at the lower slope and finally into St. Pierre Valley (Fig. 2.3B) (Piper et al., 1999; Mosher & Piper, 2007). A change in the slope inclination from 3° down to 1° between 2500 and 2800 mwd potentially slowed down the flow, allowing deposition (Fig. 2.3B) (c.f., Weirich, 1989; Talling et al., 2007; Winkelmann et al., 2008).

2.6.3 Fault and head scarps

Two major escarpment systems are distinguished at St. Pierre Slope (Figs. 2.3A & B). The first escarpment system occurs from 750 to 1300 mwd and shows lateral 8 to 24 km long type I escarpments with 20 to 100 m-high reflection offsets (Table 2.2; Figs. 2.2B, 2.3A & B). These type I escarpments are interpreted as fault scarps, as reflections (facies B, Q91 to Q99) that truncate against the upslope escarpment (footwall) are seen to offset in a normal sense and continue downslope (hanging wall) (Fig. 2.2B) (c.f., Mosher et al., 2004; Deptuck et al., 2007; Katz et al., 2015). The consistent internal thickness distribution between reflection horizons within the upper sediment column (upper 100 m) above and below these fault scarps suggests that the faults were active during a single event rather than being reactivated over time (c.f., growth fault). This theory is, however, highly speculative as further analysis of the deep reflection seismic data is needed in order to address the characteristics of this fault system. Earlier studies (e.g. Piper et al., 1999; McCall, 2006) did not recognize these escarpments as faults but identified them as head scarps of submarine landslides. The uppermost of these fault scarps (730 mwd) that shows reflection offsets of 50 to 100 m is also the highest escarpment present along St. Pierre Slope (Fig. 2.2B). Shallow, 7 to 11 m-high escarpments (type II) (Table 2.2) occur in association with this fault scarp in 700 mwd along a local failure plane and removal of this 7-11 m-thick sediment package is also observed downslope across the other fault scarps. In all cases the local failure plane is represented by reflection horizon Q99 (Fig. 2.2B). This interpretation is supported by McCall (2006), who identified the reflection horizon Q99 as sandy-mud, and interpreted this reflection as a local weak layer.

The second major escarpment system (type II) occurs in the southern part of the upper slope (1700 to 2300 mwd) and is characterised by a terraced morphology of ~40 km-long, steep (10-22°), ~21 m-high escarpments (Table 2.2; Figs. 2.3A & B). The composite stratigraphic height of these escarpments is ~50 m (Figs. 2.2C & D). In water depths >2000 m, type II escarpments are often buried below thick slide deposits (facies C, type V) (Fig. 2.2D). The terraced morphology is interpreted as result of failure along individual failure planes or weak layers within the sediment strata. Similar failure mechanisms are observed from submarine slides elsewhere (e.g. Bryn et al., 2003; Krastel et al., 2006).

These type II escarpments are, therefore, interpreted as head scarps resulting from submarine landsliding (Figs. 2.3A & B). Burial of head scarps (type V) below slide deposits initiated further upslope (Fig. 2.2D) and failure along individual bedding planes (Fig. 2.2C) leads to the interpretation that these head scarps are a consequence of translational retrogressive failure (e.g. Bryn et al., 2003; Haflidason et al., 2004; Masson et al., 2010). It is assumed that the retrogression could have occurred in a single, fast-moving event, rather than being reactivated over time. This assumption is supported by the absence of massive slide deposits in the upper sediment column that would indicate the occurrence of another major earthquake (Piper & Normark, 1982; Piper et al., 1988; Piper et al., 2003). In addition, escarpments and surficial slide deposits appear fresh during submersible dives and on deep tow side scan sonar images as only a very thin sediment layer is deposited on top of them (Hughes Clarke et al., 1989; Piper et al., 1999; Mosher & Piper, 2007). Failure most likely initiated mid-slope (2000-2300 mwd), where the slope gradient is steeper and retrogressed up-slope to ~1700 mwd (Figs. 2.2C & D).

2.6.4 Sediment budget

Regional mapping of seafloor escarpments and mass transport deposits indicates that the St. Pierre Slope is the main failure area of the 1929 landslide. The majority of sediment failures are observed from 750 to 2300 mwd covering an area of ~2000 km². St. Pierre Slope is characterised by two different types of escarpments: 1) fault scarps (type I) occur to the north (750 to 1300 mwd), and 2) head scarps (type II & V) of mass failures occur to the south (1700 to 2300 mwd) (Figs. 2.2B to D & 2.3). The distribution and volume of missing sediment and of slide deposits along the St. Pierre Slope is illustrated in Figures 2.3A and B. Localised shallow failures (5-10 m) are observed along a specific bedding plane (Q99) at the fault scarps and ~5 m-thick slide deposits (facies C) are observed along the slope from 750 to 1700 mwd (Table 2.1, Figs. 2.2B & 2.3B). A total slide deposit volume of ~4.5 km³ is mapped, while ~21 km³ of sedimentary material is assumed to have failed from the upper slope (Fig. 2.3A). Mapped sediment deposits indicate that a major part of the 1929 surficial sediment failure occurred along the retrogressive head scarps (type II & V) in 1700 to 2300 mwd (Figs. 2.2C to D, 2.3A & B). From 1700 to 2800 mwd, slide deposits reach a volume of up to 45 km³ (Fig. 2.3B). A sediment volume of ~60 km³

is estimated to have been removed during the 1929 event (Fig. 2.3A). Slide deposits within channel systems and on top of the levees (Figs. 2.2E) total $\sim 13 \text{ km}^3$, while $\sim 20 \text{ km}^3$ of sedimentary material are estimated to have been removed (Figs. 2.3A & B).

A total sediment volume of $\sim 100 \text{ km}^3$ is estimated to have failed on the St. Pierre Slope ($\sim 5200 \text{ km}^2$) during the 1929 event (Fig. 2.3A). Roughly 60 km^3 was deposited on St. Pierre Slope as mass-transport deposits (Fig. 2.3B) and $\sim 40 \text{ km}^3$ became entrained into the turbidity current that flowed downslope through Eastern Valley to the Sohm Abyssal Plain.

In addition to St. Pierre Slope, widespread failure is described to have occurred in 1929 at the western edge of the Grand Banks Valley drainage system (Mosher & Piper, 2007) and cable breaks suggest another, but smaller failure area along the shelf break ($\sim 500 \text{ mwd}$) of Western Valley (Fig. 2.1B). Eastern Valley, which lies in direct vicinity to the 1929 epicentre, however, is assumed to have been affected by only minor ($\sim 20 \text{ m}$ thick) sediment failure (Piper et al., 1999). In addition, results of PISCES IV dives (Hughes Clarke et al., 1989), SAR (Système Acoustique Remorqué) sidescan sonar surveys (Piper et al., 1999) and sediment cores (e.g. MSM47-12-02) (Krastel et al., 2016) indicate that some scarps and terraces at the head of Eastern Valley were probably present before the 1929 event. Taking failure areas in Western Valley and Grand Banks Valley into account as part of the total failure area of the 1929 submarine landslide leads to an apparent failure area of 7000 km^2 , which is in good agreement with earlier studies (Piper et al., 1999; McCall, 2006; Mosher & Piper, 2007). It is estimated that $\sim 135 \text{ km}^3$ of sediment could have failed from an area as big as 7000 km^2 assuming that sediment failure in Western Valley and Grand Banks Valley was as large as sediment failure observed on St. Pierre Slope ($\sim 100 \text{ km}^3$, 5200 km^2).

2.6.5 Implication on potential tsunami source

The numerous short (8-40 km long) and shallow (5-100 m high) fault- and head scarps of St. Pierre Slope (Figs. 2.2B, C, 2.3A & B) are incongruous with large failure head scarps typical of submarine landslides observed elsewhere (e.g., Masson et al., 2010; Bryn et al., 2005; Krastel et al., 2006). Fault escarpments, like those observed at St. Pierre Slope, are

described in regions of small and medium sized (slide deposits $<1 \text{ km}^3$) landslides on the southeastern Mediterranean Israeli coast (Katz et al., 2015), the Scotian Slope (Mosher et al., 2004) and the Southern Holocene Storegga Flank (Gafeira et al., 2007), for example. Katz et al. (2015) concluded that there is an absence of studies that address specifically the relationship between large submarine landslides and faults. As a result, there is an absence in landslide-databases of large landslides ($>1 \text{ km}^3$) (e.g., Urgeles & Camerlenghi, 2013) related to faulting. This study demonstrates that submarine fault scarps may be an important piece of evidence in the study of large submarine landslides.

The observation of fault scarps along the upper St. Pierre Slope (Fig. 2.2B) addresses the dilemma concerning the tsunami potential of widespread, retrogressive surficial sediment failure (Fine et al., 2005; Mosher & Piper, 2007) and provides a new perspective on the 1929 submarine landslide. Tsunami generation requires a rapid and significant volume displacement on the seafloor; the deeper the water, the greater the displacement needed (Fine et al., 2005; Harbitz et al., 2014). Instantaneous movement along fault zones in water depths of 750 to 1300 m is, therefore, considered a more plausible source for tsunami generation than the retrogressive head scarps observed in over 1500 mwd (Figs. 2.2C, 2.3A and B) (Harbitz et al., 2014). Deep seismic reflection data (Fig. 2.4) indicate a termination of these faults in ~ 400 m sub-bottom depth at wavy reflections, described in earlier studies as sediment waves (Piper et al., 2005). These sediment waves are considered a potential décollement surface that could have facilitated a rotation of a thick (~ 400 m) strata of unconsolidated sediment. It is, therefore, possible that the observed fault scarps could be part of a deeper sitting rotational slump that was either activated or reactivated as a result of the 1929 earthquake. Deptuck et al. (2007) describe a similar detachment surface associated with fault systems for the Hopedale-Makkovik failure complex, located along the margin of the southwestern Labrador Sea. Further analysis of the deep reflection seismic data is, however, necessary to address this hypothesis.

2.7 CONCLUSION

The 1929 Grand Banks earthquake and consequent submarine landslide and tsunami was the first and is still one of the best-case studies that show an unequivocal connection

between the three events. The earthquake, cable breaks and tsunami are matters of fact. A submarine landslide is inferred to have occurred in order to create the seafloor displacement necessary to generate the tsunami. This hypothesis was later supported by a successful, but relatively simple tsunami simulation of Fine et al. (2005). The paradox, however, is that the seafloor in the area shows no large head scarp, seafloor scar or massive deposit related to sediment mass-failure. Earlier interpretations suggested that widely distributed, retrogressive failure of the shallow sediment section (<20 m) was responsible for generation of the tsunami. It is hard to comprehend, however, how such a style of failure could result in tsunami generation, particularly in such deep water. New multibeam bathymetric and ultra-high resolution seismic reflection data allow testing of this hypothesis. The following observations were made.

- 1) Fault scarps (type I) that are 8 to 24 km long and 20 to 100 m-high were observed from 750 to 1300 mwd. A characteristic reflection offset also in the range of 20 to 100 m to both sides of the fault truncation is evident.
- 2) Head scarps (type II) with 20 m-high steps and a composite stratigraphic height of ~50 m, were identified from 1700 to 2300 mwd. Some of these head scarps are buried (type V) by slide deposits (facies C & D).
- 3) Based on seismic stratigraphic correlations and head scarp heights, an estimated ~100 km³ of sediment was evacuated from St. Pierre Slope.
- 4) The volume of slide deposits remaining on St. Pierre Slope is ~60 km³ with the thickest slide deposits mapped from 1700 to 2800 mwd.

From these observations, it is suggested that the 1929 M7.2 earthquake instigated both fault displacements that reached up to 100 m of offset and submarine landslides affecting the shallow sediment section (~20 m). Faulting and main failure processes occurred over an area of 2000 km² and in water depths of 750 to 2300 m on the St. Pierre Slope. The majority of sediment failure in form of shallow, translational landsliding that possible retrogressed up slope was restricted to deeper water (1700 to 2300 mwd). Up to 40 km³ of failed sediment rapidly transitioned into a turbidity current that was responsible for the sequential cable breaks. It is speculated that the possible retrogressive failure of shallow sediment

(<20 m) and rapid fluidization to turbidity current in deeper water (>1700 mwd) make the landsliding a less likely source for the tsunami, although possibly contributed. Movement along the faults in shallower water might be a more likely source, but further analysis is needed in order to assess the characteristics of these faults and related escarpments. Both results are to be assessed with tsunami numerical simulations (Løvholt et al., 2019).

2.8 ACKNOWLEDGMENTS

Irena Schulten is supported by NSERC CREATE Transatlantic Ocean System Science and Technology (TOSST) grant and NSERC Discovery Grants to David C. Mosher and David J. W. Piper. Seismic multibeam swath bathymetry, sub-bottom and seismic reflection data were provided by the Geological Survey of Canada Atlantic (GSCA, Natural Resources) and DFG-funded Expeditions MSM45 (Ralph Schneider) and MSM47 (Sebastian Krastel). The Geological Survey of Canada has supplied office and computing facilities of I. Schulten. The software ps32sgy developed by Hanno Keil (University of Bremen) and RegJP2000 developed by Bob Courtney (Geological Survey of Canada) were used to convert Parasound and analog ultra-high resolution seismic data into SEG-Y formats usable in IHS Kingdom Suite™."

2.9 REFERENCES CITED IN CHAPTER 2

- Bent, A. L., 1995. A complex double-couple source mechanism for the Ms 7.2 1929 Grand Banks earthquake. *Bulletin of the Seismological Society of America*, Vol. 85, p. 1003-1020.
- Bonifay, D., and Piper, D. J. W., 1988. Probable Late Wisconsinan ice margin on the upper continental slope off St. Pierre Bank, eastern Canada. *Canadian Journal of Earth Sciences*, Vol. 25, p. 853-865.
- Bryn, P., Solheim, A., Berg, K., Lien, R., Forsberg, C. F., Haflidason, H., Ottesen, D., and Rise, L., 2003. The Storegga Slide complex: repeated large scale sliding in response to climatic cyclicity. In: Locat, J., Mienert, J., and Boisvert, L. (eds), *Submarine Mass Movements and Their Consequences, Advances in Natural and Technological Hazards Research*, p. 215-222, Springer, Dordrecht.

- Bryn, P., Berg, K., Forsberg, C. F., Solheim, A., and Kvalstad, T. J., 2005. Explaining the Storegga Slide. *Marine and Petroleum Geology*, Vol. 22, p. 11-19.
- Damuth, J. E., 1975. Echo character of the western equatorial Atlantic floor and its relationship to the dispersal and distribution of terrigenous sediments. *Marine Geology*, Vol. 18, p. 17-45.
- Damuth, J. E., 1980. Use of high-frequency (3.5-12 kHz) echograms in the study of near-bottom sedimentation processes in the deep-sea: a review. *Marine Geology*, Vol. 38, p. 51-75.
- Damuth, J. E., and Olson, H. C., 2015. Latest Quaternary sedimentation in the northern Gulf of Mexico Intraslope Basin Province: I. Sediment facies and depositional processes. *Geosphere*, Vol. 11, No. 6, p. 1689-1718, doi:10.1130/GES01090.1.
- Deptuck, M. E., Mosher, D. C., Campbell, D. C., Hughes-Clarke, J. E., and Noseworthy, D., 2007. Along slope variations in mass failures and relationships to major Plio-Pleistocene morphological elements, SW Labrador Sea. In: Lykousis, V., Sakellariou, D., and Locat, J. (eds.), *Submarine Mass Movements and Their Consequences, Advances in Natural and Technological Hazards Research*, Vol. 27, p. 37-45. Springer, Dordrecht.
- Doxsee, W. W., 1948. The Grand Banks Earthquake of November 18, 1929. *Publications of the Dominion Observatory, Ottawa*, Vol. 7, No. 7, p. 323-335.
- Fine, I. V., Rabinovich, A. B., Bornhold, B. D., Thomson, R. E., and Kulikov, E. A., 2005. The Grand Banks landslide-generated tsunami of November 18, 1929: preliminary analysis and numerical modeling. *Marine Geology*, Vol. 215, p. 45-57.
- Gafeira, J., Bulat, J., and Evans, D., 2007. The southern flank of the Storegga Slide: Imaging and geomorphological analyses using 3D seismic. In: Lykousis, V., Sakellariou, D., and Locat, J. (eds.), *Submarine Mass Movements and Their Consequences, Advances in Natural and Technological Hazards Research*, Vol. 27, p. 57-65. Springer, Dordrecht.

- Giles, M. K., Mosher, D. C., Piper, D. J. W., and Wach, G. D., 2010. Mass Transport Deposits on the Southwestern Newfoundland Slope. In: Mosher, D. C., Shipp, R. C. et al. (eds.), *Submarine Mass Movements and Their Consequences, Advances in Natural and Technological Hazards Research*, Vol. 28, p. 657-665. Springer, Dordrecht.
- Haflidason, H., Sejrup, H. P., Nygård, A., Mienert, J., Bryn, P., Lien, R., Forsberg, C. F., Berg, K., and Masson D., 2004. The Storegga Slide: architecture, geometry and slide development. *Marine Geology*, Vol. 213, p. 201-234.
- Harbitz, C. B., Løvholt, F., and Bungum, H., 2014. Submarine landslide tsunamis: how extreme and how likely? *Natural Hazards*, Vol. 72, p. 1341-1374. doi: 10.1007/s11069-013-0681-3.
- Heezen, B. C., and Ewing, M., 1952. Turbidity currents and submarine slumps, and the 1929 Grand Banks earthquake. *American Journal of Science*, Vol. 250, p. 849-878.
- Heezen, B. C., Ericson, D. B., and Ewing, M., 1954. Further evidence for a turbidity current following the 1929 Grand Banks earthquake. *Deep-Sea Research*, Vol. 1, p. 193-202.
- Hodgson, E. A., and Doxsee, W. W., 1930. The Grand Banks earthquake, November 18, 1929. Eastern section of the seismological society of America, proceedings of the 1930 meeting, Washington, D. C., p. 72-81.
- Hughes Clarke, J. E., 1988. The geological record of the 1929 “Grand Banks” earthquake and its relevance to deep-sea clastic sedimentation. PhD thesis, Dalhousie University, Halifax, Nova Scotia.
- Hughes Clarke, J. E., Mayer, L. A., Piper, D. J. W., and Shor, A. N., 1989. Pisces IV submersible observations in the epicentral region of the 1929 Grand Banks earthquake. *Geological Survey of Canada Paper*, Vol. 88-20, p. 57-69.
- Hutchins, R. W., McKeown, D. L., and King, L. H., 1976. A Deep Tow High Resolution Seismic System for Continental Shelf Mapping. *Geoscience Canada*, Vol. 3, p. 95-100.
- Katz, O., Reuven, E., and Aharonov, E., 2015. Submarine landslides and fault scarps along the eastern Mediterranean Israeli continental-slope. *Marine Geology*, Vol. 369, p. 100-115.

- Kongsberg Maritime, 2017. Multibeam echosounder, Maximum depth 11000 m - EM 122. <https://www.km.kongsberg.com/ks/web/nokbg0240.nsf/AllWeb/01FB0F22974EA50FC125715E002B2143>, OpenDocument. Norway.
- Krastel, S., Wynn, R. B., Hanebuth, T. J. J., Henrich, R., Holz, C., Meggers, H., Kuhlmann, H., Georgiopoulou, A., and Schulz, H. D., (2006). Mapping of seabed morphology and shallow sediment structure of the Mauritania continental margin, Northwest Africa: some implications for geohazard potential. *Norwegian Journal of Geology*, Vol. 86, p. 163–176.
- Krastel, S., Braeunig, A., Feldens, P., et al., 2016. Geomorphology, processes and geohazards of giant submarine landslides and tsunami generation capacity, as recorded in the sedimentary record of the only historic slide of this kind: the 1929 Grand Banks landslide of the Canadian Atlantic continental margin. Cruise No. MSM47, September 30 - October 30, 2015, St. John's (Canada) - Ponta Delgada, Azores (Portugal). *Maria S. Merian-Berichte, MSM47*, p. 1-55, doi:10.2312/cr_msm47.
- Løvholt, F., Schulten, I., Mosher, D., Harbitz, C., and Krastel, S., 2019. Modelling of the 1929 Grand Banks slump and landslide tsunami. From: Lintern, D. G., Mosher, D. C., et al. (eds). *Subaqueous Mass Movements*. Geological Society, London, Special Publications, 477, <https://doi.org/10.1144/SP477.28>.
- Masson, D. G., Wynn, R. B., and Talling, P. J., 2010. Large Landslides on Passive Continental Margins: Processes, Hypotheses and Outstanding Questions. In: Mosher, D. C., Shipp, R. C. et al. (eds.), *Submarine Mass Movements and Their Consequences, Advances in Natural and Technological Hazards Research*, Vol. 28, p. 153-165. Springer, Dordrecht.
- McCall, C. W., 2006. A Geological and Geophysical study of the 1929 Grand Banks slide. M.Sc. Thesis, Saint Mary's University, Halifax, Nova Scotia.
- Mitchum, R. M. Jr, Vail, P. R., and Thompson III, S., 1977. Seismic stratigraphy and global changes of sea level, Part 2: The depositional sequence as a basic unit for stratigraphic analysis. In: *Seismic Stratigraphy - Applications to Hydrocarbon Exploration* (Ed. By C. E. Payton), American Association Petroleum Geology Memoir, Vol. 26, p. 53-62.

- Mosher, D. C., 2011. Cautionary considerations for geohazard mapping with multibeam sonar: resolution and the need for the third and fourth dimensions. *Marine Geophysics Research*, Vol. 32, p. 25-35.
- Mosher, D. C., and Simpkin, P. G., 1999. Environmental Marine Geoscience 1. Status and Trends of Marine High-Resolution Seismic Reflection Profiling: Data Acquisition. *Geoscience Canada*, Vol. 26, p. 174-188.
- Mosher, D. C., and Piper, D. J. W., 2007. Analysis of Multibeam seafloor imagery of the Laurentian Fan and the 1929 Grand Banks landslide area. In: Lykousis, V., Sakellariou, D., and Locat, J. (eds.), *Submarine Mass Movements and Their Consequences, Advances in Natural and Technological Hazards Research*, Vol. 27, p. 77-88. Springer, Dordrecht.
- Mosher, D.C., and West, M.T.N., 2007. CCGS Hudson 2007020 Cruise Report: Laurentian Fan and eastern Scotian Slope, Argentia to Halifax; Geological Survey of Canada, Open File 5668, 1 DVD.
- Mosher, D. C., Piper, D. J. W., Campbell, D. C., and Jenner K. A., 2004. Near surface geology and sediment-failure geohazards of the central Scotian Slope. *AAPG Bulletin*, Vol. 88, No. 6, p. 703-723.
- Mosher, D. C., Bigg, S., and LaPierre, A., 2006. 3D seismic versus multibeam sonar seafloor surface renderings for geohazard assessment: Case examples from the central Scotian Slope. *The Leading Edge* p. 1484-1494.
- Piper, D. J. W., and Aksu, A. E., 1987. The source and origin of the 1929 Grand Banks turbidity current inferred from sediment budgets. *Geo-Marine Letters*, Vol. 7, p. 177-182.
- Piper, D. J. W., and Normark, W. R., 1982. Acoustic interpretation of Quaternary sedimentation and erosion on the channelled upper Laurentian Fan, Atlantic margin of Canada. *Canadian Journal of Earth Sciences*, Vol. 19, p. 1974-1984.
- Piper, D. J. W., Shor, A. N., and Hughes Clarke, J. E., 1988. The 1929 "Grand Banks" earthquake, slump, and turbidity current. In: *Sedimentological Consequences of Convulsive Geologic Events* (Ed. By H. E. Clifton), Geological Society of America Special Paper, Vol. 229, p. 77- 92.

- Piper, D. J. W., Cochonat, P., and Morrison, M. L., 1999. The sequence of events around the epicentre of the 1929 Grand Banks earthquake: initiation of debris flows and turbidity current inferred from sidescan sonar. *Sedimentology*, Vol. 46, p. 79-97.
- Piper, D.J.W., Mosher, D.C., Gauley, B.-J., Jenner K. and Campbell, D.C., 2003. The chronology and recurrence of submarine mass movements on the continental slope off southeastern Canada. In: Locat, J., Mienert, J. and Boisvert, L. (eds.) *Submarine Mass Movements and Their Consequences, Advances in Natural and Technological Hazards Research*, Vol. 19., p. 299-306. Springer, Dordrecht.
- Piper, D. J. W., Macdonald, A. W. A., Ingram, S., Williams, G. L., and McCall, C., 2005. Late Cenozoic architecture of the St. Pierre Slope. *Canadian Journal of Earth Sciences*, Vol. 42, p. 1987-2000, doi:10.1139/E05-059.
- Ruffman, A., 2001. Potential for large-scale submarine slope failure and tsunami generation along the U. S. mid-Atlantic coast: Comment. *Geology*, Vol. 29, No. 10, p. 967.
- Sangree, J. B., and Widmier, J. M., 1979. Interpretation of depositional facies from seismic data. *Geophysics*, Vol. 44, No. 2, p. 131-160.
- Spieß, V., 1993. *Digitale Sedimentechographie – Neue Wege zu einer hochauflösenden Akustostratigraphie*. Berichte Fachbereich Geowissenschaften Universität Bremen, Vol. 35, pp. 1–199.
- Talling, P. J., Wynn, R. B., Masson, D. G., Frenz, M., Cronin, B. T., Schiebel, R., Akhmetzhanov, A. M., Dallmeier-Tiessen, S., Benetti, S., Weaver, P. P. E., Georgiopoulou, A., Zühlsdorff, C., and Amy, L. A., 2007. Onset of submarine debris flow deposition far from original giant landslide. *Nature letters*, Vol. 450, p. 541-544, doi:10.1038/nature06313
- Teledyne Reson, 2017. ATLAS PARASOUND Deep-Sea parametric sub-bottom profiler. <http://www.teledynemarine.com/parasound-sub-bottom-profilers?ProductLineID=79/>, Slangerup, Denmark.
- Urgeles, R., and Camerlenghi, A., 2013. Submarine landslides of the Mediterranean Sea: Trigger mechanisms, dynamics, and frequency-magnitude distribution. *Journal of Geophysic Research and Earth Surface*, Vol. 118, p. 2600-2618, doi: 10.1002/2013JF002720.

- Weirich, F. H., 1989. The generation of turbidity currents by subaerial debris flows, California. *Geological Society of America Bulletin*, Vol. 101, p. 278-291.
- Winkelmann, D., Geissler, W., Schneider, J., and Stein, R., 2008. Dynamics and timing of the Hinlopen/Yermak Megaslide north of Spitsbergen, Arctic Ocean. *Marine Geology*, Vol. 250, p. 34-50.

CHAPTER 3: A MASSIVE SLUMP ON THE ST. PIERRE SLOPE, A NEW PERSPECTIVE ON THE 1929 GRAND BANKS SUBMARINE LANDSLIDE

Chapter 3 is a submitted version of “Schulten, I., Mosher, D. C., Piper, D. J. W. and Krastel, S., A massive slump on the St. Pierre Slope, a new perspective on the 1929 Grand Banks submarine landslide” to the AGU Journal of Geophysical Research: Solid Earth on November 21st, 2018. Details on each author’s contribution are shown in Table 1.3.

Key Points:

- The 1929 Grand Banks tsunamigenic landslide included a massive slump and not just surficial landslides as described in earlier literature.
- The slump (~500 m thick, ~560 km³) occurred along oblique faults (~17°) with vertical offsets of 100 m and horizontal offsets of 330 m
- Both, the massive slump and translational surficial (upper 20 m) sediment failures likely contributed to the 1929 tsunami.

3.1 ABSTRACT

The 1929 Grand Banks submarine landslide on the southwestern Grand Banks of Newfoundland was triggered by a M_w 7.2 strike-slip earthquake. It is the first studied example of a submarine mass movement known to have caused a turbidity current and tele-tsunami. The event resulted in 28 casualties and caused severe economic damage. The St. Pierre Slope is the main source area for the sediment failure. It contains translational and probable retrogressive surficial failures (<25 m); the majority of which lie in deep water (>1700 mwd). These observations contradict what might be expected for a tsunamigenic event, thus the objective of this study is to look for other potential causal mechanisms. A comprehensive analysis of 2D seismic reflection data of various resolutions and multibeam bathymetry allowed mapping of previously unrecognized stratigraphic and structural features. Numerous, low-angle (~17°) faults are present throughout the Quaternary section (to 500-600 mbsf) of the St. Pierre Slope that are associated with seafloor escarpments (750-2000 mwd). These faults have up to 100 m-high displacement and are interpreted as

part of a massive ($\sim 560 \text{ km}^3$), complex slump. There are multiple décollements (250, 400-550 mbsf) within this slump and there is indication for slumping in at least two directions. Evidence suggests slumping as a result of the 1929 earthquake reactivated faults, with ~ 100 m seafloor displacement in places. The 1929 submarine landslide therefore involved two failure mechanisms: massive slumping (~ 500 m-thick) and consequent widespread, surficial (< 25 m) sediment failures. Both failure mechanisms possibly contributed to tsunami generation.

3.2 INTRODUCTION

The 1929 “Grand Banks” submarine landslide on the eastern Canadian continental margin, southwest of Newfoundland, demonstrates the potential impacts of submarine sediment failure that caused many casualties and severe economic damage. This landslide is presumed to have been triggered by a M_w 7.2 strike-slip earthquake with a low vertical thrust component (< 20 cm offset) (Bent, 1995). The earthquake occurred beneath the Laurentian Fan on November 18th, 1929; a region that is characterized by relatively high modern seismicity compared to other regions at the Atlantic passive continental margin (Fig. 3.1) (Bent, 1995; Mazzotti, 2007). The landslide severed twelve trans-Atlantic telecommunication cables (Fig. 3.2) (Doxsee, 1948) leading to the first recognition of naturally occurring submarine turbidity currents (Heezen & Ewing, 1952). It is further one of the few landslides known to have generated a tele-tsunami that crossed the Atlantic Ocean (Fine et al. 2005). The tsunami hit coastal areas of southern Newfoundland and parts of Nova Scotia causing 28 casualties and destruction of onshore infrastructure (Ruffman, 2001; Fine et al. 2005). Previous studies identified the landslide as a thin (upper 5-25 m), widespread slope failure (Fig. 3.2), as there is no major headwall scarp nor evidence of a single major slump deposit near the source area (Piper et al., 1988; 1999; Mosher & Piper, 2007).

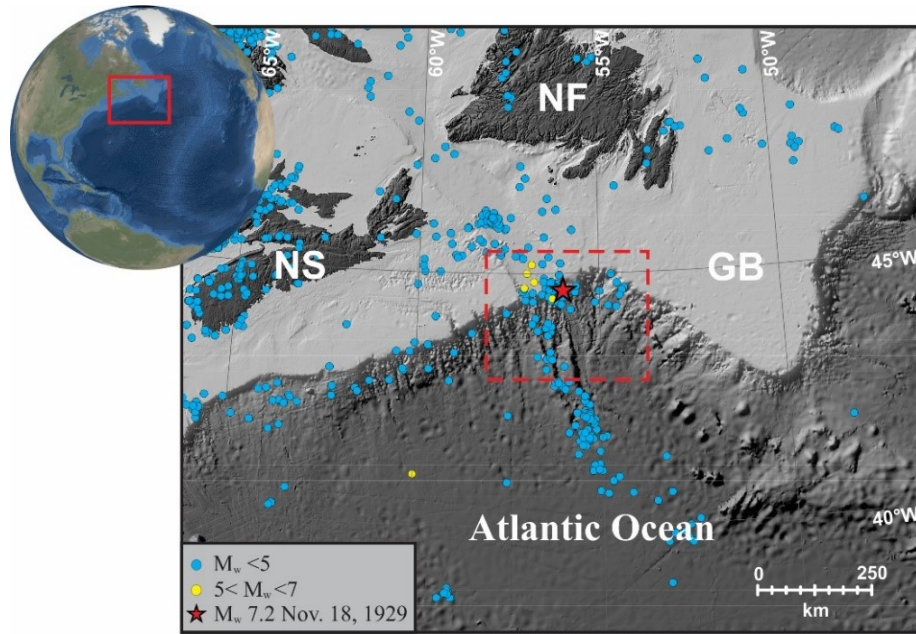


Fig. 3.1: Regional bathymetric map of Atlantic Canada with the location of the study area indicated within the red dotted rectangle off the southwestern Grand Banks of Newfoundland. Coloured dots indicate earthquake epicentres available from 1985 to present (Earthquakes Canada). The red star indicates the location of the M_w 7.2 November 18th, 1929 earthquake, as relocated by Bent (1995). The globe was created using ArcGlobe, while seafloor renders were derived using the GEBCO 2014 global bathymetric grid and imaged in ArcMap. NS = Nova Scotia, NF = Newfoundland and GB = Grand Banks of Newfoundland.

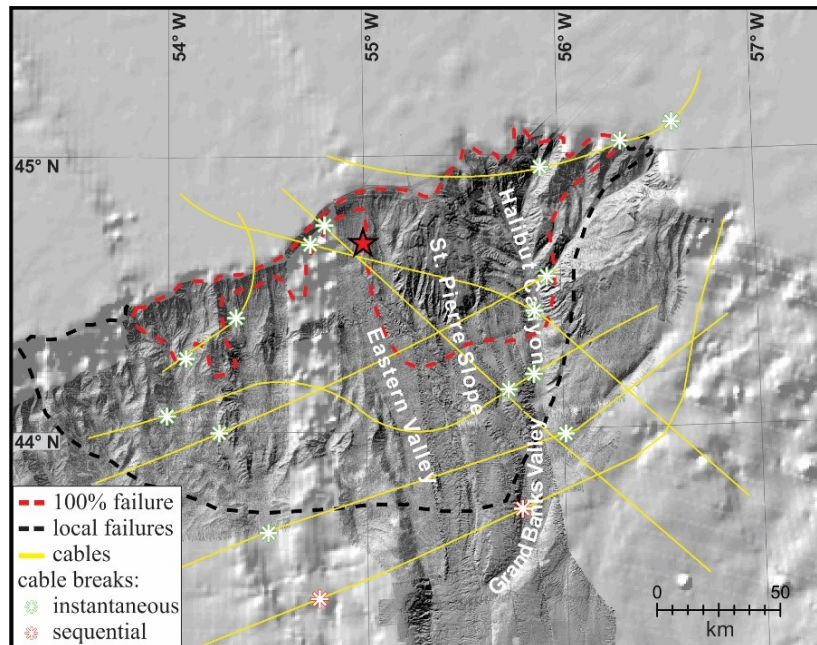


Fig. 3.2: A seafloor render of the upper slope region of the Laurentian Fan, including the St. Pierre Slope study area. The epicenter location of the M_w 7.2 1929 Grand Banks earthquake is shown with a red star. The red dashed polygon represents the area where 100% of the seafloor sustained sediment failure and the black dashed line outlines the total region where local failures are observed (Piper et al., 1999; Mosher & Piper, 2007). The dark grey areas of the seafloor render were generated from multibeam data while the light grey areas were derived from the GEBCO 2014 global bathymetric grid.

The St. Pierre Slope (Fig. 3.2), an inter-canyon high between Eastern Valley of the Laurentian Fan and Halibut Canyon is identified as the main failure area of the submarine slide. It is the location of the earthquake, the area of the instantaneous cable breaks, and hosts seafloor escarpments and slide deposits believed related to the slide (Piper et al., 1999; Mosher & Piper, 2007; Schulten et al. 2019). A near-surface sediment volume of $\sim 100 \text{ km}^3$ is estimated to have been displaced at St. Pierre Slope, with the majority being due to translational, retrogressive failures in $>1700 \text{ m}$ water depth (mwd) (Schulten et al., 2019). The average height of head scarps on the St. Pierre Slope is 20 to 50 m, and debris flows/slide deposits are generally thin ($<20 \text{ m}$) and distributed over a large area ($\sim 5200 \text{ km}^2$) (Schulten et al., 2019). Additionally, it is thought that approximately 40 km^3 of the failed sediment volume rapidly transitioned into a massive turbidity current (Piper et al., 1999; McCall, 2006; Schulten et al., 2019). These observations lead to the question as to why the 1929 submarine slope failure was tsunamigenic. The water depths in which these surficial failures occurred, their thin nature and the fact that they rapidly diluted into a turbidity current, suggest that there was insufficient water volume displacement to generate the observed tsunami. The hypothesis of this study, therefore, is that deep-seated failure, as might result from a large slump, resulted in significant seafloor displacements. These seafloor displacements resulted in generation of the observed tsunami.

The objective of this study is to determine if there are deep-seated stratigraphic and structural features that resulted from the 1929 Grand Banks earthquake that may have led to tsunami generation. This objective is met through detailed seismic-stratigraphic analysis of the region using newly acquired and legacy multi-channel, single-channel and ultra-high resolution seismic reflection data (Fig. 3.3) as well as multibeam echosounder data (Fig. 3.4). The results are important in terms of reconstruction of the 1929 slope failure and

its failure dynamics. Most models for tsunami generation by landslides require a solid mass being almost instantly displaced, thereby creating a large headscarp. Such headscarp is absent at the St. Pierre Slope. Hence, understanding the dynamics of the Grand Banks failure, which caused a significant tsunami will lead to better understanding of the geohazard and tsunami generation potential of continental margin landslides.

3.3 METHODS

This study integrates geophysical data with multiple scales of resolution that were acquired from the St. Pierre Slope over the last three decades (1984-2015). The completeness of these data sets allows for a more comprehensive study compared to earlier studies. Data were acquired by the Geological Survey of Canada (GSC) and in a co-operation project between the GSC, Dalhousie University, the University of Kiel and the University of Bremen, Germany (Fig. 3.3). Hydrocarbon industry exploration data were also used in this project.

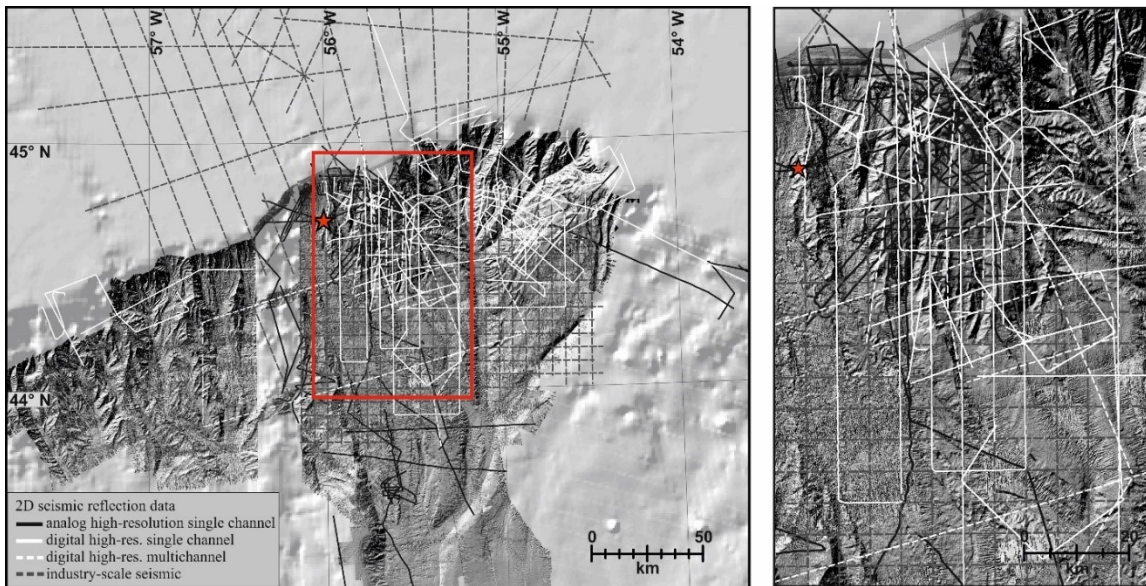


Fig. 3.3: Left: Tracklines showing the location of 2D seismic reflection data acquired in the Laurentian Fan area over the past three decades. The red star marks the epicenter of the 1929 earthquake. The red rectangle outlines the area shown to the right.

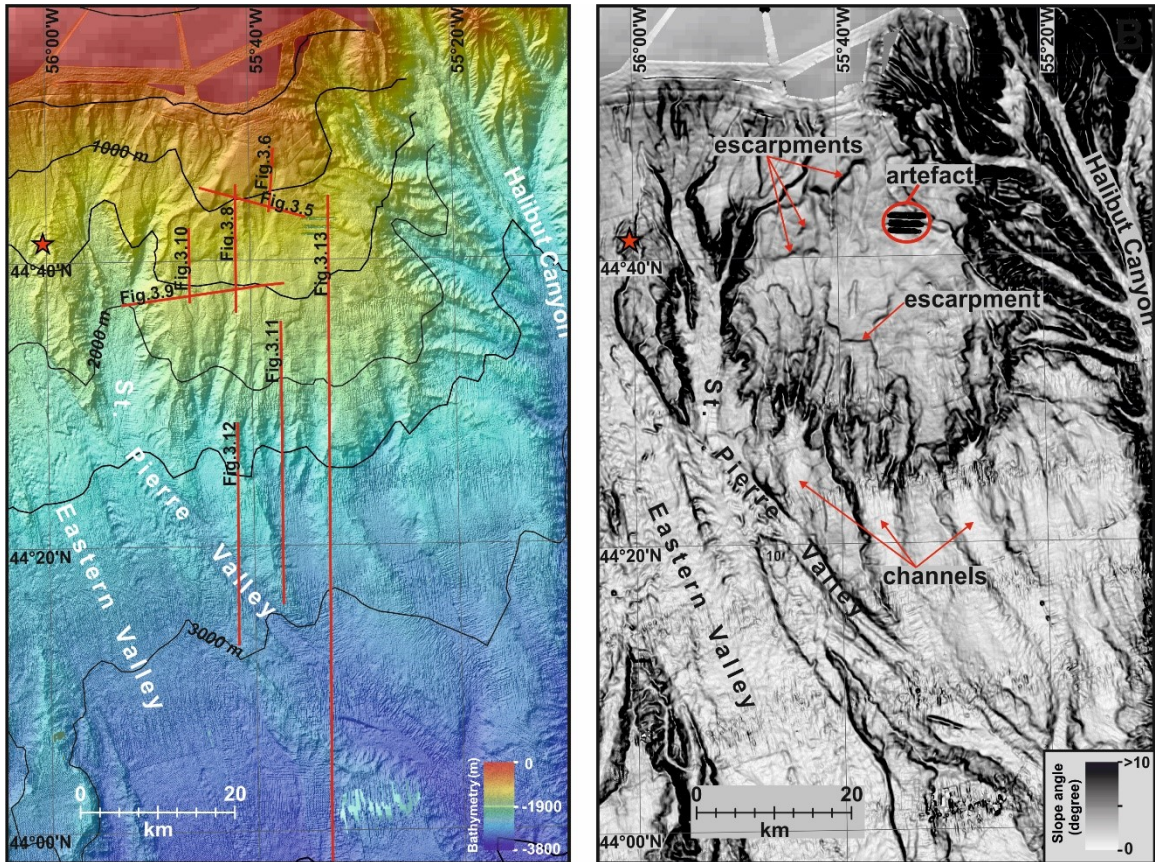


Fig. 3.4: Left: Multibeam sonar bathymetric render of the St. Pierre Slope study area. The location of the 1929 Grand Banks earthquake is shown with a red star, while the red lines represent tracks of seismic data shown in Figs. 3.5 to 3.13. Right: A slope angle map of the same area that accentuates some of the steeper morphologic features such as escarpments and channel walls; a few of which are labelled.

3.3.1 High resolution single- and multi-channel 2D seismic reflection data

A total of ~4100 km of seismic reflection data are available from the St. Pierre Slope region with ~1600 km of analog data that were acquired in the late 1980s and early 1990s as well as ~2500 km of more recent digital data (Fig. 3.3). Acquisition systems included sleeve guns, airguns, and GI guns in concert with high-resolution single- and multi-channel hydrophone arrays. Specifications on acquisition systems used are found in the expedition reports, *e.g.*, Mosher and West (2007) and Krastel et al. (2016). The processed seismic data contain bandwidths from 20 to 120 Hz that imaged the sub-bottom down to ~1 km. The pre-migrated modal horizontal resolution of the high-resolution seismic data is 60 to 74 m in 500 mwd and 195 to 235 m in 5000 mwd, as governed by the Fresnel zone. The vertical

resolution is ~ 5 m at 1500 m s^{-1} according to the Rayleigh criteria. In addition, ~ 4100 km of industry-scale (1984/85 and 1998) 2D seismic reflection data were acquired from the St. Pierre Slope (Fig. 3.3). These data image the sub-bottom down to ~ 5 km. The industry-scale seismic data have a pre-migrated modal horizontal resolution in the range of 180 m in 500 mwd to 560 m in 5000 mwd with a vertical resolution of ~ 30 m (Rayleigh criteria). The grid spacing between good quality seismic lines is highly variable and averages 4 km with larger spacing of up to 8 km between cross lines and lines in the southern part of the slope (Fig. 3.3). This sparse line spacing requires interpolation that poses a constraint on positioning and hence uncertainty. It is estimated that structural elements less than 4 to 8 km in size might not be imaged.

Scanned paper records of analog data were rectified, converted to digital seismic data (SEG-Y format), and geo-referenced. All high-resolution seismic reflection data were filtered and migrated. Details of seismic processing of single-channel seismic reflection data are provided in the expedition reports (Piper, 2006; Mosher & West, 2007). Multi-channel seismic reflection data were further processed using standard procedures including geometry set up, binning, normal-moveout corrections, and stacking.

In order to establish the stratigraphy, analyse sub-bottom structures and identify post-depositional deformation of the St. Pierre Slope, seismic reflection horizons were correlated throughout the data sets using IHS Kingdom SuiteTM. Ten stratigraphic reflection horizons were mapped across the slope area, labelled R0 to R9 from old to young. Reflection horizons were selected based on their amplitude characteristics and regional coherency. A consistent stratigraphic correlation was achieved by using the seismic grid to correlate each reflection back to its point of origin. Table 3.1 provides a list of stratigraphic horizons used in this study that are correlated to reflections described in earlier studies and their respective age estimates. Piper et al. (2005) developed a complete seismic stratigraphy for the Quaternary section of the St. Pierre Slope using glacial ice margin stratigraphy back to MIS 12, modified by Skene and Piper (2006) and Piper et al. (2007). Only horizon R9 has C-14 control and there is biostratigraphic control near horizons R0 and R1 (Uchupi & Austin, 1979; Piper & Normark, 1982, 1989; Piper et al., 2005). Sedimentation rates were

determined using the age estimates and sediment unit thicknesses of areas that appear to be un-failed.

Table 3.1: Seismic reflections recognized in this study in comparison to earlier studies and their estimated age. Horizons R2, R4 and R5 are not shown, as they do not correlate with dated reflectors of earlier studies.

| Horizons: this study | Horizons: previous studies | Age estimate | Age control |
|----------------------|---|--|---|
| | | (according to Piper & Normark, 1982; 1989; Piper et al. 2005; and Skene & Piper, 2006) | |
| R9 (green) | O (Skene & Piper, 2006) Q90 (Piper et al. 2005) B (Piper & Normark, 1989) | ~33 ka cal | Radiocarbon dating Mollusc shell from 132 cm sub-bottom in core 90015-17 (Piper et al. 2005) |
| R8 (blue) | Q70 (Piper et al. 2005) Q (Piper & Normark, 1982; Skene & Piper, 2006) | ~150 ka - MIS* 6 | Ice-margin stratigraphy (Piper et al. 2005; Skene & Piper, 2006) |
| R6 (light blue) | ~B (Skene & Piper, 2006) Q50 (Piper et al. 2005) | ~470 ka – MIS* 12 | Ice-margin stratigraphy (Piper et al., 2005) |
| R3 (dark blue) | ~A (Skene & Piper, 2006) | 880 ka (?) – MIS* 22 | Erosional surface correlated to 1 st major sea-level lowstand (Skene & Piper, 2006) |
| | Q30 (Piper et al. 2005) | ~1.1 Ma (?) | Interpolation between Q50 and Q10 (Piper et al., 2005) |
| R1 (light green) | Underneath Q10 (Piper et al., 2005) Underneath C (Piper & Normark, 1989) ~A (Piper & Normark, 1982; 1989) | ~1.5-1.8 Ma (?) | Biostratigraphic control Early Pleistocene (prev. late Pliocene) – planktonic foraminifera in mudstone sample (F.M. Gradsteine, in Piper & Normark, 1989) |
| R0 (yellow) | P50 (Piper et al. 2005) ~L (Piper & Normark, 1982; Uchupi & Austin, 1979) | ~ 2.6 Ma BP | Biostratigraphic control Begin of the early Pleistocene (prev. mid-late Pliocene) – sample recovered by DSVR Alvin (Piper & Normark, 1989) and well dated (biostrat.) base of a turbidite section at DSDP site 382 (Piper et al. 1990) |

* MIS = marine isotope stage

Five seismic facies (Table 3.2) and five seismic units (Table 3.3) are present in the seismic reflection data indicative of different depositional processes. A Wulff stereonet (Lagrange projection) was used to correct apparent dips of specific sub-bottom structures that were calculated from horizontal and vertical offset readings. Seismic units were converted from travel-time to depth using a velocity of 1500 m s⁻¹ at sub-bottom depths <150 m and 2000 m s⁻¹ for the sub-bottom >150 m. This estimate is in good agreement with estimates from previous studies *e.g.*, Giles et al. (2010) and Mosher et al. (2010c). Uchupi and Austin

(1979) used a seismic velocity of 1900 to 2100 m s⁻¹ for sediments at horizon L that lies near horizon R0 of this study.

3.3.2 Other data

Ultra-high resolution sub-bottom seismic reflection and multibeam echosounder data (Fig. 3.4) were acquired often simultaneously with high-resolution 2D seismic reflection data (Fig. 3.3). Details about both systems are presented in Schulten et al. (2019). This work provided an assessment of the near-surface sediment failures on St. Pierre Slope using the ultra-high resolution sub-bottom data. Five reflections were correlated throughout the upper study area and tied to the C-14 age control of McCall (2006).

3.4 RESULTS

3.4.1 Seismic facies distribution

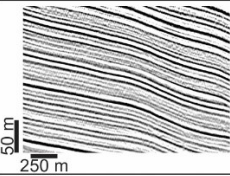
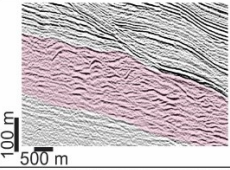
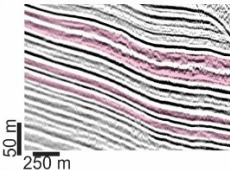
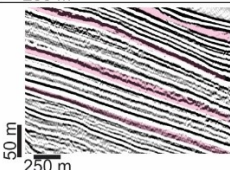
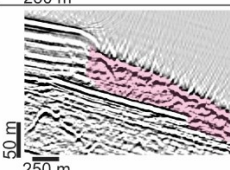
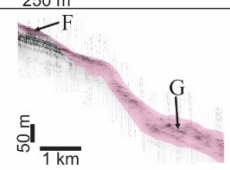
Four seismic facies are recognized in the 2D seismic reflection data:

- 1) Facies A consists of continuous parallel to semi-parallel, high amplitude reflections. This facies is present throughout the seismic data (Table 3.2, Figs. 3.5 & 3.6);
- 2) Facies B comprises irregular, wavy dipping reflections. A typical thickness for these reflections is ~75 ms (ms in two-way travel time). Facies B is abundant in sub-bottom depth >500 ms (msbsf) (Table 3.2);
- 3) Facies C is represented by ~40 ms-thick lenses and sheets of low amplitude, chaotic reflections interbedded with facies A in sub-bottom depths >300 ms (Table 3.2, Fig. 3.6);
- 4) Facies D consists of 10 ms-thin, low amplitude, amorphous reflections interbedded with facies A in <300 msbsf (Table 3.2, Fig. 3.6);
- 5) Facies E comprises chaotic and transparent reflections along parts of the present seafloor between 2000 and 2800 mwd (Table 3.2). This facies is ~45 ms thick.

The ultra-high resolution seismic data show two additional facies that are described in detail by Schulten et al. (2019).

- 6) Facies F consists of 5 to 7 ms-thick indistinct bottom echoes with incoherent reflections that occur across most of the slope from 750 to 2000 mwd and 2500 to 4000 mwd (Table 3.2, Fig. 3.7). This facies thickens below 20 to 50 ms-high escarpments present in >1700 mwd;
- 7) Facies G is equivalent to facies E of the 2D seismic reflection data and consists of indistinct regular overlapping hyperbolic bottom echoes (Table 3.2). Both, facies F and G, cover 12 to 25 ms-high escarpments that are present between 2000 and 2300 mwd.

Table 3.2: Seismic facies A to E and acoustic facies F to G on the St. Pierre Slope. Facies B to G that are interbedded with, or overly, facies A are highlighted in pink.

| Facies | Examples | Description |
|--------------|---|---|
| A |  | Continuous parallel reflections |
| B |  | Irregular, wavy dipping reflections, evident in >500 msbsf, ~75 ms thick |
| C |  | Lenses and sheets of low amplitude, chaotic reflections, evident in >300 msbsf, ~40 ms thick |
| D |  | Low amplitude, amorphous reflections, evident in <300 msbsf, ~10 ms thick |
| E |  | Chaotic, transparent reflections, evident along most of the seafloor of the St. Pierre Slope from 1700 to 2800 mwd, ~45 ms thick |
| F + G |  | F: Indistinct sub-bottom echoes with incoherent reflections, ~10 ms thick G: Indistinct overlapping hyperbolic bottom echoes, ~45 ms thick |

3.4.2 Seismic stratigraphy

Ten seismo-stratigraphic horizons, labelled R0 to R9, were mapped throughout the study area. A comparison of the mapped horizons to those from previous studies along with age estimates is provided in Table 3.1. The oldest horizon, R0 (Fig. 3.8), directly overlies facies B reflections and is apparent within the sub-bottom of most of the slope area between 1300 and 3700 mwd. In previous studies, this horizon was commonly identified as being of a late Pliocene to early Pleistocene age (Uchupi & Austin, 1979; Piper & Normark, 1989). Horizon R1 (Fig. 3.5) is a high amplitude reflection on top of a thick package of facies A reflections that correlates throughout the slope area (Table 3.2, Fig. 3.5). Thick packages of facies C are commonly found in sub-bottom depths above and below horizon R1. This horizon correlates to horizon 'A' of Piper and Normark (1982; 1989; horizon A_{P+N}) that is dated between 1.5 to 1.8 Ma. Skene and Piper (2006) argued that horizon 'A_{P+N}' of Piper and Normark (1982; 1989) may be as young as marine isotopic stages (MIS) 20-24, placing deposition around 880 ka. Mapping in this study, however, revealed that the horizon mapped by Skene and Piper (2006; horizon A_{S+P}) is not identical to horizon 'A_{P+N}' of Piper and Normark (1982; 1989).

The horizons R2 and R3 (Fig. 3.5) are proximal to each other. Reflections below R3 including horizon R2 are locally missing along the upper slope between 750 and 1400 mwd. Horizons R2 and R3 are further absent in the south-eastern part of the lower slope area. Piper et al. (2005) proposed horizon R3 (Q30) was about 1100 ka old, but this horizon might be as young as 880 ka (MIS 22), as horizon R3 is shown to correspond to horizon 'A_{S+P}' of Skene and Piper (2006). Horizon R4 (Fig. 3.5) is a high amplitude reflection that is interbedded within lower amplitude reflections. This horizon traces throughout the slope area.

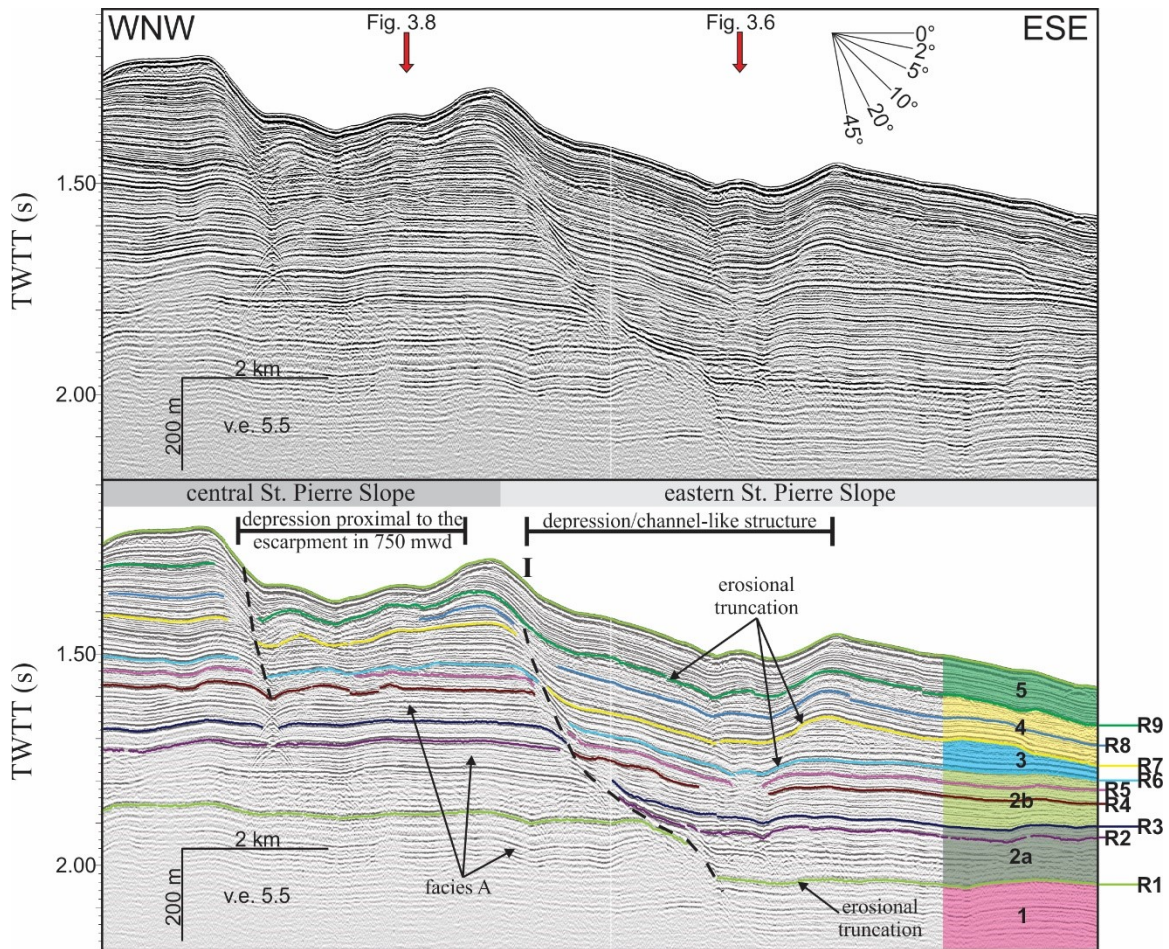


Fig. 3.5: A strike-profile across the upper St. Pierre Slope between 800 and 1000 mwd, see Fig. 3.4 for location. The upper panel is without interpretation, the lower panel is with interpretations and shows horizons mapped across the slope area (R1 to R9) and interpreted seismic units 1 to 5. The black dashed lines connect reflection offsets. Offset “I” is discussed in section “3.4.4”. Red arrows in the upper panel highlight intersections with other seismic profiles.

Reflection horizons R5 and R6 (Fig. 3.5) occur adjacent to each other within 300 to 400 msbsf. Interbedded sheets of facies C are often present between these two horizons. Horizon R6 is traceable throughout the slope area while R5 may be locally absent. Deposition of horizon R6 or Q50 of Piper et al. (2005) is estimated to be associated with MIS 12 (470 ka). The bottommost reflection of a triplet of high amplitude reflections is mapped as horizon R7 (Fig. 3.5). Another triplet is evident below horizon R7 but is largely absent within the sub-bottom in water depths >900 m (Figs. 3.6 & 3.8). Horizons R8 and R9 (Fig. 3.5) are each a topmost reflection of a doublet of high amplitude reflections that are traceable throughout the entire slope area. Facies D reflections are common between

horizon R8 and the modern seafloor (Fig. 3.6). Deposition of horizon R8 is estimated to have occurred during MIS 6 or ~150 ka (Piper et al., 2005). Horizon R9 is radiocarbon dated to ~30 ka (Piper et al., 2005). The sediment column between horizon R9 and the seafloor was mapped by Schulten et al. (2019) using ultra-high resolution seismic data (Fig. 3.7). McCall (2006) previously described the reflections in this interval, labelled Q91 to Q99 (Fig. 3.7), and provided interpolated radiocarbon ages from ~30 ka BP (Q91) to ~15 ka BP (Q99). Most of the modern seafloor of the St. Pierre Slope is formed by deposits of facies F and G.

3.4.3 Seismic units

Five seismic units (1 to 5) are distinguished on St. Pierre Slope based on the occurrence of major unconformities (Table 3.3, Figs. 3.5 & 3.6). Most unconformities are erosional truncations or disconformities. The first regionally correlatable horizons above these unconformities are, R1, R3, R6, R7, and R9 (Fig. 3.5). Horizon R3 and reflections below it are locally missing (Fig. 3.8). All units consist mostly of facies A (Table 3.3).

Table 3.3: Seismic units that are distinguished on the St. Pierre Slope and identified unit boundaries.

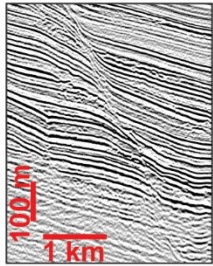
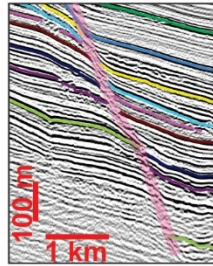
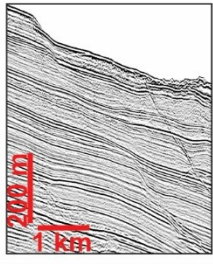
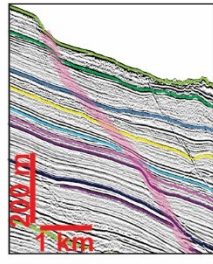
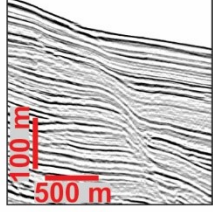
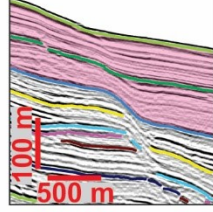
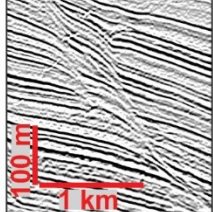
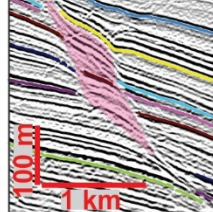
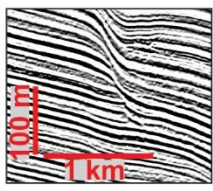
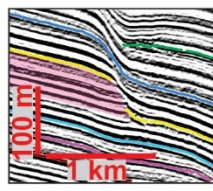
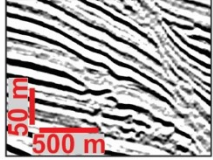
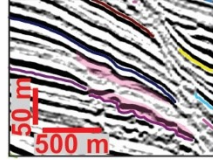
| Seismic units | Reflection boundaries | Description |
|---------------|-----------------------|--|
| 5 | seafloor | Unit overlies a unconformity at horizon R9. Facies D interbedded in facies A. Facies E, F and G are evident along most of the seafloor. |
| 4 | R9 | Facies D interbedded in facies A. A regional unconformity at horizon R9 forms the upper boundary of this unit. |
| 3 | R7 | Facies D interbedded in facies A. An unconformity at horizon R7 with reflection truncations and downslope missing section marks the upper boundary of unit 3. |
| 2b | R6 R5 | Sub-unit 2a and 2b; consists of facies A with thick packets of interbedded facies C. Unit 2a is based on a local unconformity that is covered by horizon R3. A major unconformity at horizon R5 that is overlain by horizon R6 defines the upper boundary of unit 2. |
| 2a | R3 | |
| 1 | R1 | Facies A overlying facies B. Facies C shows an increasing abundance towards the top of this unit. Horizon R1 forms a localised unconformity of this unit. |
| | R0 | |

3.4.4 Reflection offsets

3.4.4.1 GEOMETRY AND GEOGRAPHIC SETTING

Seismic reflection data display numerous reflection offsets that extend to ~700 ms below the seafloor (Table 3.4, Figs. 3.5, 3.6, 3.8). Some offsets appear as sigmoid folds rather than as truncated reflections (Table 3.4, Fig. 3.8). There are numerous examples of chaotic (facies C) and transparent (facies D) reflection packets that show a consistent thickness across offsets (Fig. 3.6). This observation indicates that the offsets are post-depositional. Most offsets lie below seafloor escarpments (Figs. 3.4, 3.6 & 3.8), but are too large or have the wrong geometry to be solely the velocity effect of different water column thicknesses. There are three short (8-24 km), 40 to 100 m-high escarpments with relatively steep gradients (~7.5°) along the upper slope in 750, 1100 and 1300 mwd (Fig. 3.4). In >1500 mwd, escarpments are 20 to 25 m high, ~40 km long, and also steep (10-22°), creating a terraced morphology towards the middle and lower slope (Fig. 3.4). Distinct differences in the characteristics of reflection offsets are apparent from east to west along the upper slope, and in the downslope direction (Figs. 3.6, 3.10 & 3.11). As a result, offsets in the upper slope (500-1700 mwd) (Figs. 3.6-3.10) are described in section 3.4.4.1.1 and for the middle and lower slope (1700-4000 mwd) (Figs. 3.11 & 3.12) are described in the section 3.4.4.1.2.

Table 3.4: Examples of structural features at the St. Pierre Slope. Important features are highlighted in pink.

| Sub-bottom feature | Example | |
|--|---|---|
| | without interpretation | with interpretation |
| Distinct reflection offset |  |  |
| Indistinct reflection offset |  |  |
| Dragged reflection unit |  |  |
| Rhombic-shaped block |  |  |
| Reflection truncation with missing section downslope |  |  |
| Small (10-20 ms high) buried escarpments adjacent to the reflection offset |  |  |

3.4.4.1.1 UPPER SLOPE (500-1700 MWD)

The upper slope is further subdivided into i) eastern, ii) central and iii) western parts because there are distinct differences in reflection offsets and escarpments in these three regions (Figs. 3.6-3.10).

i) Eastern St. Pierre Slope

An escarpment in 750 mwd extends 8 km laterally. In the eastern part of St. Pierre Slope, this escarpment shows a pronounced southward dipping reflection offset, labelled “I” on Fig. 3.6 and 3.7. This offset decreases from ~170 ms at 650 msbsf (R1) to ~70 ms at 350 msbsf (R5) (Fig. 3.6). It then increases from ~83 ms at ~300 msbsf (R6) to ~123 ms at the seafloor (Fig. 3.6). The plane of offset “I” dips at an apparent angle of 17° (Fig. 3.6). Downslope from the dipping plane, there is some missing section: ~33 ms below horizon R7 and ~80 ms below horizon R1 (Figs. 3.5 & 3.6). A strike profile (Fig. 3.5) reveals a depression or channel-like structure corresponding with the missing section below horizon R7. A rhombic-shaped block (~900 m wide, ~120 ms-high) with internal chaotic reflections is evident adjacent to offset “I” between horizon R2 and R6 (Table 3.4, Fig. 3.6). An erosional truncation in ~100 msbsf (R9) adjacent to the reflection offset shows identical morphological features (*e.g.*, depth of erosion, height of escarpments) on both sides of the reflection offset (Fig. 3.6).

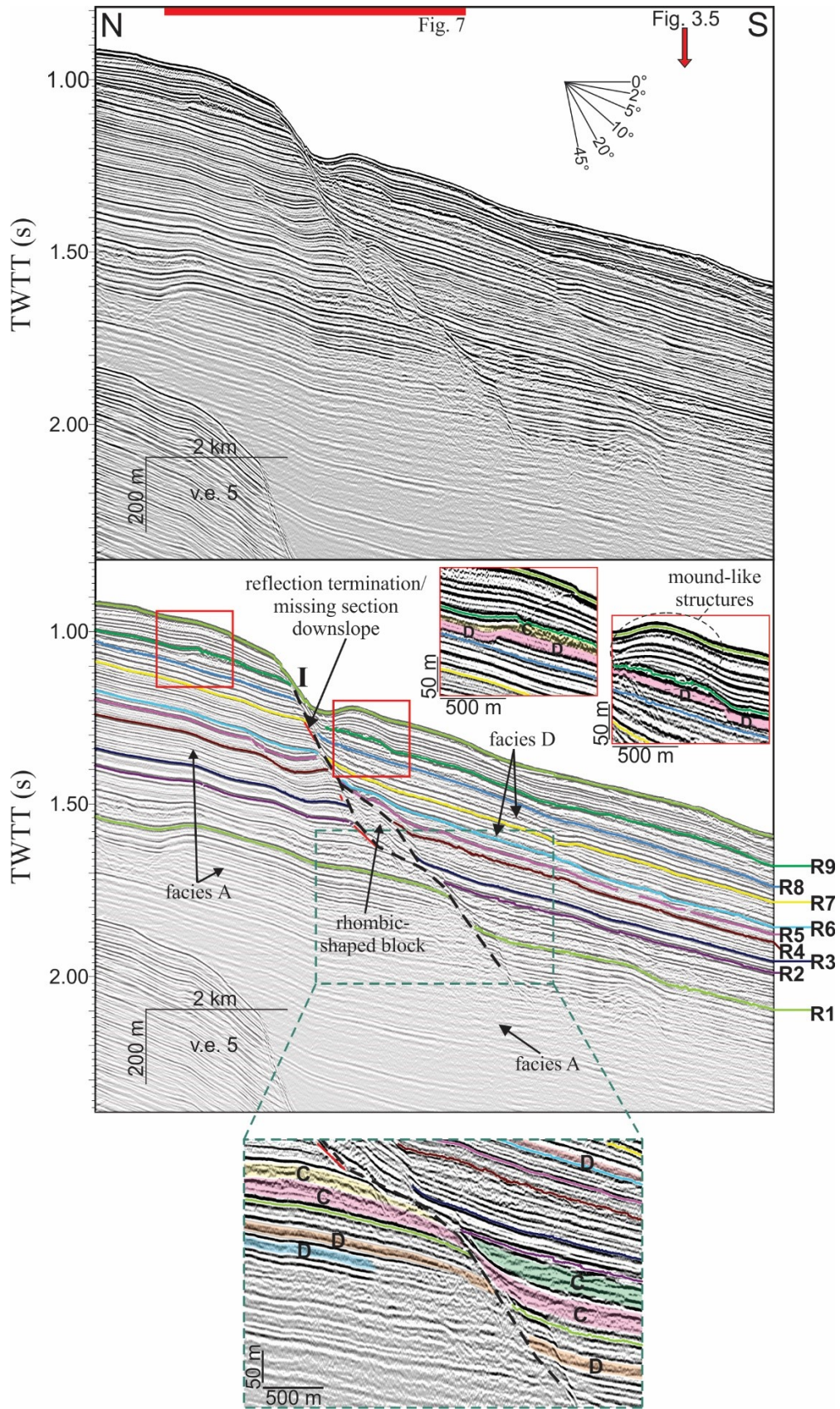


Fig. 3.6: Dip-oriented seismic reflection profile along the eastern part of the upper St. Pierre Slope (see Fig. 3.4 for location). A reflection offset is evident underneath the escarpment in ~750 mwd. The upper panel is the seismic profile without interpretation and the middle and lower panels show the interpreted section. The section of the profile that corresponds with that shown in Fig. 3.7 is indicated by the red bar. The black dashed lines follow the line of reflection offsets. This offset is labelled “I”. The inset profiles in the upper right corner of the middle panel show an enlargement of the upper strata down to ~150 m sub-bottom depth (their locations are indicated with red boxes), The bottom image shows an enlarged section of the profile (green dotted box) to highlight the nature of the offset. Facies C and D are labelled and highlighted in both insets. The red arrow in the upper panel highlight intersections with other seismic profiles.

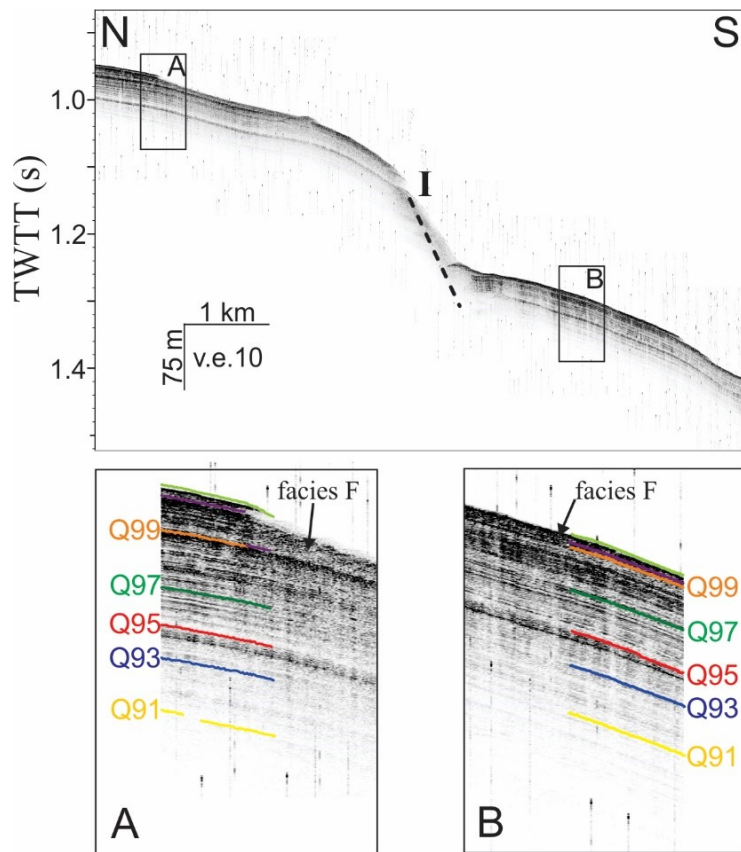


Fig. 3.7: Example of ultra-high resolution seismic data. Offset “I” is highlighted. Stratified reflections (Q91 to Q99) continue to both sides of offset “I”. Reflection interpretations are from Schulten et al. (2019). The profile location is shown in Fig. 3.6.

ii) Central St. Pierre Slope

In central St. Pierre Slope, three zones of reflection offsets associated with seafloor escarpments were mapped in 750, 1100 and 1300 mwd (Fig. 3.8). The first reflection offset

(offset “I”, Fig. 3.8) occurs underneath the 750 mwd escarpment. It is 65 to 100 ms high and is apparent down to 150 msbsf (R6) (Table 3.4, Fig. 3.8). About 50 ms of section is missing between horizons R6 and R7 downslope from offset “I” (Table 3.4, Figs. 3.5 & 3.8). The second, less distinct, reflection offset (offset “II”, Table 3.4) underneath the escarpment at 1100 mwd dips at an apparent angle of 10° (Fig. 3.8). This offset is up to 100 ms high at ~400 msbsf (R3), but only 20 ms high near the seafloor (Fig. 3.8).

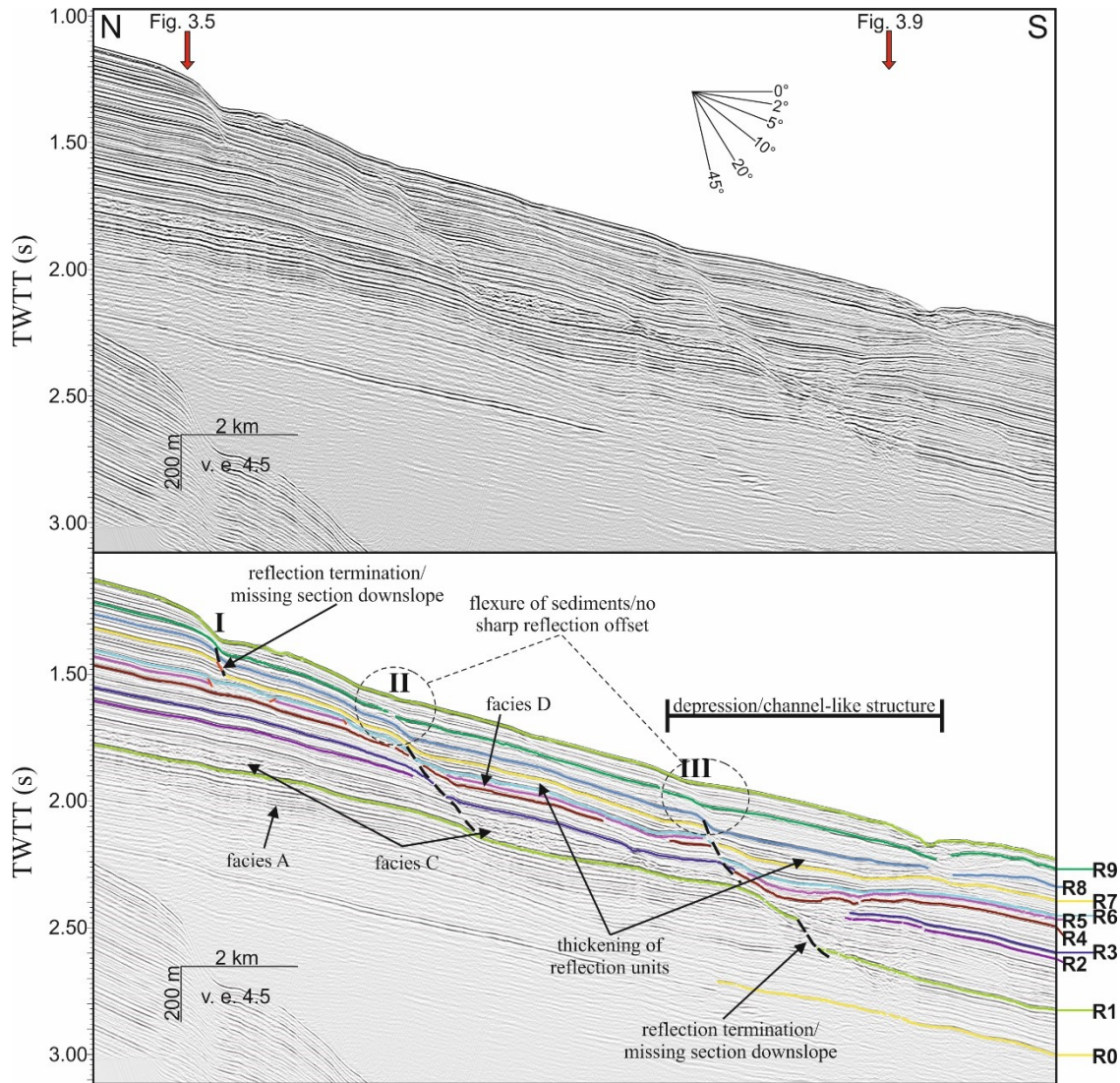


Fig. 3.8: A dip-oriented seismic reflection profile along the central part of the upper St. Pierre Slope (see Fig. 3.4 for location). The upper panel shows the profile without interpretation, the lower panel is with interpretation. The location of offsets “I”, “II” and “III” are indicated with black dashed lines. Red arrows in the upper panel highlight intersections with other seismic profiles.

Reflections from R7 to the seafloor appear deformed rather than showing a sharp offset (Table 3.4, Fig. 3.8). Horizon R2 is missing in the sub-bottom between offset “II” (1100 mwd) and the third reflection offset (offset “III”) at 1300 mwd, while a ~80 ms thick facies C deposit overlies horizon R1 (Fig. 3.8). Offset “III” is generally 90 ms high from ~550 msbsf (R1) to 100 msbsf (R8) and 20 ms high from 100 msbsf (R8) to the seafloor (Fig. 3.8). The plane of offset “III” dips at an apparent angle of 12° (Fig. 3.8). There is ~130 ms of missing section underneath horizon R1 downslope from offset “III” (Fig. 3.8). In addition, there are small reflection truncations apparent between horizons R2 and R6, with 10 to 20 ms of missing section or thinning of reflections upslope from offset “III” (Table 3.4). Reflection units thicken downslope from offset “II” and especially offset “III” (Fig. 3.8). A depression or channel-like structure is apparent in the sub-bottom (R4/5) downslope of offset “III” with R2 and R3 reflections locally missing (Fig. 3.8). A strike-profile in 1600 to 1700 mwd downslope of offset “III” displays an indistinct zone of reflection offsets that dips westward at an apparent angle of 10° (Table 3.4, Fig. 3.9).

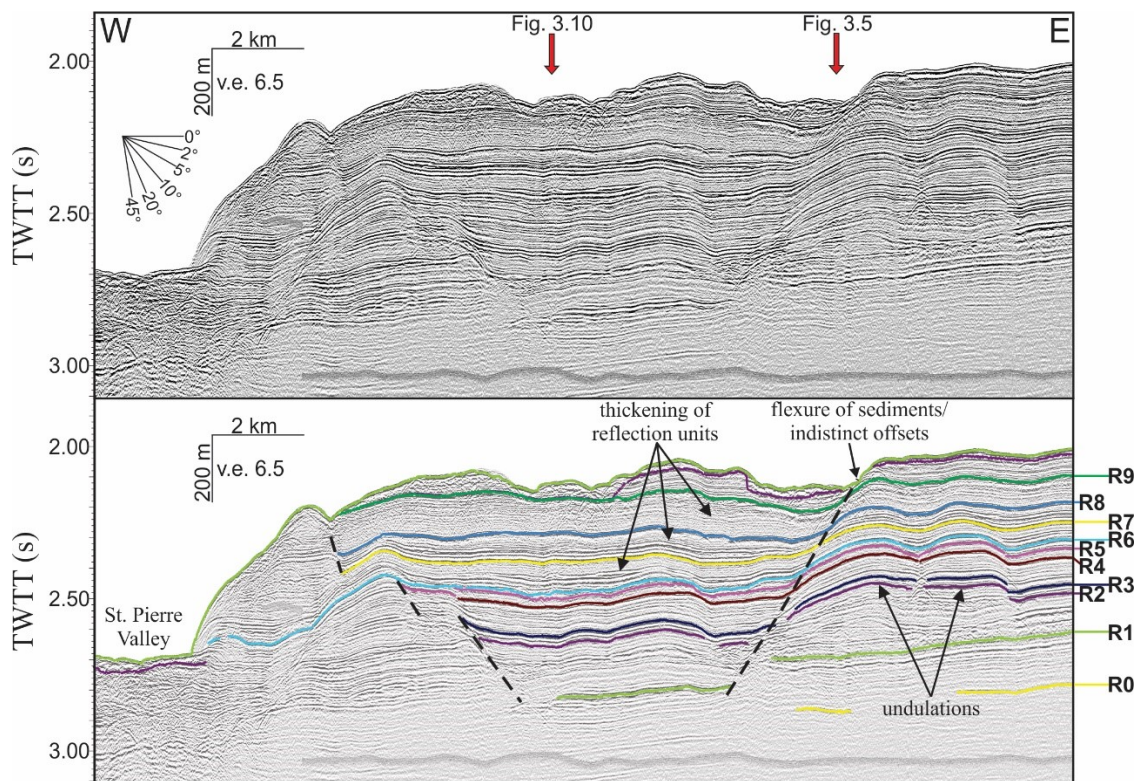


Fig. 3.9: Strike-oriented seismic reflection profile across the upper St. Pierre Slope (see Fig. 3.4 for location). The upper panel shows the seismic profile without interpretation, the lower panel is with interpreted horizons and labelled structural features. Note the indistinct, westward dipping plane of reflection offsets (black dashed line) and deep incision of St. Pierre Valley. Red arrows in the upper panel highlight intersections with other seismic profiles.

iii) Western St. Pierre Slope

Within the western upper St. Pierre Slope, offset “III” lies underneath a seafloor escarpment in 1300 mwd with the plane dipping at apparently 10° (Fig. 3.10). The vertical displacement decreases from 180 ms in 700 msbsf to ~ 85 ms at the seafloor. As in the central slope region (Fig. 3.8), reflection units thicken downslope from offset “III” (Fig. 3.10). This thickening is most apparent between horizons R3–R4 and R8–R9 (Fig. 3.10). A rhombic-shaped block (~ 250 m wide, ~ 300 ms high), with intact internal reflections, is apparent adjacent to the reflection offset between horizon R2 and R7 (Fig. 3.10) and is similar to that shown in Fig. 3.6. Below the escarpment, the seafloor shows a slightly lower gradient compared to the seafloor above the escarpment (from 2.5° above the escarpment to 1.8° below) (Fig. 3.10). Another 30 ms-high escarpment that is not associated with a reflection offset is present at ~ 1700 mwd (Fig. 3.10). The strike-profile in 1600 to 1700 mwd shows that St. Pierre Valley is incised down to horizon R6 (Fig. 3.9).

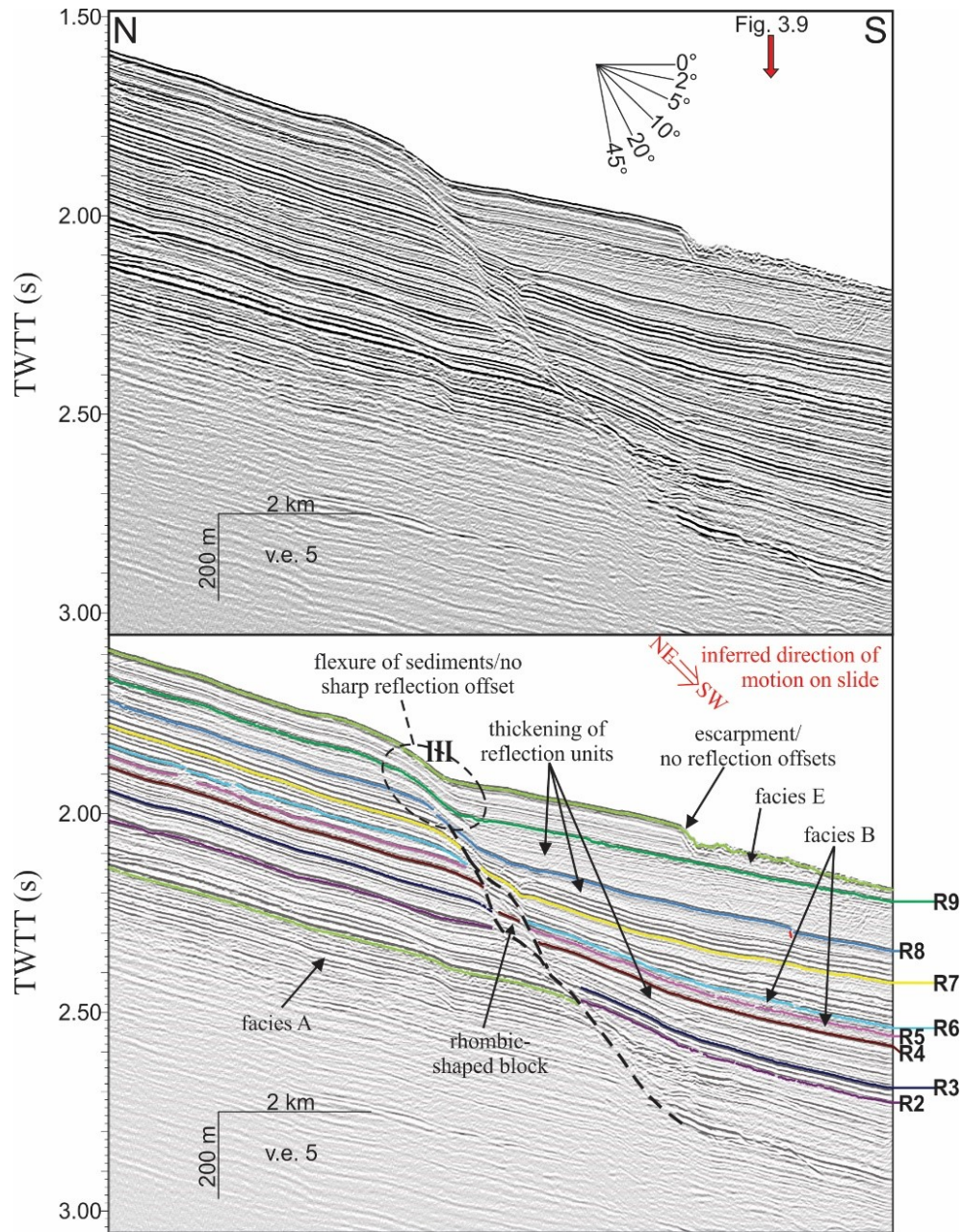


Fig. 3.10: Dip-oriented seismic reflection profile from the western upper St. Pierre Slope (see Fig. 3.4 for location). The upper panel is the profile without interpretation, the lower panel is interpreted with mapped horizons. Displacement “III”, indicated with a black dashed line, is evident beneath a low gradient seafloor escarpment. There is no displacement evident beneath a larger seafloor escarpment further downslope. A rhombic shaped body formed by offset “III” is imaged by the data and indicated in the lower panel. Reflection offsets above this rhombic shaped body are indistinct. The red arrow in the upper panel highlight intersections with other seismic profiles.

3.4.4.1.2 MIDDLE AND LOWER SLOPE (1700-4000 MWD)

Reflection offsets that typically show 50 to 60 ms of displacement are evident between the middle and lower slope. Some of these offsets (offset “IV”, Figs. 3.11 & 3.12) are adjacent to channel systems that dissect the lower slope (Fig. 3.4) down to horizon R5 (Fig. 3.11). In many cases, reflection offset “IV” is covered on the seafloor by ~45 ms-thick chaotic reflections of facies E (Table 3.2, Fig. 3.12). Other reflection offsets (offset “V”, Fig. 3.11) are associated with seafloor escarpments in >1700 mwd. Offsets of type “V” are often indistinct and do not appear to reach the seafloor (Table 3.4, Fig. 3.11). Reflection offsets “V” dip with an apparent angle of up to 20° down to horizon R0 that marks the top of wavy reflections (facies B, Table 3.2). Along the lower slope, seismic data show undulating to folded, low amplitude reflections that are mostly restricted to above horizon R4 (Fig. 3.12).

A seismic line (TGS 1258-100) that covers part of the upper, middle and lower slope indicates a concave nature of horizon R6, especially towards the lower slope (Fig. 3.13). It is further evident that Eastern Valley is incised down to horizon R5/6 at the southern end of the St. Pierre Slope (Fig. 3.13).

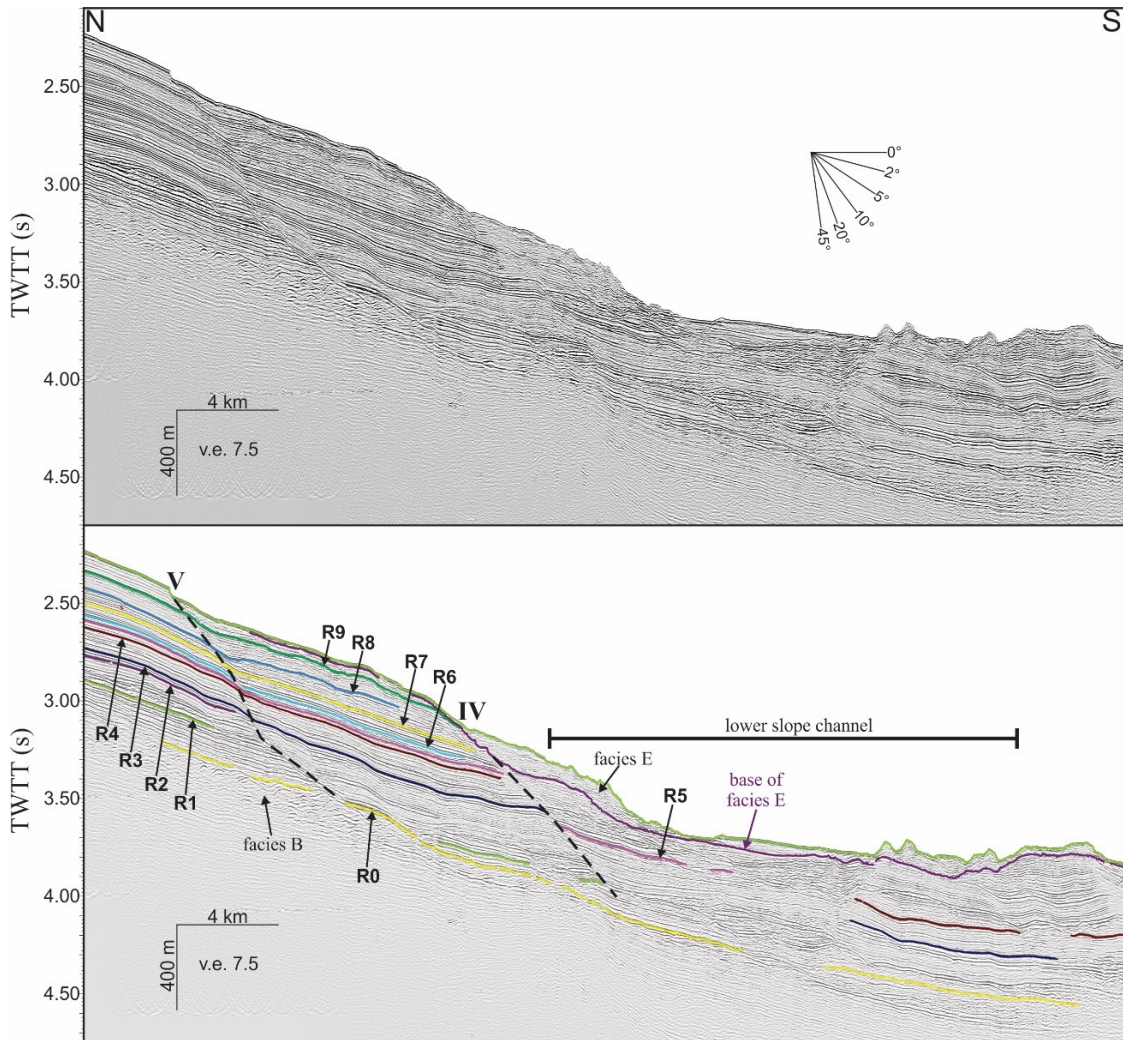


Fig. 3.11: A dip-oriented seismic reflection profile from the middle to lower slope. Its location is shown in Fig. 3.4. The upper panel is without interpretation, the lower panel is with interpretation of mapped horizons. Black dashed lines labelled “IV” and “V” indicate the location of reflection offsets. Indistinct reflection offsets (“V”) are evident underneath a 20-50 m-high escarpment. A more distinct offset (“IV”) is visible towards the lower slope channel, which shows erosion down to horizon R5.

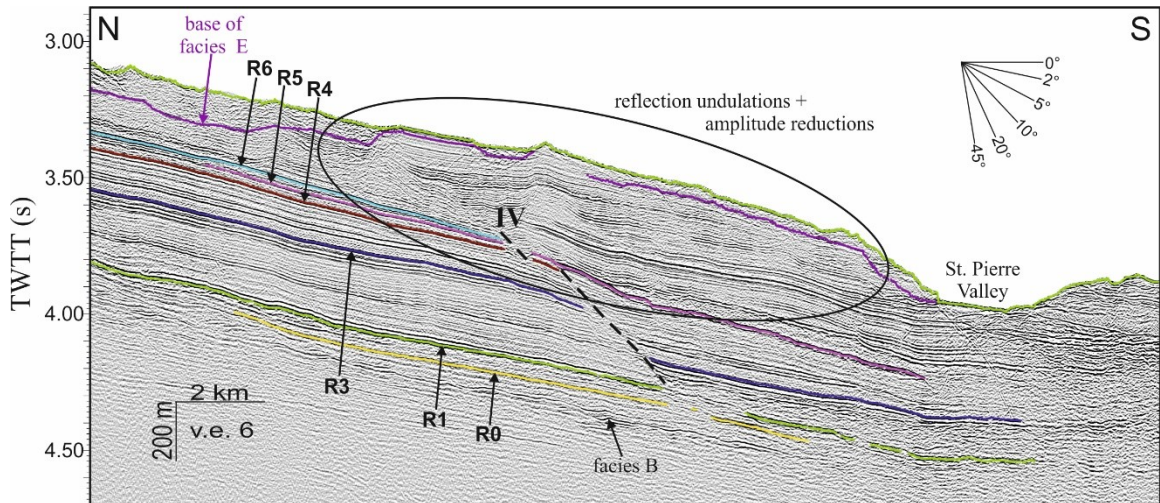


Fig. 3.12: Dip-oriented seismic reflection profile across the middle and lower St. Pierre Slope (location is shown in Fig. 3.4) with interpretation. The area encased by the oval shows undulating seismic reflections with amplitude reductions. The black dashed line connects reflection offsets (“IV”).

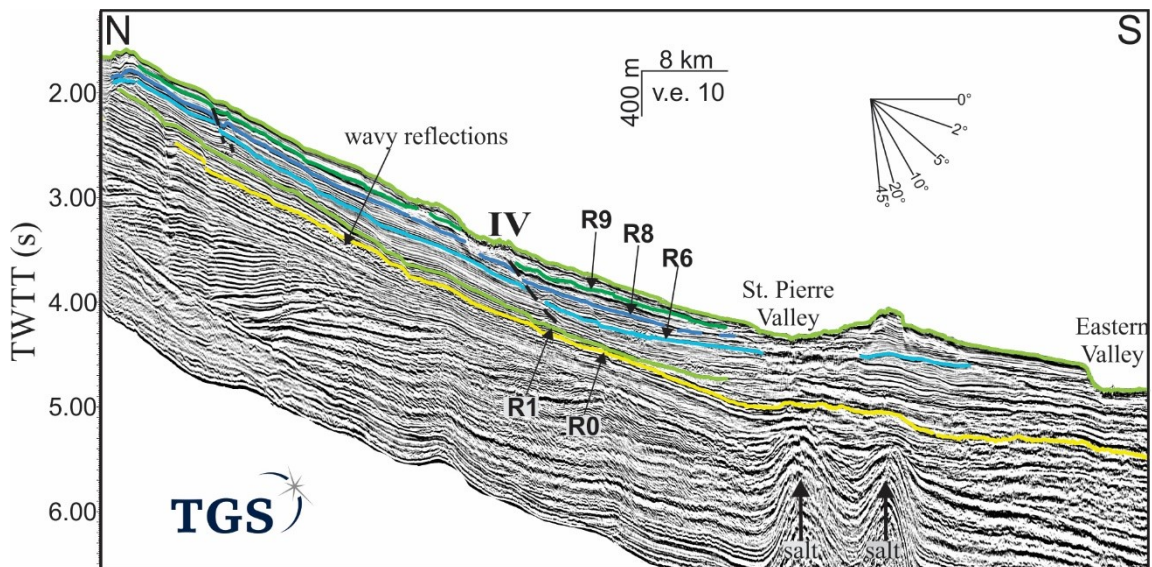


Fig. 3.13: Industry seismic profile across the eastern part of the upper, middle and lower St. Pierre Slope (see Fig. 3.4) indicating the concave nature of horizon R6. The black dashed line indicates the plane of offset “IV”. Data compliments of TGS-Nopec reproduced with permission.

3.4.4.2 SPATIAL DISTRIBUTION OF REFLECTION OFFSETS

Reflection offsets and their respective sub-bottom depths are summarized in Fig. 3.14. Different colors characterize the maximum stratigraphic depth in which offsets are evident. This planar view on the distribution of the reflection offsets indicates an overall continuous

transition to deeper offsets towards the west-southwest and southern part of the slope (Fig. 3.14). A concentration of distinct displacements occurs between 750 and 1500 mwd, while displacements towards the south are less distinct (Fig. 3.14). A similar trend is evident from east to west, where offsets become more distinct towards the western part of the St. Pierre Slope. An exception is the reflection offset along the eastern part of the uppermost escarpment (750 mwd).

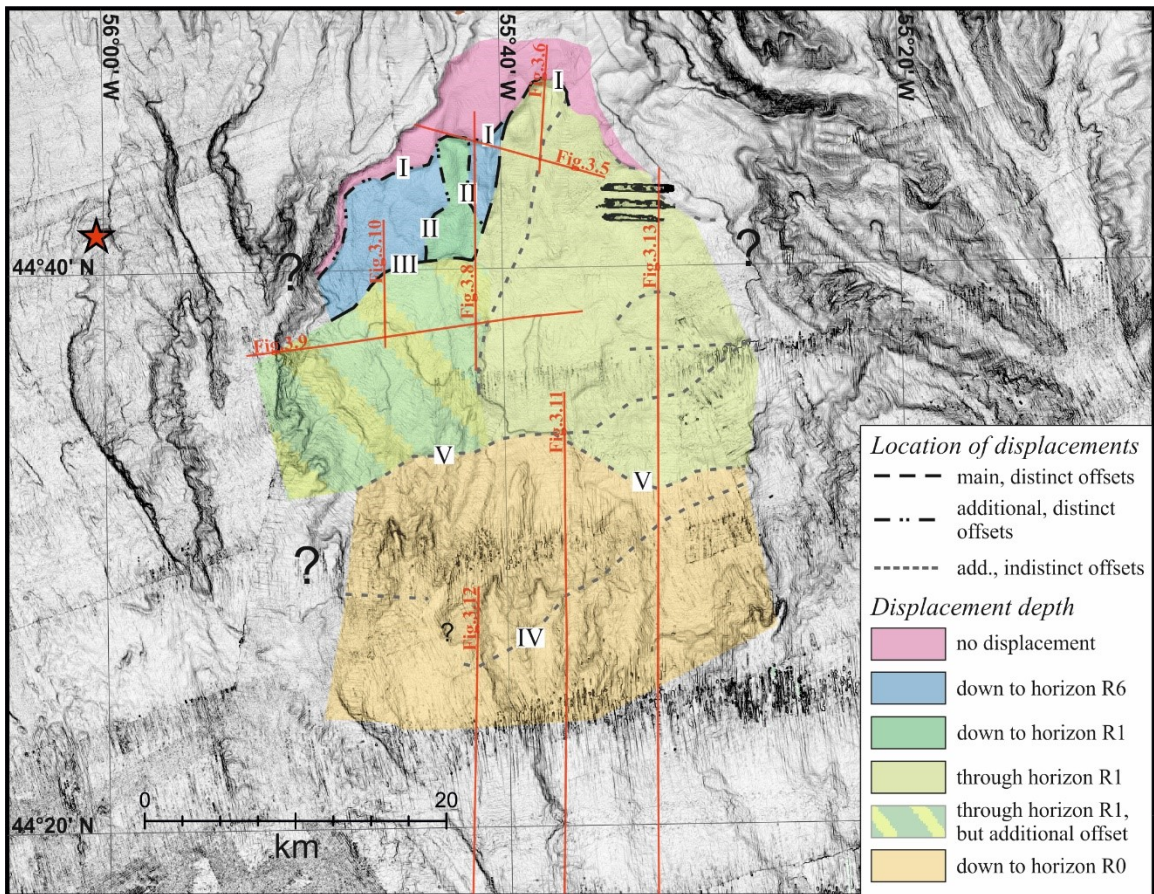


Fig. 3.14: Overview map of the St. Pierre Slope indicating the location of mapped reflection offsets and their sub-bottom depths. Dashed lines indicate reflection offsets with similar structure and depth. Question marks denote areas where seismic data did not provide sufficient information due to low seismic resolution. The red star indicates the epicenter of the 1929 earthquake. Labels “I” to “V” show the seafloor outcrop location of mapped reflection offsets. Offsets “IV” are often covered by thick, chaotic deposits.

3.5 DISCUSSION

3.5.1 Stratigraphic evolution

The ten stratigraphic reflection horizons that are evident down to 700 msbsf (600 m sub-bottom depth (mbsf)) are probably of Quaternary age (Piper et al., 2005; Skene & Piper, 2006). Three different sedimentation rates were determined based on different age models for the St. Pierre Slope stratigraphy (Table 3.1 & 3.5). Option 1 uses ages provided in Piper et al. (2005), while option 2 considers interpretations of Skene and Piper (2006) who argued that horizon 'A' or R1 may be much younger than identified in previous studies. Option 3 uses the results of this study where up- and downslope mapping of reflections indicate that horizon 'A_{S+P}' of Skene and Piper (2006) matches horizon R3 rather than horizon 'A_{P+N}' of Piper and Normark (1982; 1989). Option 1 shows an increase in sedimentation rate above horizon R6 from 20 cm ka⁻¹ to 40 cm ka⁻¹ and to >2 m ka⁻¹ above R9 before it decreases to ~10 cm ka⁻¹ after deposition of Q99 (Table 3.5). Option 2 corresponds to sedimentation rates of up to 1 m ka⁻¹ between horizon R1 and R6 (Table 3.5). Option 3 shows similar sedimentation rates to option 1, but the sedimentation rate increases above horizon R3 (Table 3.5).

Option 3 is preferred over options 1 and 2 as an increase in sedimentation rate somewhat before deposition of horizon R6 is very likely given the presence of glacial ice margin wedges down to horizon R3 (Table 3.5) (*e.g.*, Piper et al., 2005; Skene & Piper, 2006; Schulten et al., 2019). Cohen and Gibbard (2016) described MIS 22 (option 3, R3) as a profound cooling event within a sub-series of discrete events that predate MIS 12 (R6). Shelf-crossing glaciers during MIS 12 (R6), with rapid proglacial sediment discharge, are believed to have resulted in high sedimentation rates during this period (Piper et al., 1994; Giosan et al., 2002; Piper et al., 2005).

Table 3.5: Comparison of seismic stratigraphies mapped across St. Pierre Slope. Sedimentation rates are calculated using sediment thickness distribution of apparent un-failed areas.

| Reflectors | | | | | | | Option 1 (after Piper et al. 2005) | Option 2 (after Skene & Piper, 2006) | Option 3 (This study) | | | |
|------------|-----------------------|-----------------------|-----------------------|--------------------|---------------------|--------------|---------------------------------------|---|--------------------------|----------------------------------|-----------|----------------------------------|
| This study | Uchupi & Austin, 1979 | Piper & Normark, 1982 | Piper & Normark, 1989 | Piper et al., 2005 | Skene & Piper, 2006 | McCall, 2006 | age (ka) | sed. rates (m ka ⁻¹) | age (ka) | sed. rates (m ka ⁻¹) | age (ka) | sed. rates (m ka ⁻¹) |
| sf | | | | | | | present | 0.12 | present | 0.12 | present | 0.12 |
| Q99 | _____ | | | | | Q99 | 17 | | 17 | | 17 | |
| Q91 | _____ | | | | | Q91 | 33 | 2.6 | 33 | 2.6 | 33 | 2.6 |
| R9 | _____ | | A | Q90 | O | | 33 | 0.3-0.4 | 33 | 0.3-0.4 | 33 | 0.3-0.4 |
| R8 | _____ | Q | B | Q70 | Q | | 150 | | 150 | | 150 | |
| R6 | _____ | | | Q50 | B | | 470 | 0.42 | 470 | 0.42 | 470 | 0.42 |
| R3 | _____ | | | Q30 | | | 1100 | 0.23 | | | 880 | 0.35 |
| R1 | _____ | A _{P+N} | C | Q10 | | | | 0.28-0.5 | | 0.78-1.04 | | 0.21-0.32 |
| | | | A _{P+N} | | | | 1500-1800 | | 800-910 | | 1500-1800 | |
| | | | D | | | | | 0.15-0.2 | | 0.09-0.1 | | 0.15-0.2 |
| R0 | L | L | L | P50 | L | | 2600 | | 2600 | | 2600 | |
| | | | E | | | | | | | | | |

A_{S+P} (adjusted, option 3)

A_{S+P} (option 2)



A change in the abundance of facies C and D is evident after deposition of horizon R6 (MIS 12). Facies C is abundant below horizon R6, while facies D is abundant above horizon R6 (Table 3.2, Figs. 3.6 & 3.8). Based on their echo-characteristic, both facies C and D are interpreted as gravity-driven mass transport deposits (MTD's) (*e.g.*, Sangree & Widmier, 1979; Piper et al., 2005, Giles et al., 2010). It is likely that the thicker, chaotic reflections of facies C are part of a thick slump or debrite, while facies D might represent debrites or turbidites (Sangree & Widmier, 1979; Giles et al., 2010). A change in the thickness of these MTD's, especially after deposition of horizon R6, further indicates a decrease in the volume of the failed sediment involved in single events. This decrease might be associated with higher frequency of sediment failures, related to shelf-crossing glaciers and increased sediment discharge at the continental slope (*cf.*, Giles et al., 2010; Urgeles & Camerlenghi, 2013; Urlaub et al., 2013). The coherent, parallel reflections of facies A in which facies C and D deposits are interbedded is interpreted to represent stratified sediments (*cf.*, Sangree & Widmier, 1979) that are likely glaciomarine in origin.

The chronostratigraphy above horizon R9 is established based on radiocarbon dates from sediment core sampling (Table 3.5, Fig. 3.7) (Piper et al., 2005; McCall, 2006). This sequence shows facies F and G in sub-bottom reflection profiles; both interpreted as mass-flow deposits (Table 3.2) (*e.g.*, Piper et al., 1999; McCall, 2006; Giles et al., 2010). Facies F is evident along most of the near-surface of the upper St. Pierre Slope area and is interpreted as representing a debrite (Schulten et al., 2019). Facies G is recognized as slump blocks and semi-coherent slides based on its location in proximity to the escarpments and echo-characteristic (*cf.*, Damuth, 1975; Damuth & Olson, 2015; Schulten et al., 2019). Gravity cores of facies F contain poorly sorted and structureless sediment (Krastel et al., 2016). Sedimentation rates, based on core studies and ties to these stratigraphic intervals, are estimated to be $\sim 2.6 \text{ m ka}^{-1}$ (Table 3.5). These rates are reasonable for the last glacial maximum (LGM) on the western Atlantic continental margin (*cf.*, Skene & Piper, 2003).

3.5.2 Evidence of slumping

The low angle ($\sim 17^\circ$) reflection offsets that are evident down to 600 msbsf (~ 550 mbsf) along the upper and middle St. Pierre Slope are interpreted as faults (Figs. 3.5-3.11) and

resemble faults described elsewhere by Mosher et al. (2004), Deptuck et al. (2007) and Katz et al. (2015). Escarpments that are present especially in sub-seafloor depths >300 m are associated with these faults (Figs. 3.5 & 3.6). Evidence supporting interpretation of these reflection offsets as faults are: 1) a distinct break of reflections (Table 3.4, Figs. 3.6 & 3.8) (*e.g.*, as illustrated elsewhere by Mansfield & Cartwright, 1996; Childs et al., 1996); 2) offsets form a coherent line through the section (Fig. 3.10); 3) reflection packages correlate across the offsets (Figs. 3.6 & 3.8); 4) a constant thickness in MTD's on either side of the reflection offsets (Fig. 3.6); and 5) rhombic shaped blocks adjacent to reflection offsets that show strong similarities to fault-bounded lenses (Table 3.4, Figs. 3.6 & 3.10) (Childs et al., 1996; van der Zee & Urai; 2005, van der Zee et al., 2008) or horses in duplex zones (Gibbs, 1984; Walsh et al., 1999). The faults sole out at various horizons between 300 and 600 mbsf, indicating they are not related to deeper tectonic elements (Figs. 3.6 & 3.8). The faults, therefore, are interpreted to be part of a complex slump that is henceforth referred to as the "St. Pierre Slump". They enclose a 15 to 30 km-wide and 50 to 60 km-long area of the upper and middle slope that is interpreted as the upslope extensional zone of this slump (Fig. 3.14) (*cf.*, Lewis, 1971; Martinsen & Bakken, 1990; Frey-Martinez et al., 2006). The different zones of the slump, *i.e.*, the extensional and compressional zones, are described in the following sections.

3.5.2.1 EXTENSIONAL ZONE

3.5.2.1.1 INITIATION AREA

Slumping that resulted in the faults likely initiated along the eastern part of the uppermost escarpment (offset "I", 750 mwd) (Fig. 3.6) but was diverted to the third escarpment (offset "III", 1300 mwd) along the central and western part of the upper slope (Figs. 3.8 & 3.10). Evidence for this transition are the structural similarities and the depth in which the reflection offset occurs. In this case, down through horizon R1 (Figs. 3.6 & 3.8). This zone is interpreted as the main slump system (Fig. 3.14). Displacements along this system, based on reflection offset measurements, are ~110 m with the largest displacements along the easternmost and westernmost regions of the upper slope area (Figs. 3.6 & 3.10). The faults are generally low angle with dips between 10 to 17°. Some faults in the eastern part of St. Pierre Slope show listric characteristics, but this could be a result of the intersection of the

survey with the complex trend of the fault plane (Fig. 3.6). They are planar-normal in the central and western part regions° (Figs. 3.8 & 3.10). A change in the landward tilt of the hanging wall block suggests that a rotational component was involved in slumping (Fig. 3.10) (*cf.*, Martinsen & Bakken, 1990). A thickening of sediments packages in the hanging wall (Fig. 3.8 & 3.10) also indicates horizontal and vertical rotation or could be the result of a growth fault (*c.f.*, Williams et al., 1989; Hooper, 1990). Insufficient data coverage, however, does not allow to reconcile this observation more precisely.

Reflections of offset “I” terminate at ~300 mbsf in the western part of the uppermost escarpment (750 mwd) of the slope. A missing sediment section is evident downslope of offset “I” (Table 3.4, Fig. 3.8). This missing section could be interpreted as a result of previous sediment failures (*cf.*, Bryn et al., 2003; Gee et al., 2005; Georgiopoulou et al., 2007); however, lateral rotation of the slump block could account for poor correlation, creating an apparent missing section as well (*cf.*, Gibbs, 1984). Reflections across offset “II” (1100 mwd) and offset “III” (1300 mwd) in the western part of the upper slope are slightly folded (Figs. 3.8 & 3.10). This folding is interpreted as bedding flexure due to frictional drag during the slumping process. This type of flexure is common in extensional duplex systems (Gibbs, 1984).

Most of the seafloor escarpments of the St. Pierre Slope are associated with these faults (Figs. 3.4-3.8). The exceptions are 20 to 50 m-high escarpments in the western part of the slope between 1500 and 2000 mwd (Fig. 10). Ultra-high resolution seismic data show an association of these escarpments with slump deposits of facies F and G (Table 3.2) (Schulten et al., 2019), indicating that these headscarps resulted from shallow sediment mass-failure.

3.5.2.1.2 DÉCOLLEMENTS

The faults of St. Pierre Slump sole out at different depths close to horizon R6 and R1 along the upper slope and deeper down to R0 along the middle and lower slope (Figs. 3.6, 3.8, 3.11), indicating the presence of multiple décollements (Fig. 3.14), *e.g.*, similar to descriptions elsewhere by Martinsen and Bakken (1990), Mosher et al. (2004), and Frey-

Martínez et al. (2006). This stepwise transition to deeper décollements may be related with buried MTD's (Piper et al., 2005). Thick MTD's (facies C) are evident underneath horizon R6 as well as above horizon R1 and Piper et al. (2005) described facies B underneath horizon R0 as likely muddy sediment waves associated with overbank turbidite systems. In addition, horizon R6 denotes a change in the sedimentation rate as a result of shelf crossing glaciers (Piper et al., 1994). The deep incision of St. Pierre Valley and the lower slope channel systems down to horizon R6 further allows for the sediment package above horizon R6 (upper ~300 ms) to freely move towards these erosional systems (Figs. 3.4, 3.9, 3.11 & 3.14).

3.5.2.1.3 SLUMPING DIRECTION

The St. Pierre Slump identified with the planar and normal faults in the upper and mid- St. Pierre Slope region probably resulted from gravitational instability with displacement towards St. Pierre Valley and Eastern Valley in the west-southwest, and the lower slope to the south (Fig. 3.14). Evidence of this directionality includes the tilt of fault blocks and distribution of décollements in proximity to horizon R0, R1 and R6 (Figs. 3.6, 3.8, 3.11, 3.14). Free evacuation of the sediment material above horizon R6, especially towards the deeply incised valley systems in the west-southwest, is interpreted to have caused a separation of the St. Pierre Slump into lower and upper slump components.

The lower component of the St. Pierre Slump consists of a ~300 m-thick sediment package from 600 msbsf (R0) to 300 msbsf (R6). This component involves a slump area of ~1300 km², measuring a width of 15 km upslope and 30 km further downslope and a length of up to 60 km. The volume of this component is ~390 km³. The orientation of the deeper faults, especially offsets “IV” and “V”, suggests a south to southwestward slumping direction (Fig. 3.14). The upper component of the slump is smaller, affecting the sediment package from horizon R6 at ~300 msbsf or 250 mbsf to the seafloor with a width of 5 to 25 km and a length of 33 km. The total area of this slump component is approximately 700 km² with a volume of about 175 km³. The slump direction of this upper component is interpreted as mainly towards the west-southwest. Fault angles of the central and western part of the

upper slope are 17° (Figs. 3.8 & 3.10), which is similar to the dip of fault planes in the eastern part of the St. Pierre Slope (Fig. 3.6).

3.5.2.2 COMPRESSIONAL ZONE

Minor compressional structures in the form of undulations and localized amplitude reductions are present in the sediment units above horizon R4 of the middle and lower slope (Figs. 3.11 & 3.12) (*cf.*, Martinsen & Bakken, 1990). Further evidence of a compressional zone is lacking. The absence of major deformation structures above horizon R4 might be explained by the possibility that some of the sediment material freely evacuated into the deeply incised valley and channel systems, especially St. Pierre Valley (Fig. 3.9). Sediment material along horizon R6 further shows an upward bend resembling a spoon-like shape along the lower slope (Fig. 3.13). This change in the tilt might have resulted from rotation of the sediment mass.

The average vertical displacement of the St. Pierre Slump is 100 m, which translates to a horizontal displacement of ~330 m given a fault plane with a dipping angle of 17° . This horizontal displacement was likely accommodated over the ~60 km length of the slump, thus one would not necessarily expect to see a large compression zone in the toe region of the slump. In addition, seismic imaging of evidence of a possible compressional zone is restricted as data coverage is sparse along the lower slope and data quality imaging to depth is restricted as a consequence of abundant thick MTD's and coarse channel fill (Figs. 3.11 & 3.12).

3.5.3 Fault movement

The faults defining the St. Pierre Slump are interpreted as undergoing periodic reactivation. Evidence for this is the thickening of sediment packages in the hanging wall and the occurrence of shallow (10-15 m thick) missing sections in the foot wall of the third fault (offset "III", 1300 mwd) as these are common features in growth faults (Figs. 3.8 & 3.10) (Hooper 1991; Mansfield & Cartwright, 1996). Missing sedimentary sections within the stratigraphy are interpreted to be a consequence of previous mass-failure events, as indicated by shallow buried head scarps. These observations point to previous phases of

displacement along these faults. The degree of displacement generally increases with depth assuming that displacement is equal to the height of the reflection offsets (Fig. 3.15) (Mansfield & Cartwright, 1996). The displacements were corrected for the height of missing sections that are assumed to have been caused by either sediment failure or a rotation of a block of sediment. Three different scenarios for potential fault-displacement at the St. Pierre Slope are shown in Fig. 3.16. “Possibility I” (Fig. 3.16) is interpreted as the most likely scenario as explained below.

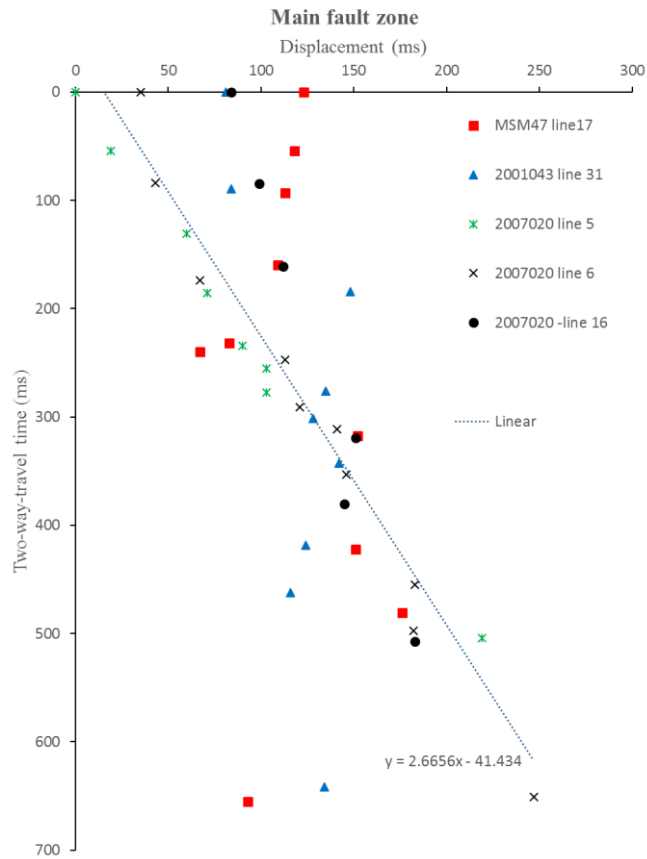
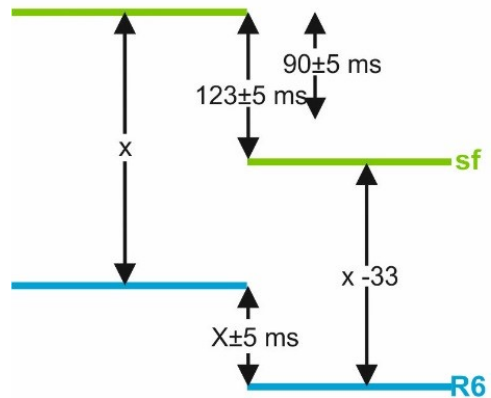


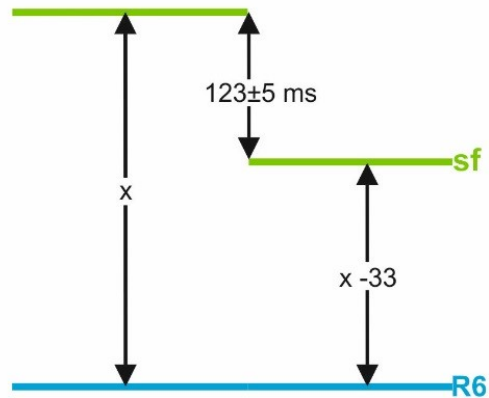
Fig. 3.15: Depth versus displacement of fault planes of the main slump system. The amount of displacement generally increases with depth.

Possibility 1: Displacement before deposition of horizon R6



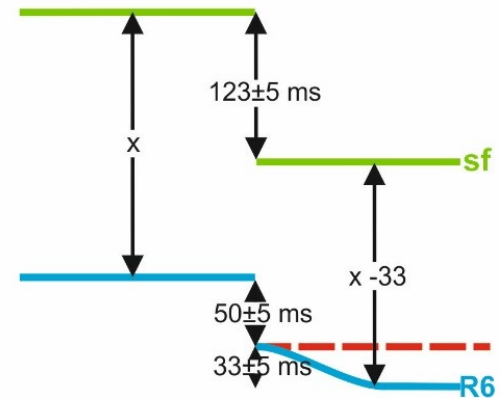
The displacement at the seafloor (sf) is 123 ± 5 ms, or 90 ± 5 ms with a correction for the missing section above horizon R6 (33 ms). If the sediment package below horizon R6 (blue) was already displaced by $X \pm 5$ ms at the time faulting affected the overlying sediment package, then the total displacement since horizon R6 is $(90 - X) \pm 5$ ms.

Possibility 2: No displacement at horizon R6 prior to faulting of the overlying sediment package.



The seafloor displacement is 123 ± 5 ms. Corrected for the missing section (33 ms) the remaining net displacement is 90 ± 5 ms. The total displacement since horizon R6 therefore is 90 ± 10 ms.

Possibility 3: The upper point of the flexure of horizon R6 reflects the true displacement and displacement occurred before deposition of R6



This scenario assumes that the flexure is not a result of movement of the fault-bounded lens. Height of the flexure is ~ 33 ms. The displacement at horizon R6 of 83 ± 5 ms corrected is 50 ± 5 ms. Seafloor displacement corrected is 90 ± 5 ms. The total displacement since horizon R6 therefore is 40 ± 10 ms.

Fig. 3.16: Three scenarios that account for displacement observed along a fault system. Examples show fault developments from horizon R6 to the seafloor.

Displacement along faults of the St. Pierre Slump probably first occurred around deposition of R2, as indicated by the shallowly buried head scarps evident in seismic unit 2b (Table 3.3 & 3.4). Given that those head scarps are in the range of 10 to 15 m high, it is likely that movement was minor during this early phase of faulting. The vertical extent of the fault-bounded lenses between horizon R2 and R6 and difference in fault displacement below and above horizon R6 suggest reactivation of faulting sometime after deposition of horizon R6 (Figs. 3.6 & 3.10). St. Pierre Valley is assumed to have formed around the time horizon R6 was deposited as it marks the onset of intense shelf crossing glaciations and a drop in the global sea-level height (Piper et al. 2005; 2007). At the St. Pierre Slope, the incision of St. Pierre Valley and Eastern Valley and the channel systems of the lower slope region undercut the upper and middle slope and potentially allowed free down-slope movement of the sediment package above horizon R6 (Figs. 3.9 & 3.11).

There is no evidence for fault-reactivation between horizons R6 and R9. The erosional truncation underneath horizon R9 shows identical morphological features to both sides of the fault with their seismic reflections aligning, if corrected for the offset (Fig. 3.6). The foot- and hanging-wall block of the fault, therefore, is assumed to have been at the same approximate level during the erosional event. This observation suggests that fault displacements prior to 30 ka BP (R9) as a consequence of earlier phases of faulting was minor, as argued above.

The faults are assumed to have been active only recently with major displacement leading to formation of the fault-bounded lenses that are evident between horizon R2 and R6 (Figs. 3.6 & 3.10). Many faults ruptured the modern seafloor that resulted in seafloor escarpments (Figs. 3.4, 3.7 & 3.14). The heights of these escarpments nearly match the total vertical displacement of the faults (Figs. 3.6, 3.7, 3.11). Ultra-high resolution seismic data further indicate a constant reflection offset from the seafloor down to R9 in 120 msbsf (Fig. 3.7), which suggests that displacement occurred in one single event.

3.5.4 Implications of the role of observed specific structures in the 1929 event

The 1929 submarine landslide was described in previous studies as a widespread, retrogressive slope failure with evidence of ~20 m-thick sediment failures along the St. Pierre Slope, the head of Eastern Valley, Western Valley and Grand Banks Valley (Piper et al., 1988, 1999; Mosher & Piper, 2007). On St. Pierre Slope, surficial failures are observed in water depths of 750 to 2300 m (Mosher & Piper, 2007; Schulten et al., 2019). Schulten et al. (2019) showed that only 7 to 11 m-thick sediment failures occurred along the escarpments in 750 to 1300 mwd. Most of the failures at the St. Pierre Slope are interpreted as shallow (~20 m), translational and probably retrogressive landslides restricted to water-depths of 1700 to 2300 m (Piper et al., 1999; Schulten et al., 2019). These failures rapidly transformed into channelized turbidity currents (Piper et al., 1999). These observations are incongruous with the volume, style and water depth of sediment failure that one would expect are required in order to generate a tsunami (e.g., Bryn et al., 2005; Harbitz et al., 2014; Krastel et al., 2019).

Observations of low-angle (~17°) planar-normal faults are interpreted here as part of a massive complex slump that involved up to 100 m of vertical displacement (Figs. 3.6, 3.10, 3.17). It is interpreted that displacement of this slump was a direct consequence of the 1929 earthquake because: 1) the faults breach the seafloor (Fig. 3.3, 3.6, 3.7), 2) shallow offsets have the same height as the seafloor escarpments, and 3) shallow sediment cores show mass-failure material on the seafloor downslope of the escarpments that has not been buried (e.g. Piper et al., 1999). The faults sole out at décollements (R0, R1 and R6) that show association with MTDs and sediment waves (Figs. 3.6 & 3.11). It is, therefore, possible that cyclic loading due to the 1929 earthquake (M_w 7.2) caused excess pore pressure and reduction of effective stress along these susceptible layers that acted or reactivated as décollements (R0, R1 and R6) (Figs. 3.8, 3.11 & 3.17). The result was slumping of a thick (~500 m) succession of sediment (Fig. 3.17) that moved ~100 m vertically and 330 m horizontally. The instantaneous seafloor displacement in 750 mwd due to this slumping was presumably a more effective source for tsunami generation than widespread, retrogressive surficial sediment failure in greater water depths as interpreted earlier (Piper

et al. 1988, 1999). It is possible that movement of the main slump block triggered these surficial failures rather than ground accelerations directly caused by the earthquake. The displacement throughout the area of the slump resulted in a possible seafloor volume displacement of 70 to 130 km³ in 750 to 4000 mwd.

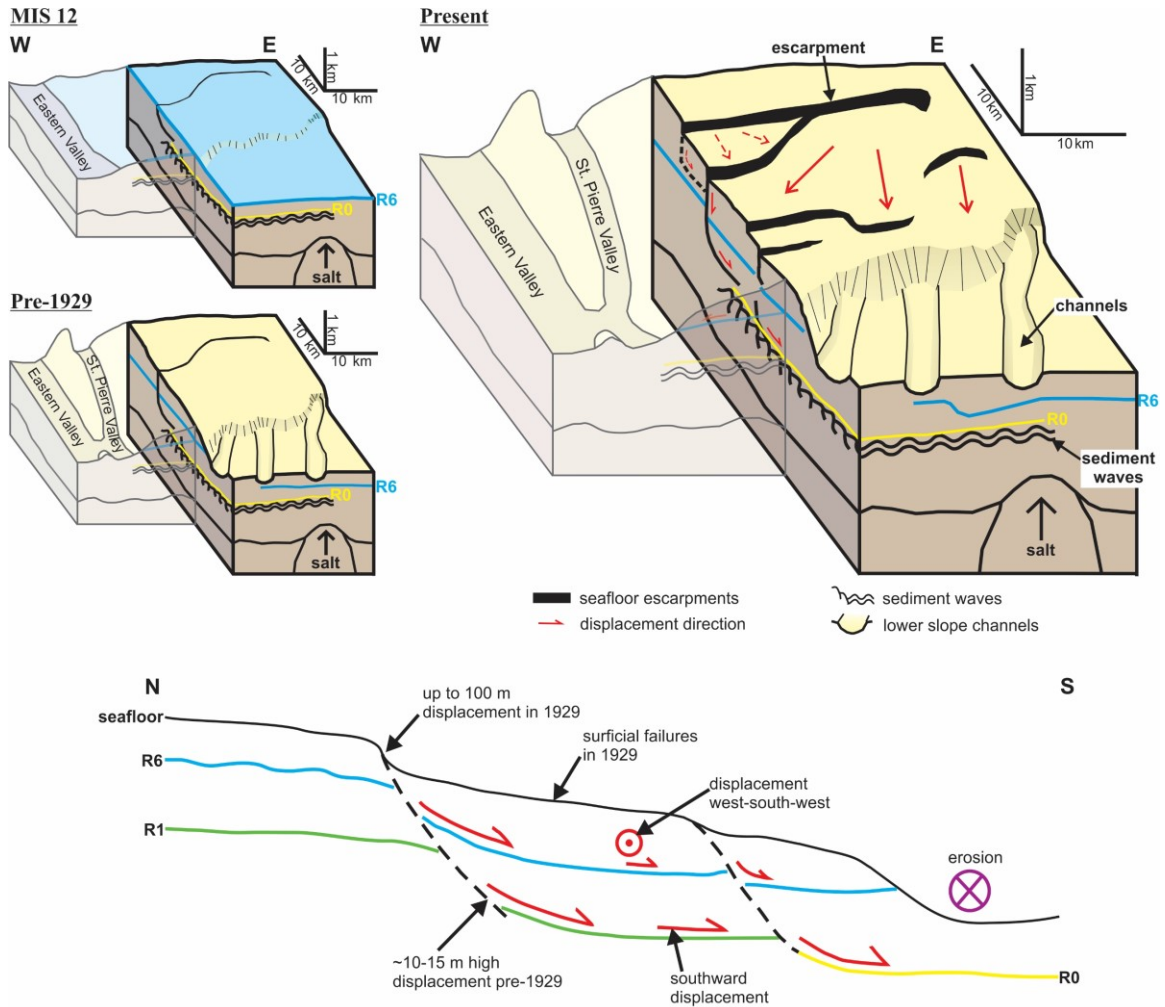


Fig. 3.17: Top: Block diagram of the St. Pierre Slope that shows development of the fault systems and related slump. The blue surface indicates displacements observed along horizon R6. Red arrows indicate the direction of sediment displacement. Bottom: Schematic N-S dipping profile illustrating the identified décollements (R6, R1, R0) and main slump direction (red arrows) along these décollements.

A recent tsunami simulation by Løvholt et al. (2019) supports this hypothesis. They simulated a tsunami that matches the observations from the 1929 event, concluding that the 1929 landslide likely was a combination of a major slump on the St. Pierre Slope, as

proposed in this study (Fig. 3.17), and more distributive surficial sediment failures that occurred in shallower water near the shelf edge of St. Pierre Slope and along the Laurentian Channel, as proposed by Piper et al. (1988). Their tsunami simulation, however, uses preliminary results of Schulten et al. (2019). Results in this study, therefore, provide important details on the dimension, volume and directionality of the slump that is needed to refine the existing tsunami simulation. This study showed that St. Pierre Slump moved more translational, rather than having a rotational component, which was used in the tsunami simulation of Løvholt et al. (2019). It is important that a new simulation includes an unconfined component to the slump at its downslope extremity (Figs. 3.9 & 3.14).

3.5.5 Comparison to other continental slopes failures

The St. Pierre Slump is unique in its complexity compared to other large-scale slumps reported in the literature (e.g., Garfunkel, 1984; Martinsen & Bakken, 1990; Frey-Martínez et al., 2006; Gafeira et al., 2007), particularly for a passive continental margin. The 1998 Papua New Guinea submarine landslide is the only other known case where an earthquake-triggered landslide rather than seismogenic fault offset was the principal cause of a tsunami (Synolakis et al., 2002; Tappin et al., 2003, 2008). The Papua New Guinea tsunami destroyed coastal villages and resulted in 2800 deaths, which demonstrates the need to assess the probability of such events (Tappin et al., 2003, 2008). In this case, however, it occurred proximal to a subduction margin, not on a passive margin as is the case for the 1929 event.

A key element involved in the development of the St. Pierre Slope Slump are: 1) high rates of sediment supply creating a thick sediment mass that lies on a slope (Table 3.5); 2) deep (~250 m) channels surrounding the main sediment mass, that allowed free evacuation of sediment (Figs. 3.9, 3.11 & 3.17); 3) geotechnically susceptible sediment horizons that acted as décollements; and 4) a relatively strong earthquake. Several of these factors are common along passive continental margins. The northeastern U.S. continental slope (Chaytor et al., 2007; Twichell et al., 2009), the Scotian Slope (Mosher et al., 2004), the Labrador Slope (Deptuck et al., 2007) and the continental slope of Norway (Bryn et al., 2003), for example, are geomorphologically and stratigraphically similar to the St. Pierre

Slope. This similarity includes periods of contourite deposition (sediment waves that have the potential to become décollement surfaces) the presence of planar-normal faults and a history of submarine landsliding (Mosher et al., 2004; Deptuck & Campbell 2012; Deptuck et al. 2007; Gafeira et al. 2007). A conventional morphological investigation of the St. Pierre Slope would probably not have considered this slope as source region for a tsunamigenic landslide, without knowledge of the historic event. It is, therefore, possible that the geohazard potential of continental slopes similar to the St. Pierre Slope might be higher than anticipated. It further implies the need for reassessment of the landslide and tsunami generation potential for these slope regions.

3.6 CONCLUSIONS

Mapping of stratigraphic and structural features beneath the St. Pierre Slope provides important information about sediment failure mechanism involved in the 1929 Grand Banks submarine landslide. The key findings in this study are as follow:

1. There is evidence for oblique low-angle ($\sim 17^\circ$) faults down to ~ 550 mbsf. The metrics on the faults suggest an average of 100 m vertical displacement and 330 m of horizontal displacement.
2. The faults are part of a massive (560 km^3) complex slump system. This slump is shown to have initiated along the eastern part of an escarpment that lies in 750 mwd. Movement of the main slump was diverted to a deeper escarpment in 1300 mwd towards the western part of the upper slope (Fig. 3.17).
3. There are indications of two-components of slumping with décollements at ~ 550 mbsf (R1 and R0) and ~ 250 mbsf (R6) (Fig. 3.17).
4. The sediment package down to 250 mbsf indicates evacuation toward the adjacent, deeply incised St. Pierre Valley and Eastern Valley in the west-southwest and southward towards the lower slope channel systems (Fig. 3.17). Slumping of the deeper component from ~ 250 to ~ 550 mbsf is inferred to have propagated towards the SSW (Fig. 3.17).
5. Major displacement (~ 100 m vertical, ~ 330 m horizontal) involving both components of the slump down to ~ 550 mbsf is interpreted as a direct consequence

of the 1929 M_w 7.2 earthquake. If the entire slump sustained 100 m of vertical displacement, then the seafloor volume displacement that is critical for tsunamis generation is on the order of 70 to 130 km³.

6. Surficial failures of the upper ~20 m of sediment are evident at the St. Pierre Slope from 750 to 2300 mwd, with the majority occurring in ~1700 mwd (Piper et al., 1999; Schulten et al., 2019). These shallow failures were translational slides and possibly resulted in retrogressive failure (Piper et al., 1999; Mosher & Piper, 2007; Schulten et al., 2019). It is possible that the surficial failures overlying the main slump area were a consequence of the slump displacement rather than a direct result of the earthquake. In the upper Laurentian Fan region, closer to the epicenter of the earthquake, the surficial failures were presumably directly related to ground accelerations caused by the earthquake (Piper et al., 1988).

It appears, from interpretation of the evidence presented in this study, that the 1929 Grand Banks submarine landslide involved two failure mechanisms: 1) a massive, complex slump of the upper ~500 m and a ~560 km³ sediment, and 2) translational, retrogressive failure of the upper ~20 m of sediment (Piper et al., 1999; Mosher & Piper, 2007; Schulten et al., 2019). It is held that the slump is a much more probable mechanism to account for generation of the observed tsunami than the surficial sediment failures. Simulations by Løvholt et al. (2019), however, show that both mechanisms are required. The main slump generated the principal component of the tsunami that impacted the south coast of Newfoundland, while the more distributive surficial sediment failures account for the more widely distributed tsunami wave that was recorded in Halifax and Cape Breton (Løvholt et al., 2019).

This conclusion has significant consequences for the probability of tsunami generation by submarine landsliding along other continental margins. According to the simulations of Løvholt et al. (2019), the more significant wave heights of the tsunami were generated by the St. Pierre Slump and not the shallow sediment failures. While shallow sediment failures are recognized as relatively common along continental margins (Chaytor et al., 2007; Mosher et al., 2004; Mosher et al., 2010a; Baeten et al., 2014), large mass movements that

are more likely to be tsunamigenic (*e.g.*, Nisbet and Piper, 1998; Legros, 2002; Haflidason et al. 2004; Mosher et al., 2010b; Deptuck and Campbell, 2012; Urlaub et al. 2013) are much less common. Rarer still are reports of near in situ slumps such as reported herein. This result is probably because of lack of evidence rather than lack of occurrence. In order to recognize such events, either high resolution 3D or closely spaced 2D seismic reflection lines are necessary. A global or even regional tsunami threat due to submarine landslides, therefore, is still difficult to quantify.

3.7 ACKNOWLEDGMENTS AND DATA

Irena Schulten is supported by NSERC CREATE Transatlantic Ocean System Science and Technology (TOSST) grant to Dalhousie University and NSERC Discovery Grants to David C. Mosher and David J. W. Piper. Seismic reflection and multibeam echosounder data were provided by the Geological Survey of Canada Atlantic (GSCA, Natural Resources) and DFG funded Expedition MSM47 (Sebastian Krastel). Thank you to TGS-Nopec for allowing use of their seismic data. The authors would like to express their gratitude to S. Kienast and M. Kienast for reviewing the manuscript and for providing guidance and administrative support to the lead author. Thank you to staff at the GSCA for advice and encouragement. The Natural Resources Canada allowed publication of this manuscript, the contribution number is 20190010. GSC data is available through the expedition database (ED.gdr.nrcan.gc.ca). All meta-data of the German expedition MSM47 are available under <https://portal.geomar.de/metadata/leg/show/333156>. Paper copies of the TGS Nopec seismic data can be requested through the Canada-Nova Scotia offshore petroleum board (<https://www.cnsopb.ns.ca/>).

3.8 REFERENCES CITED IN CHAPTER 3

Baeten, N. J., Laberg, J. S., Vanneste, M., Forsberg, C. F., Kvalstad, T. J., Forwick, M., Vorren, T. O., Haflidason, H., 2014. Origin of shallow submarine mass movements and their glide planes—Sedimentological and geotechnical analyses from the continental slope off northern Norway. *Journal of Geophysical Research*, Vol. 119: p. 2335-2360.

- Bent, A. L., 1995. A complex double-couple source mechanism for the Ms 7.2 1929 Grand Banks earthquake. *Bulletin of the Seismological Society of America*, Vol. 85, p. 1003-1020.
- Bryn, P., Solheim, A., Berg, K., Lien, R., Forsberg, C. F., Haflidason, H., Ottesen, D., and Rise, L., 2003. The Storegga Slide complex: repeated large scale sliding in response to climatic cyclicity. In: Locat, J., Mienert, J., and Boisvert, L. (eds), *Submarine Mass Movements and Their Consequences, Advances in Natural and Technological Hazards Research*, p. 215-222, Springer, Dordrecht.
- Bryn, P., Berg, K., Forsberg, C. F., Solheim, A., and Kvalstad, T. J., 2005. Explaining the Storegga Slide. *Marine and Petroleum Geology*, Vol. 22, p. 11-19.
- Chaytor, J. D., Twichell, D. C., Ten Brink, U. S., Buczkowski, B. J., and Andrews, B. D., 2007. Revisiting submarine mass movements along the U. S. Atlantic continental margin: Implications for tsunami hazards. In: Lykousis, V., Sakellariou, D., and Locat, J. (eds.), *Submarine Mass Movements and Their Consequences, Advances in Natural and Technological Hazards Research*, Vol. 27, p. 395-403, Springer, Dordrecht.
- Childs, C., Nicol, A., Walsh, J. J., and Watterson, J., 1996. Growth of vertically segmented normal faults. *Journal of Structural Geology*, Vol. 18, No. 12, p. 1389-1397.
- Cohen, K. M., and Gibbard, P. L., 2016. Global chronostratigraphical correlation table for the last 2.7 million years v. 2016a. Subcommittee on Quaternary Stratigraphy (International Commission on Stratigraphy), Cambridge, England. <http://www.stratigraphy.org/upload/QuaternaryChartExplanation.pdf>.
- Damuth, J. E., 1975. Echo character of the western equatorial Atlantic floor and its relationship to the dispersal and distribution of terrigenous sediments. *Marine Geology*, Vol. 18, p. 17-45.
- Damuth, J. E., and Olson, H. C., 2015. Latest Quaternary sedimentation in the northern Gulf of Mexico Intraslope Basin Province: I. Sediment facies and depositional processes. *Geosphere*, Vol. 11, No. 6, p. 1689-1718, doi:10.1130/GES01090.1.
- Deng, C., Fossen, H., Gawthorpe, R. L., Rotevatn, A., Jackson, C. A-L., and FazliKhani, H., 2017. Influence of fault reactivation during multiphase rifting: The Oseberg area, northern North Sea rift. *Marine and Petroleum Geology*, Vol. 86, p. 1252-1272.

- Deptuck, M. E., and Campbell, C., 2012. Widespread erosion and mass failure from the ~51 Ma Montagnais marine bolide impact off southwestern Nova Scotia, Canada. *Canadian Journal of Earth Sciences*, Vol. 49, p. 1567-1594.
- Deptuck, M. E., Mosher, D. C., Campbell, D. C., Hughes-Clarke, J. E., and Noseworthy, D., 2007. Along slope variations in mass failures and relationships to major Plio-Pleistocene morphological elements, SW Labrador Sea. In: Lykousis, V., Sakellariou, D., and Locat, J. (eds.), *Submarine Mass Movements and Their Consequences, Advances in Natural and Technological Hazards Research*, Vol. 27, p. 37-45, Springer, Dordrecht.
- Doxsee, W. W., 1948. The Grand Banks Earthquake of November 18, 1929. *Publications of the Dominion Observatory, Ottawa*, Vol. 7, No. 7, p. 323-335.
- Driscoll, N. W., Weissel, J. K., and Goff, J. A., 2000. Potential for large-scale submarine slope failure and tsunami generation along the U. S. mid-Atlantic coast. *Geology*, Vol. 28, No. 5, p. 407-410.
- Earthquakes Canada, GSC, Earthquake Search (On-line Bulletin), <http://earthquakecanada.nrcan.gc.ca/stndon/NEDB-BNDS/bull-eng.php>, *Nat. Res. Can.*, {29.01.2018}.
- Fine, I. V., Rabinovich, A. B., Bornhold, B. D., Thomson, R. E., and Kulikov, E. A., 2005. The Grand Banks landslide-generated tsunami of November 18, 1929: preliminary analysis and numerical modeling. *Marine Geology*, Vol. 215, p. 45-57.
- Frey-Martínez, J., Cartwright, J., and James, D., 2006. Frontally confined versus frontally emergent submarine landslides: A 3D seismic characterisation. *Marine and Petroleum Geology*, Vol. 23, p. 585-604.
- Gafeira, J., Bulat, J., and Evans, D., 2007. The southern flank of the Storegga Slide: Imaging and geomorphological analyses using 3D seismic. In: Lykousis, V., Sakellariou, D., and Locat, J. (eds.), *Submarine Mass Movements and Their Consequences, Advances in Natural and Technological Hazards Research*, Vol. 27, p. 57-65, Springer, Dordrecht.
- Garfunkel, Z., 1984. Large-scale submarine rotational slumps and growth faults in the eastern Mediterranean. *Marine Geology*, Vol. 55, p. 305-324.

- Gee, M. J. R., Gawthorpe, R. L., and Friedmann, J. S., 2005. Giant striations at the base of a submarine landslide. *Marine Geology*, Vol. 214, p. 287-294.
- Georgiopoulou, A., Krastel, S., Masson, D. G., and Wynn, R. B., 2007. Repeated instability of the NW African margin related to buried landslide scarps. In: Lykousis, V., Sakellariou, D., and Locat, J. (eds.), *Submarine Mass Movements and Their Consequences, Advances in Natural and Technological Hazards Research*, Vol. 27, p. 29-36, Springer, Dordrecht.
- Gibbs, A. D., 1984. Structural evolution of extensional basin margins. *Journal of the Geological Society, London*, Vol. 141, p. 609-620.
- Giles, M. K., Mosher, D. C., Piper, D. J. W., and Wach, G. D., 2010. Mass Transport Deposits on the Southwestern Newfoundland Slope. In: Mosher, D. C., Shipp, R. C. et al. (eds.), *Submarine Mass Movements and Their Consequences, Advances in Natural and Technological Hazards Research*, Vol. 28, p. 657-665, Springer, Dordrecht.
- Giosan, L., Flood, R. D., Grützner, J., and Mudie, P., 2002. Paleooceanographic significance of sediment color on western North Atlantic Drifts: II. Late Pliocene-Pleistocene sedimentation. *Marine Geology*, Vol. 189, p. 43-61.
- Haflidason, H., Sejrup, H. P., Nygård, A., Mienert, J., Bryn, P., Lien, R., Forsberg, C. F., Berg, K., and Masson, D., 2004. The Storegga Slide: architecture, geometry and slide development. *Marine Geology*, Vol. 213, p. 201-234.
- Harbitz, C. B., Løvholt, F., and Bungum, H., 2014. Submarine landslide tsunamis: how extreme and how likely? *Natural Hazards*, Vol. 72, p. 1341-1374. doi: 10.1007/s11069-013-0681-3.
- Heezen, B. C., and Ewing, M., 1952. Turbidity currents and submarine slumps, and the 1929 Grand Banks earthquake. *American Journal of Science*, Vol. 250, p. 849-878.
- Hooper, E. C. D., 1991. Fluid migration along growth faults in compacting sediments. *Journal of Petroleum Geology*, Vol. 14, No. 2, p. 161-180.
- Katz, O., Reuven, E., and Aharonov, E., 2015. Submarine landslides and fault scarps along the eastern Mediterranean Israeli continental-slope. *Marine Geology*, Vol. 369, p. 100-115.

- Krastel, S., Braeunig, A., Feldens, P., et al., 2016. Geomorphology, processes and geohazards of giant submarine landslides and tsunami generation capacity, as recorded in the sedimentary record of the only historic slide of this kind: the 1929 Grand Banks landslide of the Canadian Atlantic continental margin. Cruise No. MSM47, September 30 - October 30, 2015, St. John's (Canada) - Ponta Delgada, Azores (Portugal). Maria S. Merian-Berichte, MSM47, p. 1-55, doi:10.2312/cr_msm47.
- Krastel, S., Li, W., Urlaub, M., Georgiopoulou, A., Wynn, R. B., Schwenk, T., Stevenson, C., and Feldens, P., 2019. Mass Wasting along the NW African continental margin. From: Lintern, D. G., Mosher, D. C., et al. (eds). Subaqueous Mass Movements. Geological Society, London, Special Publications, 477, <https://doi.org/10.1144/SP477.36>.
- Legros, F., 2002. The mobility of long-runout landslides. Engineering Geology, Vol. 63, p. 301-331.
- Lewis, K. B., 1971. Slumping on a continental slope inclined at 1°-4°. Sedimentology, Vol. 16, p. 97-110.
- Løvholt, F., Schulten, I., Mosher, D., Harbitz, C., and Krastel, S., 2019. Modelling of the 1929 Grand Banks slump and landslide tsunami. From: Lintern, D. G., Mosher, D. C., et al. (eds). Subaqueous Mass Movements. Geological Society, London, Special Publications, 477, <https://doi.org/10.1144/SP477.28>.
- Mansfield, C. S., and Cartwright, J. A., 1996. High resolution fault displacement mapping from three-dimensional seismic data: evidence for dip linkage during fault growth. Journal of Structural Geology, Vol. 18, No. 2/3, p. 249-263.
- Martinsen, O. J., and Bakken, B., 1990. Extensional and compressional zones in slumps and slides in the Namurian of County Clare, Ireland. Journal of the Geological Society, London, Vol. 147, p. 153-164.
- Mazzotti, S., 2007. Geodynamic models for earthquake studies in intraplate North America. In: Stein, S., and Mazzotti, S., (ed.), Continental Intraplate Earthquakes: Science, Hazard, and Policy Issues: Geological Society of America Special Paper 425. p. 17-33. Doi: 10.1130/2007.2425(02).
- McCall, C. W., 2006. A Geological and Geophysical study of the 1929 Grand Banks slide. M.Sc. Thesis, Saint Mary's University, Halifax, Nova Scotia.

- Mosher, D. C., and Piper, D. J. W., 2007. Analysis of Multibeam seafloor imagery of the Laurentian Fan and the 1929 Grand Banks landslide area. In: Lykousis, V., Sakellariou, D., and Locat, J. (eds.), *Submarine Mass Movements and Their Consequences, Advances in Natural and Technological Hazards Research, Vol. 27*, p. 77-88, Springer, Dordrecht.
- Mosher, D.C., and West, M.T.N., 2007. CCGS Hudson 2007020 Cruise Report: Laurentian Fan and eastern Scotian Slope, Argentia to Halifax; Geological Survey of Canada, Open File 5668, 1 DVD.
- Mosher, D. C., Piper, D. J. W., Campbell, D. C., and Jenner K. A., 2004. Near surface geology and sediment-failure geohazards of the central Scotian Slope. *AAPG Bulletin*, Vol. 88, No. 6, p. 703-723.
- Mosher, D. C., Moscardelli, L., Shipp, C., Chaytor, J., Baxter, C., Lee, H., and Urgeles, R., 2010a. Submarine Mass Movements and Their Consequences. In: Mosher, D. C., Shipp, R. C. et al. (eds.), *Submarine Mass Movements and Their Consequences, Advances in Natural and Technological Hazards Research, Vol. 28*, p. 1-10, Springer, Dordrecht. DOI 10.1007/978-90-481-3071-9.
- Mosher, D. C., Xu, Z., and Shimeld, J., 2010b. The Pliocene Shelburne mass-movement and consequent tsunami, western Scotian Slope. In: Mosher, D. C., Shipp, R. C. et al. (eds.), *Submarine Mass Movements and Their Consequences, Advances in Natural and Technological Hazards Research, Vol. 28*, p. 765-776, Springer, Dordrecht. DOI 10.1007/978-90-481-3071-9.
- Mosher, D. C., Piper, D. J. W., MacKillop, K., and Jarrett, K., 2010c. Near surface geology of the Halibut Channel region of the SW Newfoundland Slope from GSC data holdings. Geological Survey of Canada, Open File 6214, p. 1-72.
- Nisbett, E.G. and Piper, D.J.W. 1998. Giant submarine landslides. *Nature*, Vol. 392, p. 329-330.
- Piper, D. J. W., 2006. Cruise Report Hudson 2003-033: Geohazards on the Continental Margin off Newfoundland. Geological Survey of Canada, Open File 5081, p. 1-48.
- Piper, D. J. W., and Normark, W. R., 1982. Acoustic interpretation of Quaternary sedimentation and erosion on the channelled upper Laurentian Fan, Atlantic margin of Canada. *Canadian Journal of Earth Sciences*, Vol. 19, p. 1974-1984.

- Piper, D. J. W., and Normark, W. R., 1989. Late Cenozoic sea-level changes and the onset of glaciation: impact on continental slope progradation off eastern Canada. *Marine and Petroleum Geology*, Vol. 6, p. 336-347.
- Piper, D. J. W., Shor, A. N., and Hughes Clarke, J. E., 1988. The 1929 "Grand Banks" earthquake, slump, and turbidity current. In: *Sedimentological Consequences of Convulsive Geologic Events* (Ed. By H. E. Clifton), Geological Society of America Special Paper, Vol. 229, p. 77- 92.
- Piper, D. J. W., Mudie, P. J., Fader, G. B., Josenhans, H. W., MacLean, B., and Vilks, G., 1990. Quaternary Geology, Chapter 10. In: Keen, M. J., and Williams, G. L. (eds). *Geology of the Continental Margin of Eastern Canada*, Geological Survey of Canada, Geology of Canada, No. 2, p. 475-607.
- Piper, D. J. W., Mudie, P., Aksu, A. E., and Skene, K. I., 1994. A 1 Ma record of sediment flux south of the grand banks used to infer the development of glaciation in southeastern Canada. *Quaternary Science Reviews*, Vol. 13, p. 23-37.
- Piper, D. J. W., Cochonat, P., and Morrison, M. L., 1999. The sequence of events around the epicentre of the 1929 Grand Banks earthquake: initiation of debris flows and turbidity current inferred from sidescan sonar. *Sedimentology*, Vol. 46, p. 79-97.
- Piper, D. J. W., Macdonald, A. W. A., Ingram, S., Williams, G. L., and McCall, C., 2005. Late Cenozoic architecture of the St. Pierre Slope. *Canadian Journal of Earth Sciences*, Vol. 42, p. 1987-2000, doi:10.1139/E05-059.
- Piper, D. J. W., Shaw, J., and Skene, K. I., 2007. Stratigraphic and sedimentological evidence for late Wisconsinan sub-glacial outburst floods to Laurentian Fan. *Palaeogeography, Palaeoclimatology, Palaeoecology*, Vol. 246, p. 101-119.
- Ruffman, A., 2001. Potential for large-scale submarine slope failure and tsunami generation along the U. S. mid-Atlantic coast: Comment. *Geology*, Vol. 29, No. 10, p. 967.
- Sangree, J. B., and Widmier, J. M., 1979. Interpretation of depositional facies from seismic data. *Geophysics*, Vol. 44, No. 2, p. 131-160.

- Schulten, I., Mosher, D. C., Krastel, S., Piper, D. J. W., and Kienast, M., 2019. Surficial sediment failures due to the 1929 Grand Banks Earthquake, St Pierre Slope. From: Lintern, D. G., Mosher, D. C., et al. (eds). *Subaqueous Mass Movements*. Geological Society, London, Special Publications, 477, <https://doi.org/10.1144/SP477.25>.
- Skene, K. I., and Piper, D. J. W., 2003. Late Quaternary stratigraphy of Laurentian Fan: a record of events off the eastern Canadian continental margin during the last deglacial period. *Quaternary International*, Vol. 99-100, p. 135-152.
- Skene, K. I., and Piper, D. J. W., 2006. Late Cenozoic evolution of Laurentian Fan: Development of a glacially-fed submarine fan. *Marine Geology*, Vol. 227, p. 67-92.
- Synolakis, C. E., Bardet, J., Borrero, J. C., Davies, H. L., Okal, E. A., Silver, E. A., Sweet, S., and Tappin, D. R., 2002. The slump origin of the 1998 Papua New Guinea Tsunami. *Proc. Royal Soc. London*, Vol. 458, p. 763-789.
- Tappin, D. R., Watts, P., and Matsumoto, T., 2003. Architecture and failure mechanisms of the offshore slump responsible for the 1998 Papua New Guinea tsunami. In: Locat, J., Mienert, J., and Boisvert, L. (eds), *Submarine Mass Movements and their Consequences, Advances in Natural and Technological Hazards Research*, p. 383-392, Springer, Dordrecht.
- Tappin, D. R., Watts, P., Grilli, S. T., 2008. The Papua New Guinea tsunami of 17 July 1998: anatomy of a catastrophic event. *Natural Hazards and Earth System Science*, Copernicus Publications on behalf of the European Geosciences Union, Vol. 8, No. 2, p. 243-266. <hal-00299504>.
- Twichell, D. C., Chaytor, J. D., ten Brink, U. S., Buczkowski, B., 2009. Morphology of late Quaternary submarine landslides along the U.S. Atlantic continental margin. *Marine Geology*, Vol. 264, p. 4-15.
- Uchupi, E., and Austin, J. A., 1979. The stratigraphy and structure of the Laurentian Cone region. *Canadian Journal Earth Science*, Vol. 16, p. 1726-1752.
- Urlaub, M., Talling, P. J., and Masson, D. G., 2013. Timing and frequency of large submarine landslides: implications for understanding triggers and future geohazard. *Quaternary Science Reviews*, Vol. 72, No. 6, p. 63-82.

- Urgeles, R., and Camerlenghi, A., 2013. Submarine landslides of the Mediterranean Sea: Trigger mechanisms, dynamics, and frequency-magnitude distribution. *Journal of Geophysical Research and Earth Surface*, Vol. 118, p. 2600-2618, doi: 10.1002/2013JF002720.
- van der Zee, W., and Urai, J. L., 2005. Processes of normal fault evolution in a siliciclastic sequence: a case study from Miri, Sarawak, Malaysia. *Journal of Structural Geology*, Vol. 27, p. 2281-2300.
- van der Zee, W., Wibberley, C. A. J., and Urai, J. L., 2008. The influence of layering and pre-existing joints on the development of internal structure in normal fault zones: the Lodève basin, France. In: Wibberley, C. A. J., Kurz, W., Imber, J., et al. (eds) *The Internal Structure of Fault Zones: Implications for Mechanical and Fluid-Flow Properties*. Vol. 299, p. 57-74.
- Walsh, J. J., Watterson, J., Bailey, W. R., and Childs, C., 1999. Fault relays, bends and branch-lines. *Journal of Structural Geology*, Vol. 21, p. 1019-1026.
- Williams, G. D., Powell, C. M., and Cooper, M. A., 1989. Geometry and kinematics of inversion tectonics. In: Cooper, M. A., and Williams, G. D. (eds), *Inversion Tectonics*, Geological Society, London, Special Publications, Vol. 44, p. 3-15.

CHAPTER 4: STRESS HISTORY AND SLOPE STABILITY IN THE 1929 GRAND BANKS FAILURE AREA

Chapter 4 is a draft for a manuscript of “Schulten, I., MacKillop, K., and Mosher, D. C., Stress history and slope stability in the 1929 Grand Banks failure area”. Details on each author’s contribution are shown in Table 1.4.

4.1 ABSTRACT

The 1929 Grand Banks submarine landslide on the southwestern Grand Banks of Newfoundland is one of the best studied examples with an unequivocal connection between earthquake, landslide and tsunami. The St. Pierre Slope is the identified main failure area. Sediments of the upper St. Pierre Slope did not fail during the 1929 Grand Banks earthquake, although much of the mid and lower slope regions did. There is evidence for translational, probably retrogressive surficial failures (upper ~25 m) and association with a massive slump down to 550 m below seafloor (mbsf). This study aims to quantitatively assess slope stability of the upper slope in order to evaluate potential failure conditions and possible pre-conditioning factors that contributed to the 1929 submarine landslide. A comprehensive geotechnical analysis and static and pseudo-static infinite slope stability analysis over a range of sediment thicknesses (2-550 m) was conducted. Physical and geotechnical properties derived from marine sediment cores in the unfailed section indicate normal consolidation with slight under-consolidation between 3 and 9 m. Underconsolidation is attributed to 1) high sedimentation rates, 2) a lithologic change due to an older mass transport deposit and/or sandy turbidites, or 3) the presence of shallow free gas. Slope stability analyses indicate present-day stable conditions and show that slope angles in excess of 6.8° and $M_w > 4.8$ earthquakes within a distance of 5 km are required to initiate failure. The lowest factor of safety (FOS) is shown to be associated with packages of clay-layers and sandy turbidites in the upper 4 to 6 m of the sediment cores. The MTD, sandy turbidites and the presence of gas coincide with the position of a potential failure plane at the base of a nearby ~10 m-high escarpment. Both ground shaking and the presence of weak layers are necessary to cause failures of sediment <550 m-thick as observed in the 1929 submarine landslide. Ground shaking such as the 1929 earthquake is shown to

facilitate instability of a 550 m-thick block. Movement of this sediment mass that may be related to excess pore pressure along one or more sedimentary layers associated with MTD's and even liquefaction.

4.2 INTRODUCTION

On November 18th, 1929 a large submarine landslide occurred along the St. Pierre Slope of the Laurentian Fan, southwestern Grand Banks of Newfoundland, as a result of a M_w 7.2 earthquake (Piper et al., 1988; 1999; Mosher & Piper, 2007). This submarine landslide led to the first recognition of naturally-occurring submarine turbidity currents (Heezen & Ewing, 1952; Piper et al., 1999) and is one of the few landslides known to have generated a tsunami (Piper et al., 1999; Fine et al., 2005; Mosher & Piper, 2007). The 1929 Grand Banks submarine landslide is described as a widespread, translational and retrogressive sediment failure that affected the upper 20-25 m of the sediment column (Piper et al., 1988; 1999; McCall, 2006; Schulten et al., 2019). There are numerous shallow escarpments (in average 20-25 m high) and debris fields below these escarpments (Piper et al., 1999; Mosher & Piper, 2007). An association of these escarpments to deep-rooted faults and a décollement at 250 and 550 m depth below seafloor (mbsf) was shown in Chapter 3. It is proposed that a massive (560 km³) slump occurred as consequence of the 1929 earthquake and that the vertical displacement (~100 m) of this slump might have caused the observed surficial failures (see Chapter 3). The 1929 submarine landslide caused a tsunami, which resulted in a significant loss of human life and severe economic damage (Ruffman, 2001). The ensuing turbidity current broke telecommunication cables across the Laurentian Fan (Hodgeson & Doxsee, 1930; Heezen & Ewing, 1952).

The earthquake, with a 20 km-deep hypocenter underneath the Laurentian Fan (Bent, 1995), is well recognized as the trigger of the 1929 submarine landslide (Piper et al., 1999). Seismicity in this region of a passive continental margin is among the highest of Eastern Canada (Fig. 4.1) (Adams & Halchuk, 2003; Mazzotti, 2007), and a consequence of tectonic movements along the Cobequid-Chedabucto transform fault and the Newfoundland Fracture Zone (Fig. 4.1) (Bent, 1995). While the trigger mechanism that lead to the submarine slope failure in 1929 is very well known, factors that preconditioned

the slope to fail are debated (Giles et al., 2010). Preconditioning factors described for this region include salt tectonics, the presence of faults, free and dissolved gas hydrates, and high sedimentation rates, which can lead to the formation of overpressure resulting in a decrease of the frictional resistance and the development of weak layers (Skene & Piper, 2003; Ledger-Piercy & Piper, 2007; Giles et al., 2010; Mosher, 2011). Slope failure in 1929 affected certain areas of the slope, while other areas remained stable. It is important to narrow down the factors that primarily contributed to slope instability in order to evaluate a potential recurrence of slope failure under present-day conditions and to improve the understanding of the 1929 slope failure.

The objective of this study is to quantitatively assess slope stability of the St Pierre Slope (Fig. 4.1). This study examines an area of the slope that did not fail in the 1929 earthquake. Assessment of geotechnical information in this area, therefore, provides information on the stability of the slope. It also allows for assessment of potential failure conditions and possible contributing factors including ground accelerations that may have contributed to the 1929 Grand Banks submarine landslide. Static and pseudo-static infinite slope stability analyses are used to test slope stability under present day conditions and to evaluate the 1929 slope failure that occurred during earthquake ground accelerations.

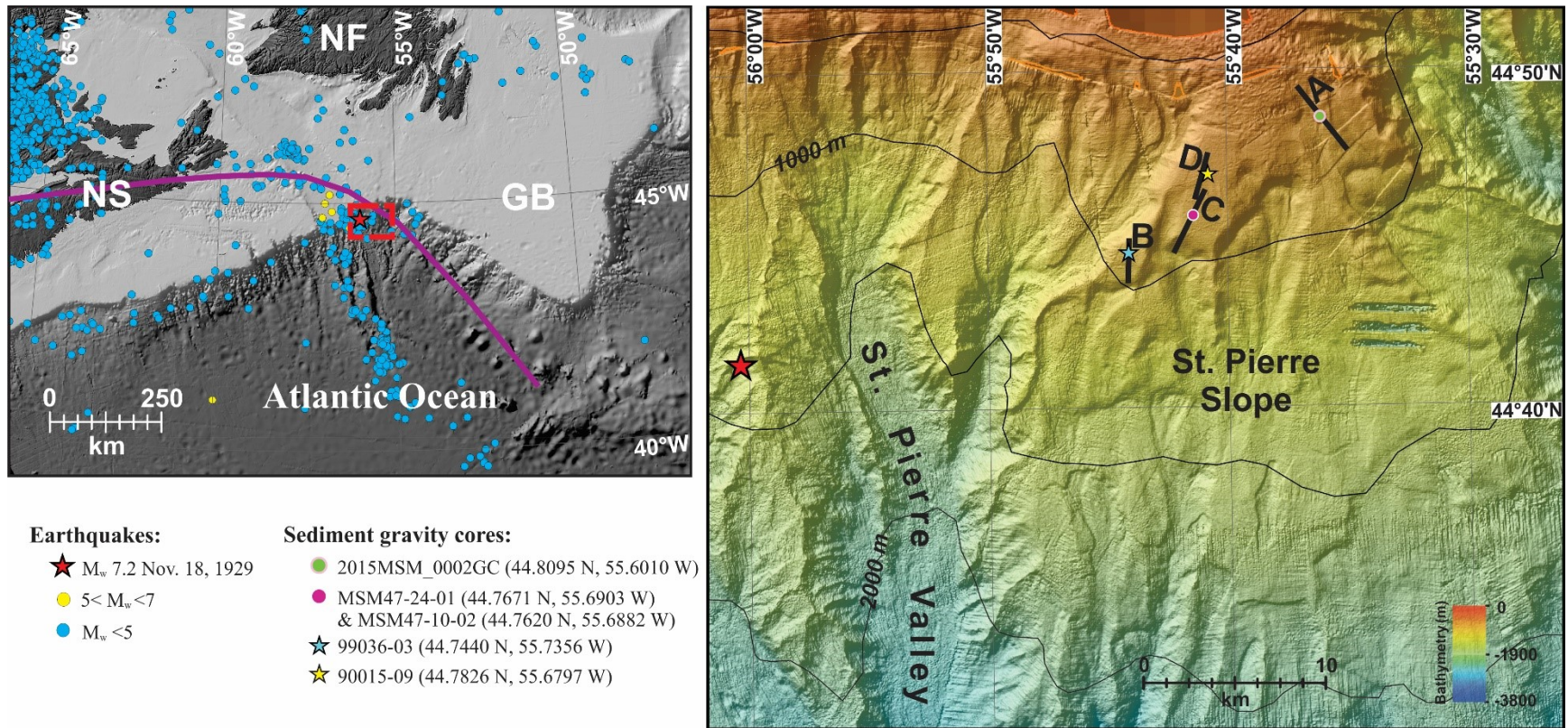


Fig. 4.1: Right: Regional overview map of Atlantic Canada. The location of the study area is shown within the red box and the red star indicates the location of the M_w 7.2 1929 earthquake. Other earthquakes are highlighted as coloured dots as recorded since 1985 by Earthquake Canada (2018). The violet line indicates approximate location of the Cobequid-Chedabucto transform fault and the Newfoundland Fracture Zone. GEBCO 2014 global bathymetric grid was used and imaged in ArcMap. NS = Nova Scotia, NF = Newfoundland and GB = Grand Banks of Newfoundland. Left: Location map showing core sites used in this study and 1929 earthquake epicentre (red star). Black lines (A to D) indicate the location of ultra-high resolution profiles shown in Fig. 4.2.

4.3 METHODS

4.3.1 Sediment coring

Slope stability is evaluated analyzing marine sediment gravity core 2015MSM_0002GC (902 cm long, 688 m water depth) and MSM47-24-01 (770 cm long, 825 m water depth) that were collected in 2015 during RV Maria S. Merian cruises MSM45 and MSM47 respectively (Figs. 4.1 & 4.2) (Schneider et al., 2015; Krastel et al., 2016). Both cores were collected in undisturbed, stratified sediments next to a shallow, approximately 8 m high escarpment. This geologic setting is verified through ultra-high resolution seismic profiles that were acquired over the core location prior to sampling (Figs. 4.1 & 4.2).

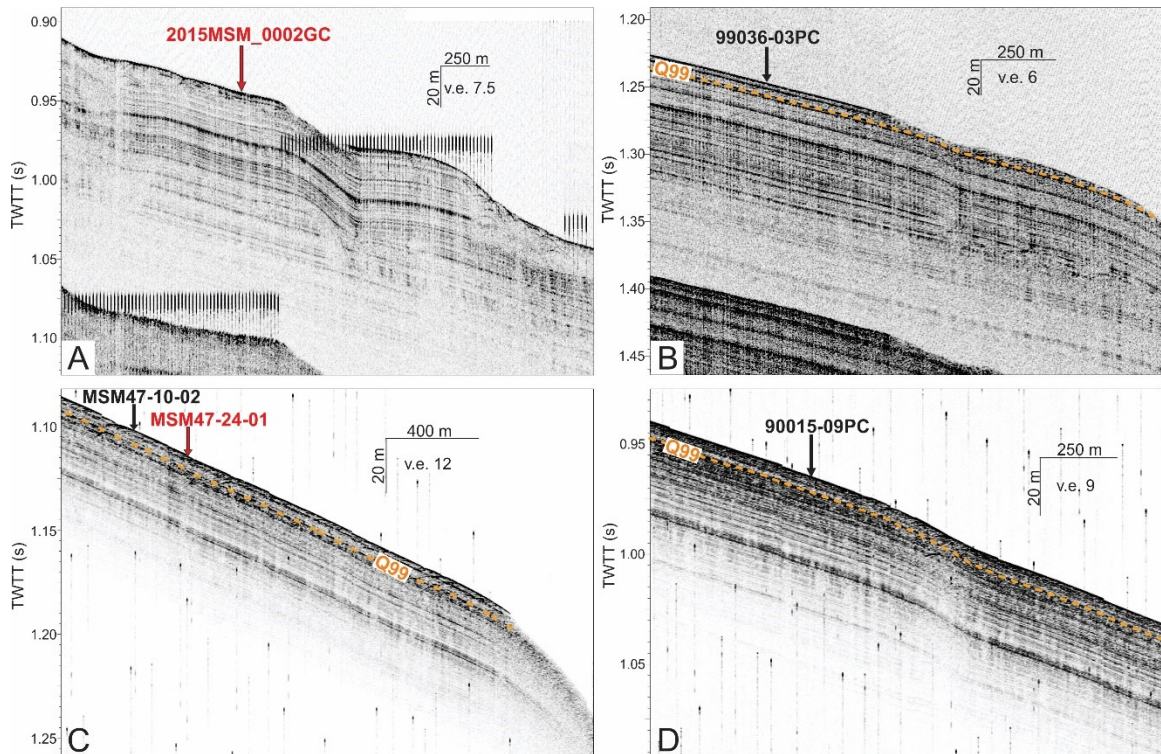


Fig. 4.2: (A & B) Hunttec DTS sparker profile, acquired during CCGS Hudson cruise 2007-020 and (C & D) parasound subbottom profiler data acquired during RV Maria S. Merian cruise MSM47. Locations of the seismic profiles are shown in Fig. 4.1. The seismic profiles show undisturbed, stratified sediments at the core locations (red & black arrow). A small, approximately 8 m-high escarpment is present to the south of the core location. The orange line shows the location of a failure plane, Q99 (McCall, 2006; Schulten et al., 2019).

Individual core sections were transported and stored in an upright position to minimize core disturbances. Physical property measurements and advanced geomechanical testing were performed in the sedimentological and geomechanical laboratories at the NRCan laboratory in Dartmouth, Nova Scotia (2015MSM_0002GC) and at the Center for Marine Environmental Science (Marum) of the University of Bremen, Germany (MSM47-24-01). Results from two other sediment cores collected in vicinity of core MSM47-24-01 during CCGS Hudson cruises (90015-009pc, 99036-003pc) and a core (MSM47-10-02) collected almost at the same location as MSM47-24-01 during RV Maria S. Merian cruise were integrated into this study (Figs. 4.1 & 4.2) (Piper, 1999; Krastel et al., 2016).

4.3.2 Core Physical properties

Measurement of physical properties followed a standard sedimentological core processing procedure (Blum, 1997). Unsplit core sections of sediment core 2015MSM_0002GC were X-radiographed to identify sedimentary structures and show any evidence of coring disturbance. This step allowed for selection of the best whole round subsamples for geomechanical testing analysis. Sediment disturbance due to gas expansion was observed from 620 cm down core. Whole-core sections of 2015MSM_0002GC were processed in a multi-sensor core logger (MSCL) that measured bulk density, p-wave acoustic velocity and magnetic susceptibility. Measurements were taken at a spacing of one-centimeter intervals. Bulk density measurements are based on gamma ray attenuation due to Compton scattering, which relates the degree of attenuation to density given a constant sediment thickness (~11.5 cm) (Carter et al., 1999). Acoustic velocity was measured using a compressional wave logger, but measurements were restricted to the upper 620 cm of the sediment core due to the presence of gas deeper in the core, which prevents the transmission of p-waves. Following the MSCL measurements, two whole round samples, 105.5 - 130.5 cm and 552 - 577.5 cm, were removed from the core sections of 2015MSM_0002GC for further geomechanical testing.

MSCL and X-radiographic measurements were not made on core MSM47-24-01. A nearby core (MSM47-10-02) was used as a reference for MSM47-24-01. The two cores were correlated using magnetic susceptibility data. Based on these correlations and assessment

of the structures in the nearby core, three whole round samples (190.5-260 cm, 350-384 cm and 712 - 770 cm) were selected from core MSM47-24-01 for geomechanical testing. Core sections were then split lengthwise into working and archive halves. Core halves of 2015MSM_0002GC were again X-radiographed to help identify sediment structures. Cores were photographed and, visually described, assessing sediment lithology and sedimentary structures, colour (Munsell Colour Chart), and a qualitative assessment of stiffness.

Digital colour measurements were performed on the working halves of the sediment core 2015MSM_0002GC, using a Minolta Spectrophotometer that reports L* (black to white), a* (green to red) and b* (blue to yellow) values according to the reflectance of visible light (wavelength from 400 to 700 nm) at the sediment surface (Carter et al., 1999). Core working halves of sediment core 2015MSM_0002GC were further run through the MSCL, measuring the same parameters but velocimeter and magnetic susceptibility sensors were able to contact directly with the sediment. P-wave velocity (transverse and longitudinal) measurements were made on core 2015MSM_0002GC with probes inserted into the sediment at 10 cm intervals. Measurements were not taken below 620 cm due to extensive gas induced core disturbance.

Discrete measurements of undrained shear strength were made at 10 cm intervals. For sediment core 2015MSM_0002GC a motorized laboratory miniature vane shear for undrained shear strength (peak and remoulded) was used following the ASTM D 4648 standard (2010). Fall cone measurements were taken on sediment core MSM47-24-01 (Hansbo, 1957). Discrete constant volume samples were taken from the upper 590 cm of core 2015MSM_0002GC and the upper 500 cm of core MSM47-24-01 at an interval of two to three samples per meter. Index properties such as wet bulk density, dry bulk density, water content, void ratio and porosity were determined from these constant volume samples using ASTM standard D 2216 (2010). These discrete samples allowed calibration of the MSCL densities and allowed direct calculation of porosity and void ratio of the sediment (Carter et al., 1999). For detailed equations regarding the sediment properties, see appendix A2.1.1.

Undrained shear strength data were further obtained for piston cores 99036-003pc and 900015-09pc from the NRCan database and for a gravity core MSM47-10-02 using the MSM47 expedition database (Krastel et al., 2016). Bulk density information was available for core 99036-003pc through the NRCan database. McCall (2006) provides a general description of core 99036-003pc.

Atterberg limits tests following the standard procedure of ASTM D 4318 were made to determine liquid and plastic limits (ASTM D 4318, 2010). Both, the plasticity index (PI) and liquidity index (LI) were calculated from these data.

$$PI = LL - PL \quad (1)$$

$$LI = \frac{w - PL}{PI} \quad (2)$$

with LL = liquid limit (%); PL = plastic limit (%); w = water content (%)

4.3.3 Advanced Geomechanical Testing

Advanced geomechanical analyses consisted of consolidation (ROWE cell, oedometer) testing (ASTM D-2435, 2011) to determine stress state and stress history of the sediment, and triaxial shear (ASTM D-4767, 2011) and direct shear testing (ASTM D 3080, 2011) to determine strength properties of the sediment.

4.3.3.1 CONSOLIDATION TESTING

Four consolidation tests were carried out on samples taken from sediment core 2015MSM_0002GC and MSM47-24-01. Important parameters derived from these tests are the effective pre-consolidation stress (P'_c), the overconsolidation ratio (OCR), the compression index (C_c), the coefficient of consolidation (C_v), and the hydraulic conductivity (k).

The Cassagrande (1936), Silva (1970) and Work (Becker et al., 1987) methods were used to estimate the effective pre-consolidation stress (P'_c), which describes the maximum stress

the sediment underwent in the past (Braja, 2010). All three methods determine the P'_c graphically from the void ratio (e) versus logarithmic-effective stress (P'_{vo}) curve (appendix A2.1.2, Fig. A2.1), further referred to as $e - \log-P'$ curve. The change in void ratio (e) for each load increment was derived from changes in sample height (appendix A2.1.2) (Braja, 2010), while Taylor's square root time versus displacement relationship was used to determine the rate of consolidation (C_v) for each load increment (appendix A2.1.2, Fig. A2.2). The hydraulic conductivity (k) is calculated using the relation to C_v and changes in the void ratio (e). A linear relationship of $e - \log-k$ (appendix A2.1.2, Fig. A2.3) is used to determine the hydraulic conductivity equivalent to the void ratio of the sediment at the P'_c . The compression index (C_c) can be derived from the modulus of the slope of the virgin compression curve in the $e - \log-P'$ curve (appendix A2.1.2, Fig. A2.1), while the slope of the unloading section of the $e - \log-P'$ curve is referred to as the recompression index (C_r).

The total effective overburden stress (P'_{vo}) is a function of unit weight over depth and can be derived using the measured bulk density (appendix A2.1.2). A comparison of P'_{vo} and the P'_c is used to derive the OCR value of the sediment.

$$OCR = \frac{P'_c}{P'_{vo}} \quad (3)$$

The OCR value describes the stress state of the sediment. Sediments with OCR values of approximately one are considered to be normally consolidated (NC), while sediments with $OCR < 1$ are underconsolidated (UC) and $OCR > 1$ are overconsolidated (OC). In this study, the OCR value is calculated as the average of the Cassagrande (1936), Silva (1970) result and the Work (Becker et al., 1987) result.

4.3.3.1.1 2015MSM_0002GC – ROWE CONSOLIDATION CELL

A Global Digital Systems (GDS) consolidation system designed for testing soft soils was used for a one-dimensional consolidation test according to ASTM D 2435 (2011). The

system consists of a ROWE consolidation cell, two pressure volume controllers, linear displacement transducer, a pore pressure transducer and a data-acquisition system.

A sediment sample 2.55 cm high with a diameter of 6.35 cm was extracted from the whole round sample at a core depth of 553 to 555.5 cm using a sampling ring. The metal consolidation ring containing the sample was placed inside the ROWE consolidation cell. Porous stones on top and bottom of the sample specimen allowed the sample to drain during the test. The sample was back pressured to 200 kPa in order to ensure 100% saturation. This procedure ensures that any air/gas in the voids of the sediment get re-dissolved into the pore fluid. The sample was then loaded incrementally using a load increment ratio of 0.5. Each load increment was applied until at least 90% of primary consolidation was reached, or a maximum of 24 hours. In total, eleven loading increments from 2 kPa to 173 kPa were applied to the specimen. After the final load increment of 173 kPa was complete, the specimen was unloaded. At the end of the test, the final height and dry weight of the test specimen were determined.

4.3.3.1.2 MSM47-24-01 – STANDARD ODOMETER CELL

A standard oedometer consolidation system was used for a one-dimensional consolidation test according to ASTM D 2435 (2011). The system consists of a consolidation cell, a linear displacement transducer and a data-acquisition system.

Sediment samples ~1.5 cm high with a diameter of ~5 cm were extracted from the whole round samples at core depth 351 to 353 cm, 357 to 358.5 cm and 713 to 714.5 cm using a metal sampling ring. The consolidation ring with the specimen was fixated inside the oedometer cell with porous stones on top and bottom to allow drainage of the sample during consolidation. Distilled water was used to keep the sample saturated. The load on the sample was incrementally doubled. Each load increment was applied for at least 24 hours. In total, eight loading increments from 2 kPa to 314 kPa were applied to the specimen. After the final load increment of 314 kPa was completed, the specimen was unloaded. At the end of the test the final height and dry weight of the test specimen were determined.

4.3.3.2 TRIAXIAL TESTING

Two multistage isotropically-consolidated undrained triaxial (CIU) tests were performed on sediment samples of core 2015MSM-0002GC according to ASTM D 4767 (2011). The triaxial tests were used to define the Mohr Coulomb criterion, which describes the cohesion (c') and frictional component of sediment strength (Braja, 2010).

A sediment sample, 9.47 cm in height and 4.90 cm in diameter, was extracted from the whole round samples at core depth 116.5 to 128.5 cm and 563 to 575 cm. Each sample was extruded into an impermeable rubber membrane inside a Bishop and Wesly triaxial cell, which was then filled with de-aired water. The sample was back-pressured with the de-aired water to 200 kPa to ensure full saturation of the voids. Skempton's B-value was determined (B-check) to verify full saturation of the specimen. At full saturation, an increase (~ 70 kPa) in cell pressure should cause an equivalent increase in the pore pressure of the specimen under undrained condition. After a B-value of >0.95 was obtained, the first consolidation pressure was applied. In total each sample was exposed to three consolidation and three shearing stages. After each consolidation stage, Bender elements at the top and bottom of the sample were used to measure the shear wave velocity in the sediment. The sample was then sheared at a rate of $0.067\% \text{ min}^{-1}$ until the stress-strain curve leveled off. The three shearing stages were performed under undrained conditions, which results in an increase in pore water pressure as the axial stress (σ_1) on the sample increases. Skempton's pore pressure parameter at failure (A_f) describes this relationship (appendix A2.1.3, Fig. A2.4) (Skempton, 1954).

The stress path of each stage was plotted as a function of effective average mean stress (s') versus maximum shear stress (t') in order to derive the failure envelope of the Mohr-Coulomb failure criterion (appendix A2.1.3, Fig. A2.4) (Braja, 2010), which defines the specific effective friction angle (ϕ') and the effective cohesion (c') of the sediment.

$$\tau_f = c' + P'_{vo} * \tan \phi' \quad [kPa] \quad (4)$$

with τ_f = shear strength (kPa); c' = effective cohesion; P'_{vo} = total effective stress (kPa); ϕ' = consolidated undrained effective angle of shearing resistance

The normalized strength ratio (S_u/P'_v) is derived from the CIU triaxial test. The consolidation pressure acting on the sample should be in the normal consolidation range (OCR of 1). The measured S_u/P'_v derived from the CIU triaxial test needs to be corrected for isotropic consolidation. Roberts and Cramp (1996) described the Normalized Soil Properties (NSP) methodology:

$$\frac{S_u}{P'_{vo}} = A_c * A_r * S * (OCR)^m \quad (5)$$

with P'_{vo} = total effective vertical stress (kPa); A_c = correction for anisotropic consolidation, assumed to be 0.8; A_r = correction for cyclic loading, assumed to be 1; S = ratio of measured S_u to triaxial consolidation stress; $OCR = 1$ and m = a soil constant, assumed to be 0.8

Rearranging equation (5) allows to estimate the normalized shear strength ($S_{u\ NSP}$) with increasing overburden.

The modified Mohr-Coulomb relationship is another method to obtain a continuous profile of undrained shear strength (S_u), using the parameters obtained from triaxial testing (Morgenstern, 1967).

$$S_u = P'_{vo} * \frac{(K_o + A_f * (1 - K_o)) * \sin \phi' + (\frac{c'}{P'_{vo}} * \cos \phi')}{1 + (2 * A_f - 1) * \sin \phi'} \quad (6)$$

with P'_{vo} = total effective vertical stress (kPa); K_o = coefficient of lateral earth pressure at rest and can be approximated using ($K_o = 1 - \sin \phi'$); ϕ' =

consolidated undrained angle of shearing resistance; c' = cohesion; A_f = Skempton's pore pressure parameter at failure.

Both, undrained shear strength derived from the Mohr-Coulomb relationship and using NSP, are used to evaluate the sediment's consolidation state.

4.3.3.3 SINGLE-DIRECT SHEAR

Direct shear is another method of determining shear strength of the sediment. Three direct shear tests were carried out using the GIESA direct shear apparatus at Marum according to ASTM D 3080 (2011). Cylindrical sediment samples were extracted from core depth 190 to 204 cm of core MSM47-24-01. Each sample specimen was placed inside a shear box filled with seawater. Porous stones on top and bottom of the sample allowed drainage. Shear tests were conducted using different consolidation states for each sample (100, 200 and 300 kPa). Horizontal shearing was initiated after primary consolidation was concluded. Samples were then sheared horizontally at a rate of 0.04 mm min^{-1} until they reached residual stress (P_r'). Parameters recorded include effective average mean stress (s') and static peak shear strength (t'). The envelope of the Mohr-Coulomb failure criterion was used to derive effective cohesion (c') and the friction angle (ϕ') (appendix A2.1.3).

4.3.4 Factor of Safety – Infinite Slope Analysis

Infinite slope analysis was used to evaluate slope stability under the assumption that sediment failures occur with sheet-like behaviour (Poulos, 1988; Roberts & Cramp, 1996). Sediment failure at the St. Pierre Slope is generally described to be surficial, widespread, and retrogressive occurring along bedding planes (Piper et al., 1999; Mosher & Piper, 2007; Schulten et al., 2019). The infinite slope analysis derives the factor of safety (FOS) as a ratio of shear strength (τ_f) to shear stress (τ_m)

$$FOS = \frac{\tau_f}{\tau_m} \quad (7)$$

A FOS smaller than unity indicates theoretical slope instability, while a FOS greater than one indicates stable conditions. Under static condition the shear stress (τ_m) is essentially a function of the effective overburden pressure (P'_{vo}) and the slope angle (β). Substituting all shear stress related factors into the equation for the FOS gives the following relationship:

$$FOS = \frac{\tau_f}{P'_{vo} * \sin \beta * \cos \beta} \quad (8)$$

Non-static failure must be considered in assessing slope stability at the St. Pierre Slope, due to the relative high seismicity in the region and the fact that the 1929 event occurred as a result of an earthquake. A modification of equation (8) was used to derive the FOS in relation to peak ground acceleration (PGA) due to earthquake loading under pseudo static conditions.

$$FOS_e = \frac{\tau_f}{P'_{vo} * \cos^2 \beta * (\tan \beta + PGA)} \quad (9)$$

The FOS was calculated for both sediment cores analysed in this study and for core 99036-003 from ~4 km west of MSM47-24-01 (Fig. 4.1). Equations from Atkinson and Boore (2006) and Campbell and Bozorgnia (2008), further termed AB2006 and CB2008, were used to convert known seismic magnitudes into PGA (appendices A2.2.1 & A2.2.2).

Surficial sediment failures observed at St. Pierre Slope are 10 to 25 m thick (Piper et al., 1999; Mosher & Piper, 2007; Schulten et al., 2019). Potential décollements are identified in 250 and 550 m sub-bottom depth (Piper et al., 2005; see Chapter 3). The undrained shear strength (S_u) and total effective stress (P'_{vo}), therefore, were extrapolated down to the maximum failed sediment thickness of 550 m.

The effective overburden stress at 550 m depth was estimated in two ways: i) the trend in effective overburden from core measurements was extrapolated to depth assuming fully hydrostatic conditions ($P'_{vo \text{ trend}}$), and ii) a porosity-depth profile was generated using the

equation of Kominz et al. (2011) (appendix A2.2.3.1). Porosity was used to calculate sediment bulk density assuming a constant grain density of silica (2.65 g cm^{-3}) and effective overburden assuming hydrostatic conditions ($P'_{vo \text{ porosity}}$) (appendix A2.2.3.2). Two methods were used to extrapolate undrained shear strength (S_u) to 550 m depth: A) the trend in shear strength measured in shallow sediment cores was linearly extrapolated ($S_{u \text{ trend}}$), and B) results from the triaxial tests were used to compute shear strength at depth ($S_{u \text{ NSP}}$) using the calculated effective overburden derived from the porosity information.

Three different cases were evaluated for slope stability analysis of sediment slabs using different combinations of the derived shear strength and effective overburden and are differentiated for the two different FOS calculations as follow:

| Static slope stability analysis | Pseudo-static slope stability analysis: |
|--|--|
| SSA-case 1: $S_{u \text{ trend}}$ and $P'_{vo \text{ trend}}$ | PGA-case 1: $S_{u \text{ trend}}$ and $P'_{vo \text{ trend}}$ |
| SSA-case 2: $S_{u \text{ trend}}$ and $P'_{vo \text{ porosity}}$ | PGA-case 2: $S_{u \text{ trend}}$ and $P'_{vo \text{ porosity}}$ |
| SSA-case 3: $S_{u \text{ NSP}}$ and $P'_{vo \text{ porosity}}$ | PGA-case 3: $S_{u \text{ NSP}}$ and $P'_{vo \text{ porosity}}$ |

4.3.5 Uncertainty assessment

Core physical and geomechanical properties may differ from in-situ conditions. Sample disturbance associated with sediment coring, removal of material from in situ pressure conditions and extraction of test-specimens may cause this difference (Marsters, 1986; Poulos, 1988; Ai et al., 2014). While repetitive experimentation permits assessing the precision of laboratory analysis, there is no real way to test accuracy relative to in situ conditions. Results from physical and geomechanical testing are therefore considered approximations to in-situ conditions.

Insufficient data coverage, particularly with respect to core sample locations, represents a significant constraint to this study in that it is not possible to capture the full scope of variability in sediment physical properties. Only two cores (2015MSM_0002GC, MSM47-24-01) were fully analysed (consolidation, triaxial etc.) and physical property data from another three cores (Mosher & Piper, 2007; McCall, 2006; Schulten et al., 2019) form part

of this study. MacKillop et al. (2019) discuss uncertainties connected with spatial and temporal variations of sediments and the effect on the slope stability assessment for the near-by Scotian Slope.

PGA conversion from magnitude and distance proved to be challenging, as there are various methods reported in the literature. AB006 and CB2008 showed similar results and were chosen as most suitable for this study. AB2006 is based on a hybrid model developed for eastern North America and CB2008 is based on an empirical ground motion model developed for shallow continental earthquakes in western North America and regions with similar tectonic regimes (Atkinson & Boore, 2006; Campbell & Borzogna, 2008). The models require information about earthquake magnitude, distance to source and shear wave velocity in 30 m sub-bottom depth (v_{30}), the latter of which is not well constrained (appendix A2.2.1 & A2.2.2). Some assumptions needed to be made especially for CB2008, which introduces uncertainty (appendix A2.2.1 & A2.2.2).

4.4 RESULTS

4.4.1 Physical Properties

The cores consist of bioturbated, stratified muddy (clay and silt) sediment (Fig. 4.3 & 4.4; appendix A2.3.1). Atterberg testing characterises the sediment as lean clay (CL) of a low to intermediate plasticity (Table 4.1; appendix A2.3.2). The clay content, sediment stiffness and abundance of mottled features increases towards the base of the cores (Fig. 4.3 & 4.4). Shell and shell fragments as well as burrows are observed throughout the cores, but with a higher abundance in sandier sediment layers (Fig. 4.4). Thin sandy beds or siltier layers and lenses are interbedded with more typical fine-grained silty-clay sediment. The transition from olive-grey to grey-brown mud in the upper meter of both sediment cores shows 10 to 15 cm-thick very-fine sand layers (Fig. 4.3 & 4.4). A distinct multilayer package of sandier and siltier layers interbedded with clay-rich mud is present in 400 to 600 cm core depth and shows characteristic colour alterations (Figs. 4.3 & 4.4). In core MSM47-24-01 the sandier intervals contain gravel, small rocks and shell fragments (Fig. 4.4). Mottled features are often observed at the base of this multilayer package (Figs. 4.3 & 4.4). Rusty coloured lenses and layers are present in the lower sections of the cores from

510 cm downcore (Figs. 4.3 & 4.4). Lense-shaped features and inclined layers occur around 600 cm core depth. Gas expansion cracks and mottled features are present underneath these layers, from 620 cm to the end of the sediment cores. A more concise description of the lithofacies and the legend is given in the appendices A2.3.1.1 and A2.3.1.2 (Fig. A2.5 & A2.6).

Table 4.1: Results from Atterberg testing on samples from core 2015MSM_0002GC and MSM47-24-01 with percentage of natural water content (w), liquid limit (LL), plastic limit (PL), plasticity index (PI), liquidity index (LI) and sediment classification. See appendix A2.3.2 (Figs. A2.7-A2.14).

| core | depth | w (%) | LL (%) | PL (%) | PI (%) | LI (%) | Classification |
|----------------|------------|-------|--------|--------|--------|--------|----------------|
| 2015MSM_0002GC | 106-114 cm | 46.56 | 34.23 | 19.73 | 14.50 | 1.85 | CL |
| 2015MSM_0002GC | 114-130 cm | 41.25 | 30.26 | 19.67 | 10.59 | 2.04 | CL |
| 2015MSM_0002GC | 552-560 cm | 43.85 | 39.62 | 20.30 | 19.32 | 1.22 | CL |
| MSM47-24-01 | 190-195 cm | 58.51 | 45.02 | 22.13 | 22.89 | 1.59 | CL |
| MSM47-24-01 | 195-200 cm | 57.50 | 45.63 | 19.82 | 25.81 | 1.46 | CL |
| MSM47-24-01 | 350-355 cm | 65.90 | 48.04 | 24.42 | 23.62 | 1.76 | CL |
| MSM47-24-01 | 355-360 cm | 61.38 | 43.71 | 23.17 | 20.54 | 1.86 | CL |
| MSM47-24-01 | 712-717 cm | 45.05 | 44.47 | 21.60 | 22.87 | 1.03 | CL |

Measured index properties and undrained shear strength are sensitive to changes in the lithofacies (Figs. 4.3 & 4.4). The bulk density generally varies between 1.5 to 1.9 mg m⁻³, with higher densities associated with interbedded sandier beds (Figs. 4.3 & 4.4). Overall, density increases with depth (Fig. 4.3). Bulk densities from core 99036-003pc are consistent with results from this study (Fig. 4.5). Variations in magnetic susceptibility values broadly correlate with variations in density, likely responding to lithologic change in both cases (Figs. 4.3 & 4.4). Alternations in the bottom part of core 2015MSM_0002GC, where there is a higher rock content, however, are much more pronounced in magnetic susceptibility than in bulk density. An increase in magnetic susceptibility is also shown for the red-brown (rusty) layers (Figs. 4.3 & 4.4). P-wave velocities range between 1,450 to 1,600 m s⁻¹; higher values occur where the sediment is sandier (Fig. 4.3). Shear wave velocities determined during triaxial testing provide a velocity of 152 m s⁻¹ (v₃₀) at pressure conditions equivalent to a sub-bottom depth of 30 m (Table 4.2). Water content values also decrease with depth from 65% to 40% (Figs. 4.3 & 4.4). Higher water contents correlate to

higher clay content. Void ratio (e) and porosity (η) follow the same trend as water content, with a void ratio ranging from 1.1 to 2 and porosity in the range of 52 to 81 %.

Undrained shear strength (S_u) generally shows low sediment strength values of 3 to 15 kPa (Figs. 4.3-4.5). Shear strength increases over the upper 200 to 250 cm to ~10 kPa, before it decreases to 5 kPa, and then slowly increases with depth (Figs. 4.3-4.5). Higher shear strength values correlate to sandier sediments (Figs. 4.3 & 4.4). X-ray images show that small rocks are present in these sections. Remoulded shear strength follows the same trend, but in a range of 0 to 5 kPa (Fig. 4.3).

Four units can be distinguished, based on the lithofacies and physical property characteristics (Figs. 4.3 & 4.4):

- **Unit 1**, silt-rich olive-grey mud with an increase in sand towards the base; characterised by distinct changes in colour, bulk density, velocity and magnetic susceptibility, water content and shear strength
- **Unit 2**, clay-rich mud, high water content and low shear strength
- **Unit 3**, muddy sediment interbedded with layers of high sand content, shell fragments and small rocks; alternation in colour, shear strength, and magnetic susceptibility and gradual increasing shear strength with depth
- **Unit 4**, clay-rich mud with abundant rocks, sand patches and mottled features, variable changes in colour and magnetic susceptibility; there are numerous gas expansion and distinct rusty layers

St. Pierre Slope, SW Grand Banks 2015MSM Gravity Core 0002

TD 902 cm 44.809583 N -55.601067 W Water depth 688 m

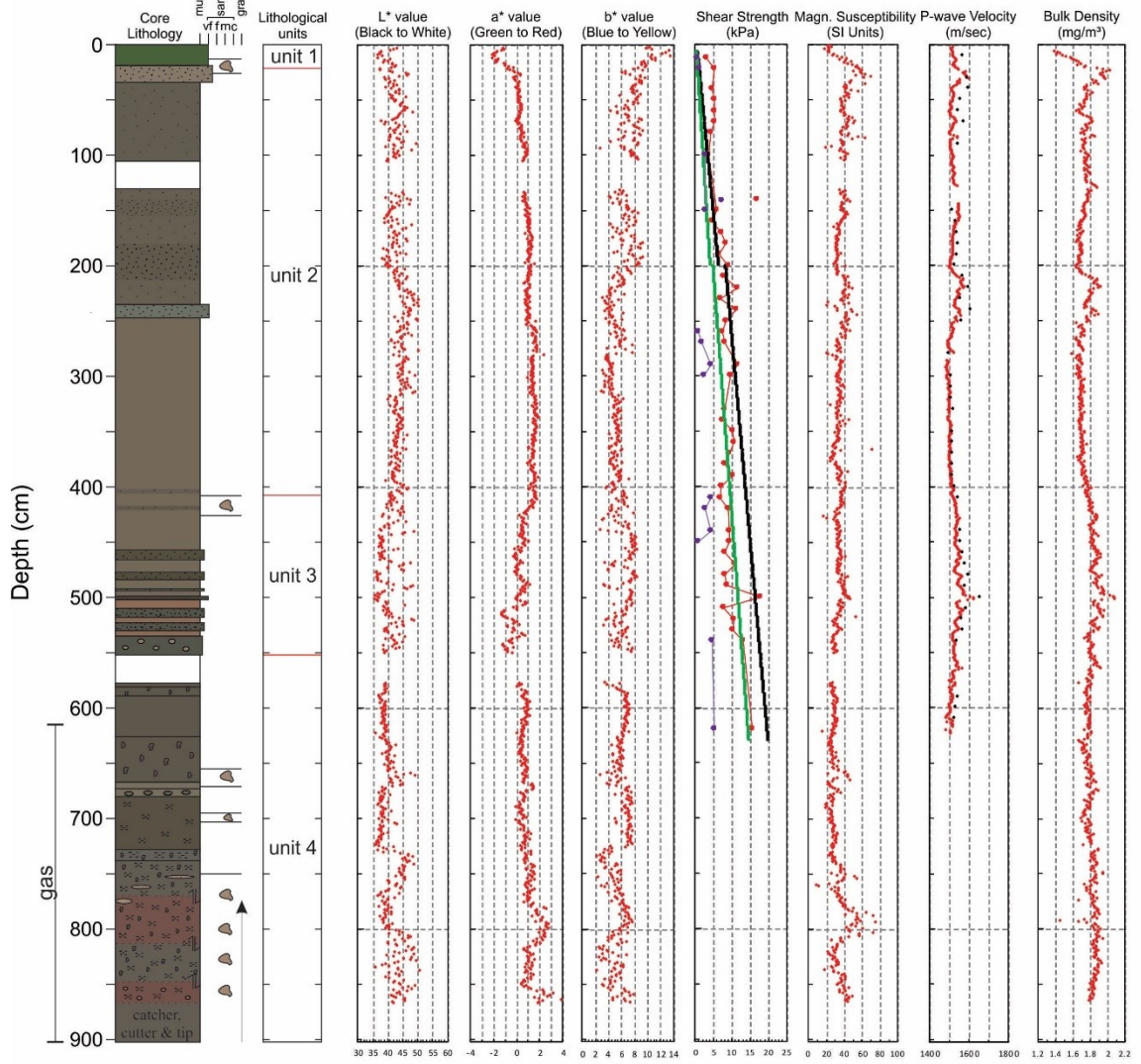


Fig. 4.3: Lithology and physical property measurements for core 2015MSM_0002GC.

St. Pierre Slope, SW Grand Banks MSM47 Gravity Core 24-01

TD 770 cm 44.7617 N -55.6903 W Water depth 825 m

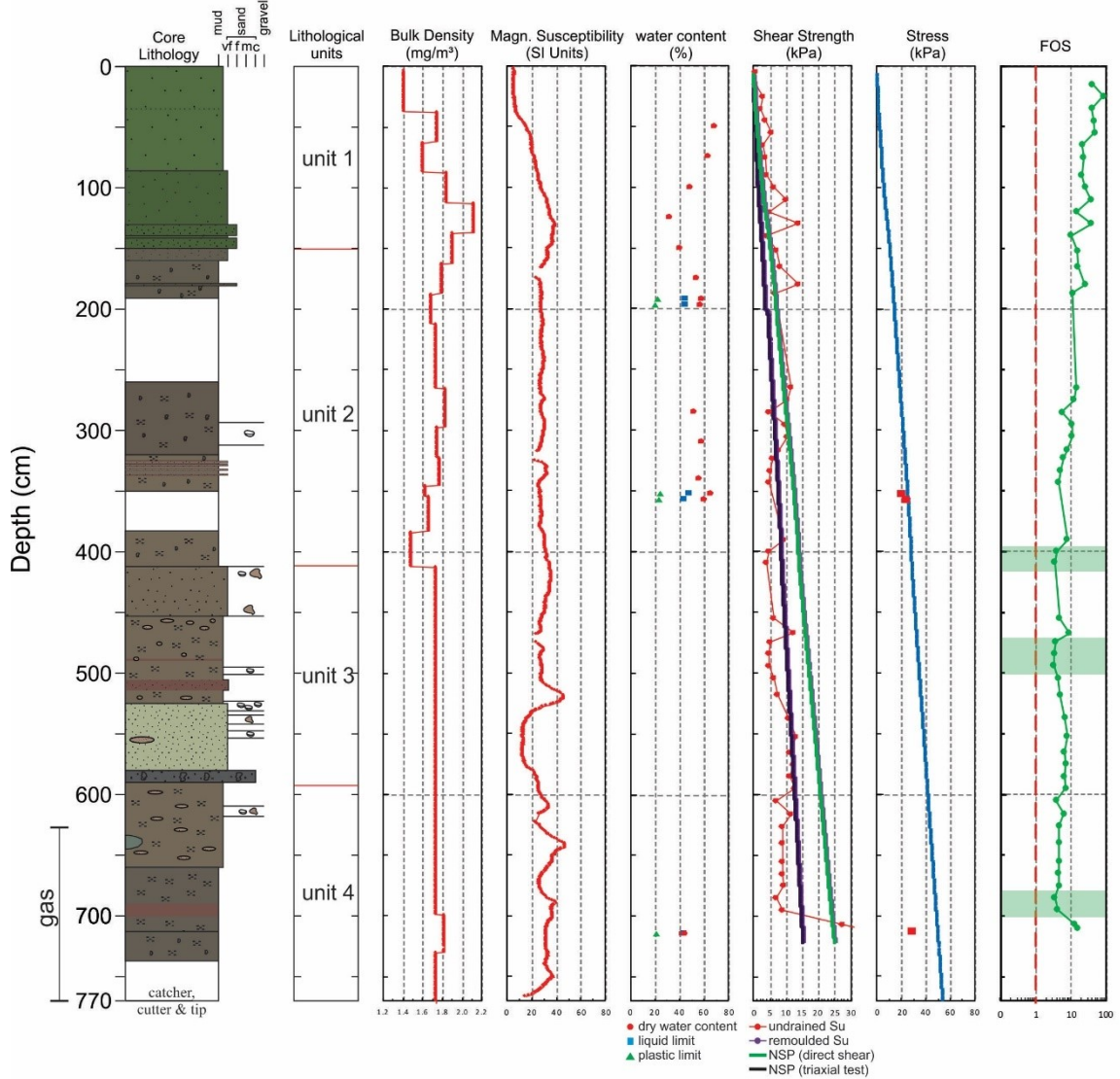


Fig. 4.4: Lithology and geotechnical properties measured from physical and geomechanical testing on sediment core MSM47-24-01 and its FOS. Minimum FOS observed within the core are highlighted as transparent green boxes.

St. Pierre Slope, SW Grand Banks 99-036 Piston Core 003

TD 1380 cm 44.744 N -55.7356 W Water depth 899 m

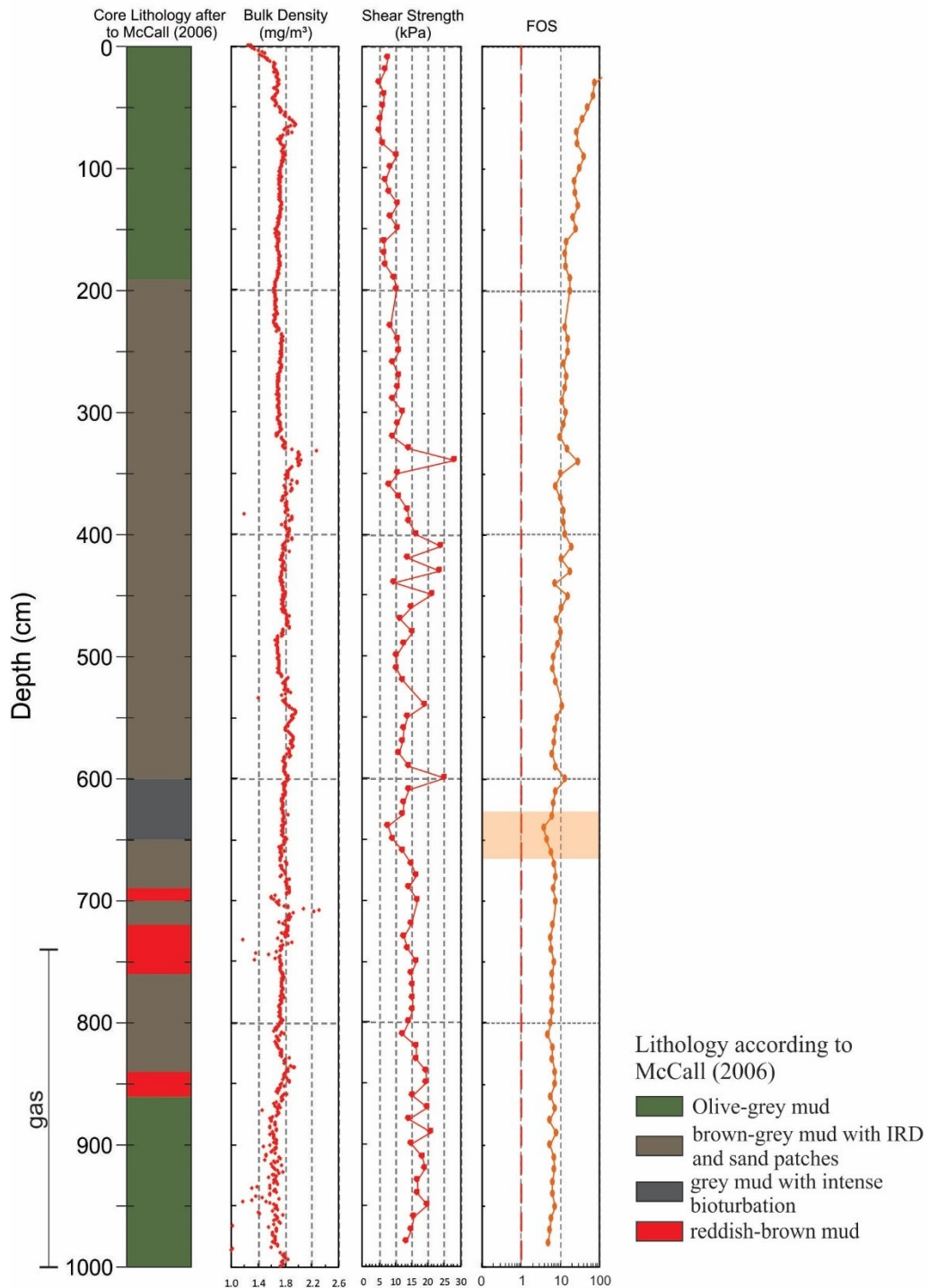


Fig. 4.5: Lithology and geotechnical properties of sediment core 99036-003pc retrieved from the NRCan database. The lithological description is published in McCall (2006). The FOS values were calculated as part of this study. The minimum FOS at ~640 cm is highlighted.

4.4.2 Geomechanical properties

Geomechanic test results for the two cores are summarized in Table 4.2. The measured P'_c for the samples taken from 350 to 553 cm core depth were in the range from 19 to 33 kPa using the Cassagrande (1936), Silva (1970) and Work (Becker et al., 1987) methods (appendix A2.3.3; Figs. A2.15-A2.17). The resultant OCR values of 0.76 to 0.89 indicate that these sediments are normally consolidated (NC) to slightly underconsolidated (UC) and have not fully adjusted to present day effective overburden stress (Figs. 4.4 & 4.6; Table 4.2). A P'_c of 27 kPa was measured on a sample from ~710 cm core depth, which corresponds to an OCR value of 0.53 indicating UC (Figs. 4.4 & A2.18; Table 4.2). Hydraulic conductivity (k) at the pre-consolidation stress was determined to be 1.34 to 5.35 $\times 10^{-7}$ cm s^{-1} , which is expected for clay rich muddy sediments (Table 4.2). The compression index (C_c) is ~0.52 in the upper 350 cm and 0.33 to 0.37 in the deeper part (>500 cm) of the sediment cores (Table 4.2). The parameters are similar to the behaviour of the Boston blue clay (Braja, 2010).

Table 4.2: Summary of the most important sediment properties derived from geomechanical testing. For more information see appendices A2.3.3 and A2.3.4.

Consolidation

| core | depth | C_c | C_r | C_{ce} | k (cm s^{-1}) | P'_c (kPa) | P'_{vo} (kPa) | OCR |
|----------------|--------------|-------|-------|----------|----------------------------|--------------|-----------------|-------|
| 2015MSM_0002GC | 553-555.5 cm | 0.37 | 0.06 | 0.17 | 1.54E-07 | 33 | 42.75 | 0.76 |
| MSM47-24-01 | 351-353 cm | 0.55 | 0.075 | 0.199 | 4.63E-07 | 19 | 25.20 | 0.87 |
| MSM47-24-01 | 357-358.5 cm | 0.52 | 0.064 | 0.204 | 5.35E-07 | 23 | 25.92 | 0.89 |
| MSM47-24-01 | 713-714.5 cm | 0.33 | 0.065 | 0.147 | 2.03E-07 | 27 | 51.01 | 0.53 |

Triaxial CIU

| core | depth | Φ' | c' | S_u/P'_v | $S_u/P'_{v,corr}$ | A_f | v_{30} (m s^{-1}) |
|----------------|----------------|---------|------|------------|-------------------|-------|--------------------------------|
| 2015MSM_0002GC | 116.5-128.5 cm | 26.79 | 0.00 | 0.32 | 0.25 | 0.18 | 152 |
| 2015MSM_0002GC | 563-575 cm | 27.89 | 2.71 | 0.38 | 0.30 | 0.47 | 152 |

Single-direct shear

| core | depth | Φ' | c' | S_u/P'_v |
|-------------|------------|---------|-------|------------|
| MSM47-24-01 | 190-204 cm | 30.36 | 22.11 | 0.62 |

The failure envelope defined from the triaxial test results on samples of core 2015MSM_0002GC showed no cohesion (c') in 116 cm core depth and a c' of 2.7 kPa in

563 cm core depth with friction angles (ϕ') of 26.8 and 27.9° that is typical for silts (Table 4.2; appendix A2.3.4, Figs. A2.19 & A2.20) (Braja, 2010). Skempton's pore pressure parameter at failure (A_f) of 0.18 indicates over consolidation (OC) at 116 cm, while an A_f value of 0.47 at 563 cm indicates normal consolidation (NC) (Table 4.2) (Braja, 2010). A normalized strength ratio (S_u/P'_v) was determined to be 0.25 to 0.30 for the sediment and correlates with Skempton's NC range of 0.2 to 0.5 (Table 4.2) (Skempton, 1970). The failure envelope defined from the single-direct shear test on samples from core MSM47-24-01 provided a c' value of 22 kPa indicating OC (Table 4.2) (Braja, 2010). The friction angle (ϕ') of 30.36° is within a typical range for silts (Braja, 2010). The normalized strength ratio (S_u/P'_v) is 0.62 (Table 4.2).

Shear strength measured from cores are compared to shear strength calculated from the NSP methodology and Mohr-Coulomb relationship. The NSP methodology using results from the triaxial test (NSP_{triax}) indicates apparent overconsolidation (AOC) for the upper 350 cm, NC with UC between 350 and 600 cm core depth and UC below 600 cm (Figs. 4.4 & 4.6). The Mohr-Coulomb relationship indicates that sediments are AOC above 100 cm, NC between 100 and 350 cm and UC in the lower part of the core (Fig. 4.6). NSP results from the direct shear test (NSP_{ds}) indicate AOC for the upper 300 cm and UC below 300 cm (Fig. 4.4).

St. Pierre Slope, SW Grand Banks 2015MSM Gravity Core 0002

TD 902 cm 44.809583 N -55.601067 W Water depth 688 m

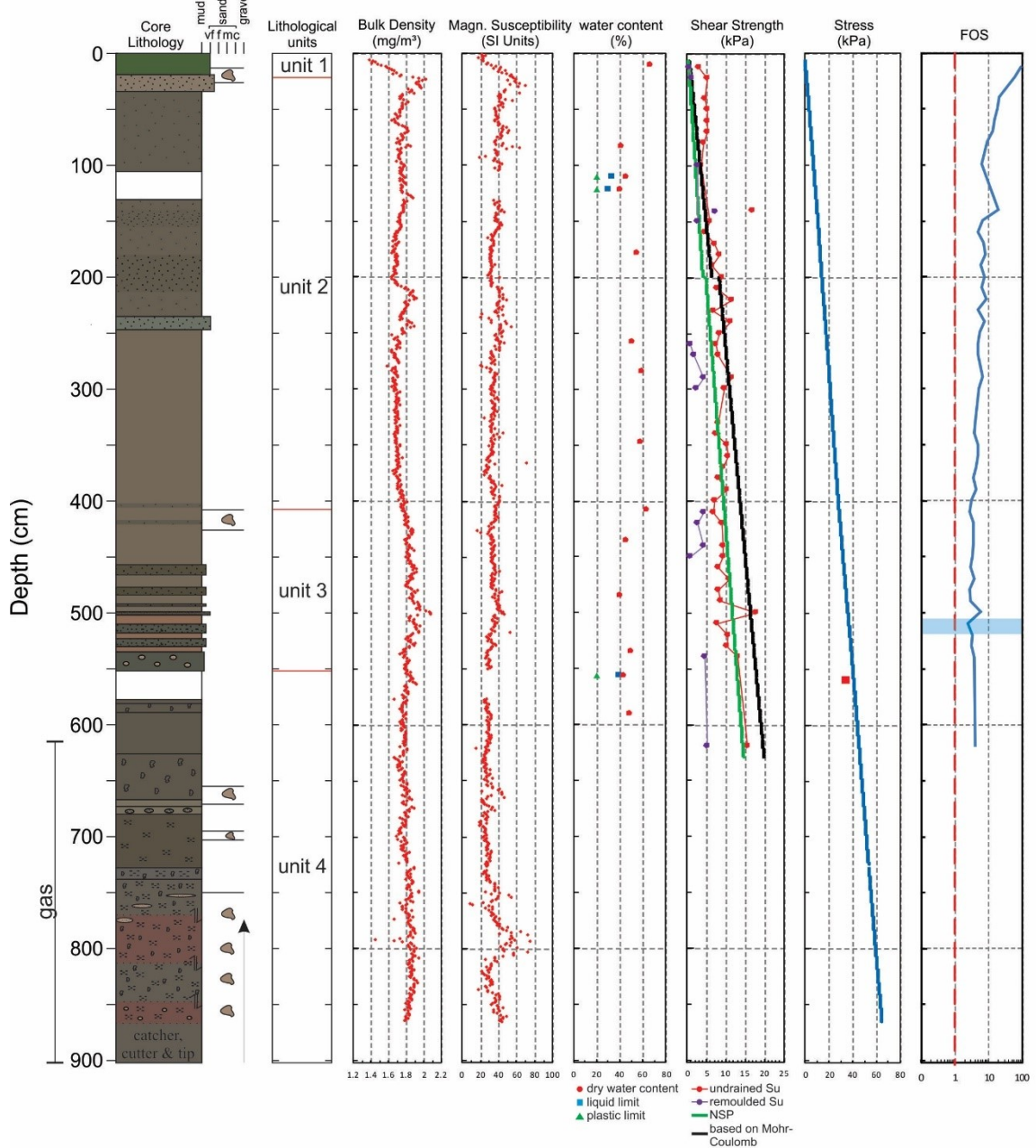


Fig. 4.6: A plot of geotechnical properties measured from physical and geomechanical testing on the sediment core and its FOS. Minimum FOS observed within the core is highlighted as transparent blue box.

4.4.3 Infinite Slope Stability Analysis

Slope stability evaluation is based on four different FOS calculations for undrained static and pseudo-static conditions of cores and sediment slabs (2-550 m) using equations (8) and (9) respectively (Table 4.3). The analysis was performed for different slope angles and earthquake induced PGA down to 550 m sub-bottom depth, which is the depth of observed décollements at St. Pierre Slope (Table 4.3) (see Chapter 3).

Table 4.3: Summary of parameters used in the four different scenarios and resultant critical FOS.

| Slope stability analysis | | Parameters used | | | | Results critical FOS |
|--------------------------|------------|--------------------------------------|---------|-------------------------------|---------------------|-------------------------|
| | | slope angle (β) | PGA | undrained shear strength | effective stress | |
| static cores | | 0-50° | - | S_u (vane shear, fall cone) | P'_{vo} (MSCL) | 8.1° |
| static slabs | SSA-case 1 | 0-50° | - | $S_{u\ trend}$ | $P'_{vo\ trend}$ | 10.6° |
| | SSA-case 2 | 0-50° | - | $S_{u\ trend}$ | $P'_{vo\ porosity}$ | 6.8° |
| | SSA-case 3 | 0-50° | - | $S_{u\ NSP}$ | $P'_{vo\ porosity}$ | >15.3 |
| pseudo-static cores | | β at individual core locations | 0 - 1 g | S_u (vane shear, fall cone) | P'_{vo} (MSCL) | >0.09 g |
| pseudo-static slabs | PGA-case 1 | 2° | 0 - 1 g | $S_{u\ trend}$ | $P'_{vo\ trend}$ | 0.15 g |
| | PGA-case 2 | 2° | 0 - 1 g | $S_{u\ trend}$ | $P'_{vo\ porosity}$ | 0.08 g |
| | PGA-case 3 | 2° | 0 - 1 g | $S_{u\ NSP}$ | $P'_{vo\ porosity}$ | >0.22 g |

Slope stability analysis over a range of sediment slabs used average $S_{u\ trend}$ and $P'_{vo\ trend}$ values derived from all core data as well as $S_{u\ NSP}$ calculated from triaxial test results and $P'_{vo\ porosity}$ that was calculated after Kominz et al. (2011) (Table 4.3). The $S_{u\ trend}$ derived from different cores on St. Pierre Slope match well (Fig. 4.7). $S_{u\ NSP}$ derived from triaxial test results is at least 1.7 times the average shear strength from cores (Fig. 4.7).

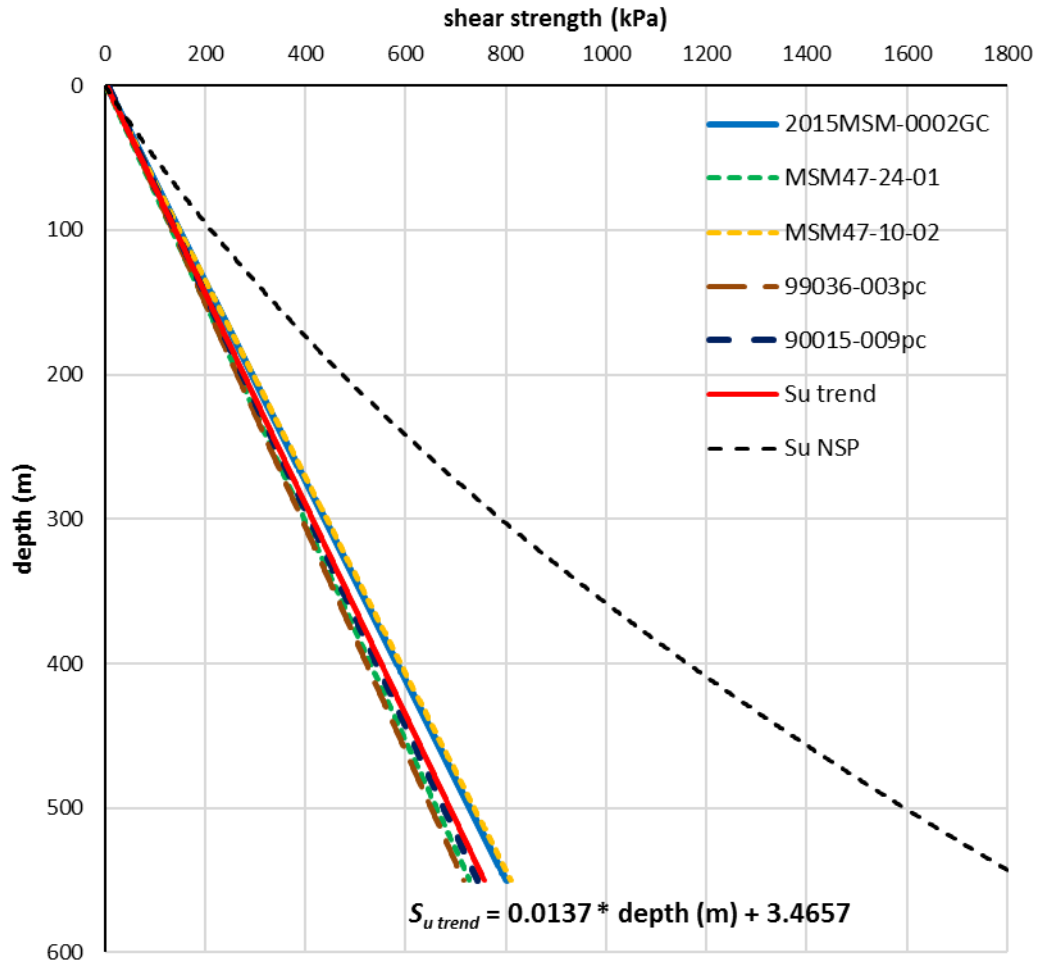


Fig. 4.7: A comparison of shear strength trends from each single core and a compiled trend (red line) from five undisturbed cores. Significant outliers were removed before calculation of the trends.

Pseudo-static infinite slope stability analysis evaluates the FOS in response to earthquake loading. A critical PGA is given for a $FOS < 1$. The PGA values were converted to magnitude and distance using AB2006 and CB2008. Both equations use the shear wave velocity at 30 m sub-bottom depth (v_{30}) that was measured during triaxial testing ($v_{30} = 152 \text{ m s}^{-1}$), but there are some differences in results depending on the equation (appendix A2.2.1, A2.2.2 & A2.3.5). For example, the 1929 earthquake, a $M_w 7.2$ earthquake at ~ 26 km epicentre distance from the core sites corresponds to a PGA of ~ 0.20 g using AB2006 and 0.13 g using CB2008 (Figs. 4.8 & 4.9).

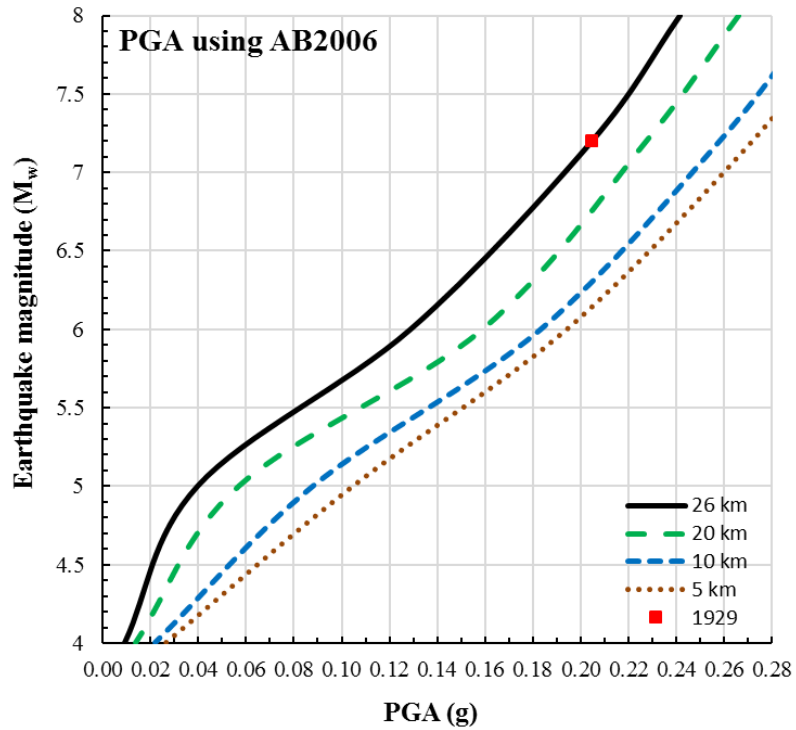


Fig. 4.8: Peak-ground acceleration (PGA) at the St. Pierre Slope for different earthquake magnitudes (M_w) and distances using an equation from Atkinson and Boore (2006) (AB2006). The red square shows the 1929 earthquake (M_w 7.2, 26 km).

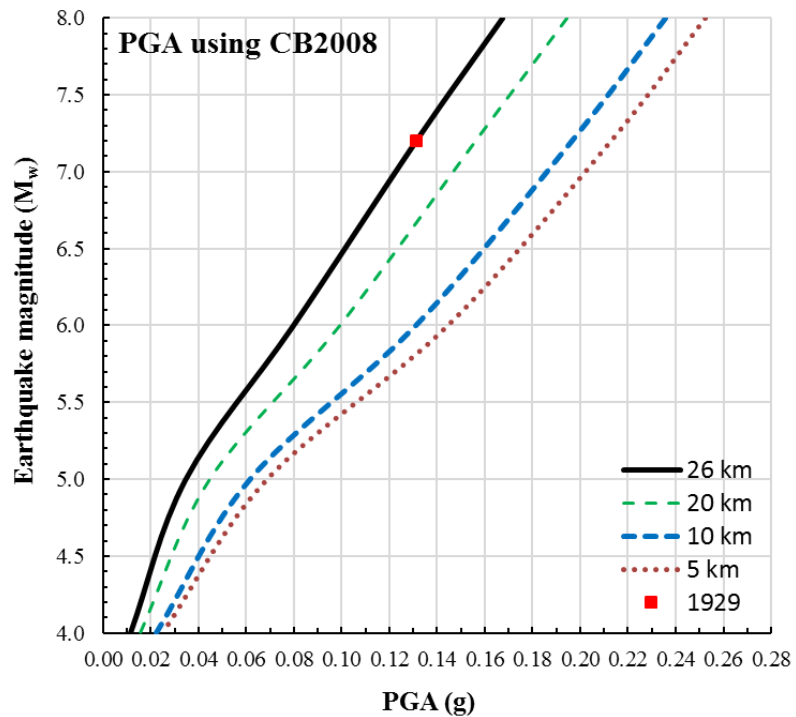


Fig. 4.9: Peak-ground acceleration (PGA) at the St. Pierre Slope for different earthquake magnitudes (M_w) and distances using an equation from Campbell and Bozorgnia (2008) (CB2008). The red square shows the 1929 earthquake (M_w 7.2, 26 km).

1) Static FOS for cores

A static slope stability analysis on core data was calculated for the core depth and over a range of slope angles (Fig. 4.10). All core locations show a FOS>2 (Figs. 4.4-4.6, 4.10). Minimum FOS are found at a depth of 510 cm in core 2015MSM_0002GC, 412, 494 and 680 cm in MSM47-24-1 and 640 cm in 99036-003pc. These minimum FOS align with lithological boundaries of the sediment cores (Figs. 4.4-4.6). The critical slope angle is 8.1° (Fig. 4.10).

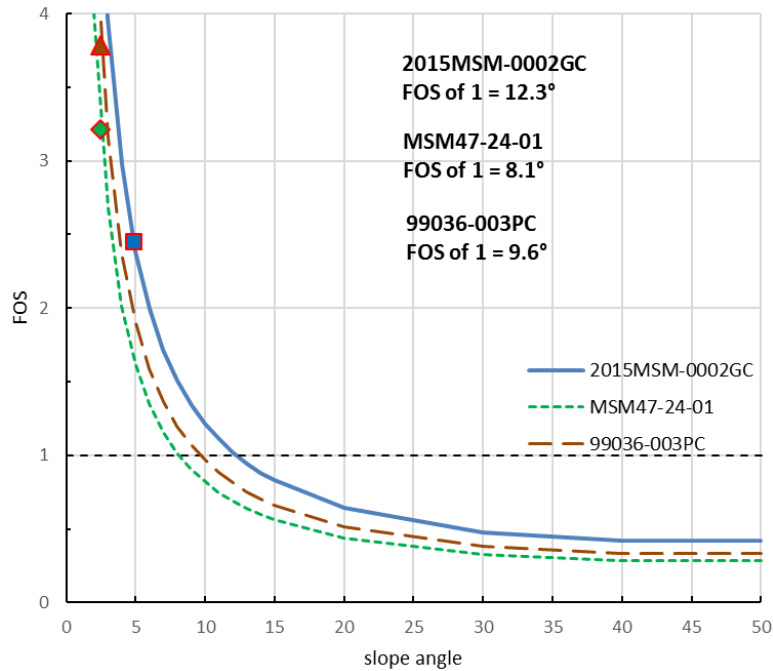


Fig. 4.10: Results of infinite slope stability analysis over a range of slope angles for sediment cores 2015MSM_0002GC, MSM47-24-01 and 99036-003pc. The marker on each line indicates present day slope angle in the study area of 2.5-4.9°, that corresponds to a FOS>1.

2) Static FOS for slab thicknesses

FOS calculated for a range of sediment slabs (2-550 m; Fig. 4.11) provides a critical slope angle for a 550 m-thick slab of 10.6° using $S_{u\ trend}$ and $P'_{vo\ trend}$ (SSA-case 1) and 6.8° using $S_{u\ trend}$ and $P'_{vo\ porosity}$ (SSA-case 2) (Fig. 4.11). For SSA-case 1 and 2 the 550 m-thick block of sediment is shown to be more susceptible to unstable slope conditions than thinner (2-250 m-thick) sediment slabs (Fig. 4.11). In contrast, $S_{u\ NSP}$ and $P'_{vo\ porosity}$ (SSA-case 3) shows the lowest stability for the 2 m-

thick slab with a critical slope angle of $\sim 15^\circ$. All other slabs (>5 m) of case 3 show the same stability trend.

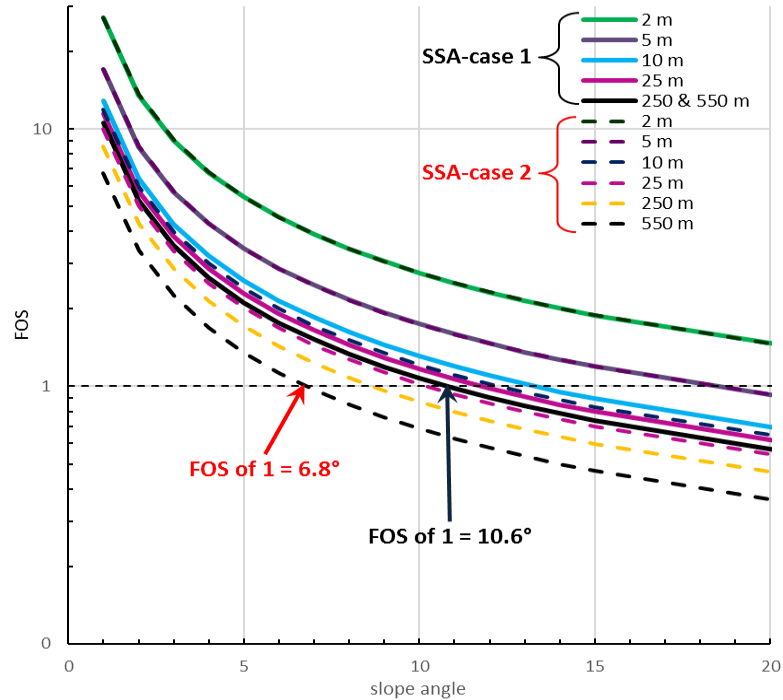


Fig. 4.11: Results of a slope stability analysis over a range of sediment failure thicknesses (2-550 m). Solid lines represent results using extrapolated trends in shear strength and effective overburden (SSA-case 1). Dashed lines represent results using the Kominz et al. (2011) equation to estimate sediment bulk density (SSA-case 2).

3) Pseudo-static FOS for cores

The FOS in response to different seismic loads at different core sites indicates a FOS of 1 for PGA's >0.09 g (Fig. 4.12). At the core sites of 2015MSM_0002GC and 99036-003pc, however, a PGA of 0.125 g is needed to reach a FOS of 1 (Fig. 4.12). Results from AB2006 and CB2008 conversions are used to estimate corresponding earthquake magnitudes and epicentre distance (Figs. 4.8 & 4.9). A PGA of 0.09 g corresponds to a M_w 4.8 earthquake in 5 km epicentral distance and M_w 5.3 in 20 km distance using AB2006 or an earthquake of at least M_w 5.3 in 5-10 km epicentral distance and M_w 5.8 in 20 km distance using CB2008 (Figs. 4.8 & 4.9, Table 4.4).

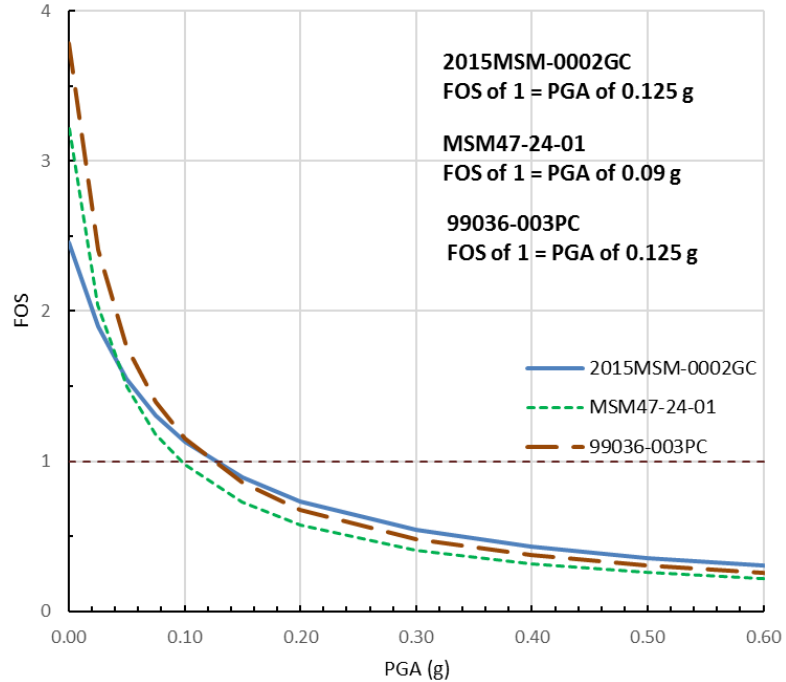


Fig. 4.12: Slope stability analysis over a range of PGA's. The critical PGA in the study area under present day and pseudo-static conditions is 0.09-0.125 g.

Table 4.4: Summary of results from pseudo-static infinite slope stability analysis showing the critical PGA (g) corresponding to a FOS of 1 and conversion to magnitude and distance using AB2006 and CB2008.

| PGA case | critical PGA (g) | minimum earthquake magnitude (M_w) in 5 km distance from St. Pierre Slope using | | influence of the 1929 earthquake (M_w 7.2, 26 km) | | |
|-------------------|------------------|---|-----------|--|------------------------|-----|
| | | AB2006 | CB2008 | AB2006 1929 was 0.2 g | CB2008 1929 was 0.13 g | |
| cores | 0.09 | M_w 4.8 | M_w 5.3 | yes | yes | |
| 550 m-thick slab | case 1 | 0.15 | M_w 5.5 | M_w 6.1 | yes | no |
| | case 2 | 0.09 | M_w 4.8 | M_w 5.3 | yes | yes |
| | case 3 | 0.27 | M_w 7.2 | $M_w > 7.2$ | no | no |
| 250 m-thick slabs | case 1 | 0.15 | M_w 5.5 | M_w 6.1 | yes | no |
| | case 2 | 0.13 | M_w 5.3 | M_w 5.8 | yes | yes |
| | case 3 | 0.27 | M_w 7.2 | $M_w > 7.2$ | no | no |
| 25 m-thick slab | case 1 | 0.16 | M_w 5.6 | M_w 6.1 | yes | no |
| | case 2 | 0.20 | M_w 6.1 | M_w 6.9 | yes | no |
| | case 3 | 0.27 | M_w 7.2 | $M_w > 7.2$ | no | no |

4) Pseudo-static FOS for slab thicknesses

The pseudo-static infinite slope stability analysis over a range of sediment thicknesses (2-550 m) indicates a critical FOS for a 550 m-thick slab at a PGA of ~0.15 g using PGA-case 1, 0.09 g using PGA-case 2 and 0.27 g using PGA-case 3 (Fig. 4.13). Compared to case 1 and 2, a 2 m-thick sediment slab is shown to be more sensitive (PGA 0.22 g) than thicker (5-550 m) slabs (Fig. 4.13). PGA-case 1 shows similar stability trends for sediment slabs that are >25 m thick (Fig. 4.13). PGA-case 2 shows differences in the stability trends of each slab. PGA-case 3 shows the same trend for all slabs >5 m (Fig. 4.13).

The minimum earthquake and epicentre needed to generate the critical PGA and the correspondence to a re-occurrence of the 1929 earthquake are shown in Table 4.4. For example, a PGA of 0.15 g corresponds to a M_w 5.5 at 5 km distance from the epicentre or M_w 5.9 at 20 km using AB2006 (Fig. 4.8, Table 4.4). In comparison, a PGA of 0.15 g corresponds to a M_w 6.1 at 5 km or M_w 7 at 20 km distance using CB2008 (Fig. 4.9). The earthquake magnitude and/or epicenter distance increases respectively with the critical PGA (Figs. 4.8 & 4.9, Table 4.4). AB2006 provides a higher PGA for smaller earthquakes compared to CB2008 (Figs. 4.8 & 4.9, Table 4.4).

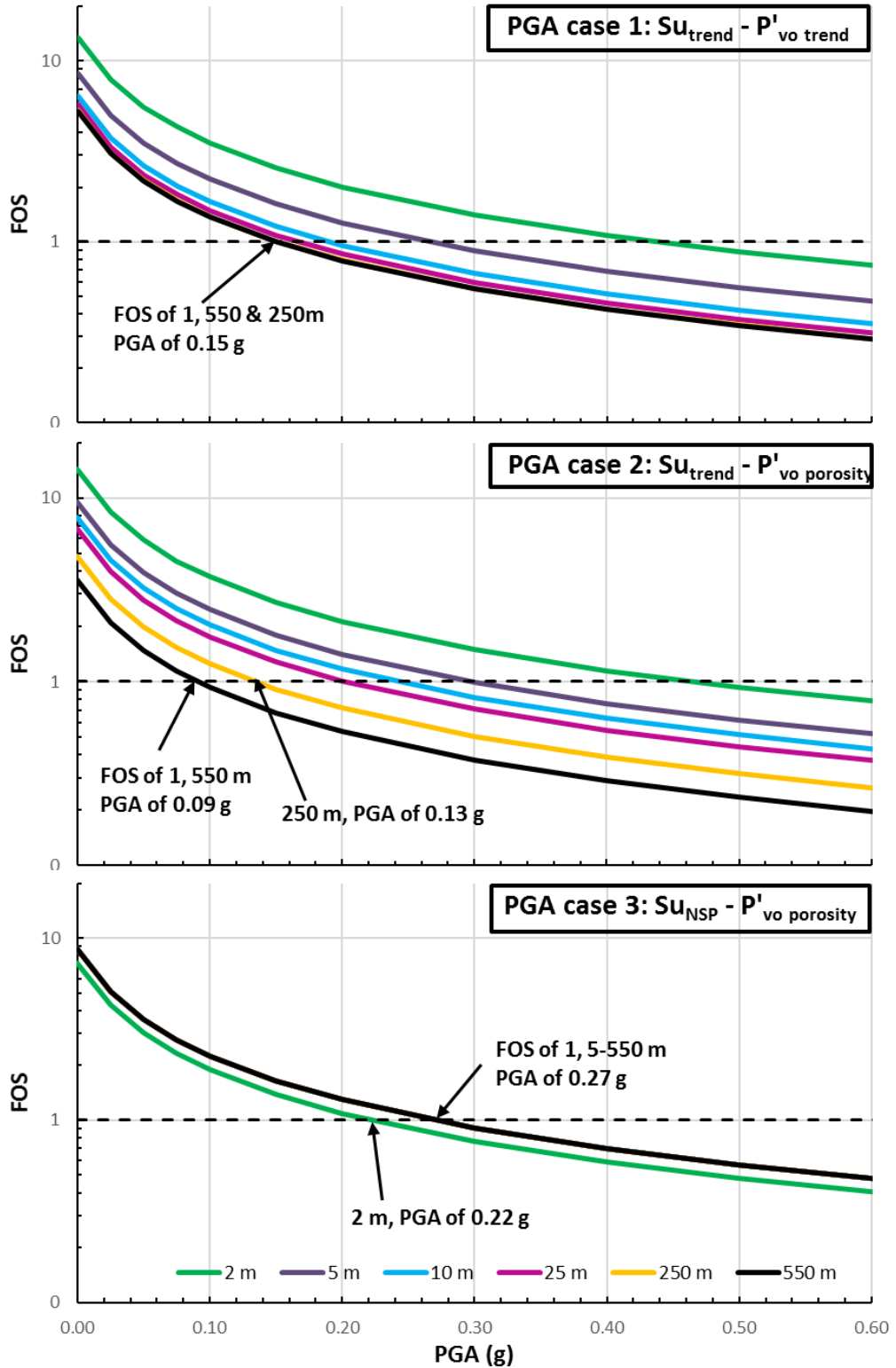


Fig. 4.13: Results of a stability analysis for different PGA's over a range of sediment failure thicknesses (2-550 m). From top to bottom: Results of slope stability analysis using PGA-case 1 ($S_{u\text{trend}}, P'_{vo.trend}$), PGA-case 2 ($S_{u\text{trend}}, P'_{vo.porosity}$) and PGA-case 3 ($S_{u\text{NSP}}, P'_{vo.porosity}$) (Table 4.3).

4.5 DISCUSSION

4.5.1 Consolidation status

Physical property and geomechanical testing indicates general normal consolidation (NC) to slight underconsolidation (UC) of the upper 9 m of sediment (Figs. 4.4 & 4.6). Apparent over-consolidation (AOC), however, is indicated for the upper 300 cm by the normalized shear strength ratio (S_u/P'_{vo}). The Mohr Coulomb relationship indicates slight UC of the sediment deeper than 300 cm, while S_u/P'_{vo} indicates NC (Figs. 4.4 & 4.6).

4.5.1.1 APPARENT OVERCONSOLIDATION

There are three plausible explanations for the AOC in the upper 300 cm of the sediment column (**unit 1 & 2**):

1) Core sampling:

Loss and distortion of the upper sediment column is commonly observed in gravity and piston cores (Morton & White, 1997; Skinner & McCave, 2003). Holocene sediments on the upper St. Pierre Slope are typically 1-3 m thick (Piper et al., 1999). The olive-grey hemipelagic mud of **unit 1** that is mid to late Holocene in age is only 19 cm-thick in core 2015MSM_0002GC and 150 cm in core MSM47-24-01 indicating that part of the Holocene sediments may be missing (Figs. 4.4 & 4.6) (*cf.*, Mosher et al., 1994; Piper & Skene, 1998). As a result, the mudline of the sediment is difficult to locate and P'_{vo} might be underestimated (*cf.*, Marsters, 1986).

2) Bioturbation:

Residuals organic material in the topmost sediment material can leave the sediment in a state of AOC (Marsters, 1986; Poulos, 1988; Christian et al., 1991). The reason is that organic bonding can maintain a relatively high void ratio at low stresses depending on the organic decomposition state (Christian et al., 1991). Bioturbation and mottled features are common within the upper 100 to 250 cm of the cores (**unit 1 & 2**) (Figs. 4.4 & 4.6). Bioturbation may also lead to AOC through increased binding by organic secretions from the animals that consume and excrete the

sediments after primary deposition. This organic material eventually decomposes, thus breaking down particle binding that leads to a more normal consolidation state with time (Christian et al., 1991).

3) Erosion or mass failure:

Removal of overlying sediment leaves strata with a higher consolidation state at the surface or near surface (Skempton, 1970; Christian et al., 1991). The upper St. Pierre Slope area did not fail as a consequence of the 1929 earthquake (Piper et al., 1999, Mosher & Piper, 2007). Erosion due to currents and smaller failures, however, cannot be excluded. Core 2015MSM-0002GC for example was collected from one of the tributary systems of Grand Banks Valley to the east of St. Pierre Slope where bottom currents are likely (Fig. 4.1).

4.5.1.2 NORMAL- TO UNDERCONSOLIDATION

Sediments below 300 cm are normal- to slightly underconsolidated (**unit 2 to 4**) (Figs. 4.4-4.6). Identification of UC is an important factor when assessing present day slope stability, since it indicates the presence of excess pore pressure (Poulos, 1988). Excess pore pressure results in a reduction of effective stress and, therefore, sediment shear strength (S_u) (Poulos, 1988). Knowing the factors that cause UC, therefore, enables a better understanding of possible preconditioning and trigger mechanisms. On St. Pierre Slope the observed slight UC is most likely the result of 1) high post-glacial sedimentation rates, 2) loading by deposition of mass transport deposits (MTD's) on top of unfailed sediment, and 3) the presence of gas (Poulos, 1988; Marsters, 1986).

- 1) High sedimentation rates occurred during the late Pleistocene, as a consequence of high sediment-laden meltwater discharge during deglaciation (Fig. 4.1) (Skene & Piper, 2003; Shaw et al., 2006; Ledger-Piercy & Piper, 2007). Rapid deposition of the sediment prevented dissipation of pore water that resulted in an increase in excess pore pressure with burial as sediment load is increased (Morgenstern, 1967; Poulos, 1988). The cores contained a high abundance of ice rafted debris (IRD) and sand layers that are indicative of deglaciation and glacial meltwater events. These

episodes correspond to higher sedimentation rates (**unit 3 & 4**) (Piper and Skene, 1998; Skene & Piper, 2003). Sedimentation rates are estimated as being between $\sim 0.4 \text{ m ka}^{-1}$ and $\sim 2.6 \text{ m ka}^{-1}$ during the last glacial maximum (LGM) (Skene & Piper, 2003; McCall, 2006; see Chapter 3).

- 2) Similar to high-sedimentation rates, mass failure deposition may have led to UC by rapid loading of underlying strata, and generated an increase in pore pressure (Morgenstern, 1967; Poulos, 1988). Evidence of MTD's in the cores include tilted laminae, lens-shaped units, and clasts of distinct lithologies (**unit 3 & 4**).
- 3) In situ gas would have caused an increase in pore pressure and overall reduction of effective stress (Morgenstern, 1967, Sultan et al., 2004). Cracks in core sediments caused by expansion of free gas was observed in both cores in this study (**unit 4**) and noted from previous studies (Figs. 4.4-4.6) (Marsters, 1986; Mayer et al., 1988; Piper et al., 1988; 1999). Gas expansion occurs as cores are recovered from depth where they are under hydrostatic pressure, to the surface (Poulos, 1988).

4.5.2 Present day slope stability

4.5.2.1 *STATIC SLOPE STABILITY*

Infinite static slope stability analysis indicates a $FOS > 1$ for present day conditions. The FOS describes a 50% probability of failure with a FOS of 1 (MacKillop et al., 2019). It is therefore interpreted that under static and present-day conditions, the sediments in the study area are stable ($FOS > 1$). Slope stability analysis based on measured vane shear strengths indicate a critical slope angle of 8.1° to reach a FOS of 1 (Fig. 4.10; Table 4.3). Stability analysis covering a range of hypothetical failed sediment thicknesses also indicate present-day stable conditions (Fig. 4.11) (Piper et al., 1988; 1999; McCall, 2006, Schulten et al., 2019; see Chapter 3). The minimum critical slope angle calculated for static failure at all depths assessed is 6.8° (Fig. 4.11, Table 3). A 550 m-thick sediment slab shows the lowest stability in SSA-case 1 and 2 due to the higher total effective overburden stress in comparison to the shear strength (Fig. 4.11). The present-day slope angle at St. Pierre Slope varies from 2° to 5° , as calculated from multibeam echosounder data (Piper et al., 1999;

Mosher & Piper, 2007). At these angles, gravitational force alone is not capable of causing instability in the upper slope area. Other factors that generate excess pore pressure (reduction of effective stress) are required to facilitate sediment mass failure. In the St. Pierre Slope region, these factors could include earthquakes, rapid sedimentation, and free gas from conventional hydrocarbon sources or gas hydrate dissociation.

4.5.2.2 PSEUDO-STATIC SLOPE STABILITY

Pseudo-static infinite slope stability analysis was conducted for core sites and a variety of hypothetical slab thicknesses, to a maximum of 550 m. Through the various techniques used, the minimum conditions for failure (i.e., FOS of 1) requires a critical PGA of 0.09 g (i.e. PGA-case 2, cores). Using the AB2006 method for PGA estimation 0.09 g is reached with a $M_w > 4.8$ earthquake at an epicentre distance of < 5 km (Table 4.4). The CB2008 method of PGA estimation requires ~ 1.5 times higher earthquake magnitudes compared to the AB2006 method (Table 4.4). The same is true for PGA-case 1 and 3 versus PGA-case 2 for slope stability estimation (Table 4.3 & 4.4). It is argued that PGA-case 3 might be a more realistic choice to evaluate slope stability in response to earthquake loading. PGA-case 3 uses normalized shear strengths ($S_{u\ NSP}$) and considers sediment diagenesis with depth ($P'_{vo\ porosity}$) (Table 4.3). By contrast, PGA-case 1 assumes a uniform distribution of the sediment material from the cores down to 550 mbsf but neglects diagenesis (Table 4.3). PGA-case 2 considers a decrease in the sediment porosity using $P'_{vo\ porosity}$ and therefore indirectly considers sediment diagenesis but neglects a corresponding increase in shear strength using $S_{u\ trend}$ (equation 4) (Table 4.3) (Skempton, 1954; Christian et al., 1991). Using results from PGA-case 3 and CB2008 to convert the critical PGA for a 550 m-thick slab shows a 50% likelihood of sediment failure (FOS of 1) for earthquakes $M_w > 7.2$ at 5 km epicentre distance from the slope area (Table 4.4).

Earthquake monitoring over the past 30 years indicates that most earthquakes in the region with M_w 2 to 4 are clustered around a zone southward of the Laurentian Channel toward Sohm Abyssal Plain (Fig. 4.1) (Mazzotti, 2007; Earthquakes Canada, 2018). Some of these earthquakes with a M_w 3 to 4 occurred less than 20 km away from the core sites, but no

earthquakes with a $M_w > 4$ were recorded less than 5 km from the St. Pierre Slope (Earthquakes Canada, 2018).

The upper slope, therefore, is interpreted to be stable under present-day and pseudo-static conditions. Earthquake loading from a $M_w < 4.8$ at 5 km epicentre distance from the slope is not sufficient to cause slope failure. It is concluded that pre-conditioning factors, such as excess pore pressure, are needed to facilitate slope instability (Piper et al., 1988; 1999; Schulten et al., 2019). A repetition of the 1929 earthquake could cause slope failure of a 550 m-thick slab, but only if there is an additional factor that causes underconsolidation of the sediment as indicated by case 1 and 2 (Table 4.4).

4.5.2.3 GEOMECHANICAL WEAK LAYERS EVIDENT IN CORES

The FOS minima evident from static slope stability analysis are interpreted as weak layers (Figs. 4.4-4.6). These weak layers correspond to lithological changes between sandier or siltier layers and clay-rich mud with shear strength contrasts between these layers (Figs. 4.4-4.6) (*c.f.*, Sultan et al., 2004; Locat et al., 2014). Some of the interbedded layers are only 5 to 10 cm thick and often rusty coloured (Figs. 4.4 & 4.5). Clay-rich mud is bonded either to the top or at the bottom by the siltier to sandier mud that was likely deposited as debris flows or turbidity currents, as evident through the presence of tilted laminae and high abundance of rocks and shell fragments (**unit 3**) (Figs. 4.4-4.6).

Previous studies showed that the depth of weak layers and core sections affected by gas expansion cracks (**unit 4**) correspond to the Q99 reflection that often forms the base of shallow (~10 m-high) sediment failures along a nearby escarpment (Fig. 4.2) (McCall, 2006; Schulten et al., 2019). These surficial failures are interpreted as a result of the 1929 earthquake (Piper et al., 1988; 1999; McCall, 2006; Schulten et al., 2019). The Q99 reflection is dated to ~14.4 ka BP, which corresponds to the end of the LGM when sedimentation rates changed from ~2.6 m ka⁻¹ to 0.12 m ka⁻¹ (Skene & Piper, 2003; McCall, 2006; see Chapter 3). High sedimentation rates are believed to have caused UC within the sediment package underneath Q99 (*c.f.*, Sultan et al., 2004). The fact that the core section with gas expansion cracks also correspond with this failure surface indicates potential gas

dissociation as response to external forces such as earthquakes. An MTD deposit characterised by lens shaped clasts is often present on top of this section indicating that MTD's might act as a potential cap for the underlying free gas (Fig. 4.6).

On the St Pierre Slope, excess pore pressure development probably facilitated slope instability, in addition to gravitational forces and earthquake loading (*cf.*, Sultan et al., 2004; Kvalstad et al., 2005; Flemings et al., 2008). Evidence for this observation is provided through the pseudo-static stability analysis that uses FOS minima calculated from the core data (Fig. 4.12 & 4.13). There are two types of weak layers described by Locat et al. (2014) that may be relevant to sediments described in the cores in this study: 1) inherited weak layers, which are pre-conditioned to fail through excess pore pressure underneath MTD's (Figs. 4.4 & 4.6), and within rapidly deposited sediment packages, and 2) induced weak layers, where earthquake loading can result in excess pore pressure underneath less permeable clay-rich mud as a result of water inflow from underlying coarser sediments (Figs. 4.4-4.6) or through gas dissociation capped off by overlying MTD's (*cf.*, Skempton, 1970; Sultan et al., 2004; Flemings et al., 2008).

4.5.3 Implications for the 1929 event

The 1929 submarine landslide is described as a widespread, translational and retrogressive failure that affected the upper ~25 m of the sediment column (Piper et al., 1988; 1999; McCall, 2006; Mosher & Piper, 2007). Failures along the upper slope between 750 and 1300 m water depth (mwd) are shown to be rather localised and ~10 m-thick, while the majority of ~25 m-thick failures was concentrated in >1700 mwd (Schulten et al., 2019). 10 m-thick localised sediment failures occurred along the upper part of a <100 m-high escarpment in ~750 mwd (Fig. 4.2) (Schulten et al., 2019). This escarpment is described as a fault scarp that is part of a massive slump with up to 100 m of vertical displacement (see Chapter 3). Surficial failures are suggested to be a consequence of displacement of the slump rather than being triggered by the earthquake itself (Schulten et al., 2019; see Chapter 3). The slump is interpreted to be a consequence of the 1929 earthquake with décollements at 250 and 550 mbsf (see Chapter 3).

Results from pseudo-static infinite slope stability analysis indicate that a repetition of the 1929 earthquake could cause instability of a 550 m-thick slab, if there are additional factors involved (case 1 & 2 versus case 3) (Fig. 4.13; Table 4.4). Sediment cores indicate a critical PGA of 0.09 for the upper 5 to 10 m of the sediment column (Fig. 4.12). Without any weak layers this value could be as high as ~ 0.28 g given results from case 1 to 3 (Fig. 4.13), indicating that shallower depths are stable if only ground shaking is considered. Other factors such as weak layers are considered necessary to explain sediment failures (Table 4.4). Characteristics of the décollements and failure surfaces and how these might have contributed to failure are as follows:

1. The 550 m deep décollement is overlain by a ~ 40 m-thick MTD in the shallower part of the slump and underlain by 40-45 m-thick bed of sediment waves further downslope (Chapter 3). The sediment waves are described as part of overbank turbidite systems (Piper et al., 2005). It is possible that cyclic loading due to the earthquake caused excess pore pressure and therefore a reduction of the effective stress: a) underneath the MTD's that are present in the shallower part of the slump, and b) by reducing the grain-to-grain friction within the sediment waves causing potential liquefaction.
2. The 250 m deep décollement corresponds to a regional unconformity that denotes a change in the depositional characteristic as a result of shelf crossing glaciers and resulting increase in sedimentation rate. Thick (30-40 m) MTD's are present underneath this décollement (see Chapter 3). These MTD's might have induced overpressure within underlying layers. The décollement surface, however, mostly overlies the MTD's. It is believed that rapidly deposited, probably less permeable glaciogenic mud on top of the unconformity prevented pore pressure dissipation of earthquake induced pore fluid pressure from the underlying MTD's, which ultimately decreased the effective stress along the décollement (c.f., described elsewhere by Flemmings et al., 2008).

3. Surficial failures at 10 and 25 m were likely a consequence of weak layers associated with rapid deposition of MTD's and turbidity currents, interbedded sediment of different permeability and/or gas hydrate dissociation. Some of these weak layers were likely induced as a result of the earthquake. Displacement of a slump initiated along the 550 m deep décollement, however, needs to be considered as another potential trigger for shear stress induced shallower failures.

It is evident that both earthquake loading and geomechanical weak layers as a consequence of overpressure were necessary to cause slope instability in 1929. A similar conclusion was derived for sediment failure at the neighboring Scotian Slope (MacKillop et al., 2019). At the St. Pierre Slope, earthquake loading in combination with weak layers could have caused slumping along décollements in 550 and 250 mbsf. Movement of the St. Pierre Slump may have ceased as excess pore pressure partly dissipated by release of fluids along fault planes or into adjacent valleys. It is possible that slumping contributed to surficial failure (upper 25 m) initiation in addition to the earthquake loading.

4.6 CONCLUSION

Sediment on the upper St. Pierre Slope is generally normally consolidated with a tendency to apparent overconsolidation (AOC) in the upper 3 m and normally to slightly under-consolidated (NC and UC) in the lower 3 to 9 m, as determined on measurements from shallow sediment cores. The AOC is likely the result of sampling disturbance during coring, organic compounds in the sediment and/or removal of upper sediment strata. Under-consolidation is possibly caused by: 1) high sedimentation rates, 2) overpressures due to loading by mass transport deposits, and 3) the presence of shallow gas. Overall the sediment in this location can be assumed to be stable under present day and static conditions (FOS of 1). A $M_w > 4.8$ earthquake is shown to cause instability at the St. Pierre Slope if the epicentre distance is < 5 km distant ($PGA > 0.09$ g).

Potential weak layers are indicated in the upper 10 m of the sediment cores. These weak layers correspond to, a) clay-rich layers interbedded with sandy-mud, interpreted as sandy turbidites; especially where less permeable clay-rich mud overlays more porous sandy-

mud, and b) gas charged sediment that is overlain by an MTD where the MTD acts as a potential seal. The presence of these weak layers could be important preconditioning factors that need to be considered in terms of failure potential.

A pseudo-static slope stability analysis and two potential décollements mapped on seismic reflection data indicate that the M_w 7.2 1929 earthquake could have caused slope instability of a 550 m-thick sediment slab. The need to consider the role of potential weak layers depends on the model used to convert magnitude to PGA and which shear strength and effective overburden stress is used to estimate the critical PGA necessary to initiate FOS of 1. Potential liquefaction within mapped sediment waves in response to the earthquake and UC due to mass transport deposition is necessary to explain failure of the 550 m-thick block. Additionally, the slope analysis conducted in this chapter included static and pseudo-static conditions only, while cyclic loading tests would be necessary to fully simulate the response of the sediment to an earthquake. A combination of earthquake loading and geomechanical weak layers is necessary to explain surficial (upper 25 m) sediment failure in the 1929 event. Displacement of the thicker slump might have contributed to failure of overlying surficial sediments by causing local ground accelerations.

4.7 ACKNOWLEDGEMENTS

The gravity cores were collected as part of cooperation project during joint research cruises with the German vessel RV *Maria S. Merian* (MSM45 & MSM47). The cooperation project involved the University of Kiel and the University of Bremen, Germany, the Bedford Institute of Oceanography (BIO), and Dalhousie University. I would like to thank the researchers at BIO and Marum for their help with analysing and describing the core. Thanks goes especially to Mr. Kevin MacKillop for offering his geotechnical lab for the triaxial and consolidation testing and for his advice in regard to geomechanical testing. I also would like to thank Dr. Achim Kopf for hosting me at Marum. I also thank Dr. Gauvain Wiemer for helping me with the geomechanical testing at Marum. Thanks to Drs. Christian Hilgenfeldt and Tilo von Döbeneck, I was able to do magnetic susceptibility measurements on the core, which helped in choosing the geotechnical samples. I thank Ms. Jenna Higgins

assisting in the sedimentology lab for the physical property testing. Also, thanks to Dr. David Piper and Ms. Kimberly Jenner for advising me in terms of lithological core description. At last I also want to thank my supervisor, Dr. David Mosher for his advice and expertise (and judicious editing!!).

4.8 REFERENCES CITED IN CHAPTER 4

- Adams, J., and Halchuk, S., 2003. Fourth generation seismic hazard maps of Canada: Values for over 650 Canadian localities intended for the 2005 National Building Code of Canada, Geological Survey of Canada, Open File 4459, p. 155.
- Ai, F., Strasser, M., Preu, B., Hanebuth, T. J. J., Krastel, S., and Kopf, A., 2014. New constraints on oceanographic vs. seismic control on submarine landslide initiation: a geotechnical approach off Uruguay and northern Argentina. *Geo-Marine Letters*, Vol. 34, p. 399-417. Doi: 10.1007/s00367-014-0373-3.
- ASTM Standard D 2216, 2010. Laboratory Determination of Water (Moisture) Content of Soil and Rock by Mass. ASTM International, West Conshohocken, PA, 2013. DOI: 10.1520/D2216-10.
- ASTM Standard D 2435, 2011. One-dimensional Consolidation properties of soils. ASTM International, West Conshohocken, PA, 2013. DOI: 10.1520/D2435-11.
- ASTM Standard D 3080, 2011. Direct Shear Test of Soils Under Consolidated Drained Conditions. ASTM International, West Conshohocken, PA, 2013. DOI: 10.1520/D3080-11.
- ASTM Standard D 4318, 2010. Liquid Limit, Plastic Limit and Plasticity Index of Soils. ASTM International, West Conshohocken, PA, 2013. DOI: 10.1520/4318-10.
- ASTM Standard D 4648, 2010. Laboratory Miniature Vane Shear Test for Saturated Fine-Grained Clayey Soil. ASTM International, West Conshohocken, PA, 2013. DOI: 10.1520/D4648-10.
- ASTM Standard D 4767, 2011. Consolidated Undrained Triaxial Compression Test for Cohesive Soils. ASTM International, West Conshohocken, PA, 2013. DOI: 10.1520/D4767-11.

- Atkinson, G. M., and Boore, D. M., 2006. Earthquake Ground-Motion Prediction Equations for Eastern North America. *Bulletin of the Seismological Society of America*, Vol. 96, p. 2181-2205.
- Becker, D. E., Crooks, J. H. A., Been, K., and Jefferies, M. G., 1987. Work as a criterion for determining in situ and yield stresses in clays. *Canadian Geotechnical Journal*. Vol. 24, p. 549-564.
- Bent, A. L., 1995. A complex double-couple source mechanism for the Ms 7.2 1929 Grand Banks earthquake. *Bulletin of the Seismological Society of America*, Vol. 85, p. 1003-1020.
- Blum, P., 1997. Physical properties handbook: a guide to the shipboard measurement of physical properties of deep-sea cores. *ODP Tech. Note*, 26 [Online]. Available from World Wide Web: <http://www-odp.tamu.edu/publications/tnotes/tn26/INDEX.HTM>. [Cited 2018-02-22].
- Braja, M. D., 2010. *Principles of Geotechnical Engineering*, 7th Edition. Cengage Learning, Stamford, USA, p. 294-422.
- Campbell, K. W., and Bozorgnia, Y., 2008. NGA ground motion model for the geometric mean horizontal component of PGA, PGV, PGD and 5% damped linear elastic response spectra for periods ranging from 0.01 to 10 s. *Earthquake Spectra*, Vol. 24, p. 139–171.
- Carter, R. M., McCave, I. N., Richter, C., Carter, L., et al., 1999. Proc. ODP, Init. Repts., 181: College Station, TX (Ocean Drilling Program), p. 1–65. doi:10.2973/odp.proc.ir.181.102.2000.
- Cassagrande, A., 1936. The Determination of the Pre-Consolidation Load and its Practical Significance. *Proceedings, 1st Int. Conf. Soil Mech. Fnd. Eng., Harvard*, Vol. 3, p. 60-64.
- Christian, H. A., Piper, D. J. W., and Armstrong, R., 1991. Strength and consolidation properties of surficial sediments, Flemish Pass: effects of biological processes. *Deep-Sea Research*, Vol. 38, p. 663-676.
- Earthquakes Canada, GSC, Earthquake Search (On-line Bulletin), <http://earthquakescanada.nrcan.gc.ca/stndon/NEDB-BNDS/bull-eng.php>, Nat. Res. Can., {29.01.2018}.

- Fine, I. V., Rabinovich, A. B., Bornhold, B. D., Thomson, R. E., and Kulikov, E. A., 2005. The Grand Banks landslide-generated tsunami of November 18, 1929: preliminary analysis and numerical modeling. *Marine Geology*, Vol. 215, p. 45-57.
- Flemings, P. B., Long, H., Dugan, B., Germaine, J., John, C. M., Behrmann, J. H., Sawyer, D., et al., 2008. Pore pressure penetrometers document high overpressure near the seafloor where multiple submarine landslides have occurred on the continental slope offshore Louisiana, Gulf of Mexico. *Earth and Planetary Science Letters*, Vol. 269, p. 309-325.
- Giles, M. K., Mosher, D. C., Piper, D. J. W., and Wach, G. D., 2010. Mass Transport Deposits on the Southwestern Newfoundland Slope. In: Mosher, D. C., Shipp, R. C. et al. (eds.), *Submarine Mass Movements and Their Consequences, Advances in Natural and Technological Hazards Research*, Vol. 28, p. 657-665, Springer, Dordrecht.
- Hansbo, S., 1957. A new approach to the determination of the shear strength of clay by the fall-cone test. *Proceedings of the Royal Swedish. Geotechnology Institute*, Vol. 14, p. 1-49.
- Heezen, B. C., and Ewing, M., 1952. Turbidity currents and submarine slumps, and the 1929 Grand Banks earthquake. *American Journal of Science*, Vol. 250, p. 849-878.
- Hodgson, E. A., and Doxsee, W. W., 1930. The Grand Banks earthquake, November 18, 1929. Eastern section of the seismological society of America, proceedings of the 1939 meeting, Washington, D. C., p. 72-81.
- Kominz, M. A., Patterson, K., and Odette, D., 2011. Lithology dependence of porosity in slope and deep marine sediments. *Journal of Sedimentary Research*, Vol. 81, p. 730-742. Doi: 10.2110/jsr.2011.60.
- Krastel, S., Braeunig, A., Feldens, P., et al., 2016. Geomorphology, processes and geohazards of giant submarine landslides and tsunami generation capacity, as recorded in the sedimentary record of the only historic slide of this kind: the 1929 Grand Banks landslide of the Canadian Atlantic continental margin. Cruise No. MSM47, September 30 - October 30, 2015, St. John's (Canada) - Ponta Delgada, Azores (Portugal). *Maria S. Merian-Berichte, MSM47*, p. 1-55, doi:10.2312/cr_msm47.

- Kvalstad, T. J., Nadim, F., Kaynia, A. M., Mokkelbost, K. H., and Bryn, P., 2005. Soil conditions and slope stability in the Ormen Lange area. *Marine and Petroleum Geology*, Vol. 22, p. 299-310.
- Ledger-Piercy, S., and Piper, D. J. W., 2007. Late Quaternary geological history of the SW Grand Banks Slope and Rise off Green Bank and Whale Bank: implications for geohazard assessment. Geological Survey of Canada, Open File 5663, p. 1-86.
- Locat, J., Leroueil, S., Locat, A., and Lee, H. J., 2014. Weak layers: Their definition and classification from a geotechnical perspective. In: Krastel, S., Behrmann, J. H., Völker, D., et al. (eds.), *Submarine Mass Movements and Their Consequences*, Advances in Natural Hazard Research, Vol. 37, p. 3-21, Springer, Dordrecht.
- MacKillop, K., Fenton, G., Mosher, D., Latour, V., and Mitchelmore, P., 2019. Assessing Submarine Slope Stability through Deterministic and Probabilistic Approaches: A Case Study on the West-Central Scotia Slope. *Geosciences*, Vol. 9, p. 1-18.
- Marsters, J. C., 1986. Geotechnical Analysis of Sediments from the Eastern Canadian Continental Slope-South of the St. Pierre Bank. MEng Project Report, Technical University of Nova Scotia, Halifax, N.S.
- Mayer, L. A., Shor, A. N., Hughes Clarke, J., and Piper, D. J. W., 1988. Dense biological communities at 3850 m on the Laurentian Fan and their relationship to the deposits of the 1929 Grand Banks earthquake. *Deep-Sea Research*, Vol. 35, p. 1235-1246.
- Mazzotti, S., 2007. Geodynamic models for earthquake studies in intraplate North America. In: Stein, S., and Mazzotti, S., (ed.), *Continental Intraplate Earthquakes: Science, Hazard, and Policy Issues: Geological Society of America Special Paper 425*. p. 17-33. Doi: 10.1130/2007.2425(02).
- McCall, C. W., 2006. A Geological and Geophysical study of the 1929 Grand Banks slide. M.Sc. Thesis, Saint Mary's University, Halifax, Nova Scotia.
- Morgenstern, N. M., 1967. Submarine Slumping and Initiation of Turbidity Currents. In: Richards, F. A., (ed.), *Marine Geotechnique*. University of Illinois Press, Urbana, p. 189-220.
- Morton, R. A., and White, W. A., 1997. Characteristics of and Corrections for Core Shortening in Unconsolidated Sediments. *Journal of Coastal Research*, Vol. 13, p. 761-789.

- Mosher, D. C., 2011. Cautionary considerations for geohazard mapping with multibeam sonar: resolution and the need for the third and fourth dimensions. *Marine Geophysics Research*, Vol. 32, p. 25-35.
- Mosher, D. C., and Piper, D. J. W., 2007. Analysis of Multibeam seafloor imagery of the Laurentian Fan and the 1929 Grand Banks landslide area. In: Lykousis, V., Sakellariou, D., and Locat, J. (eds.), *Submarine Mass Movements and Their Consequences, Advances in Natural and Technological Hazards Research*, Vol. 27, p. 77-88, Springer, Dordrecht.
- Mosher, D. C., Moran, K., and Hiscott, R.N., 1994. Late Quaternary Sediment, Sediment Mass Flow Processes and Slope Stability on the Scotian Slope, Canada, *Sedimentology*, Vol. 41, p.1039-1061.
- Pacheco Silva F., (1970). A new graphical construction for determination for the pre-consolidation stress of a soil sample. In: *Proceedings of the 4th Brazilian Conference on Soil Mechanics and Foundation Engineering*, Rio de Janeiro, Brazil. Vol. 2, No. 1, p. 225-232.
- Piper, D. J. W., 1999. Cruise Report Hudson 99-036: Sydney, N. S. – BIO, 19 August – 8 September 1999. Geological Survey of Canada (Atlantic), p. 1-93.
- Piper, D. J. W., and Skene, K. I., 1998. Latest Pleistocene ice-rafting events on the Scotian Margin (eastern Canada) and their relationship to Heinrich events. *Paleoceanography*, Vol. 13, No. 2, p. 205-214.
- Piper, D. J. W., Shor, A. N., and Hughes Clarke, J. E., 1988. The 1929 “Grand Banks” earthquake, slump, and turbidity current. In: *Sedimentological Consequences of Convulsive Geologic Events* (Ed. By H. E. Clifton), Geological Society of America Special Paper, Vol. 229, p. 77- 92.
- Piper, D. J. W., Cochonat, P., and Morrison, M. L., 1999. The sequence of events around the epicentre of the 1929 Grand Banks earthquake: initiation of debris flows and turbidity current inferred from sidescan sonar. *Sedimentology*, Vol. 46, p. 79-97.
- Piper, D. J. W., Macdonald, A. W. A., Ingram, S., Williams, G. L., and McCall, C., 2005. Late Cenozoic architecture of the St. Pierre Slope. *Canadian Journal of Earth Sciences*, Vol. 42, p. 1987-2000, doi:10.1139/E05-059.

- Poulos, H. G., 1988. *Marine Geotechnics*. Academic Division of Unwin Hyman Ltd, London, p. 1-473.
- Roberts, J. A., and Cramp, A., 1996. Sediment stability on the western Flanks of the Canary Islands. *Marine Geology*, Vol. 134, p. 13-30.
- Ruffman, A., 2001. Potential for large-scale submarine slope failure and tsunami generation along the U. S. mid-Atlantic coast: Comment. *Geology*, Vol. 29, No. 10, p. 967.
- Schneider, R., 2015. Short Cruise Report, Maria S. Merian cruise MSM45, Nuuk (Greenland) – Halifax (Canada), 01.08.2015-22.08.2015. Maria S. Merian-Berichte, MSM47, p. 1-7.
- Schulten, I., Mosher, D. C., Krastel, S., Piper, D. J. W., and Kienast, M., 2019. Surficial sediment failures due to the 1929 Grand Banks Earthquake, St Pierre Slope. From: Lintern, D. G., Mosher, D. C., et al. (eds). *Subaqueous Mass Movements*. Geological Society, London, Special Publications, 477, <https://doi.org/10.1144/SP477.25>.
- Shaw, J., Piper, D.J.W., Fader, G.B., King, E.L., Todd, B.J., Bell, T., Batterson, M.J., and Liverman, D.J.E., 2006. A conceptual model of the deglaciation of Atlantic Canada. *Quaternary Science Reviews*, Vol. 25, p. 2059-2081.
- Skempton, A. W., 1954. The Structure of Inorganic Soil (discussion). *Proceedings, ASCE*, Vol. 80, separate 478, p. 19-22.
- Skempton, A. W., 1970. The Consolidation of Clays by Gravitational compaction. *Quarterly Journal of the Geological Society of London*, Vol. 125, p. 373-412.
- Skene, K. I., and Piper, D. J. W., 2003. Late Quaternary stratigraphy of Laurentian Fan: a record of events off the eastern Canadian continental margin during the last deglacial period. *Quaternary International*, Vol. 99-100, p. 135-152.
- Skinner, L. C., and McCave, I. N., 2003. Analysis and modelling of gravity- and piston coring based on soil mechanics. *Marine Geology*, Vol. 199, p. 181-204.
- Sultan, N., Cochonat, P., Canals, M., et al., 2004. Triggering mechanisms of slope instability processes and sediment failures on continental margins: a geotechnical approach. *Marine Geology*, Vol. 213, p. 291-321.

CHAPTER 5: CONCLUSIONS

The 1929 event is one of the best studied cases of submarine landsliding with an unequivocal connection between an earthquake, sediment mass failure and consequent tsunami (*e.g.*, Bent, 1995; Piper et al., 1988; 1999; Fine et al., 2005). Yet, it is hard to comprehend that a submarine landslide previously identified as a widely distributed, retrogressive surficial failure (~20-25 m) in deep water (>750 mwd) resulted in tsunami generation. This study hypothesised, therefore, that a thick sediment slump block displaced a large region of the seafloor of the St. Pierre Slope as a result of the 1929 earthquake. If shown to be the case, then this displacement is more likely to have generated the observed tsunami. To address this hypothesis, the objective of this thesis was to quantitatively assess slope stability and investigate different styles and volumes of sediment mass failure on the St. Pierre Slope. Surficial failures and stratigraphic structures were analysed to identify failure styles and failure mechanisms. In addition, static and pseudo-static slope stability analyses were conducted to evaluate factors that may have contributed to sediment failure. These results contribute to increased knowledge of the factors involved in sediment mass failure processes and tsunami generation potential of continental margin landslides.

5.1 DIMENSION, DISTRIBUTION AND KINEMATICS OF 1929 SURFICIAL SEDIMENT FAILURES

The 1929 submarine landslide is one of the first studied examples known to have caused a submarine turbidity current and a tele-tsunami. Newly acquired multibeam bathymetric data and ultra-high resolution seismic data have permitted a reassessment of the areas and volumes involved in surficial sediment failures that occurred in this event, with the following observations:

- a. Surficial sediment failure was widely distributed, translational and possible retrogressive.
- b. ~100 km³ of sediment failed on St. Pierre Slope with a total failure area of ~5200 km² but could be as large as ~135 km² accounting for additional failures from

Western and Grand Banks Valley (~7000 km²) that were identified as part of the main failure area.

- c. ~60 km³ of sediment material was deposited directly on the slope, especially where there is a change in slope gradient from 3° to 1° between 2300 and 2800 mwd.
- d. ~40 km³ of the failed sediment became entrained into channelized turbidity currents.

Significant new findings in this study are:

- i) seafloor escarpments (<100 m in height) in 730 to 1300 mwd are associated with faults shown as reflection offsets in the underlying stratigraphy.
- ii) sediment failure deposits in the area occur downslope of these faults. They are local and resulted in thin (~5 m thick) mass flow deposits.
- iii) these small local failure deposits may be the result of the fault displacement and not earthquake ground accelerations.
- iv) seafloor escarpments in 1700 to 2800 mwd are interpreted as headwall scarps resulting from sediment mass failure.
- v) sediment failure deposits below these scarps are thicker (~35 m) and account for the majority of failed surficial sediment on the St. Pierre Slope.

Based on these observations, two trigger mechanisms are proposed to be responsible for the observed surficial sediment failures on St. Pierre Slope: 1) faulting in the upslope region, and 2) earthquake ground accelerations causing translational and retrogressive failure in the mid slope region.

5.2 REFLECTION OFFSETS WITHIN THE QUATERNARY SECTION OF THE SLOPE - THE ST. PIERRE SLUMP

Sediment failure at St. Pierre Slope is far more complex than previous studies estimated. Beside widely distributed surficial failures, numerous up to 100 m-high reflection offsets are present throughout the Quaternary section of St. Pierre Slope as evident in 2D ultra-high resolution seismic and 2D high resolution reflection seismic data (Fig. 5.1). The

reflection offsets are interpreted as oblique low angle ($\sim 17^\circ$) faults. These faults extend underneath modern seafloor escarpments down to 550 mbsf with vertical displacement of up to 100 m and horizontal displacement of ~ 330 m.

The faults are interpreted as part of a massive (560 km^3) slump, that is termed St. Pierre Slump. There is evidence that slumping occurred in at least two directions and along multiple décollements at 550 and 250 mbsf (Fig. 5.1). The lower décollement at 550 mbsf is associated with sediment waves interpreted as overbank turbidites. The upper décollement at 250 mbsf overlies a regional unconformity and thick MTD's (Fig. 5.1). St. Pierre Valley and Eastern Valley to the west of St. Pierre Slope are shown to be incised down to this upper décollement at 250 mbsf (Fig. 5.1), which suggests that the sediment package from the seafloor down to this décollement could have freely evacuated into the adjacent valley and canyon systems. Movement of the upper component is therefore interpreted to have been mainly towards the WSW, while the deeper component likely moved towards the SW (Fig. 5.1). A compressional zone is largely absent. Small indications for compression are given in form of undulating reflections with localized amplitude reductions. The absence of a major compressional zone is attributed to the free evacuation of the upper component and the fact that the ~ 330 m of horizontal displacement was accommodated over the 60 km length of the slump.

Major displacement (~ 100 m vertical, ~ 330 m horizontal) involving both components of the slump down to ~ 550 mbsf is interpreted as a direct consequence of the 1929 M_w 7.2 earthquake. An important indication of recent reactivation is that the height of escarpments nearly matches the height of vertical displacement along faults. Fault offsets appear constant at least down to 120 mbsf (~ 90 mbsf) indicating displacement in one single event. It is suggested that the 1929 Grand Banks submarine landslide involved two failure mechanisms: 1) a massive (560 km^3), complex slump, and 2) translational, retrogressive failure of the upper ~ 20 m of the sediment column. It is possible that displacement of the slump caused the surficial failures rather than ground accelerations due to the earthquake.

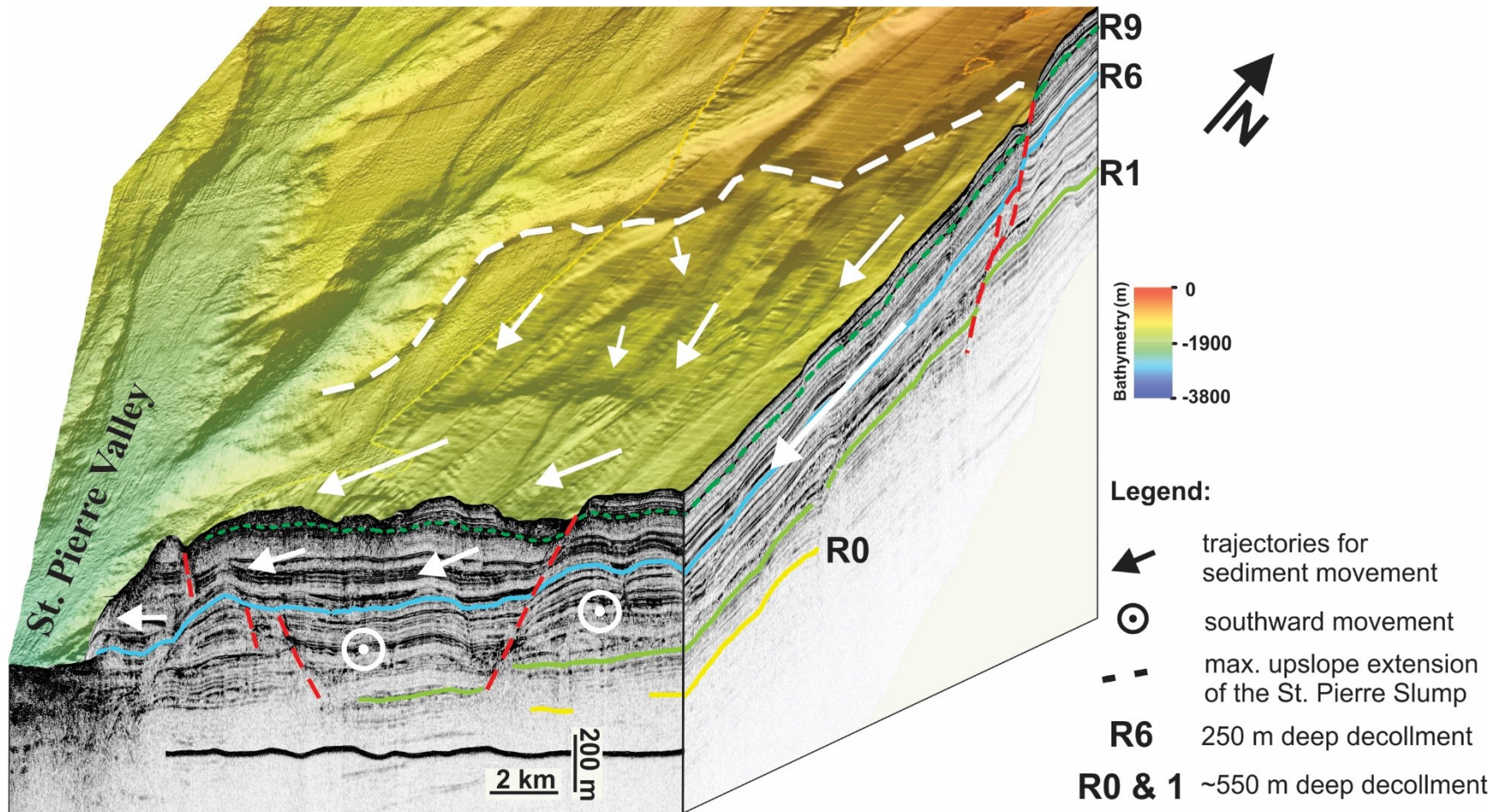


Fig. 5.1: 3D image of the St. Pierre Slope with 2D reflection seismic (envelope) showing structures in the sub-bottom down ~550 m. Identified décollements (R0, R1 & R6) are highlighted and trajectories indicate the suggested movement of the St. Pierre Slump. The red dashed lines show the position of reflection offsets interpreted as faults.

5.3 PRESENT-DAY SLOPE STABILITY AND IMPLICATIONS ON THE 1929 EVENT

Assessment of geotechnical information from an area of the slope that did not fail in the 1929 earthquake provides information on the stability of the slope. Both, static and pseudo-static infinite slope stability analysis were used to test present day slope stability and to evaluate factors that contributed to the 1929 slope failure. Results show that the slope at all depths, with gradients less than 6.8° is stable under static conditions; thus, the St. Pierre Slope is stable. Pseudo-static infinite slope stability analysis indicates that minimum conditions for failure require a peak ground acceleration (PGA) of 0.09 g. At a conservative estimate, this PGA force requires an earthquake of magnitude >4.8 at <5 km distance from the slope to initiate failure. Historical earthquakes in this region occur ~ 20 km distance from this portion of the slope.

A recurrence of the 1929 earthquake (PGA ~ 0.2 g) possible would cause failure of a 550 m-thick sediment slab (FOS of 1 at PGA 0.15 g). It is shown that pre-conditioning factors are needed in addition to ground shaking in order to explain slope failure in 1929, including the surficial sediment failures (<25 m thick).

Analysis on sediment cores and reflection seismic data from St. Pierre Slope provide three possible factors that account for underconsolidation in connection with excess pore pressure and the formation of geomechanical weak layers: 1) high sedimentation rates, 2) rapid deposition of MTD's and sandy turbidites, and 3) the presence of gas. FOS minima in cores occur at boundary layers between siltier or sandier mud such as MTD's and sandy turbidites and less permeable clay-rich mud. Layers may be geotechnical weak due to inherent properties (e.g., high pore pressure due to rapid deposition), or induced properties (e.g., high pore pressure response due to ground accelerations). It is interpreted that décollements of the St. Pierre Slump at 250 and 550 mbsf are a result of the presence of one of these two types of weak layers. The 550 m-deep décollement is underlain by sediment waves, while the 250 m-deep décollement overlies an unconformity and thick MTD's. In addition, St. Pierre Valley and Eastern Valley incise down to the 250 m-deep décollement, so the unit lies on a free slope without downslope support (i.e., an unconfined slope) (Fig. 5.1).

5.4 POTENTIAL SOURCE MECHANISMS OF THE 1929 TSUNAMI

Previous interpretations of sediment failure on the St. Pierre Slope suggested that it occurred as widespread, retrogressive failure of the upper sediment section (<25 m). It was interpreted that this failure generated the devastating tsunami; despite the fact that it is difficult to reconcile generation of such a large tsunami with these thin, distributed failures in deep water.

This study has shown that sediment failure on the St. Pierre Slope was more complex than reported in previous studies. The St. Pierre Slump interpreted in this study generated fault-related seafloor escarpments throughout the slope. The slump involved 560 km³ of sediment with 100 m of vertical and 330 m of horizontal displacement. The shallowest escarpment related to this slump is located in ~750 mwd. Near instantaneous displacement of this slump seems a much more probable mechanism for generation of the tsunami than widespread, surficial failures. If the entire slump sustained 100 m of vertical displacement, the displacement throughout the area of the slump resulted in a possible seafloor volume displacement of 70 to 130 km³.

Simulations of the 1929 tsunami by Løvholt et al. (2019) indicate that both shallow and deep failure mechanisms are needed to explain the near and far-field tsunami. They showed that the slump could have generated the near-field tsunami component that impacted the south coast of Newfoundland. Surficial failures explain the far field and distributed tsunami that was recorded in Nova Scotia and the Azores.

5.5 IMPLICATIONS ON OTHER, MORPHOLOGIC SIMILAR AREAS

This thesis demonstrates that the 1929 submarine landslide involved two failure mechanisms: 1) a massive (560 km³) slump, and 2) translational, probable retrogressive surficial (upper 25 m) failures. Yet, escarpments such as those along the St. Pierre Slope are commonly observed in relation to small- and medium-sized landslides (<1 km³ of slide deposits). Shallow sediment failures are frequently recognized along continental margins (*e.g.*, Chaytor et al., 2007; Mosher et al., 2004; Mosher et al., 2010; Baeten et al., 2014). Large-scale sediment failures, however, are less often reported (*e.g.*, Nisbet & Piper, 1998;

Mosher et al., 2010b; Deptuck & Campbell, 2012). In situ slumps, such as the St. Pierre Slump are reported even less often. Reporting of such features might be a result of lack of observation rather than lack of occurrence. Recognition of these features requires either high resolution 3D or closely spaced 2D reflection seismic data. Even with historic documentation of the 1929 event, it was possible to recognize and analyze such a feature only through detailed investigations of data sets of multiple resolutions and dense coverage.

Passive margins and particularly glaciated passive margins are areas that are geomorphologically and stratigraphically similar to St. Pierre Slope with known surficial failures. Factors described to have resulted in development of the St. Pierre Slope Slump such as high sedimentation rates, glacial erosion, slope undercutting, and relatively strong earthquakes are common in these environments. It can, therefore, be concluded that the geohazard potential of continental slopes similar to the St. Pierre Slope might be higher than anticipated; although the frequency of such events has yet to be determined. The geohazard and tsunami threat on a global or even regional scale is still difficult to quantify due to the absence of sufficient data. These data include 1) observations of such features, 2) quantification of their metrics, 3) age control, 4) assessment of causal factors, and 5) an appropriate global database that captures all of these parameters.

REFERENCES

- Adams, J., and Halchuk, S., 2003. Fourth generation seismic hazard maps of Canada: Values for over 650 Canadian localities intended for the 2005 National Building Code of Canada, Geological Survey of Canada, Open File 4459, p. 155.
- Ai, F., Strasser, M., Preu, B., Hanebuth, T. J. J., Krastel, S., and Kopf, A., 2014. New constraints on oceanographic vs. seismic control on submarine landslide initiation: a geotechnical approach off Uruguay and northern Argentina. *Geo-Marine Letters*, Vol. 34, p. 399-417. Doi: 10.1007/s00367-014-0373-3.
- ASTM Standard D 2216, 2010. Laboratory Determination of Water (Moisture) Content of Soil and Rock by Mass. ASTM International, West Conshohocken, PA, 2013. DOI: 10.1520/D2216-10.
- ASTM Standard D 2435, 2011. One-dimensional Consolidation properties of soils. ASTM International, West Conshohocken, PA, 2013. DOI: 10.1520/D2435-11.
- ASTM Standard D 3080, 2011. Direct Shear Test of Soils Under Consolidated Drained Conditions. ASTM International, West Conshohocken, PA, 2013. DOI: 10.1520/D3080-11.
- ASTM Standard D 4318, 2010. Liquid Limit, Plastic Limit and Plasticity Index of Soils. ASTM International, West Conshohocken, PA, 2013. DOI: 10.1520/4318-10.
- ASTM Standard D 4648, 2010. Laboratory Miniature Vane Shear Test for Saturated Fine-Grained Clayey Soil. ASTM International, West Conshohocken, PA, 2013. DOI: 10.1520/D4648-10.
- ASTM Standard D 4767, 2011. Consolidated Undrained Triaxial Compression Test for Cohesive Soils. ASTM International, West Conshohocken, PA, 2013. DOI: 10.1520/D4767-11.
- Atkinson, G. M., and Boore, D. M., 2006. Earthquake Ground-Motion Prediction Equations for Eastern North America. *Bulletin of the Seismological Society of America*, Vol. 96, p. 2181-2205.

- Baeten, N.J., Laberg, J.S., Vanneste, M., Forsberg, C.F., Kvalstad, T.J., Forwick, M., Vorren, T.O., Haflidason, H., 2014. Origin of shallow submarine mass movements and their glide planes—Sedimentological and geotechnical analyses from the continental slope off northern Norway. *Journal of Geophysical Research*, Vol. 119: p. 2335-2360.
- Becker, D. E., Crooks, J. H. A., Been, K., and Jefferies, M. G., 1987. Work as a criterion for determining in situ and yield stresses in clays. *Canadian Geotechnical Journal*. Vol. 24, p. 549-564.
- Bent, A. L., 1995. A complex double-couple source mechanism for the Ms 7.2 1929 Grand Banks earthquake. *Bulletin of the Seismological Society of America*, Vol. 85, p. 1003-1020.
- Blum, P., 1997. Physical properties handbook: a guide to the shipboard measurement of physical properties of deep-sea cores. *ODP Tech. Note*, 26 [Online]. Available from World Wide Web: <http://www-odp.tamu.edu/publications/tnotes/tn26/INDEX.HTM>. [Cited 2018-02-22].
- Bonifay, D., and Piper, D. J. W., 1988. Probable Late Wisconsinan ice margin on the upper continental slope off St. Pierre Bank, eastern Canada. *Canadian Journal of Earth Sciences*, Vol. 25, p. 853-865.
- Braja, M. D., 2010. *Principles of Geotechnical Engineering*, 7th Edition. Cengage Learning, Stamford, USA, p. 294-422.
- Bryn, P., Solheim, A., Berg, K., Lien, R., Forsberg, C. F., Haflidason, H., Ottesen, D., and Rise, L., 2003. The Storegga Slide complex: repeated large scale sliding in response to climatic cyclicity. In: Locat, J., Mienert, J., and Boisvert, L. (eds), *Submarine Mass Movements and Their Consequences, Advances in Natural and Technological Hazards Research*, p. 215-222, Springer, Dordrecht.
- Bryn, P., Berg, K., Forsberg, C. F., Solheim, A., and Kvalstad, T. J., 2005. Explaining the Storegga Slide. *Marine and Petroleum Geology*, Vol. 22, p. 11-19.
- Campbell, K. W., and Bozorgnia, Y., 2008. NGA ground motion model for the geometric mean horizontal component of PGA, PGV, PGD and 5% damped linear elastic response spectra for periods ranging from 0.01 to 10 s. *Earthquake Spectra*, Vol. 24, p. 139–171.

- Carter, R. M., McCave, I. N., Richter, C., Carter, L., et al., 1999. Proc. ODP, Init. Repts., 181: College Station, TX (Ocean Drilling Program), p. 1–65. doi:10.2973/odp.proc.ir.181.102.2000.
- Cassagrande, A., 1936. The Determination of the Pre-Consolidation Load and its Practical Significance. Proceedings, 1st Int. Conf. Soil Mech. Fnd. Eng., Harvard, Vol. 3, p. 60-64.
- Chaytor, J. D., Twichell, D. C., Ten Brink, U. S., Buczkowski, B. J., and Andrews, B. D., 2007. Revisiting submarine mass movements along the U. S. Atlantic continental margin: Implications for tsunami hazards. In: Lykousis, V., Sakellariou, D., and Locat, J. (eds.), Submarine Mass Movements and Their Consequences, Advances in Natural and Technological Hazards Research, Vol. 27, p. 395-403, Springer, Dordrecht.
- Childs, C., Nicol, A., Walsh, J. J., and Watterson, J., 1996. Growth of vertically segmented normal faults. Journal of Structural Geology, Vol. 18, No. 12, p. 1389-1397.
- Christian, H. A., Piper, D. J. W., and Armstrong, R., 1991. Strength and consolidation properties of surficial sediments, Flemish Pass: effects of biological processes. Deep-Sea Research, Vol. 38, p. 663-676.
- Clare, M. A., Talling, P. J., Challenor, P., Malgesini, G., and Hunt, J., 2014. Distal turbidites reveal a common distribution for large (>0.1 km³) submarine landslide recurrence. Geology, Vol. 42, p. 263-266. Doi: 10.1130/G35160.1.
- Cohen, K. M., and Gibbard, P. L., 2016. Global chronostratigraphical correlation table for the last 2.7 million years v. 2016a. Subcommittee on Quaternary Stratigraphy (International Commission on Stratigraphy), Cambridge, England. <http://www.stratigraphy.org/upload/QuaternaryChartExplanation.pdf>.
- Damuth, J. E., 1975. Echo character of the western equatorial Atlantic floor and its relationship to the dispersal and distribution of terrigenous sediments. Marine Geology, Vol. 18, p. 17-45.
- Damuth, J. E., 1980. Use of high-frequency (3.5-12 kHz) echograms in the study of near-bottom sedimentation processes in the deep-sea: a review. Marine Geology, Vol. 38, p. 51-75.

- Damuth, J. E., and Olson, H. C., 2015. Latest Quaternary sedimentation in the northern Gulf of Mexico Intraslope Basin Province: I. Sediment facies and depositional processes. *Geosphere*, Vol. 11, No. 6, p. 1689-1718, doi:10.1130/GES01090.1.
- Deng, C., Fossen, H., Gawthorpe, R. L., Rotevatn, A., Jackson, C. A-L., and FazliKhani, H., 2017. Influence of fault reactivation during multiphase rifting: The Oseberg area, northern North Sea rift. *Marine and Petroleum Geology*, Vol. 86, p. 1252-1272.
- Deptuck, M. E., and Campbell, C., 2012. Widespread erosion and mass failure from the ~51 Ma Montagnais marine bolide impact off southwestern Nova Scotia, Canada. *Canadian Journal of Earth Sciences*, Vol. 49, p. 1567-1594.
- Deptuck, M. E., Mosher, D. C., Campbell, D. C., Hughes-Clarke, J. E., and Noseworthy, D., 2007. Along slope variations in mass failures and relationships to major Plio-Pleistocene morphological elements, SW Labrador Sea. In: Lykousis, V., Sakellariou, D., and Locat, J. (eds.), *Submarine Mass Movements and Their Consequences, Advances in Natural and Technological Hazards Research*, Vol. 27, p. 37-45, Springer, Dordrecht.
- Doxsee, W. W., 1948. The Grand Banks Earthquake of November 18, 1929. *Publications of the Dominion Observatory, Ottawa*, Vol. 7, No. 7, p. 323-335.
- Driscoll, N. W., Weissel, J. K., and Goff, J. A., 2000. Potential for large-scale submarine slope failure and tsunami generation along the U. S. mid-Atlantic coast. *Geology*, Vol. 28, No. 5, p. 407-410.
- Earthquakes Canada, GSC, Earthquake Search (On-line Bulletin), <http://earthquakescanada.nrcan.gc.ca/stndon/NEDB-BNDS/bull-eng.php>, Nat. Res. Can., {29.01.2018}.
- Fine, I. V., Rabinovich, A. B., Bornhold, B. D., Thomson, R. E., and Kulikov, E. A., 2005. The Grand Banks landslide-generated tsunami of November 18, 1929: preliminary analysis and numerical modeling. *Marine Geology*, Vol. 215, p. 45-57.
- Flemings, P. B., Long, H., Dugan, B., Germaine, J., John, C. M., Behrmann, J. H., Sawyer, D., et al., 2008. Pore pressure penetrometers document high overpressure near the seafloor where multiple submarine landslides have occurred on the continental slope offshore Louisiana, Gulf of Mexico. *Earth and Planetary Science Letters*, Vol. 269, p. 309-325.

- Frey-Martínez, J., Cartwright, J., and James, D., 2006. Frontally confined versus frontally emergent submarine landslides: A 3D seismic characterisation. *Marine and Petroleum Geology*, Vol. 23, p. 585-604.
- Gafeira, J., Bulat, J., and Evans, D., 2007. The southern flank of the Storegga Slide: Imaging and geomorphological analyses using 3D seismic. In: Lykousis, V., Sakellariou, D., and Locat, J. (eds.), *Submarine Mass Movements and Their Consequences, Advances in Natural and Technological Hazards Research*, Vol. 27, p. 57-65, Springer, Dordrecht.
- Garfunkel, Z., 1984. Large-scale submarine rotational slumps and growth faults in the eastern Mediterranean. *Marine Geology*, Vol. 55, p. 305-324.
- Gee, M. J. R., Gawthorpe, R. L., and Friedmann, J. S., 2005. Giant striations at the base of a submarine landslide. *Marine Geology*, Vol. 214, p. 287-294.
- Georgiopoulou, A., Krastel, S., Masson, D. G., and Wynn, R. B., 2007. Repeated instability of the NW African margin related to buried landslide scarps. In: Lykousis, V., Sakellariou, D., and Locat, J. (eds.), *Submarine Mass Movements and Their Consequences, Advances in Natural and Technological Hazards Research*, Vol. 27, p. 29-36, Springer, Dordrecht.
- Gibbs, A. D., 1984. Structural evolution of extensional basin margins. *Journal of the Geological Society, London*, Vol. 141, p. 609-620.
- Giles, M. K., Mosher, D. C., Piper, D. J. W., and Wach, G. D., 2010. Mass Transport Deposits on the Southwestern Newfoundland Slope. In: Mosher, D. C., Shipp, R. C. et al. (eds.), *Submarine Mass Movements and Their Consequences, Advances in Natural and Technological Hazards Research*, Vol. 28, p. 657-665, Springer, Dordrecht.
- Giosan, L., Flood, R. D., Grützner, J., and Mudie, P., 2002. Paleoceanographic significance of sediment color on western North Atlantic Drifts: II. Late Pliocene-Pleistocene sedimentation. *Marine Geology*, Vol. 189, p. 43-61.
- Haflidason, H., Sejrup, H. P., Nygård, A., Mienert, J., Bryn, P., Lien, R., Forsberg, C. F., Berg, K., and Masson D., 2004. The Storegga Slide: architecture, geometry and slide development. *Marine Geology*, Vol. 213, p. 201-234.

- Hansbo, S., 1957. A new approach to the determination of the shear strength of clay by the fall-cone test. Proceedings of the Royal Swedish. Geotechnology Institute, Vol. 14, p. 1-49.
- Harbitz, C. B., Løvholt, F., and Bungum, H., 2014. Submarine landslide tsunamis: how extreme and how likely? *Natural Hazards*, Vol. 72, p. 1341-1374. doi: 10.1007/s11069-013-0681-3.
- Heezen, B. C., and Drake, G. L., 1964. Grand Banks slump. *American Association of Petroleum Geologist Bulletin*, Vol. 48, p. 221-233.
- Heezen, B. C., and Ewing, M., 1952. Turbidity currents and submarine slumps, and the 1929 Grand Banks earthquake. *American Journal of Science*, Vol. 250, p. 849-878.
- Heezen, B. C., Ericson, D. B., and Ewing, M., 1954. Further evidence for a turbidity current following the 1929 Grand Banks earthquake. *Deep-Sea Research*, Vol. 1, p. 193-202.
- Hodgson, E. A., and Doxsee, W. W., 1930. The Grand Banks earthquake, November 18, 1929. Eastern section of the seismological society of America, proceedings of the 1930 meeting, Washington, D. C., p. 72-81.
- Hooper, E. C. D., 1991. Fluid migration along growth faults in compacting sediments. *Journal of Petroleum Geology*, Vol. 14, No. 2, p. 161-180.
- Hughes Clarke, J. E., 1988. The geological record of the 1929 "Grand Banks" earthquake and its relevance to deep-sea clastic sedimentation. PhD thesis, Dalhousie University, Halifax, Nova Scotia.
- Hughes Clarke, J. E., Mayer, L. A., Piper, D. J. W., and Shor, A. N., 1989. Pisces IV submersible observations in the epicentral region of the 1929 Grand Banks earthquake. *Geological Survey of Canada Paper*, Vol. 88-20, p. 57-69.
- Hutchins, R. W., McKeown, D. L., and King, L. H., 1976. A Deep Tow High Resolution Seismic System for Continental Shelf Mapping. *Geoscience Canada*, Vol. 3, p. 95-100.
- Katz, O., Reuven, E., and Aharonov, E., 2015. Submarine landslides and fault scarps along the eastern Mediterranean Israeli continental-slope. *Marine Geology*, Vol. 369, p. 100-115.

- Kominz, M. A., Patterson, K., and Odette, D., 2011. Lithology dependence of porosity in slope and deep marine sediments. *Journal of Sedimentary Research*, Vol. 81, p. 730-742. Doi: 10.2110/jsr.2011.60.
- Kongsberg Maritime, 2017. Multibeam echosounder, Maximum depth 11000 m - EM 122. <https://www.km.kongsberg.com/ks/web/nokbg0240.nsf/AllWeb/01FB0F22974EA50FC125715E002B2143>, OpenDocument. Norway.
- Krastel, S., Wynn, R. B., Hanebuth, T. J. J., Henrich, R., Holz, C., Meggers, H., Kuhlmann, H., Georgiopoulou, A., and Schulz, H. D., (2006). Mapping of seabed morphology and shallow sediment structure of the Mauritania continental margin, Northwest Africa: some implications for geohazard potential. *Norwegian Journal of Geology*, Vol. 86, p. 163–176.
- Krastel, S., Braeunig, A., Feldens, P., et al., 2016. Geomorphology, processes and geohazards of giant submarine landslides and tsunami generation capacity, as recorded in the sedimentary record of the only historic slide of this kind: the 1929 Grand Banks landslide of the Canadian Atlantic continental margin. Cruise No. MSM47, September 30 - October 30, 2015, St. John's (Canada) - Ponta Delgada, Azores (Portugal). *Maria S. Merian-Berichte, MSM47*, p. 1-55, doi:10.2312/cr_msm47.
- Krastel, S., Li, W., Urlaub, M., Georgiopoulou, A., Wynn, R. B., Schwenk, T., Stevenson, C., and Feldens, P., 2019. Mass Wasting along the NW African continental margin. From: Lintern, D. G., Mosher, D. C., et al. (eds). *Subaqueous Mass Movements*. Geological Society, London, Special Publications, 477, <https://doi.org/10.1144/SP477.36>.
- Kvalstad, T. J., Nadim, F., Kaynia, A. M., Mokkelbost, K. H., and Bryn, P., 2005. Soil conditions and slope stability in the Ormen Lange area. *Marine and Petroleum Geology*, Vol. 22, p. 299-310.
- Ledger-Piercy, S., and Piper, D. J. W., 2007. Late Quaternary geological history of the SW Grand Banks Slope and Rise off Green Bank and Whale Bank: implications for geohazard assessment. *Geological Survey of Canada, Open File 5663*, p. 1-86.
- Lee, H., Ryan, H., Kayen, R. E., Haeussler, P. J., Dartnell, P., and Hampton, M. A., 2006. Varieties of submarine failure morphologies of seismically-induced landslides in Alaskan fjords. *Norwegian Journal of Geology*, Vol. 86, p. 221-230.

- Legros, F., 2002. The mobility of long-runout landslides. *Engineering Geology*, Vol. 63, p. 301-331.
- Lewis, K. B., 1971. Slumping on a continental slope inclined at 1°-4°. *Sedimentology*, Vol. 16, p. 97-110.
- Locat, J., Leroueil, S., Locat, A., and Lee, H. J., 2014. Weak layers: Their definition and classification from a geotechnical perspective. In: Krastel, S., Behrmann, J. H., Völker, D., et al. (eds.), *Submarine Mass Movements and Their Consequences, Advances in Natural Hazard Research*, Vol. 37, p. 3-21, Springer, Dordrecht.
- Løvholt, F., Schulten, I., Mosher, D., Harbitz, C., and Krastel, S., 2019. Modelling of the 1929 Grand Banks slump and landslide tsunami. From: Lintern, D. G., Mosher, D. C., et al. (eds). *Subaqueous Mass Movements*. Geological Society, London, Special Publications, 477, <https://doi.org/10.1144/SP477.28>.
- MacKillop, K., Fenton, G., Mosher, D., Latour, V., and Mitchelmore, P., 2019. Assessing Submarine Slope Stability through Deterministic and Probabilistic Approaches: A Case Study on the West-Central Scotia Slope. *Geosciences*, Vol. 9, p. 1-18.
- Mansfield, C. S., and Cartwright, J. A., 1996. High resolution fault displacement mapping from three-dimensional seismic data: evidence for dip linkage during fault growth. *Journal of Structural Geology*, Vol. 18, No. 2/3, p. 249-263.
- Marsters, J. C., 1986. Geotechnical Analysis of Sediments from the Eastern Canadian Continental Slope-South of the St. Pierre Bank. MEng Project Report, Technical University of Nova Scotia, Halifax, N.S.
- Martinsen, O. J., and Bakken, B., 1990. Extensional and compressional zones in slumps and slides in the Namurian of County Clare, Ireland. *Journal of the Geological Society*, London, Vol. 147, p. 153-164.
- Masson, D. G., Wynn, R. B., and Talling, P. J., 2010. Large Landslides on Passive Continental Margins: Processes, Hypotheses and Outstanding Questions. In: Mosher, D. C., Shipp, R. C. et al. (eds.), *Submarine Mass Movements and Their Consequences, Advances in Natural and Technological Hazards Research*, Vol. 28, p. 153-165. Springer, Dordrecht.

- Mayer, L. A., Shor, A. N., Hughes Clarke, J., and Piper, D. J. W., 1988. Dense biological communities at 3850 m on the Laurentian Fan and their relationship to the deposits of the 1929 Grand Banks earthquake. *Deep-Sea Research*, Vol. 35, p. 1235-1246.
- Mazzotti, S., 2007. Geodynamic models for earthquake studies in intraplate North America. In: Stein, S., and Mazzotti, S., (ed.), *Continental Intraplate Earthquakes: Science, Hazard, and Policy Issues: Geological Society of America Special Paper 425*. p. 17-33. DOI: 10.1130/2007.2425(02).
- McCall, C. W., 2006. A Geological and Geophysical study of the 1929 Grand Banks slide. M.Sc. Thesis, Saint Mary's University, Halifax, Nova Scotia.
- Mitchum, R. M. Jr, Vail, P. R., and Thompson III, S., 1977. Seismic stratigraphy and global changes of sea level, Part 2: The depositional sequence as a basic unit for stratigraphic analysis. In: *Seismic Stratigraphy - Applications to Hydrocarbon Exploration* (Ed. By C. E. Payton), American Association Petroleum Geology Memoir, Vol. 26, p. 53-62.
- Morgenstern, N. M., 1967. Submarine Slumping and Initiation of Turbidity Currents. In: Richards, F. A., (ed.), *Marine Geotechnique*. University of Illinois Press, Urbana, p. 189-220.
- Morton, R. A., and White, W. A., 1997. Characteristics of and Corrections for Core Shortening in Unconsolidated Sediments. *Journal of Coastal Research*, Vol. 13, p. 761-789.
- Mosher, D. C., 2008. Submarine Mass Movements in Canada: Geohazards with far-reaching implications. In: Locat, J., Perret, D., Turmel, D., Demers, D., and Leroueil, S., (eds.): *4e Conférence canadienne sur les géorisques: des causes à la gestion, 4th Canadian Conference on Geohazards: From Causes to Management*. Presse de l'Université Laval, Québec, p. 55-62.
- Mosher, D. C., 2011. Cautionary considerations for geohazard mapping with multibeam sonar: resolution and the need for the third and fourth dimensions. *Marine Geophysics Research*, Vol. 32, p. 25-35.
- Mosher, D. C., and Simpkin, P. G., 1999. Environmental Marine Geoscience 1. Status and Trends of Marine High-Resolution Seismic Reflection Profiling: Data Acquisition. *Geoscience Canada*, Vol. 26, p. 174-188.

- Mosher, D. C., and Piper, D. J. W., 2007. Analysis of Multibeam seafloor imagery of the Laurentian Fan and the 1929 Grand Banks landslide area. In: Lykousis, V., Sakellariou, D., and Locat, J. (eds.), *Submarine Mass Movements and Their Consequences, Advances in Natural and Technological Hazards Research*, Vol. 27, p. 77-88, Springer, Dordrecht.
- Mosher, D.C., and West, M.T.N., 2007. CCGS Hudson 2007020 Cruise Report: Laurentian Fan and eastern Scotian Slope, Argentia to Halifax; Geological Survey of Canada, Open File 5668, 1 DVD.
- Mosher, D. C., Moran, K., and Hiscott, R.N., 1994. Late Quaternary Sediment, Sediment Mass Flow Processes and Slope Stability on the Scotian Slope, Canada, *Sedimentology*, Vol. 41, p.1039-1061.
- Mosher, D. C., Piper, D. J. W., Campbell, D. C., and Jenner K. A., 2004. Near surface geology and sediment-failure geohazards of the central Scotian Slope. *AAPG Bulletin*, Vol. 88, No. 6, p. 703-723.
- Mosher, D. C., Bigg, S., and LaPierre, A., 2006. 3D seismic versus multibeam sonar seafloor surface renderings for geohazard assessment: Case examples from the central Scotian Slope. *The Leading Edge* p. 1484-1494.
- Mosher, D. C., Moscardelli, L., Shipp, C., Chaytor, J., Baxter, C., Lee, H., and Urgeles, R., 2010a. Submarine Mass Movements and Their Consequences. In: Mosher, D. C., Shipp, R. C. et al. (eds.), *Submarine Mass Movements and Their Consequences, Advances in Natural and Technological Hazards Research*, Vol. 28, p. 1-10, Springer, Dordrecht. DOI 10.1007/978-90-481-3071-9.
- Mosher, D. C., Xu, Z., and Shimeld, J., 2010b. The Pliocene Shelburne mass-movement and consequent tsunamis, western Scotian Slope. In: Mosher, D. C., Shipp, R. C. et al. (eds.), *Submarine Mass Movements and Their Consequences, Advances in Natural and Technological Hazards Research*, Vol. 28, p. 765-776, Springer, Dordrecht. DOI 10.1007/978-90-481-3071-9.
- Mosher, D. C., Piper, D. J. W., MacKillop, K., and Jarrett, K., 2010c. Near surface geology of the Halibut Channel region of the SW Newfoundland Slope from GSC data holdings. Geological Survey of Canada, Open File 6214, p. 1-72.

- Nisbett, E.G. and Piper, D.J.W. 1998. Giant submarine landslides. *Nature*, Vol. 392, p. 329-330.
- Pacheco Silva F., (1970). A new graphical construction for determination for the pre-consolidation stress of a soil sample. In: *Proceedings of the 4th Brazilian Conference on Soil Mechanics and Foundation Engineering*, Rio de Janeiro, Brazil. Vol. 2, No. 1, p. 225-232.
- Piper, D. J. W., 1985. Cruise Report Hudson 85-001: BIO to St Johns, 18-29 March 1985, Scotian Slope and Laurentian Fan. Geological Survey of Canada (Atlantic), p. 1-3.
- Piper, D. J. W., 1986. Cruise Report Hudson 86-034: St. John's – BIO, 4 November – 16 November 1986. Geological Survey of Canada (Atlantic), p. 1-25.
- Piper, D. J. W., and Mudie, P. J., 1991. Cruise Report Hudson 91-020: BIO – St. John's, 11 June – 4 July 1991. Geological Survey of Canada (Atlantic), p. 1-179.
- Piper, D. J. W., 1992. Cruise Report Hudson 92-52: BIO – BIO, 7 December – 17 December 1992. Geological Survey of Canada (Atlantic), GSC projects 810047 & 820044, p. 1-30.
- Piper, D. J. W., 1999. Cruise Report Hudson 99-036: Sydney, N. S. – BIO, 19 August – 8 September 1999. Geological Survey of Canada (Atlantic), p. 1-93.
- Piper, D. J. W., 2001. Cruise Report Hudson 2001-043: St. John's – BIO, 4 August – 19 August 2001. Geological Survey of Canada (Atlantic), p. 1-39.
- Piper, D. J. W., 2005. Cruise Report Hudson 2004-024: Geohazards on the continental margin off Newfoundland. Geological Survey of Canada, Open File 4965, p. 1-55.
- Piper, D. J. W., 2006. Cruise Report Hudson 2003-033: Geohazards on the Continental Margin off Newfoundland. Geological Survey of Canada, Open File 5081, p. 1-48.
- Piper, D. J. W., and Aksu, A. E., 1987. The source and origin of the 1929 Grand Banks turbidity current inferred from sediment budgets. *Geo-Marine Letters*, Vol. 7, p. 177-182.
- Piper, D. J. W., and Normark, W. R., 1982. Acoustic interpretation of Quaternary sedimentation and erosion on the channelled upper Laurentian Fan, Atlantic margin of Canada. *Canadian Journal of Earth Sciences*, Vol. 19, p. 1974-1984.

- Piper, D. J. W., and Normark, W. R., 1989. Late Cenozoic sea-level changes and the onset of glaciation: impact on continental slope progradation off eastern Canada. *Marine and Petroleum Geology*, Vol. 6, p. 336-347.
- Piper, D. J. W., and Skene, K. I., 1998. Latest Pleistocene ice-rafting events on the Scotian Margin (eastern Canada) and their relationship to Heinrich events. *Paleoceanography*, Vol. 13, No. 2, p. 205-214.
- Piper, D. J. W., and Mosher, D. C., 2002. Cruise Report Hudson 2002-046: Scotian Slope, August 15 – September 5, 2002. Geological Survey of Canada, project 980013, p. 1-63.
- Piper, D. J. W., Shor, A. N., and Hughes Clarke, J. E., 1988. The 1929 “Grand Banks” earthquake, slump, and turbidity current. In: *Sedimentological Consequences of Convulsive Geologic Events* (Ed. By H. E. Clifton), Geological Society of America Special Paper, Vol. 229, p. 77- 92.
- Piper, D. J. W., Mudie, P. J., Fader, G. B., Josenhans, H. W., MacLean, B., and Vilks, G., 1990. Quaternary Geology, Chapter 10. In: Keen, M. J., and Williams, G. L. (eds). *Geology of the Continental Margin of Eastern Canada*, Geological Survey of Canada, Geology of Canada, No. 2, p. 475-607.
- Piper, D. J. W., Mudie, P., Aksu, A. E., and Skene, K. I., 1994. A 1 Ma record of sediment flux south of the grand banks used to infer the development of glaciation in southeastern Canada. *Quaternary Science Reviews*, Vol. 13, p. 23-37.
- Piper, D. J. W., Cochonat, P., and Morrison, M. L., 1999. The sequence of events around the epicentre of the 1929 Grand Banks earthquake: initiation of debris flows and turbidity current inferred from sidescan sonar. *Sedimentology*, Vol. 46, p. 79-97.
- Piper, D.J.W., Mosher, D.C., Gauley, B.-J., Jenner K. and Campbell, D.C., 2003. The chronology and recurrence of submarine mass movements on the continental slope off southeastern Canada. In: Locat, J., Mienert, J. and Boisvert, L. (eds.) *Submarine Mass Movements and Their Consequences*, Advances in Natural and Technological Hazards Research, Vol. 19., p. 299-306. Springer, Dordrecht.
- Piper, D. J. W., Macdonald, A. W. A., Ingram, S., Williams, G. L., and McCall, C., 2005. Late Cenozoic architecture of the St. Pierre Slope. *Canadian Journal of Earth Sciences*, Vol. 42, p. 1987-2000, doi:10.1139/E05-059.

- Piper, D. J. W., Shaw, J., and Skene, K. I., 2007. Stratigraphic and sedimentological evidence for late Wisconsinan sub-glacial outburst floods to Laurentian Fan. *Palaeogeography, Palaeoclimatology, Palaeoecology*, Vol. 246, p. 101-119.
- Poulos, H. G., 1988. *Marine Geotechnics*. Academic Division of Unwin Hyman Ltd, London, p. 1-473.
- Rebesco, M., Mosher, D., and Piper, D. J. W., 2017. Advancements in Understanding Deep-Sea Clastic Sedimentation Processes: a preface. *Marine Geology*, Vol. 393, p. 1-3.
- Roberts, J. A., and Cramp, A., 1996. Sediment stability on the western Flanks of the Canary Islands. *Marine Geology*, Vol. 134, p. 13-30.
- Ruffman, A., 2001. Potential for large-scale submarine slope failure and tsunami generation along the U. S. mid-Atlantic coast: Comment. *Geology*, Vol. 29, No. 10, p. 967.
- Sangree, J. B., and Widmier, J. M., 1979. Interpretation of depositional facies from seismic data. *Geophysics*, Vol. 44, No. 2, p. 131-160.
- Schneider, R., 2015. Short Cruise Report, Maria S. Merian cruise MSM45, Nuuk (Greenland) – Halifax (Canada), 01.08.2015-22.08.2015. Maria S. Merian-Berichte, MSM47, p. 1-7.
- Schulten, I., Mosher, D. C., Krastel, S., Piper, D. J. W., and Kienast, M., 2019. Surficial sediment failures due to the 1929 Grand Banks Earthquake, St Pierre Slope. From: Lintern, D. G., Mosher, D. C., et al. (eds). *Subaqueous Mass Movements*. Geological Society, London, Special Publications, 477, <https://doi.org/10.1144/SP477.25>.
- Shaw, J., Piper, D.J.W., Fader, G.B., King, E.L., Todd, B.J., Bell, T., Batterson, M.J., and Liverman, D.J.E., 2006. A conceptual model of the deglaciation of Atlantic Canada. *Quaternary Science Reviews*, Vol. 25, p. 2059-2081.
- Skempton, A. W., 1954. The Structure of Inorganic Soil (discussion). *Proceedings, ASCE*, Vol. 80, separate 478, p. 19-22.
- Skempton, A. W., 1970. The Consolidation of Clays by Gravitational compaction. *Quarterly Journal of the Geological Society of London*, Vol. 125, p. 373-412.

- Skene, K. I., and Piper, D. J. W., 2003. Late Quaternary stratigraphy of Laurentian Fan: a record of events off the eastern Canadian continental margin during the last deglacial period. *Quaternary International*, Vol. 99-100, p. 135-152.
- Skene, K. I., and Piper, D. J. W., 2006. Late Cenozoic evolution of Laurentian Fan: Development of a glacially-fed submarine fan. *Marine Geology*, Vol. 227, p. 67-92.
- Skinner, L. C., and McCave, I. N., 2003. Analysis and modelling of gravity- and piston coring based on soil mechanics. *Marine Geology*, Vol. 199, p. 181-204.
- Spieß, V., 1993. Digitale Sedimentechographie – Neue Wege zu einer hochauflösenden Akustostratigraphie. *Berichte Fachbereich Geowissenschaften Universität Bremen*, Vol. 35, pp. 1–199.
- Sultan, N., Cochonat, P., Canals, M., et al., 2004. Triggering mechanisms of slope instability processes and sediment failures on continental margins: a geotechnical approach. *Marine Geology*, Vol. 213, p. 291-321.
- Synolakis, C. E., Bardet, J., Borrero, J. C., Davies, H. L., Okal, E. A., Silver, E. A., Sweet, S., and Tappin, D. R., 2002. The slump origin of the 1998 Papua New Guinea Tsunami. *Proc. Royal Soc. London*, Vol. 458, p. 763-789.
- Talling, P. J., Wynn, R. B., Masson, D. G., Frenz, M., Cronin, B. T., Schiebel, R., Akhmetzhanov, A. M., Dallmeier-Tiessen, S., Benetti, S., Weaver, P. P. E., Georgiopoulou, A., Zühlsdorff, C., and Amy, L. A., 2007. Onset of submarine debris flow deposition far from original giant landslide. *Nature letters*, Vol. 450, p. 541-544, doi:10.1038/nature06313.
- Tappin, D. R., Watts, P., McMurty, G. M., Lafoy, Y., and Matsumoto, T., 2001. The Sissano, Papua New Guinea tsunami of July 1998 – offshore evidence on the source mechanism. *Marine Geology*, Vol. 175, p. 1-23.
- Tappin, D. R., Watts, P., and Matsumoto, T., 2003. Architecture and failure mechanisms of the offshore slump responsible for the 1998 Papua New Guinea tsunami. In: Locat, J., Mienert, J., and Boisvert, L. (eds), *Submarine Mass Movements and their Consequences, Advances in Natural and Technological Hazards Research*, p. 383-392, Springer, Dordrecht.

- Tappin, D. R., Watts, P., Grilli, S. T., 2008. The Papua New Guinea tsunami of 17 July 1998: anatomy of a catastrophic event. *Natural Hazards and Earth System Science*, Copernicus Publications on behalf of the European Geosciences Union, Vol. 8, No. 2, p. 243-266. <hal-00299504>.
- Teledyne Reson, 2017. ATLAS PARASOUND Deep-Sea parametric sub-bottom profiler. <http://www.teledynemarine.com/parasound-sub-bottom-profilers?ProductLineID=79/>, Slangerup, Denmark.
- Twichell, D. C., Chaytor, J. D., ten Brink, U. S., and Buczkowski, B., 2009. Morphology of late Quaternary submarine landslides along the U. S. Atlantic continental margin. *Marine Geology*, Vol. 264, p. 4-15.
- Uchupi, E., and Austin, J. A., 1979. The stratigraphy and structure of the Laurentian Cone region. *Canadian Journal Earth Science*, Vol. 16, p. 1726-1752.
- Urlaub, M., Talling, P. J., and Masson, D. G., 2013. Timing and frequency of large submarine landslides: implications for understanding triggers and future geohazard. *Quaternary Science Reviews*, Vol. 72, No. 6, p. 63-82.
- Urgeles, R., and Camerlenghi, A., 2013. Submarine landslides of the Mediterranean Sea: Trigger mechanisms, dynamics, and frequency-magnitude distribution. *Journal of Geophysical Research and Earth Surface*, Vol. 118, p. 2600-2618, doi: 10.1002/2013JF002720.
- van der Zee, W., and Urai, J. L., 2005. Processes of normal fault evolution in a siliciclastic sequence: a case study from Miri, Sarawak, Malaysia. *Journal of Structural Geology*, Vol. 27, p. 2281-2300.
- van der Zee, W., Wibberley, C. A. J., and Urai, J. L., 2008. The influence of layering and pre-existing joints on the development of internal structure in normal fault zones: the Lodève basin, France. In: Wibberley, C. A. J., Kurz, W., Imber, J., et al. (eds) *The Internal Structure of Fault Zones: Implications for Mechanical and Fluid-Flow Properties*. Vol. 299, p. 57-74.
- Walsh, J. J., Watterson, J., Bailey, W. R., and Childs, C., 1999. Fault relays, bends and branch-lines. *Journal of Structural Geology*, Vol. 21, p. 1019-1026.
- Weirich, F. H., 1989. The generation of turbidity currents by subaerial debris flows, California. *Geological Society of America Bulletin*, Vol. 101, p. 278-291.

- Williams, G. D., Powell, C. M., and Cooper, M. A., 1989. Geometry and kinematics of inversion tectonics. In: Cooper, M. A., and Williams, G. D. (eds), *Inversion Tectonics*, Geological Society, London, Special Publications, Vol. 44, p. 3-15.
- Winkelmann, D., Geissler, W., Schneider, J., and Stein, R., 2008. Dynamics and timing of the Hinlopen/Yermak Megaslide north of Spitsbergen, Arctic Ocean. *Marine Geology*, Vol. 250, p. 34-50.

APPENDIX 1: CHAPTER 1

Table A1.1: Multibeam swath bathymetry data used in this research thesis.

| cruise ID | year of acquisition | System | expedition reports |
|------------------|----------------------------|---------------|---------------------------|
| 2007020 | 2007 | EM120 | Mosher and West, 2007 |
| MSM45 | 2015 | EM122 | Schneider et al., 2015 |
| MSM47 | 2015 | EM122 | Krastel et al., 2016 |

Table A1.2: Ultra-high resolution seismic data used in this research thesis.

| cruise ID | year of acquisition | Hunted (H)/ 3.5 kHz data (3.5)/ Parasound (P) | digitized from scan | digital | expedition reports |
|------------------|----------------------------|--|--------------------------------|----------------|---------------------------|
| 86034 | 1986 | H | x | | Piper, 1986 |
| 90015 | 1990 | 3.5 | x | | |
| 91020 | 1991 | H | x | | Piper and Mudie, 1991 |
| 9252 | 1992 | H | x | | Piper, 1992 |
| 99036 | 1999 | H | | x | Piper, 1999 |
| 2001043 | 2001 | H | | x | Piper, 2001 |
| 2002046 | 2002 | H | | x | Piper and Mosher, 2002 |
| 2003033 | 2003 | H | | x | Piper, 2006 |
| 2004024 | 2004 | H | | x | Piper, 2005 |
| 2007020 | 2007 | H | | x | Mosher and West, 2007 |
| MSM45 | 2015 | P | | x | Schneider et al., 2015 |
| MSM47 | 2015 | P | | x | Krastel et al., 2016 |

Table A1.3: 2D seismic reflection data used in this thesis. All data are high-resolution seismic (<2 km signal penetration), except for TGS and STP data sets that are industry-scale seismic data (>5 km signal penetration).

| cruise ID | year of acquisition | sleevegun (SG)/airgun (AG) | digitized from scan | digital | single-channel | multi-channel | expedition reports and publications showing data | data source and processing |
|-----------|---------------------|----------------------------|---------------------|---------|----------------|---------------|--|---|
| 81044 | 1981 | AG | X | | | X | Geomarine Associates Ltd., 1982 | processed by GSI in Calgary; GSC Holding, scanned copy |
| 84040 | 1984 | AG | X | | X | | | GSC Holding, scanned copy |
| STP | 1984-1985 | AG | | X | | X | MacLean and Wade, 1992 | GSC Holding, digital SEG-Y data |
| 85001 | 1985 | AG | X | | X | | Piper, 1985 | GSC Holding, scanned copy |
| 86034 | 1986 | AG | X | | X | | Piper, 1986 | GSC Holding, scanned copy |
| 87003 | 1987 | AG | X | | X | | Manchester, 1987 | GSC Holding, scanned copy |
| 90015 | 1990 | SG | X | | X | | | GSC Holding, scanned copy |
| 91020 | 1991 | SG | X | | X | | Piper and Mudie, 1991 | GSC Holding, scanned copy |
| 9252 | 1992 | SG | X | | X | | Piper, 1992 | GSC Holding, scanned copy |
| TGS Nopec | 1998 | | | X | | X | Shimeld, 2005 | processed by TGS Nopec |
| 99036 | 1999 | SG | | X | X | | Piper, 1999 | from tape |
| 2001043 | 2001 | SG | | X | X | | Piper, 2001 | from tape |
| 2002046 | 2002 | SG | | X | X | | Piper and Mosher, 2002 | from tape |
| 2003033 | 2003 | GI AG | | X | X | | Piper, 2006 | GSC Holding, digital SEG-Y data |
| 2004024 | 2004 | GI AG | | X | X | | Piper, 2005 | GSC Holding, digital SEG-Y data |
| 2007020 | 2007 | GI AG | | X | X | | Mosher and West, 2007 | GSC Holding, processed digital SEG-Y data (GSCA in-house software GDBatch 2, v. 1.40, bild 0010; Gedco VISTA 6; 25/40/250/300 OBF, surgical mute) |
| MSM47 | 2015 | AG | | X | | X | Krastel et al., 2016 | Data used in this study were processed by Schulten, I. using the VISTA 12 (Schlumberger) NRCan license; standard processing flow included a 20/40/600/1000 Hz Ormsby Band Pass Filter (OBPF), geometry set up, binning to 4x25 m, normal moveout (NMO) correction, trace editing, common-mid-point (CMP) stacking and a finite-difference (FD) migration with a constant velocity of 1500 m s ⁻¹ |

APPENDIX 2: CHAPTER 4

A2.1 DETERMINATION OF SEDIMENT PROPERTIES

A2.1.1 Core Physical properties

A. Undrained shear strength from laboratory miniature shear vane measurements

The torque that a four bladed vane requires to shear a cylindrical surface of the sediment is measured and the undrained shear strength calculated as follow (Carter et al., 1999; Braja, 2010):

$$S_u = \frac{T}{K_f} \left[\frac{kN}{m^2} \text{ or } kPa \right] \quad (1)$$

with S_u = undrained shear strength (kPa)

T = torque at failure, in Nm, measured by the instrument in kg cm, converted using $T [Nm] = 0.0981 * T [kg cm]$

$$K_f = \pi * \left(\frac{d^2 * h}{2} + \frac{d^3}{6} \right) [m^3]$$

with d = width and h = length of the vane

B. Water content (w)

$$w = \frac{w_t - w_s}{w_s - s * w_t} * 100 [\%] \quad (2)$$

with w_t = total weight of soil (g)

w_s = weight of solids

s = correction for salinity = 0.035

C. Void ratio (e)

$$e = \frac{V_V}{V_S} \quad (3)$$

with V_V = volume of voids (cm³) $V_V = 1 - V_S$ (3a)

$$V_s = \text{volume of solids (cm}^3\text{)} \quad V_s = \frac{M_s}{\rho_s} \quad (3b)$$

with $M_s = \text{mass of solids (g)}$

$\rho_s = \text{density of the solids (g cm}^{-3}\text{)}$

D. Porosity (η)

$$\eta = \frac{V_v}{V_t} \quad (4)$$

with $V_v = \text{volume of voids (cm}^3\text{)}$

$V_t = \text{total volume (cm}^3\text{)}$

$$\eta = \frac{\rho_s - \rho_t}{\rho_s - \rho_w} \quad (5)$$

with $\rho_s = \text{density of the solids (g cm}^{-3}\text{)}$

$\rho_t = \text{total density (g cm}^{-3}\text{)}$

$\rho_w = \text{density of the fluid (g cm}^{-3}\text{)}$

$$\eta = \frac{e}{1 + e} * 100 \quad (6)$$

with $e = \text{void ratio, see equation (3) of appendix.}$

A2.1.2 Consolidation testing

A. E-log- p' curve to determine P'_c :

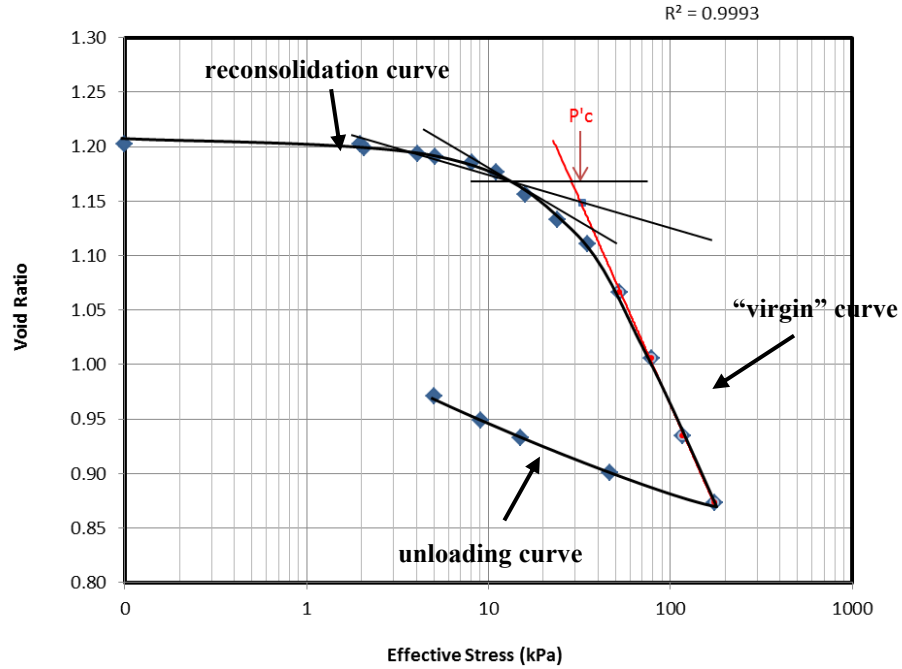


Fig. A2.1: E - log p' curve derived from the consolidation testing on a sample (553 cm) from sediment core 2015MSM_0002GC. Cassagrande's method to derive P'_c over the point of maximum curvature is illustrated.

B. Initial void ratio (e_0)

$$e_0 = \frac{V_v}{V_s} = \frac{H_v * A}{H_s * A} = \frac{H_v}{H_s} \quad (7)$$

with: V_v = volume of voids (cm^3)

V_s = volume of solids (cm^3)

$$H_s = \text{height solids (cm)}, \left[H_s = \frac{W_s}{A * G_s * \gamma_w} = \frac{M_s}{A * G_s * \rho_w} \right], \quad (7a)$$

where W_s = weight of the solids (g), G_s = specific gravity of the sediment solids, γ_w = unit weight of water (kN cm^{-3}), M_s = mass of solids (g), and ρ_w = density of water (g cm^{-3})

$$H_v = \text{height of voids (cm), calculated as } [H_v = H - H_s], \quad (7b)$$

with H = initial height of specimen (cm)

A = area of specimen (cm^2)

C. Void ratio at different stages (e_x)

$$\Delta e_x = \frac{\Delta H_x}{H_s} \quad (8)$$

$$e_x = e_{x-1} - \Delta e_x \quad (9)$$

with Δe_x = difference of void ratio between two stages
 ΔH_x = difference in height between two stages (cm)
 H_s = height of solids (cm)
 e_x = void ratio at stage x
 e_{x-1} = void ratio of the stage before stage x

D. Coefficient of consolidation (C_v)

Taylor's square-root-of-time method (1942) was used to determine the coefficient of consolidation (C_v). The coefficient of consolidation (C_v) provides the rate of compression of sediment and is calculated as follow (Braja, 2010):

$$C_v = \frac{T_{90} * H_{DR}^2}{t_{90}} \left[\frac{cm}{min} \right] \quad (10)$$

with T_{90} = dimensionless time factor for 90% consolidation = 0.848
 t_{90} = time needed to reach 90% consolidation (min), determined graphically (Fig. A2.2)
 H_{DR} = average longest drainage path during consolidation, for one-side drainage equal to the average height of the specimen during consolidation (cm)

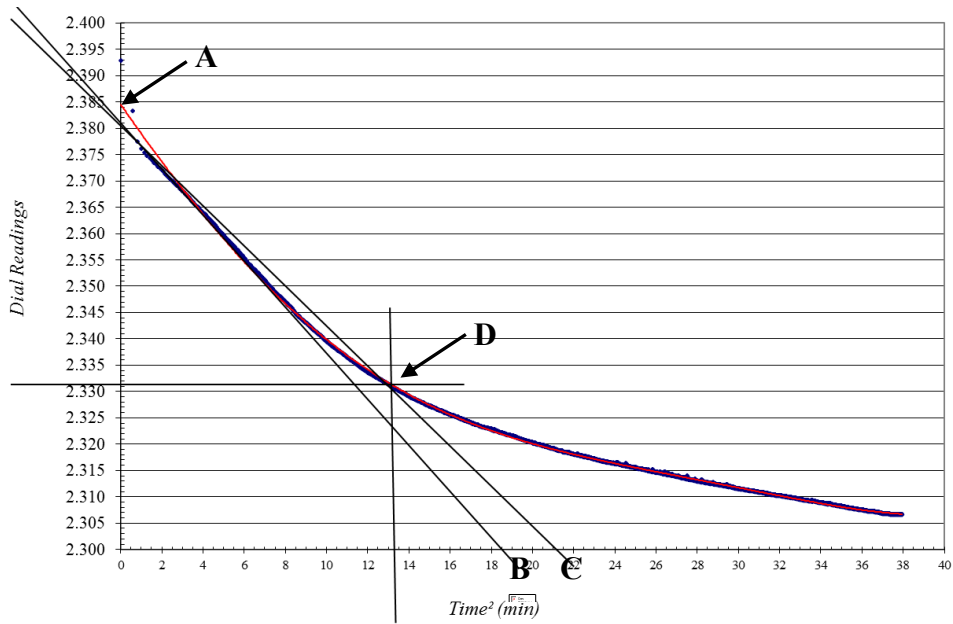


Fig. A2.2: Square-root-of-time method according to Taylor (1942).

- a) Line AB, drawn through the early portion of the curve
- b) Line AC, with $C = 1.15 * B$, the intersection (D) of AC with the consolidation curve then gives the square root of time for 90% of the consolidation ($\sqrt{t_{90}}$)

E. Hydraulic conductivity

$$k = C_v * M_v * \rho_w * g \quad [cm \ s^{-2}] \quad (11)$$

with: C_v = coefficient of consolidation ($cm \ min^{-1}$)

M_v = change in void ratio with changing consolidation ($N \ cm^{-1}$)

g = gravitational acceleration

ρ_w = density of water = $\sim 1000 \ (kg \ cm^{-3})$

Hydraulic conductivity vs. void ratio

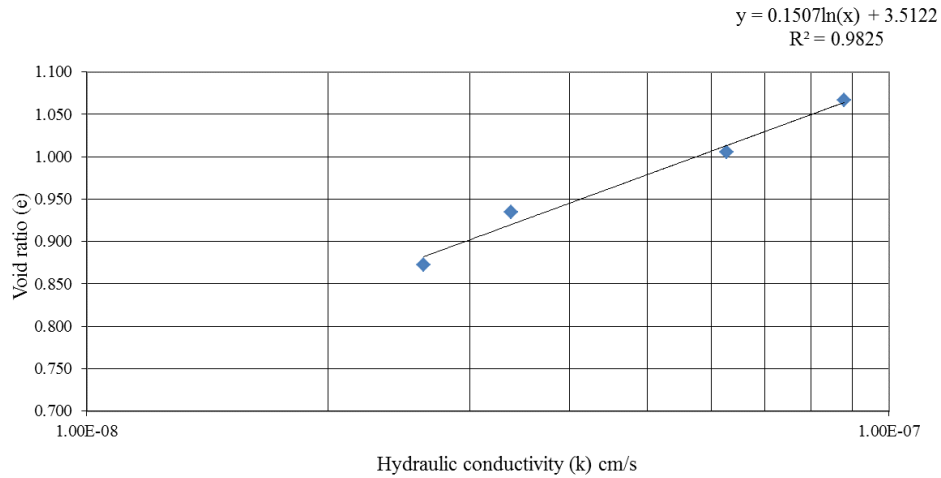


Fig. A2.3: Plot of derived void ratio (e) versus the hydraulic conductivity (k) derived for different load increments. The derived linear relationship of this $e - \log k$ curve can be used to calculate the hydraulic conductivity at the effective pre-consolidation state.

F. Hydrostatic effective stress or total effective overburden stress (P'_{vo})

$$P'_{vo} = P_{vo} - u \quad [kPa] \quad (12)$$

with P_{vo} = total overburden stress (kPa)
 u = pore pressure = $u = \Delta u + u_h$, with Δu = overpressure and u_h = hydrostatic pore pressure

$$P'_{vo} = \gamma_s * depth \quad (12a)$$

$$P'_{vo} = \rho_s * a_g * depth \quad (12b)$$

with γ_s = unit weight of solids (kN/cm³)
 ρ_s = density of solids (g cm⁻³) equal to $(\rho - \rho_w)$, with ρ = MST bulk density (g cm⁻³) and ρ_w = density of water = 1.024 g cm⁻³
 a_g = acceleration gravity (m s⁻²)

A2.1.3 Triaxial testing

A. Skempton's pore pressure parameter at failure (A_f)

$$A_f = \frac{\Delta u_f}{\Delta \sigma_d} \quad (13)$$

with Δu_f = pore pressure increase at failure
 $\Delta \sigma_d$ = deviator stress at failure

B. Mohr Coulomb failure criteria

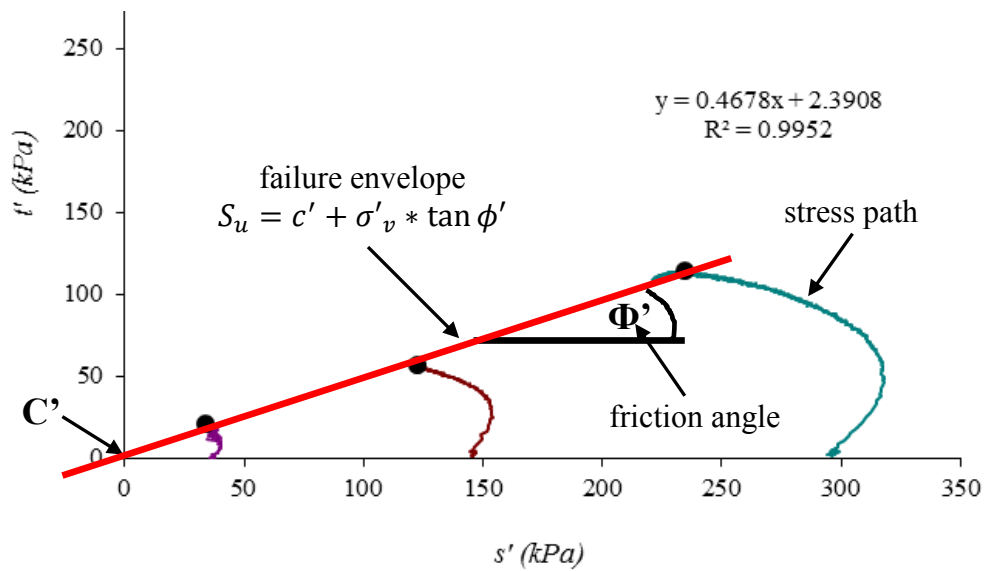


Fig. A2.4: Stress path's derived for the triaxial sample of sediment core 2015MSM_0002GC, 563-575cm. Red line shows the derived failure envelope, as described by the Mohr-Coulomb criterion.

A2.2 FACTOR OF SAFETY – PEAK GROUND ACCELERATION CONVERSIONS

A2.2.1 Equation used according to Atkinson and Boore (2006)

$$\log PGA = c_1 + c_2 * M + c_3 * M^2 + (c_4 + c_5 * M) * f_1 + (c_6 + c_7 * M) * f_2 + (c_8 + c_9 * M) * f_0 + c_{10} * R_{cd} + S \text{ [cm s}^{-2}\text{]} \quad (14)$$

with: c_{0-6} = empirical coefficients: $c_0 = -1.715$; $c_1 = 0.5$; $c_2 = -0.53$; $c_3 = -0.262$; $c_4 = -2.118$; $c_5 = 0.17$; $c_6 = 5.6$; $c_7 = 0.28$; $c_8 = -0.12$; $c_9 = 0.49$; $c_{10} = 1.058$ (cm s⁻²)

f_{0-2} = coefficients depending on the rupture distance

M = earthquake magnitude

R_{cd} = closest distance to rupture surface (km) e.g. 33 km

S = correction for soil sites, if $pgaBC > 60$ cm s⁻²:

$$S = \log \left\{ \exp \left[b_{lin} * \ln \left(\frac{V_{30}}{V_{ref}} \right) + b_{nl} * \ln \left(\frac{pgaBC}{100} \right) \right] \right\} \quad (14a)$$

if $pgaBC < 60$ cm s⁻²:

$$S = \log \left\{ \exp \left[b_{lin} * \ln \left(\frac{V_{30}}{V_{ref}} \right) + b_{nl} * \ln \left(\frac{60}{100} \right) \right] \right\} \quad (14b)$$

with: $pgaBC$ = from equation (14) without S

v_{30} = time-averaged-shear wave velocity
= ~152 m s⁻¹ from triaxial testing

v_{ref} = reference velocity 760 m s⁻¹

b_{lin} = -0.361

b_{nl} = a nonlinear factor; $b_{nl} = b_1$, if $V_{30} < V_1$
with $V_1 = 180$ m s⁻¹

b_1 = -0.641

A2.2.2 Equations used according to Campbell and Bozorgnia (2008)

$$\ln PGA = f_{mag} + f_{dis} + f_{flt} + f_{hng} + f_{site} + f_{sed} \quad [g] \quad (15)$$

with: f_{mag} = earthquake magnitude; f_{dis} = rupture distance; f_{flt} = fault component; f_{hng} = hanging wall component; f_{site} = site, and f_{sed} = sediment correction, f_{hng} is zero according to Campbell and Bozorgnia (2008) specifications

M_w 4 & M_w 5

$$\ln PGA = (c_0 + c_1 * M) + [(c_4 + c_5 * M) * \ln(\sqrt{R_{RUP}^2 + c_6^2})] + (c_8 * F_{NM}) + c_{10} * \ln\left(\frac{v_{30}}{k_1}\right) + k_2 \left\{ \ln \left[A_{1100} + c \left(\frac{v_{30}}{k_1} \right)^n \right] - \ln[A_{1100} + c] \right\} + \{c_{12} * k_3 * e^{-0.75} [1 - e^{-0.25 * (Z_{2.5} - 3)}]\} \quad (15a)$$

M_w 6

$$\ln PGA = [(c_0 + c_1 * M) + c_2 * (M - 5.5)] + [(c_4 + c_5 * M) * \ln(\sqrt{R_{RUP}^2 + c_6^2})] + (c_8 * F_{NM}) + c_{10} * \ln\left(\frac{v_{30}}{k_1}\right) + k_2 \left\{ \ln \left[A_{1100} + c \left(\frac{v_{30}}{k_1} \right)^n \right] - \ln[A_{1100} + c] \right\} + \{c_{12} * k_3 * e^{-0.75} [1 - e^{-0.25 * (Z_{2.5} - 3)}]\} \quad (15b)$$

M_w 7.2

$$\ln PGA = [(c_0 + c_1 * M) + c_2 * (M - 5.5) + c_3 * (M - 6.5)] + [(c_4 + c_5 * M) * \ln(\sqrt{R_{RUP}^2 + c_6^2})] + (c_8 * F_{NM}) + c_{10} * \ln\left(\frac{v_{30}}{k_1}\right) + k_2 \left\{ \ln \left[A_{1100} + c \left(\frac{v_{30}}{k_1} \right)^n \right] - \ln[A_{1100} + c] \right\} + \{c_{12} * k_3 * e^{-0.75} [1 - e^{-0.25 * (Z_{2.5} - 3)}]\} \quad (15c)$$

with: c_{0-6} = empirical coefficients: $c_0 = -1.715$; $c_1 = 0.5$; $c_2 = -0.53$; $c_3 = -0.262$; $c_4 = -2.118$; $c_5 = 0.17$; $c_6 = 5.6$; $c_7 = 0.28$; $c_8 = -0.12$; $c_9 = 0.49$; $c_{10} = 1.058$ (g)

M = earthquake magnitude

R_{RUP} = closest distance to rupture surface (km) e.g. 33 km for 1929

R_{JB} = Joyner-Boore distance to epicentre (km) e.g. 26 km for 1929

Z_{TOR} = depth to top of rupture surface (km) = 20 km for 1929, for recent earthquakes = 18 km

F_{NM} = indicator variable for normal and normal-oblique faulting = 1 ($\lambda \approx 140^\circ$, Bent, 1995)

δ = dip of rupture surface ($^\circ$)

v_{30} = time-averaged-shear wave velocity $\approx 152 \text{ m s}^{-1}$ from triaxial testing

A_{1100} = median estimate of PGA on a reference rock outcrop
 ($v_{30}=1100 \text{ m s}^{-1}$) = unknown, tested 0.01-1.0 g
 $Z_{2.5}$ = depth to 2.5 km s^{-1} shear-wave velocity horizon or sediment depth
 (km) = ~ 3.5 km from 2D seismic data
 $k_1 = 865 \text{ m s}^{-1}$; $k_2 = -1.186 \text{ g}$; $k_3 = 1.839 \text{ g}$; $c = 1.88$; $n = 1.18$

A2.2.3 Sediment density calculation using porosity information derived from Kominz et al. (2011)

A2.2.3.1 KOMINZ ET AL. (2011) POROSITY TREND

Kominz et al. (2011) suggested a change in porosity with increasing sub-bottom depth for different sediment material on the basis of ODP core data. Kominz et al. (2011) trend for clay-rich sediments >172 m was used in this study, as constant volume samples from the core show lower porosities than those presented in Kominz et al. (2011) for sediments <172 m.

$$\eta = 61.4 * \exp\left(\frac{-d}{1671}\right) \quad (16)$$

with $d =$ depth (m)

A2.2.3.2 SEDIMENT DENSITY (ρ_t) USING POROSITY INFORMATION

$$\rho_t = \frac{\rho_s}{\left(\frac{\eta}{100}\right) * (\rho_s - \rho_w)} - 1 \left[\frac{\text{g}}{\text{cm}^{-3}} \right] \quad (17)$$

with $\rho_t =$ total density (g cm^{-3})

$\rho_s =$ density of the solids (g cm^{-3}) = $\sim 2.65 \text{ g cm}^{-3}$

$\eta =$ porosity

$\rho_w =$ density of the fluid (g cm^{-3}) = $\sim 1.024 \text{ g cm}^{-3}$

A2.3 RESULTS

A2.3.1 Lithological core description

A2.3.1.1 2015MSM-0002GC

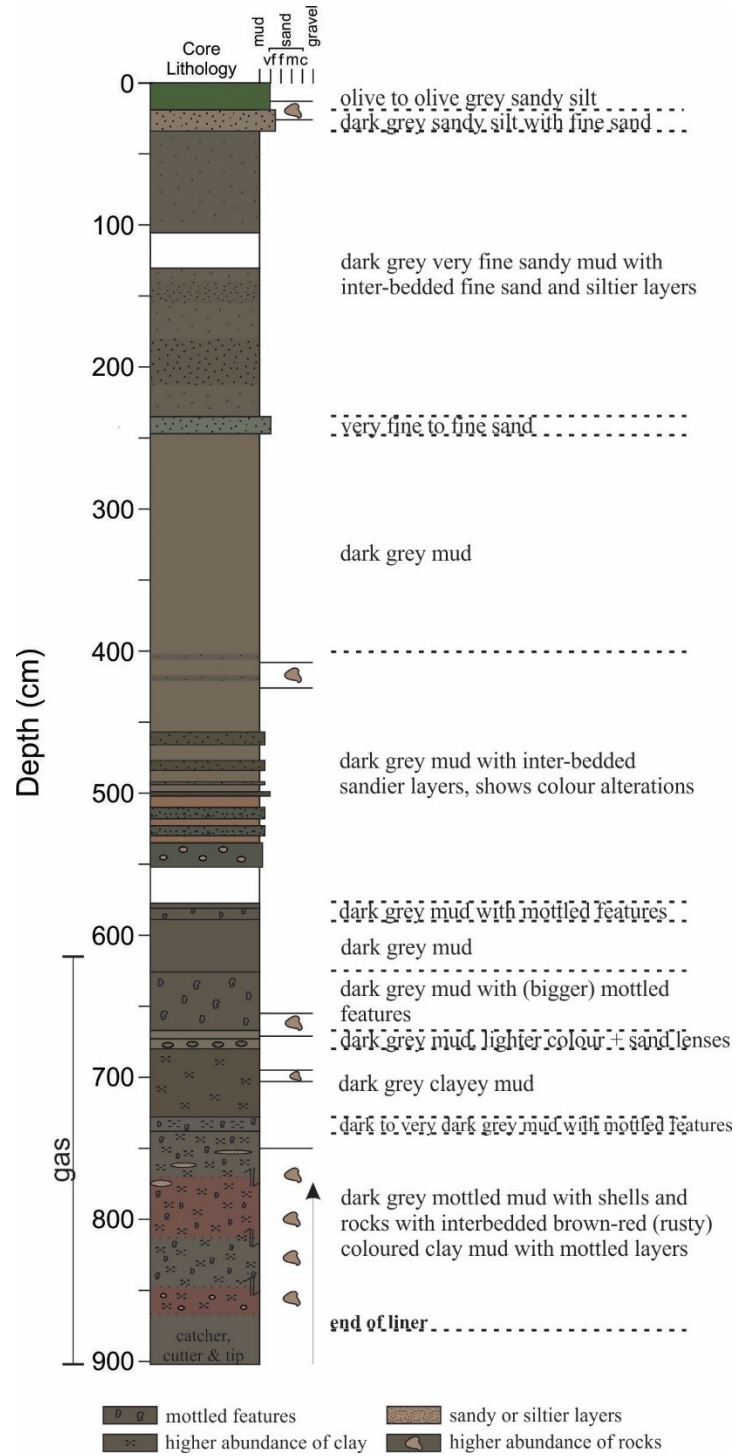


Fig. A2.5: Results of the lithological core description of marine sediment core 2015MSM_0002GC.

A2.3.1.2 MSM47-24-01

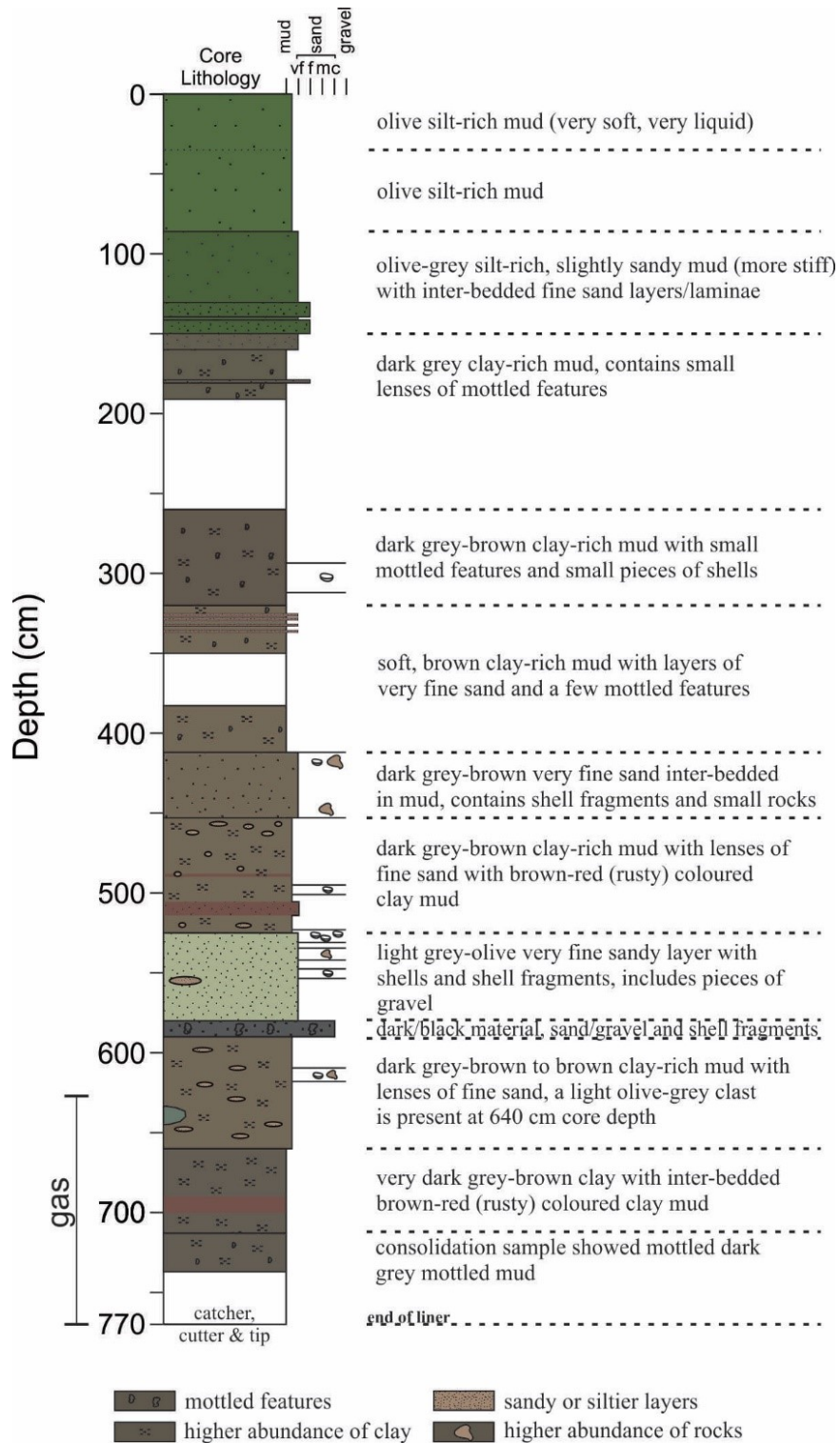


Fig. A2.6: Results of the lithological core description of marine sediment core MSM47-24-01.

A2.3.2 Results Atterberg testing

A2.3.2.1 2015MSM-0002GC, 106-114 CM CORE DEPTH

| <u>Atterberg Limits</u> | |
|-------------------------|-----------------------------|
| Analyst name: | <u>Irena Schulten</u> |
| Test date: | <u>September 26th, 2016</u> |
| Sample description: | <u>2015MSM</u> |
| Sample Number | <u>0002GC</u> |
| Depth (cm) | <u>106-114cm</u> |
| Water Content (%): | <u>46.56</u> |
| Liquid Limit (%): | <u>34.23</u> |
| Plastic Limit (%): | <u>19.73</u> |
| Plasticity Index (%): | <u>14.50</u> |
| Liquidity Index: | <u>1.85</u> |
| Classification: | <u>CL</u> |

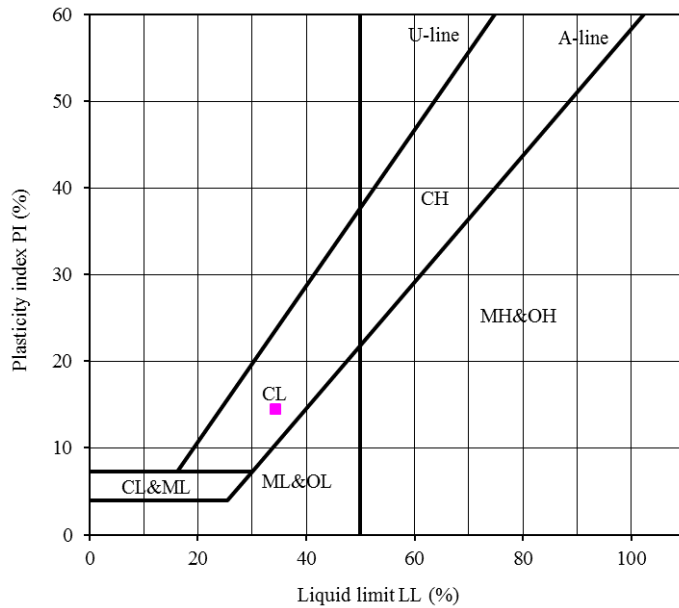


Fig. A2.7: Result of the Atterberg limits testing according to the Cassagrande diagram. Sample at 106 cm core depth of sediment core 2015MSM_0002GC is a lean clay with low to intermediate plasticity.

A2.3.2.2 2015MSM-0002GC, 114-130 CM CORE DEPTH

| <u>Atterberg Limits</u> | |
|-------------------------|-----------------------------|
| Analyst name: | <u>Irena Schulten</u> |
| Test date: | <u>September 28th, 2016</u> |
| Sample description: | <u>2015MSM</u> |
| Sample Number | <u>0002GC</u> |
| Depth (cm) | <u>114-130cm</u> |
| Water Content (%): | <u>41.25</u> |
| Liquid Limit (%): | <u>30.26</u> |
| Plastic Limit (%): | <u>19.67</u> |
| Plasticity Index (%): | <u>10.59</u> |
| Liquidity Index: | <u>2.04</u> |
| Classification: | <u>CL</u> |

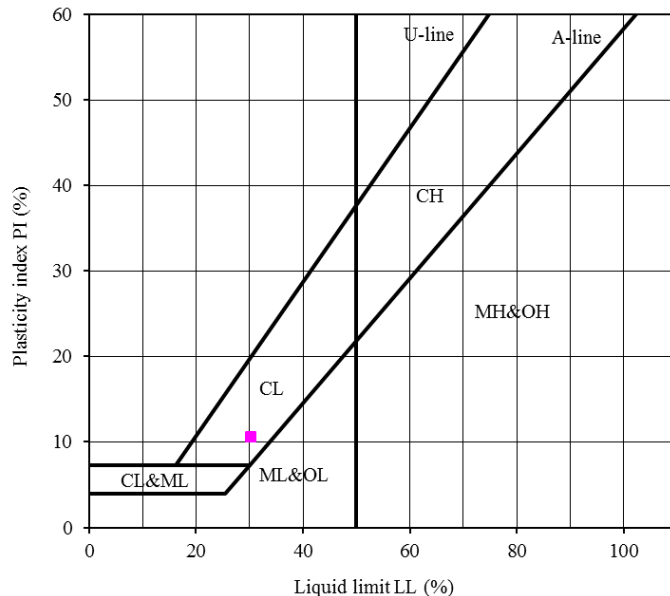


Fig. A2.8: Result of the Atterberg limits testing according to the Cassagrande diagram. Sample at 114 cm core depth of sediment core 2015MSM-0002GC is a lean clay with low to intermediate plasticity.

A2.3.2.3 2015MSM-0002GC, 552-560 CM CORE DEPTH

| <u>Atterberg Limits</u> | |
|-------------------------|---------------------------|
| Analyst name: | <u>Irena Schulten</u> |
| Test date: | <u>February 3rd, 2016</u> |
| Sample description: | <u>2015MSM</u> |
| Sample Number | <u>0002GC</u> |
| Depth (cm) | <u>552-560cm</u> |
| Water Content (%) | <u>43.85</u> |
| Liquid Limit (%) | <u>39.62</u> |
| Plastic Limit (%) | <u>20.30</u> |
| Plasticity Index (%) | <u>19.32</u> |
| Liquidity Index: | <u>1.22</u> |
| Classification: | <u>CL</u> |

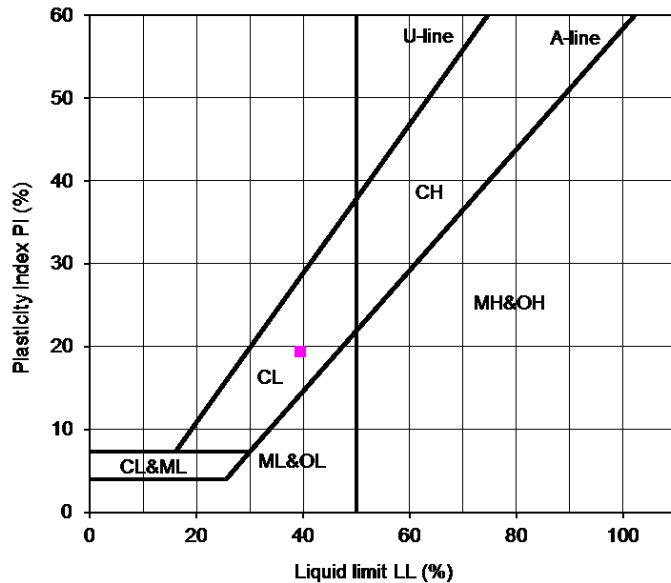


Fig. A2.9: Result of the Atterberg limits testing according to the Cassagrande diagram. Sample at 552 cm core depth of sediment core 2015MSM_0002GC is a lean clay with low to intermediate plasticity.

A2.3.2.4 MSM47-24-01, 190-195 CM CORE DEPTH

| <u>Atterberg Limits</u> | |
|-------------------------|----------------------------|
| Analyst name: | <u>Irena Schulten</u> |
| Test date: | <u>23.05.2017</u> |
| Sample description: | <u>dark olive grey mud</u> |
| Sample Number | <u>2</u> |
| Depth (cm) | <u>190-195 cm</u> |
| Water Content (%) | <u>58.51</u> |
| Liquid Limit (%) | <u>45.02</u> |
| Plastic Limit (%) | <u>22.13</u> |
| Plasticity Index (%) | <u>22.89</u> |
| Liquidity Index: | <u>1.59</u> |
| Classification: | <u>CL</u> |

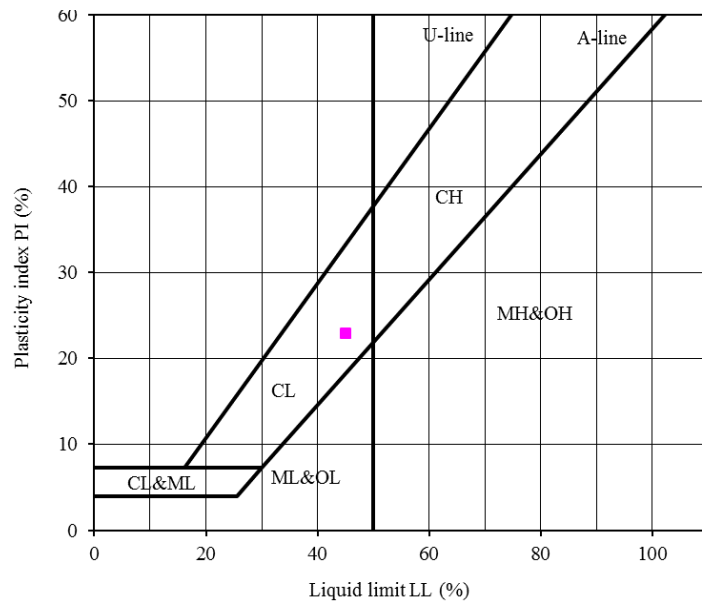


Fig. A2.10: Result of the Atterberg limits testing according to the Cassagrande diagram. Sample at 190 cm core depth of sediment core MSM47-24-01 is a lean clay with low to intermediate plasticity.

A2.3.2.5 MSM47-24-01, 195-200 CM CORE DEPTH

| <u>Atterberg Limits</u> | |
|-------------------------|----------------------------|
| Analyst name: | <u>Irena Schulten</u> |
| Test date: | <u>23.05.2017</u> |
| Sample description: | <u>dark olive grey mud</u> |
| Sample Number | <u>3</u> |
| Depth (cm) | <u>195-200 cm</u> |
| Water Content (%): | <u>57.50</u> |
| Liquid Limit (%): | <u>45.63</u> |
| Plastic Limit (%): | <u>19.82</u> |
| Plasticity Index (%): | <u>25.81</u> |
| Liquidity Index: | <u>1.46</u> |
| Classification: | <u>CL</u> |

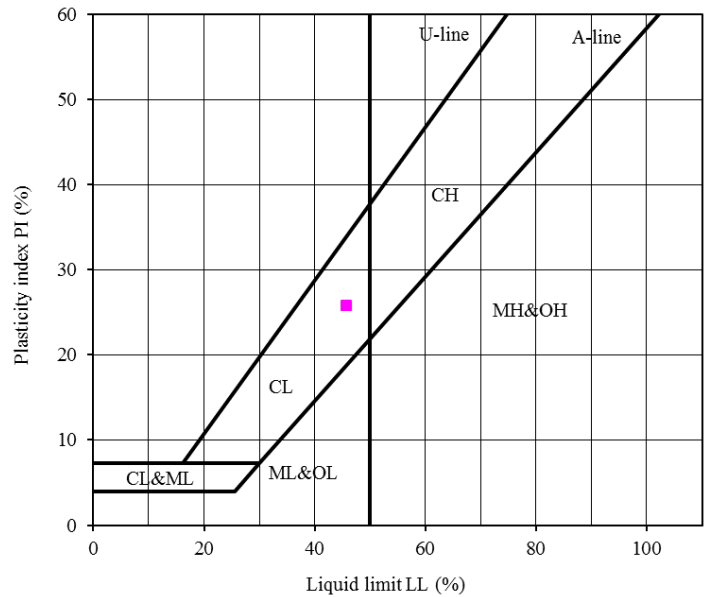


Fig. A2.11: Result of the Atterberg limits testing according to the Cassagrande diagram. Sample at 195 cm core depth of sediment core MSM47-24-01 is a lean clay with low to intermediate plasticity.

A2.3.2.6 MSM47-24-01, 350-355 CM CORE DEPTH

| <u>Atterberg Limits</u> | |
|-------------------------|-----------------------|
| Analyst name: | <u>Irena Schulten</u> |
| Test date: | <u>19.05.2017</u> |
| Sample description: | <u>MSM47 024 1</u> |
| Sample Number | <u>1</u> |
| Depth (cm) | <u>350-355</u> |
| Water Content (%): | <u>65.90</u> |
| Liquid Limit (%): | <u>48.04</u> |
| Plastic Limit (%): | <u>24.42</u> |
| Plasticity Index (%): | <u>23.62</u> |
| Liquidity Index: | <u>1.76</u> |
| Classification: | <u>CL</u> |

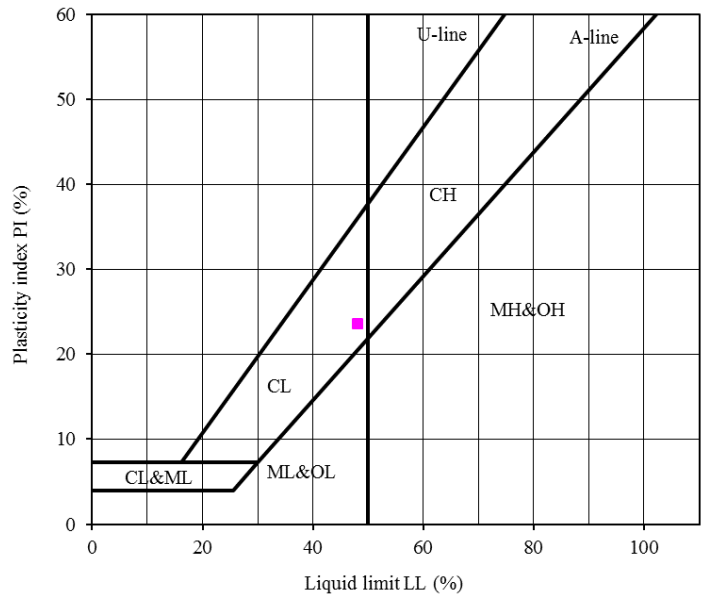


Fig. A2.12: Result of the Atterberg limits testing according to the Cassagrande diagram. Sample at 350-355 cm core depth of sediment core MSM47-24-01 is a lean clay with low to intermediate plasticity.

A2.3.2.7 MSM47-24-01, 355-360 CM CORE DEPTH

| <u>Atterberg Limits</u> | |
|-------------------------|-----------------------|
| Analyst name: | <u>Irena Schulten</u> |
| Test date: | <u>27.05.2017</u> |
| Sample description: | <u>MSM47_024_01</u> |
| Sample Number | <u>4</u> |
| Depth (cm) | <u>355-360</u> |
| Water Content (%): | <u>61.38</u> |
| Liquid Limit (%): | <u>43.71</u> |
| Plastic Limit (%): | <u>23.17</u> |
| Plasticity Index (%): | <u>20.54</u> |
| Liquidity Index: | <u>1.86</u> |
| Classification: | <u>CL</u> |

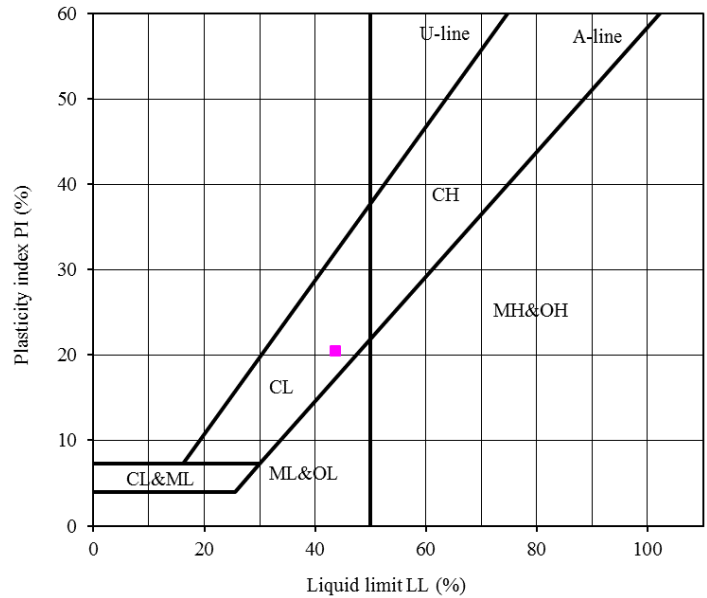


Fig. A2.13: Result of the Atterberg limits testing according to the Cassagrande diagram. Sample at 355-360 cm core depth of sediment core MSM47-24-01 is a lean clay with low to intermediate plasticity.

A2.3.2.8 MSM47-24-01, 712-717 CM CORE DEPTH

| <u>Atterberg Limits</u> | |
|-------------------------|-----------------------|
| Analyst name: | <u>Irena Schulten</u> |
| Test date: | <u>08.06.2017</u> |
| Sample description: | <u>MSM47_024_01</u> |
| Sample Number | <u>5</u> |
| Depth (cm) | <u>712-717</u> |
| Water Content (%): | <u>45.05</u> |
| Liquid Limit (%): | <u>44.47</u> |
| Plastic Limit (%): | <u>21.60</u> |
| Plasticity Index (%): | <u>22.87</u> |
| Liquidity Index: | <u>1.03</u> |
| Classification: | <u>CL</u> |

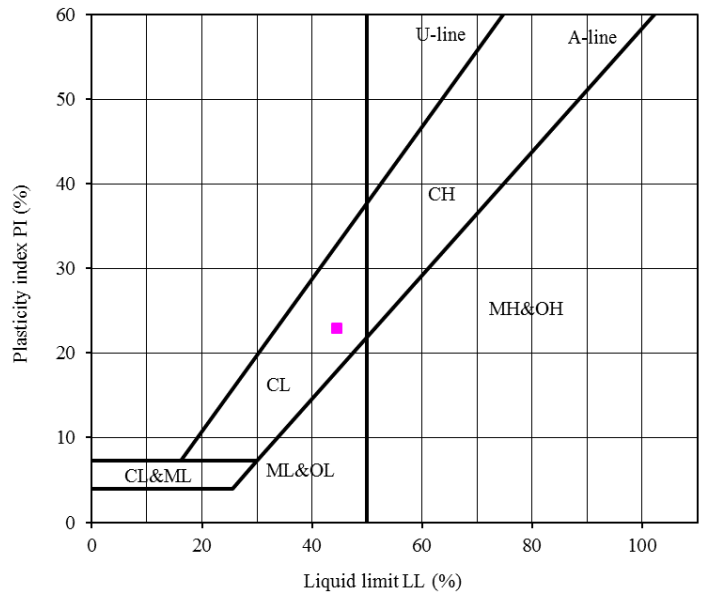


Fig. A2.14: Result of the Atterberg limits testing according to the Cassagrande diagram. Sample at 712-717 cm core depth of sediment core MSM47-24-01 is a lean clay with low to intermediate plasticity.

A2.3.3 Results consolidation testing

A2.3.3.1 2015MSM-0002GC, 553-555.5 CM CORE DEPTH

| | | |
|---|-----------------|--------------------------------|
| Cruise ID: 2015MSM | | |
| Borehole/Core: 0002gc | | |
| Depth (cm): 553-555.5 | | |
| Date: 21-Jan-15 | | |
| Description of Sample: Dark Olive grey Clay | | |
| Condition of Sample: <u>VG</u> | | |
| Test Type: <u>ASTM 2435</u> | | |
| Water Content W_c (%): <u>44.33</u> | | |
| Specific Gravity (measured) : | <u>2.7</u> | Cc: <u>0.37</u> |
| Bulk Density r_w (g/cm ³): | <u>1.81</u> | Cr: <u>0.06</u> |
| Unit Weight g_w (kN/m ³): | <u>17.78</u> | P'o: <u>42.75</u> |
| Dry Density r_d (g/cm ³): | <u>1.26</u> | <u>C_{ce} 0.17</u> |
| Void Ratio: | <u>1.20</u> | P'c (kPa) OCR |
| Porosity (%): | <u>54.59</u> | Cass <u>33</u> <u>0.8</u> |
| Back Pressure (kPa): | <u>200</u> | Work <u>30</u> <u>0.7</u> |
| Calculated $k_{p'c}$ void ratio (m/sec): | <u>1.34E-07</u> | Silva <u>34</u> <u>0.8</u> |
| Liquid Limit (%): | <u>39.62</u> | Prob <u>23</u> <u>0.5</u> |
| Plastic Limit (%): | <u>20.30</u> | Min <u>25</u> <u>0.6</u> |
| Plasticity Index (%): | <u>19.32</u> | Max <u>50</u> <u>1.2</u> |
| Liquidity Index: | <u>1.22</u> | |
| Classification: | <u>CL</u> | |
| Sand %: | <u>NA</u> | |
| Silt %: | <u>NA</u> | |
| Clay %: | <u>NA</u> | |

Fig. A2.15: Summary derived from the consolidation testing on a sample extracted from 553-555.5 cm core depth of sediment core 2015MSM_0002GC. The corresponding $e - \log p'$ curve is shown in Fig. A2.1.

A2.3.3.2 MSM47-24-01, 351-353 CM CORE DEPTH

| | |
|---|------------------------------|
| Cruise ID: <u>MSM47</u> | |
| Borehole/Core: <u>024_01gc</u> | |
| Depth (cm): <u>351-353</u> | |
| Date: <u>2017-May-18</u> | |
| Description of Sample: <u>brown-grey Clay</u> | |
| Condition of Sample: <u>VG</u> | |
| Test Type: <u>ASTM 2435</u> | |
| Water Content w_c (%): <u>64.33</u> | |
| Specific Gravity (measured): <u>2.7</u> | C_c : <u>0.55</u> |
| Bulk Density ρ_w (g/cm ³): <u>1.65</u> | C_r : <u>0.08</u> |
| Unit Weight γ_w (kN/m ³): <u>16.21</u> | $P'_{o'}$: <u>25.20</u> |
| Dry Density ρ_d (g/cm ³): <u>1.01</u> | C_{ce} : <u>0.20</u> |
| Void Ratio: <u>1.78</u> | P'_c (kPa) |
| Porosity (%): <u>63.97</u> | OCR |
| Calculated $k_{p'c}$ void ratio (m/sec): <u>4.63E-07</u> | Cass <u>19</u> <u>0.9</u> |
| Liquid Limit (%): <u>48.04</u> | Work <u>19</u> <u>0.9</u> |
| Plastic Limit (%): <u>24.42</u> | Silva <u>19</u> <u>0.9</u> |
| Plasticity Index (%): <u>23.62</u> | Prob <u>0</u> <u>0.0</u> |
| Liquidity Index: <u>1.76</u> | Min <u>16</u> <u>0.7</u> |
| Classification: <u>CL</u> | Max <u>25</u> <u>1.2</u> |

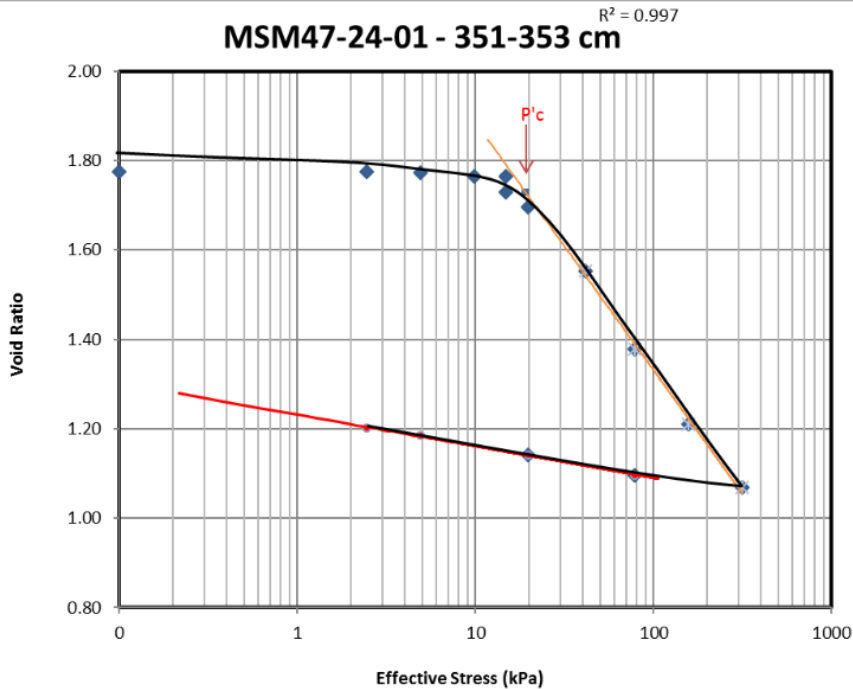


Fig. A2.16: Summary (top) and $e - \log p'$ curve (bottom) derived from the consolidation testing on a sample extracted from 351-353 cm core depth of sediment core MSM47-24-01. Cassagrande's method to derive P'_c over the point of maximum curvature is illustrated.

A2.3.3.3 MSM47-24-01, 357-358.5 CM CORE DEPTH

| | | | |
|--|-------------------|-----|-----|
| Cruise ID: | MSM47 | | |
| Borehole/Core: | 024_01gc | | |
| Depth (cm): | 357-358.5 | | |
| Date: | 2017-May-23 | | |
| Description of Sample: | Brown-grey clay | | |
| Condition of Sample: | VG | | |
| Test Type: | ASTM 2435 | | |
| Water Content w_c (%): | 62.27 | | |
| Specific Gravity (measured): | 2.7 | | |
| Bulk Density ρ_w (g/cm ³): | 1.76 | | |
| Unit Weight γ_w (kN/m ³): | 17.31 | | |
| Dry Density ρ_d (g/cm ³): | 1.09 | | |
| Void Ratio: | 1.53 | | |
| Porosity (%): | 60.46 | | |
| Back Pressure (kPa): | 0 | | |
| Calculated $k_{p'c}$ void ratio (m/sec): | 5.35E-07 | | |
| Liquid Limit (%): | 43.71 | | |
| Plastic Limit (%): | 23.17 | | |
| Plasticity Index (%): | 20.54 | | |
| Liquidity Index: | 1.86 | | |
| Classification: | CL | | |
| | C_c : 0.52 | | |
| | C_r : 0.06 | | |
| | $P'_{o'}$: 25.92 | | |
| | C_{ce} : 0.20 | | |
| | $P'c$ (kPa) | OCR | |
| | Cass | 24 | 0.9 |
| | Work | 18 | 0.7 |
| | Silva | 27 | 1.0 |
| | Prob | 0 | 0.0 |
| | Min | 21 | 0.8 |
| | Max | 32 | 1.2 |

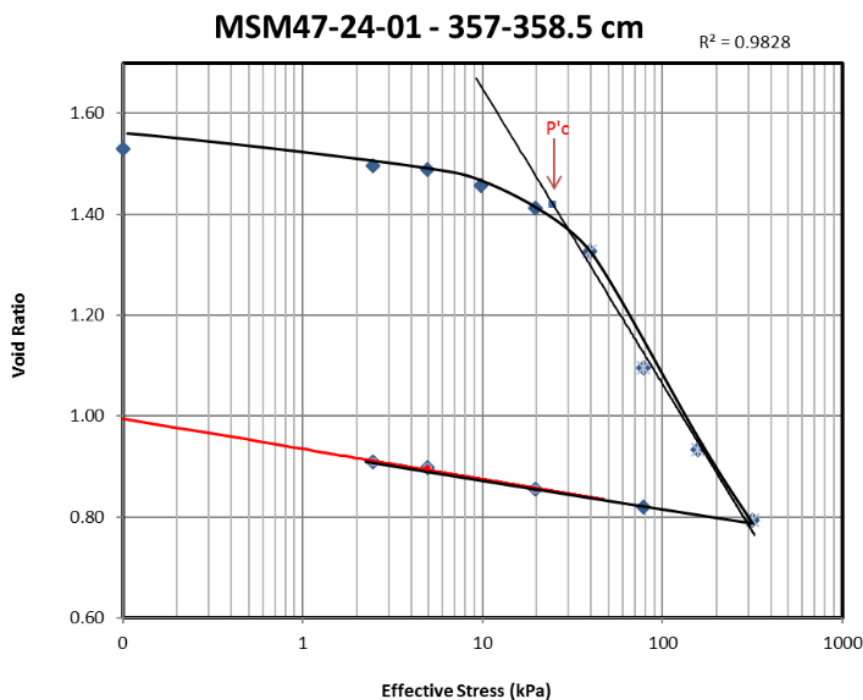


Fig. A2.17: Summary (top) and $e - \log p'$ curve (bottom) derived from the consolidation testing on a sample extracted from 357-358.5 cm core depth of sediment core MSM47-24-01. Cassagrande's method to derive $P'c$ over the point of maximum curvature is illustrated.

A2.3.3.4 MSM47-24-01, 713-714.5 CM CORE DEPTH

| | | | |
|--|-------------------------------------|-----------|------------|
| Cruise ID: | MSM47 | | |
| Borehole/Core: | 024_01gc | | |
| Depth (cm): | 713-714.5 | | |
| Date: | 2017-June-07 | | |
| Description of Sample: | Slight stiff dark greyish brown mud | | |
| Condition of Sample: | <u>VG</u> | | |
| Test Type: | <u>ASTM 2435</u> | | |
| Water Content w_c (%): | <u>43.60</u> | | |
| Specific Gravity (measured): | <u>2.7</u> | | |
| Bulk Density ρ_w (g/cm ³): | <u>1.75</u> | | |
| Unit Weight γ_w (kN/m ³): | <u>17.20</u> | | |
| Dry Density ρ_d (g/cm ³): | <u>1.22</u> | | |
| Void Ratio: | <u>1.26</u> | | |
| Porosity (%): | <u>55.84</u> | | |
| Calculated $k_{p'c}$ void ratio (m/sec): | <u>2.03E-07</u> | | |
| Liquid Limit (%): | <u>44.47</u> | | |
| Plastic Limit (%): | <u>21.60</u> | | |
| Plasticity Index (%): | <u>22.87</u> | | |
| Liquidity Index: | <u>1.03</u> | | |
| Classification: | <u>CL</u> | | |
| | C_c : <u>0.33</u> | | |
| | C_r : <u>0.06</u> | | |
| | $P'_{o'}$: <u>51.01</u> | | |
| | C_{ce} : <u>0.15</u> | | |
| | P'_{c} (kPa) | OCR | |
| | Cass | <u>28</u> | <u>0.5</u> |
| | Work | <u>25</u> | <u>0.5</u> |
| | Silva | <u>28</u> | <u>0.5</u> |
| | Prob | <u>0</u> | <u>0.0</u> |
| | Min | <u>19</u> | <u>0.4</u> |
| | Max | <u>50</u> | <u>1.0</u> |

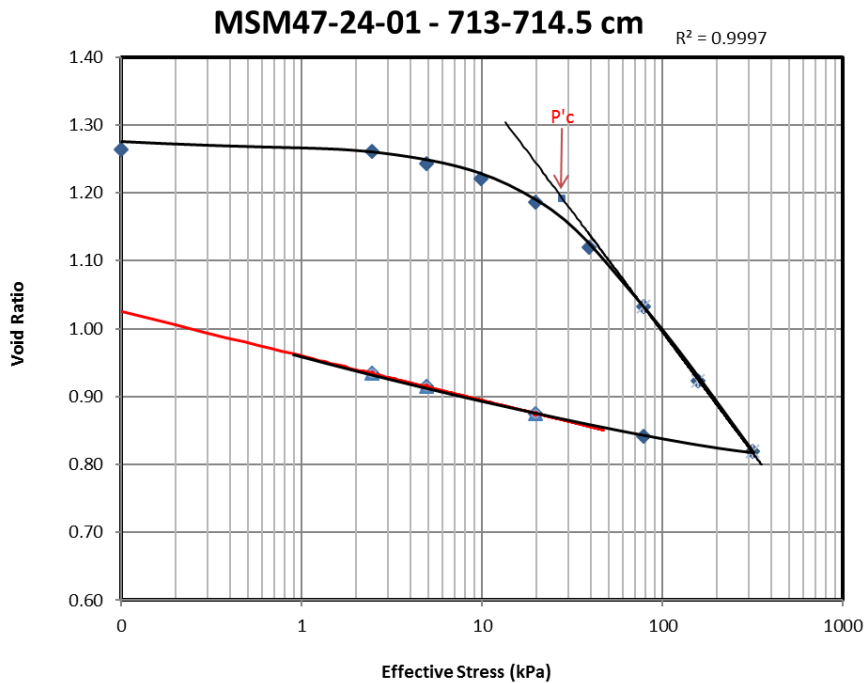


Fig. A2.18: Summary (top) and $e - \log p'$ curve (bottom) derived from the consolidation testing on a sample extracted from 713-714.5 cm core depth of sediment core MSM47-24-01. Cassagrande's method to derive P'_{c} over the point of maximum curvature is illustrated.

A2.3.4 Results Triaxial testing

A2.3.4.1 2015MSM_0002GC, 116.5-128 CM CORE DEPTH

| Sample Identification | | | |
|--|---------------------------------|-------------------------------------|-------------|
| Cruise ID: | 2015MSM | | |
| Borehole/Core: | 0002gc | | |
| Test No: | 0 | | |
| Depth (cm): | 116.5-128 | | |
| Description of Sample: | <u>dark grey mud (10YR 4/1)</u> | | |
| Condition of Sample: | <u>0.000</u> | | |
| Test Type: | <u>CU multistage test</u> | | |
| Date: | <u>26th September 2016</u> | | |
| Water Content Salt corr W_c (%): | <u>43.85</u> | Φ' : | <u>26.8</u> |
| Diameter of Sample (cm): | <u>4.78</u> | C': | <u>0.0</u> |
| Bulk Density ρ_w (g/cm ³): | <u>1.82</u> | Su/σ'_v | <u>0.32</u> |
| Unit Weight γ_w (kN/m ³): | <u>17.90</u> | $Su/\sigma'_{v(corr)}$: | <u>0.25</u> |
| Dry Density ρ_d (g/cm ³): | <u>1.27</u> | A_f : | <u>0.18</u> |
| Void Ratio: | <u>0.00</u> | Initial Young's modulus E_i (mPa) | <u>3.7</u> |
| Porosity (%): | <u>54.45</u> | Young's modulus E_{50} = | |
| Back Pressure (kPa): | <u>390.0</u> | Poisson ratio n = | |
| Saturation Coefficient (B value): | <u>0.97</u> | | |

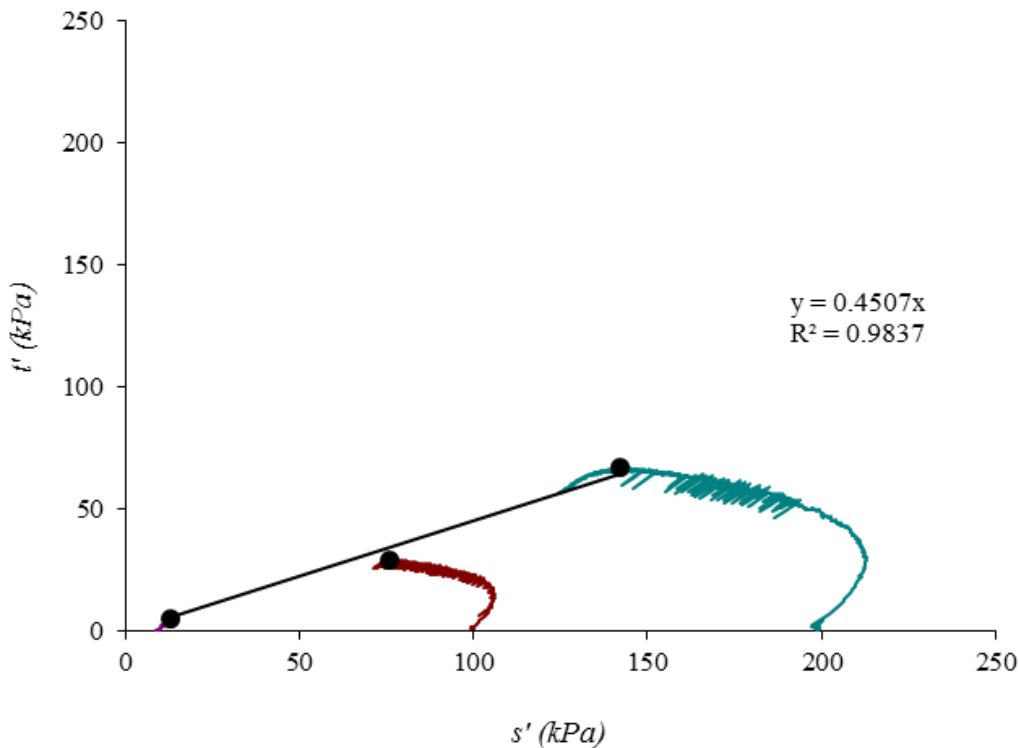


Fig. A2.19: Summary (top) and the Mohr Coloumb failure envelope (bottom) derived from the triaxial testing on a sample extracted from 116.5-128 cm core depth of sediment core 2015MSM_0002GC.

A2.3.4.2 2015MSM_0002GC, 563-575 CM CORE DEPTH

| Sample Identification | |
|--|---|
| Cruise ID: 2015MSM | |
| Borehole/Core: 0002GC | |
| Test No: 1 | |
| Depth (cm): 563-575cm | |
| Description of Sample: <u>Olive Grey Soft Clay</u> | |
| Condition of Sample: <u>good</u> | |
| Test Type: <u>CU multistage test</u> | |
| Date: <u>10-02-2016</u> | |
| Water Content Salt corr W_c (%): <u>46.38</u> | Φ' : <u>27.9</u> |
| Diameter of Sample (cm): <u>4.80</u> | C' : <u>2.7</u> |
| Bulk Density ρ_w (g/cm^3): <u>1.79</u> | Su/σ'_v : <u>0.38</u> |
| Unit Weight γ_w (kN/m^3): <u>17.60</u> | $Su/\sigma'_{v(corr)}$: <u>0.30</u> |
| Dry Density ρ_d (g/cm^3): <u>1.23</u> | A_f : <u>0.47</u> |
| Void Ratio: <u>1.27</u> | Initial Young's modulus E_i (mPa) <u>13.2</u> |
| Porosity (%): <u>56.00</u> | Young's modulus E_{50} = <u>13.9</u> |
| Back Pressure (kPa): <u>390.0</u> | Poisson ratio n = <u>N/A</u> |
| Saturation Coefficient (B value): <u>0.97</u> | |

Fig. A2.20: Summary derived from the triaxial testing on a sample extracted from 563-575 cm core depth of sediment core 2015MSM_0002GC. The derived Mohr Coloumb failure envelope is shown in Fig. A2.4.

A2.3.5 Infinite Slope stability Analysis – Magnitude-PGA conversions

Table A2.1: PGA (g) using equations from Atkinson and Boore (2006).

| magnitude: | 8.0 | 7.2 | 6 | 5 | 4 |
|----------------|------|------|------|------|------|
| distance (km): | | | | | |
| 26 | 0.24 | 0.20 | 0.13 | 0.04 | 0.01 |
| 20 | 0.27 | 0.23 | 0.16 | 0.06 | 0.01 |
| 10 | 0.30 | 0.26 | 0.18 | 0.09 | 0.02 |
| 5 | 0.31 | 0.27 | 0.19 | 0.10 | 0.03 |

Table A2.2: PGA (g) using equations from Campbell and Borzognia (2008).

| magnitude: | 8.0 | 7.2 | 6 | 5 | 4 |
|----------------|------|------|------|------|------|
| distance (km): | | | | | |
| 26 | 0.17 | 0.13 | 0.08 | 0.03 | 0.01 |
| 20 | 0.19 | 0.16 | 0.10 | 0.04 | 0.02 |
| 10 | 0.24 | 0.20 | 0.13 | 0.06 | 0.02 |
| 5 | 0.25 | 0.21 | 0.14 | 0.07 | 0.03 |